“Development of a Multi-Modular siRNA Carrier System for Epidermal Growth Factor Receptor Specific Delivery”

Inaugural Dissertation

zur

Erlangung des Doktorgrades
Dr. nat. med.

der Medizinischen Fakultät
und
der Mathematisch-Naturwissenschaftlichen Fakultät
der Universität zu Köln

vorgelegt von

Felix Alexander Heß
aus Köln

2026

Betreuer/Betreuerin:	Prof Dr. Dr. Michal R. Schweiger
Referent/Referentin:	Prof. Dr. Ines Neundorf
	Prof. Dr. Renata Stripecke
Datum der mündlichen Prüfung:	09.03.2026

„Wer kämpft, kann verlieren. Wer nicht kämpft, hat schon verloren.“

- Bertolt Brecht -

Dedicated to my beloved family.

Acknowledgement

This report documents my research work carried out between May 2022 and September 2025 at the Institute for Translational Epigenetics under the supervision of Prof. Dr. Dr. Michal-Ruth Schweiger.

I would like to express my special thanks to Prof. Dr. Dr. Michal-Ruth Schweiger for assigning me this interesting topic, as well as for her intensive supervision, inspiring leadership and all the productive discussions. I would also like to thank Prof. Dr. Ines Neundorf and Prof. Dr. Renata Stripecke for their supervision within the framework of the Interdisciplinary Postgraduate Program in Molecular Medicine (IPMM).

Additionally, I would like to thank the members of the Schweiger lab for their collegial support, the amusing lunch breaks and for the pleasant working atmosphere during the practical laboratory phase.
First, I thank Elena Wasserburger-Zichel for an amazing support in the lab.
Special thanks go to Prof. Dr. Dr. Michal-R. Schweiger, Dr. Christina Grimm, and Fee Sophia Heß for their critical review of this work.

Moreover, I would like to thank Prof. Dr. Ines Neundorf, Prof. Dr. Stefanie Kath-Schorr, Prof. Dr. Margarete Odenthal, and Prof. Dr. Renata Stripecke for their support and for the many productive discussions and cooperations.

I would like to thank the members of the Kath-Schorr lab for their support and for synthesizing the RNAs and linkers used.
Special thanks go to Dr. Christof Domnick for his outstanding cooperation.

I would like to thank the members of the Stripecke lab for their support and assistance in carrying out CRISPR Cas9 gene editing.
Special thanks go to Michael Damrat for his great cooperation.

Finally, I would like to express my deepest gratitude to my family, who made it possible for me to study molecular biomedicine and biotechnology and complete my doctorate. I am grateful every day for your support, your motivating words and your unwavering trust. Without you, none of this would have been possible.

Danksagung

Die vorgelegte Arbeit dokumentiert meine Forschungsergebnisse, die ich zwischen Mai 2022 und September 2025 am Institut für Transaltionale Epigenetik unter der Leitung von Prof. Dr. Dr. Michal-Ruth Schweiger gewonnen habe.

Mein besonderer Dank gilt Prof. Dr. Dr. Michal-Ruth Schweiger für die Zuweisung dieses interessanten Themas sowie für ihre intensive Betreuung, ihre inspirierende Führung und all die produktiven Diskussionen. Ich möchte mich auch bei Prof. Dr. Ines Neundorf und Prof. Dr. Renata Stripecke für ihre Betreuung im Rahmen des Interdisziplinären Postgraduiertenprogramms Molekulare Medizin (IPMM) bedanken.

Außerdem möchte ich den Mitgliedern des Schweiger-Labors für ihre kollegiale Unterstützung, die unterhaltsamen Mittagspausen und die angenehme Arbeitsatmosphäre während der praktischen Laborphase danken.
Ganz besonders danke ich Elena Wasserburger-Zichel für ihre großartige Unterstützung im Labor.
Besonderer Dank gilt Prof. Dr. Dr. Michal-R. Schweiger, Dr. Christina Grimm und Fee Sophia Heß für ihre kritische Durchsicht dieser Arbeit.

Prof. Dr. Ines Neundorf, Prof. Dr. Stefanie Kath-Schorr, Prof. Dr Margarete Odenthal und Prof. Dr. Renata Stripecke danke ich für ihre Unterstützung sowie für die vielen produktiven Diskussionen und Kooperationen.

Den Mitgliedern der Arbeitsgruppe Kath-Schorr danke ich für ihre Unterstützung und für die Synthese der verwendeten RNAs und Linker. Ein Besonderer Dank gilt Prof. Dr. Stefanie Kath-Schorr für die positive Kooperation.
Mein besonderer Dank gilt Dr. Christof Domnick für die hervorragende Zusammenarbeit.

Den Mitgliedern der Arbeitsgruppe Stripecke danke ich für ihre Unterstützung und Hilfe bei der durchführung des CRISPR Cas9 Gen Editings.
Mein besonderer Dank gilt Michael Damrat für die hervorragende Zusammenarbeit.

Abschließend möchte ich meiner Familie meinen tiefsten Dank aussprechen, die es mir ermöglicht hat, Molekulare Biomedizin und Biotechnologie zu studieren und meine Promotion abzuschließen. Ich bin jeden Tag dankbar für eure Unterstützung, eure motivierenden Worte und euer unerschütterliches Vertrauen.
Ohne euch wäre all dies nicht möglich gewesen.

Table of contents

1 Abstract

Long non-coding RNAs (lncRNAs) transcribed from pericentromeric satellite repeats III (HSat3) are involved in stress-responsive splicing mechanisms and the preservation of genome stability. Elevated levels of HSat3 RNA have been observed across various cancer types, as well as under heat stress conditions and chemotherapeutic induced cytotoxic stress. Clinically, increased expression of satellite RNAs is detectable in multiple cancer tissues. Additionally, induction of murine major Satellites has been shown to accelerate tumour onset in mice, resulting in reduced survival rates. Moreover, HSat3 transcripts are linked with the resistance to the topoisomerase 2a (TOP2A) inhibitor etoposide in non-small cell lung cancer (NSCLC). Recently, novel regulators of HSat3 expression have been discovered. When combined with etoposide, these agents can reverse therapy resistance and effectively inhibit cell proliferation. However, achieving tumor-specific delivery of such agents remains challenging. Therefore, this project aims to develop a receptor-targeted, multi-modular siRNA delivery system to address this issue. Since compound development depends on the effectiveness of its development platform, this work is divided into two parts: Establishing a new compound development platform (Section One) and developing an siRNA delivery system targeting epidermal growth factor receptor (EGFR) (Section Two). The initial section demonstrates the successful development of a sensitive dual fluorescence-based assay called FluoroDetect. The assay is designed to evaluate small interfering RNAs (siRNAs), antisense oligonucleotides (ASOs), and RNA-binding compounds. Assay results can be obtained using fluorescence microscopy, plate readers, or flow cytometry, enabling quantification of knockdown efficiency. Consequently, the FluoroDetect assay serves as a valuable tool for screening nucleic acid drug candidates and aids in optimizing and quantifying nucleic acid delivery in therapies. The second section outlines the development of an aptamer-siRNA conjugate against HSat3 RNA utilizing solid-phase synthesis, in vitro transcription, and hybrid approaches. All drug candidates were assessed using *in vitro* cell culture models. The final nucleic-acid based conjugate successfully targets EGFR positive cells and is incorporated into the cells, but faces limitations related to endosomal escape. In sum, in this thesis I was able to develop tools for NA-based compound selections and provide first steps towards a HSat3-directed aptamer treatment.

2 Zusammenfassung

Lange nicht-kodierende RNAs (lncRNAs), die von perizentromeischen Satelliten III-Repeats (HSat3) transkribiert werden, sind an stressabhängigen Spleißmechanismen und der Erhaltung der Genomstabilität beteiligt. Erhöhte HSat3-RNA-Spiegel wurden bei verschiedenen Krebsarten sowie unter Hitzestressbedingungen und bei cytototoxischem Stress durch chemotherapeutische Behandlung beobachtet. Darüber hinaus wurde gezeigt, dass die Induktion von murinen Hauptsatelliten das Tumorauftreten bei Mäusen beschleunigt, was zu einer Verringerung der Überlebensraten führt. HSat3-Transkripte stehen auch im Zusammenhang mit der Resistenz gegen den Topoisomerase-2a-Inhibitor (TOP2A) Etoposid bei nicht-kleinzelligem Lungenkrebs (NSCLC). Kürzlich wurden neue Regulatoren der HSat3-Expression entdeckt. In Kombination mit Etoposid können diese Wirkstoffe die Therapieresistenz aufheben und die Zellproliferation wirksam hemmen. Die tumorspezifische Verabreichung solcher Wirkstoffe stellt jedoch nach wie vor eine Herausforderung dar. Daher zielt dieses Projekt darauf ab, ein tumorzellspezifisches, modulares siRNA-Verabreichungssystem zu entwickeln, um dieses Problem zu lösen. Da die Entwicklung von Wirkstoffen von der Effektivität der Entwicklungsplattform abhängt, gliedert sich diese Arbeit in zwei Teile: Der erste Abschnitt zeigt die erfolgreiche Entwicklung eines sensitiven dualen Fluoreszenz-basierten Assays namens FluoroDetect. Der Assay wurde entwickelt, um kleine interferierende RNAs (siRNAs), Antisense-Oligonukleotide (ASOs) und RNA-bindende Verbindungen zu evaluieren. Die Assay-Ergebnisse können mittels Fluoreszenzmikroskopie, Plattenlesegeräten oder Durchflusszytometrie über mehrere Zeitpunkte hinweg quantifiziert werden. Der zweite Abschnitt beschreibt die Entwicklung eines Aptamer-siRNA-Konjugats unter Verwendung von Festphasensynthese, In-vitro-Transkription und Hybridansätzen. Alle Wirkstoffkandidaten wurden anhand von In-vitro-Zellkulturmodellen bewertet. Es konnte gezeigt werden, dass die Kandidaten erfolgreich und spezifisch in EGFR – positive Zellen aufgenommen wird. In weiterführenden Experimenten muss für eine effektive Anwendung die endosomale Freisetzung verbessert werden. Insgesamt konnten damit wichtige Grundlagen für die Entwicklung einer nukleinsäure-basierten, gegen HSat3 gerichtete und spezifisch für EGFR-positive Zellen angesetzte Therapie gelegt werden.

3 Introduction

3.1 Cancer - Facts and Numbers

With an incidence of 19,98 million new cases and 9,7 million deaths worldwide in 2022 cancer still remains one of the biggest burdens of humanity.[1,2] To put this in relation this are approximately 137% of all COVID19 associated deaths or 105% of the Austrian population every year.[3,4] Despite better healthcare in industrialized countries, 85% of all cancer cases and 83.7% of all cancer deaths occurred in Asia, North America, and Europe in 2022.[1,2] Combined with the demographic changes, in fact an aging population, this draws a frightening picture. The world health organization (WHO) prognoses an increase of the incidence by 76,6% and an increase of the word wide cancer deaths by 89,7% till 2050.[5,6] In numbers this are 18,5 million people every year, which actually equals the todays population of the Netherlands.[7] Summing this up is not just a human tragedy but also a financial. As projected in JAMA Oncology in 2020, cancer will cost 25.2 trillion international dollars (int$) till 2050.[8,9] What is equal to a cost of 26.612 int$ per second from 2020 to 2050. These emerging numbers underline the necessity to improve cancer therapies and reducing their cost to create a better tomorrow. To do so a deeper understanding of pathological processes in tumor tissues as well as about carcinogenesis is indispensable, as this identifies new targets and prediction markers.

Carcinogenesis is a complex biological reaction caused by the accumulation of mutations in genes and the dysregulation of regulatory mechanisms. The causes of these processes can be manifold and may lie, for example, in environmental influences or genetic predisposition. In this context, mechanisms such as epigenetics, which influence the function of the genome, must also be considered.[10,11] The characteristics of tumor cells defined by *Hanahan and Weinberg*, are summarized in the so-called '*Hallmarks of Cancer*' and include[10]:

1.	Self-sufficiency in growth signals	**6.**	Massive tissue invasion
2.	Resistance to growth inhibitors	**7.**	Genomic in-stability
3.	Resisting cell death	**8.**	Immune evasion
4.	Unlimited replication potential	**9.**	Inflammation
5.	Angiogenesis	**10.**	Metabolic dysregulation

Some of the characteristics listed in the '*Hallmarks of Cancer*' are closely related to epigenetic regulatory mechanisms.[12,13] For example, tumor suppressor genes are often inactivated by deoxyribonucleic acid (DNA) methylation while repetitive DNA regions are demethylated, which can lead to genomic instability. Another example of epigenetic deregulation is the proteotoxic

stress response, which is a crucial metabolic process in the development of therapy resistance. Therapy resistance which for example often occurs in lung cancer, the most common cancer worldwide in 2022 with an global incidence of 12,4%.[2]

3.2 Non-Small Cell Lung Cancer

With 85% of lung cancer cases, non-small cell lung cancer (NSCLC) accounts for the majority of lung cancer cases. With its high frequency NSCLC is not only the most common type of lung cancer, but also the most common cause of cancer deaths, accounting for 18.7% of all cancer deaths in 2022.[14] This is not only due to the high frequency but also to the low progression-free survival (PFS). For example, the 50% PFS in the case of standard chemotherapy is 4.6 months and, despite new target therapy approaches, can only be extended to 13.1 months.[15] This poor prognosis is mainly caused by the resistance to chemotherapy that often develops within the first year.[16] Even today, the 5-year survival rate for NSCLC is still low at 32%.[17] This means that non-small cell lung cancer is one of the tumors with a poor prognosis and difficult to treat.[18] A decisive step towards improving prognosis and increasing treatment success is therefore the revision of chemotherapy resistance in tumor tissue and the resulting higher treatment response.

3.3 Repetitive Elements

As previously mentioned, a deeper understanding of pathological process in tumor tissues as well as about carcinogenesis is indispensable to improve cancer therapies. For example, improvements to overcome therapy resistance. So, for better understanding a closer look to the human genome is necessary.

The human genome contains 98% non-protein coding regions of which 51-71% can be categorized as repetitive DNA.[19-21] A specific DNA sequence which repeats multiple times in the genome is called repetitive DNA or a repetitive element. Depending on the type and length of the repetition, repetitive elements are categorized differently. A distinction is made between units that occur consecutively (‘tandem’) and those that occur sporadically (‘interspersed’ or ‘dispersed’).[22-24] Both groups can be divided into further subgroups (e.g. telomeres, minisatellites and satellite DNAs (satDNA)).[22,25] A detailed classification of repetitive elements can be found in **Figure 1**. What they all have in common is that the ribonucleic acid (RNA) transcribed from the repetitive elements is also structurally repetitive. One basis for this work is the satDNA, which belongs to the tandem repetitive elements.

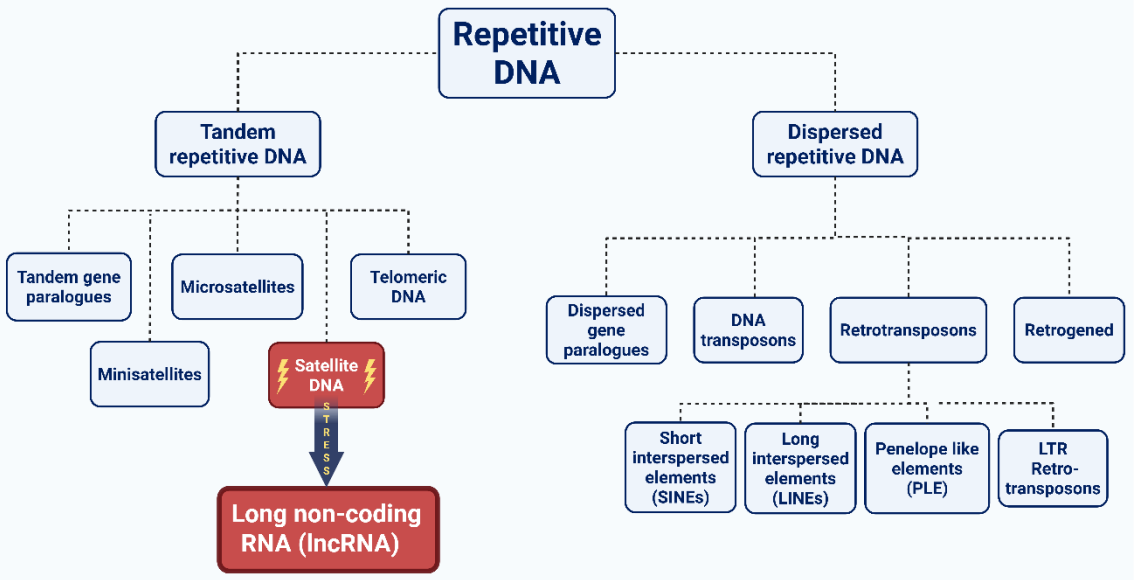

Figure 1 Classification hierarchy of repetitive DNAs. *Repetitive DNAs are divided into two major subgroups, the tandem repetitive DNAs and the dispersed repetitive DNAs. One subclass of the tandem repetitive DNAs are the so-called Satellite DNAs. Satellite DNAs are transcribed under stress conditions as long non-coding RNAs (lncRNAs).*

3.4 Satellite DNA

Despite the fact that human satellites have been the first biochemically characterized and isolated human DNA sequences they are still poorly understood. Which was mainly caused by the limitations of DNA sequencing and assembling during the genomics era.[26] These limitations were overcome when 2022 the Telomere-to-Telomere (T2T) consortium published the first human genome which assembled all satellite sequences.[27] Although the T2T genome has improved our current understanding of satellite DNA, there are still many unknowns. In former times satDNA got its name from its behavior during density gradient centrifugation, in which the satDNA separates from the main DNA as a single band due to its high AT content.[28] As already mentioned, satDNA belongs to the tandem repetitive elements and is often located in transcriptionally inactive heterochromatic regions. Moreover, it can be recognized as a long repetitive sequence.[29] The subdivision of satDNA is based on the varying complexity of the monomer structures of the repetitive elements. Human α-satellites, for example, can be identified by a 171-base pair (bp) long monomer, which functions as the main structural element of centromeric and pericentromeric regions.[30] In contrast, the human satellite II and III sequences can be identified by their short 10 bp and 5 bp monomers.[26,31] Specific satDNA repeats are located in centromeric and more specific pericentromeric regions.[26,32,33] Functionally, the involvement of satDNA transcripts in kinetochore assembly, telomere regulation, heterochromatin establishment, transcriptional stress response, and gene expression has been observed.[26,34,35] In particular, it was shown that a general stress response in human cells is accompanied by the transcription of satellite III non-coding RNA (HSat3 RNA).[36]

3.5 Human Satellite 3 RNA

The HSat3 RNA which is in focus of this work has a monomeric repeat sequence defined as the motif $(CATTC)_n$ with n describing the number of tandem repeats.[26] Despite the presence of HSat3 DNA in the pericentromeric regions of seven chromosomes (9, 13, 14, 15, 21, 22 and Y) HSat3 RNA is under stress conditions mainly transcribed from its largest DNA locus on chromosome nine (9q12).[36] Surprisingly there is a significantly higher transcription of the C-rich HSat3 DNA strand creating a tremendous amount of G-rich HSat3.[36] Fascinatingly the transcribed HSat3 RNA stays associated with the transcription locus on chromosome nine. The local increase of RNA & proteins causes a liquid-liquid phase separation, leading to the formation of membrane less compartments, also called nuclear stress bodies (nSBs).[37] The formation of such nSBs is defined by the recruitment of heat shock factor 1 (HSF1) as well as HSat3 RNA and is frequent observed in the proteotoxic stress response (PSR).[38-41] A schematic structure of nSBs is shown in **Figure 2**. An epigenetic dysregulation which avoids cell death as mentioned in the '*Hallmarks of Cancer*'. Moreover, the PSR is involved in the development of therapy resistance.

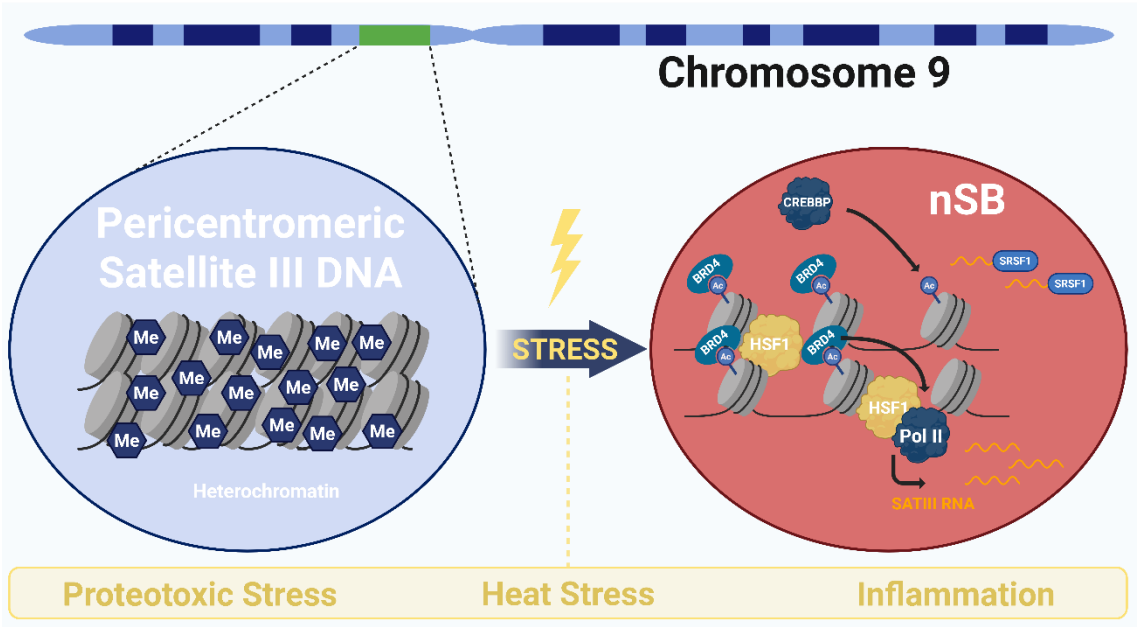

Figure 2 Schematic structure of the pericentromeric nuclear stress bodies (nSBs) in human cells. *The Human Satellite 3 DNA (HSat3) located in the pericentromeric region of Chromosome 9 is heavily transcribed under Proteotoxic, Heat and inflammation related stress conditions. The recruitment of various proteins as well as the local increase of HSat3 RNA leads to the formation of this membrane less compartments by liquid-liquid phase separation.*

The affected cells are triggered by toxins during the PSR. Toxins such as cytostatic drugs, which leads to a state of stress similar to that experienced during the heat shock response (HSR).[42] Another common observation in malignant tissues is the loss of methylation in repetitive sequences such as the satellite repeats.[43] In patients derived xenograft (PDX) mouse models of NSCLC patients the hypomethylation of pericentromeric HSat3 DNA and the resulting increased

expression of HSat3 RNA, was correlated with the resistance to etoposide treatment. Furthermore, it has been observed that a small interfering RNA (siRNA) targeting HSat3 RNA, increases sensitivity to etoposide in cell culture models.[44]

3.6 The Mechanism of RNA Interference

With the identification of HSat3 RNA as a therapeutic target to reverse chemotherapy resistance, RNA interference (RNAi) is becoming the focus of attention. To improve understanding, the following mechanisms must be considered: The RISC (RNA-induced silencing complex)-dependent and the RISC-independent mechanism. When focusing on the RISC-dependent mechanism, the endogenous occurrence of this pathway during interaction with microRNAs (miRNAs) must first be considered. MicroRNAs (miRNAs) are a class of small, non-coding RNAs that play a central role in post-transcriptional gene regulation by guiding the RISC to target messenger RNAs (mRNAs) for degradation or translational repression. The biogenesis of miRNAs begins in the nucleus, where primary miRNA transcripts (pri-miRNAs) are synthesized predominantly by RNA Polymerase II.[45] These pri-miRNAs are processed by the microprocessor complex, composed of the RNase III enzyme DROSHA and its cofactor DGCR8, which cleaves the stem-loop structure of the pri-miRNA to generate precursor miRNAs (pre-miRNAs) of approximately 70 nucleotides.[46] The pre-miRNA is then exported to the cytoplasm via Exportin-5 (XPO5) in a Ran-GTP–dependent manner.[47] In the cytoplasm, the pre-miRNA undergoes further cleavage by DICER, another RNase III enzyme, which removes the terminal loop to produce a ~22-nucleotide miRNA duplex.[48] One strand of this duplex, known as the guide strand, is selectively loaded into the RISC complex, where it associates with Argonaute 2 (Ago2), the catalytic core of RISC. Ago2 facilitates the recognition of complementary sequences within target mRNAs, leading to either endonucleolytic cleavage (in cases of near-perfect complementarity) or translational repression and mRNA destabilization via deadenylation and decapping.[49-51] This finely tuned regulatory mechanism is essential for diverse biological processes including development, differentiation and disease pathogenesis. The dysregulation of miRNA gene Regulation has been implicated in various cancers and neurological disorders.[52] A schematic overview of this process is shown in **Figure 3**.

Unlike miRNAs siRNAs do not need processing through the DROSHA and DICER as these therapeutic compounds are already tailored for a direct interaction with Ago2. As mentioned earlier there is a mechanistically RISC independent alternative to canonical small interfering RNA (siRNA) approaches. Unlike siRNAs, which require incorporation into the RNA-induced silencing complex (RISC) and subsequent endonucleolytic cleavage of target transcripts by Ago2, Antisense oligonucleotides (ASOs) and gapmers primarily exert their effects via recruitment of endogenous ribonucleases hybrid 1 (RNase H1). Gapmers are chimeric oligonucleotides composed

of a central DNA region flanked by chemically modified ribonucleotides (e.g. locked nucleic acids (LNAs) or 2'-O-methyl RNA) that enhance target affinity and confer nuclease resistance.[53,54] Upon hybridization to complementary RNA sequences, the DNA-RNA duplex is recognized by RNase H1, which selectively cleaves the RNA strand, leading to transcript degradation and suppression of protein expression.

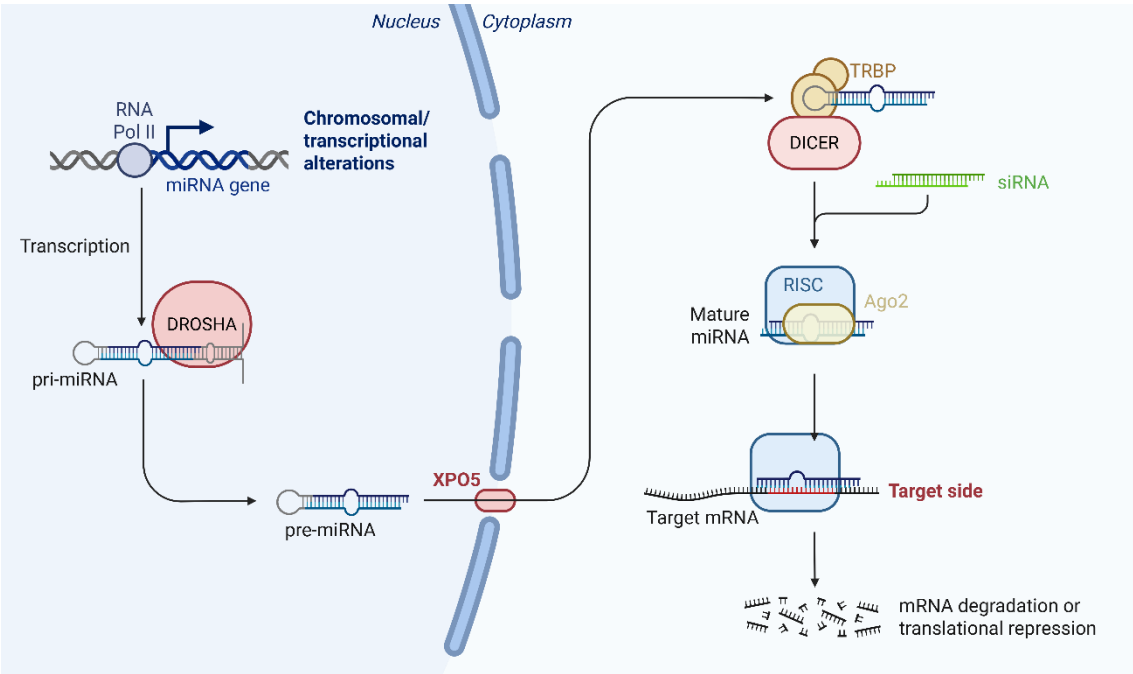

Figure 3 Schematic figure of the endogenous miRNA gene regulation pathway. *The miRNA gene is transcribed into pri-miRNA. The pri-miRNA is processed by the DROSHA to the pre-miRNA. The pre-miRNA is transported through the Exportin 5 (XPO5) into the cytoplasm. Reported by TRBP the pre-miRNA is further processed by the DICER to the mature miRNA. The mature miRNA can interact with the Argonaut 2 (Ago2) promoting the formation of the RNA induced silencing complex (RISC). The RISC mediates a sequence specific gene regulation. The miRNA maturation can be bypassed by a synthetic siRNA, which immediately interacts with the Ago2 without intracellular preprocessing.*[55]

In addition to RNase H1–mediated cleavage, ASOs may also function through steric blockade of RNA-binding proteins or spliceosomal components, thereby modulating pre-mRNA splicing or inducing exon skipping.[56] Such alterations can result in the introduction of premature termination codons and activation of nonsense-mediated decay (NMD), further reducing transcript abundance.[57] Notably, gapmer binding may also influence local RNA secondary structure and accessibility, potentially affecting the efficacy of other oligonucleotides targeting adjacent regions.[58] These RISC independent mechanisms expands the therapeutic versatility of oligonucleotide-based interventions.

3.7 siRNA Therapeutics – State of The Art

The versatility of RNA therapeutics and oligonucleotide-based interventions is underlined by the steadily increasing amount of clinical trials and approvals of RNA-based drugs. Since the Food and Drug Administration (FDA) approved the first siRNA-based therapy in 2018 (Onpattro™ - Patisiran) there have been 36 clinical approvals and 1,297 preclinical and clinical candidates up

to now (Q2 2025, including 14 mRNA vaccines).[59] Specifically, these new tools are being applied to monogenic disorders as well as infectious and oncologic diseases.[59] Despite its broad indication spectrum the targeted delivery of siRNA therapeutics and oligonucleotide-based interventions still remains challenging thereby limiting its field of application. The landscape of siRNA- and oligonucleotide-based drugs is shown in **Figure 4**. One major limitation is the instability of RNA under physiological conditions, which can be addressed through chemical modifications that enhance its stability. A second, and currently more challenging issue, is the endosomal escape problem, which prevents RNA from reaching its target site inside cells. This remains one of the biggest bottlenecks in the development of effective RNA-based therapies.

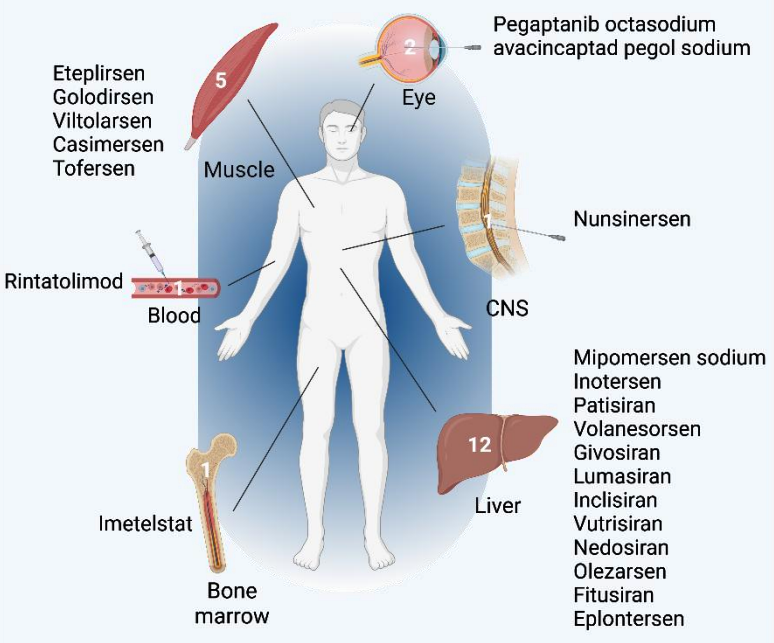

Figure 4 The landscape of siRNA- and oligonucleotide-based drugs. *Schematic figure showing the numbers of FDA approved therapies and their target tissues. (Based on ASGCT Landscape Report 2025 Q2)*

3.8 The Endosomal Escape Problem

Unlike small-molecule drugs, siRNAs and ASOs are large, negatively charged, and hydrophilic, which prevents them from passively diffusing across cell membranes. Instead, they need to be internalized via endocytosis. Endocytosis through endosomes that rarely permit escape into the cytosol. Quantitative studies have shown that less than 1% of internalized siRNA or ASO molecules successfully escape the endosome to reach their site of action.[60,61] This inefficiency significantly limits therapeutic efficacy and necessitates higher dosing, which can increase the risk of off-target effects and toxicity. Despite this challenge, several siRNA-based therapies have received approval from the FDA, primarily for liver-targeted indications. The liver is particularly amenable to siRNA delivery due to its high passive targeting rate, high endocytic activity and the presence of specific receptors that facilitate uptake. For example, patisiran (Onpattro™), the first FDA-approved siRNA drug, treats hereditary transthyretin-mediated amyloidosis using lipid nanoparticles (LNPs) to enhance cellular uptake and promote endosomal escape.[62] LNPs are designed to destabilize endosomal membranes, thereby facilitating the release of siRNA into the

cytoplasm. Other FDA-approved siRNA therapies, such as givosiran (Givlaari™) and inclisiran (Leqvio®), utilize a different strategy: Conjugation with N-acetylgalactosamine (GalNAc). This ligand targets the asialoglycoprotein receptor (ASGPR) on hepatocytes, enabling receptor-mediated endocytosis.[63] Although GalNAc-conjugated siRNAs are efficiently internalized, studies indicate that only approximately 0.3% of the siRNA escapes the endosome.[60,64] Nevertheless, the liver's high uptake capacity and the depot effect of endosomal retention allow for sustained therapeutic effects from infrequent dosing.[60] As shown from *O'Reilly, Daniel et al.* the passive targeting also works inside the central nervous system (CNS) using a combination of increased molecular weight and intra athecal injection.[65] Outside the liver and the CNS the endosomal escape remains a big issue, which needs to be overcome to achieve efficient delivery into tumor tissues. Up to date there is a variety of approaches aiming for increasing endosomal escape and simultaneously avoiding intolerable toxicity. As proven in the past chemical modification of therapeutic RNA have been the key to overcome the RNAs innate instability. Based on this its most likely to overcome the endosomal escape combining advanced chemical modifications and precise choice of targets, to increase endosomal escape and cell drug interaction.

3.9 Chemical RNA Modifications

As previously mentioned, chemical modifications of RNA therapeutics have been essential to overcome the instability of RNA molecules in ribonuclease containing environments. Besides these modifications are often integrated to improve the pharmacological properties of RNA like efficacy, immunogenicity and target specificity. For efficient RISC interaction and gene silencing, the 5' phosphorylation of the guide strand is essential. As endogenous DICER processing generates a 5' phosphate, synthetic siRNAs often require chemical phosphorylation for proper RISC interaction.[66] To address the instability of the 5' phosphate group, vinyl phosphonate (VP) modifications have been introduced. These analogs preserve the negative charge and spatial orientation of the endogenous phosphate, enhancing RISC loading while resisting phosphatase-mediated degradation.[62,66,67] Ribose modifications, such as 2'-O-methyl (2'-OMe) and 2'-fluoro (2'-F) substitutions, are commonly employed to enhance nuclease resistance and minimize off-target effects. These modifications also reduce activation of innate immune sensors such as Toll-like receptors (TLRs), which can be triggered by unmodified RNA.[62] In addition, phosphorothioate (PS) linkages, where a non-bridging oxygen is replaced by sulfur, are used to enhance serum stability and protein binding. However, their use in siRNA is typically limited to terminal positions to avoid interference with RISC activity.[68] Besides the chemical modification of an siRNA the positioning inside the strands is essential to maintain functionality. Therefore, a critical consideration in siRNA design is the seed region. Spanning the nucleotides 2–8 of the guide strand. The

seed region is responsible for initial target recognition and plays a central role in both on-target and off-target interactions. As the seed region can bind partially complementary sequences, its sequence composition and chemical modification are crucial for minimizing off-target gene silencing. Incorporation of 2'-OMe or other stabilizing modifications within the seed region has been shown to reduce off target binding while preserving silencing efficacy.[62] **Figure 5** shows a state of the art siRNA therapeutic modification pattern as used today. The field of RNA therapeutics has been drastically advanced by innovations such as vinyl phosphonate stabilization, backbone optimization and seed region engineering. Innovations that facilitated RNA based therapies. To conclude, it is evident that chemical modifications play a central role in the clinical translation of RNA-based therapy today and in the future.

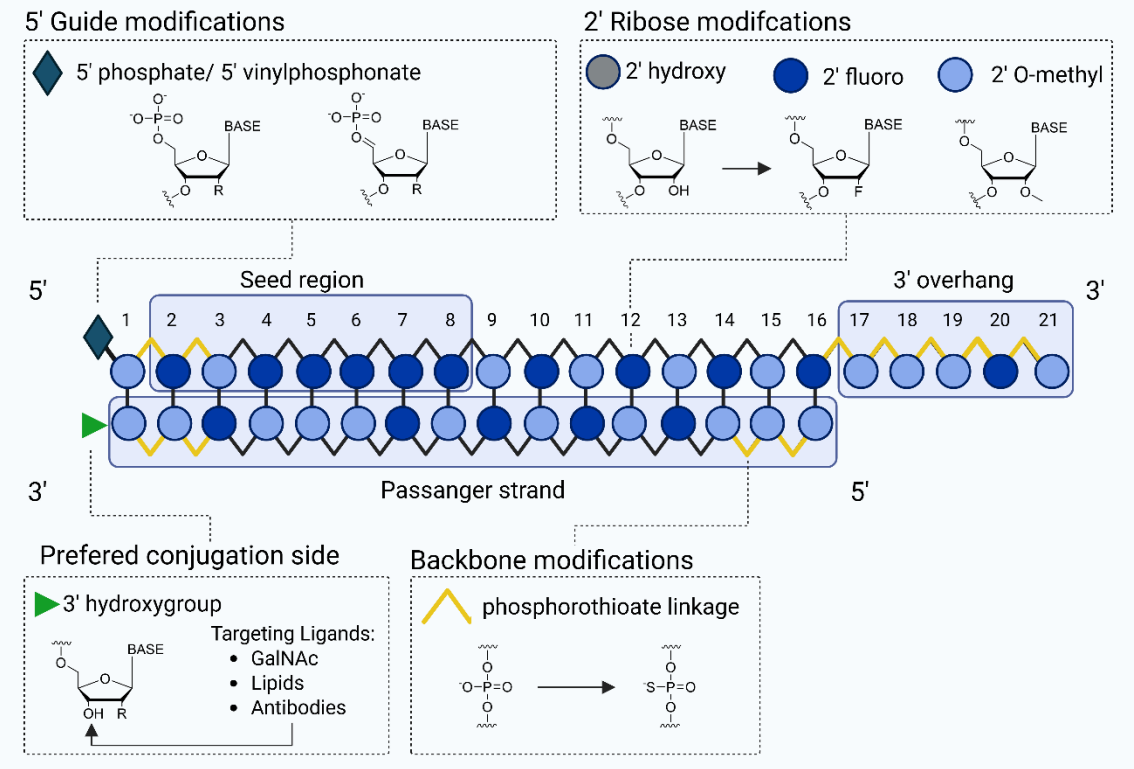

Figure 5 Schematic RNA modification pattern of todays state of the art siRNA therapeutics. *The 5' end of guide strand is modified using a phosphate or a vinylphosphonate group to increase the RISC interaction. Besides this both strands are fully 2' modified to increase endonuclease resistance and reduce immunogenicity. The terminal positions of each siRNA strand contain an additional backbone modification by integration of thiophosporo groups to increase exonuclease resistance. In case of conjugation to a targeting ligand the 3' end is the preferred conjugation side.*[62]

3.10 RNA Synthesis

As chemical modification of RNA is in center of clinical translation, synthesis and scalability become focus. In sense of synthesis two dominant methodologies serve distinct roles depending on the length and complexity of the RNA product. Solid-phase synthesis (SPS) and in vitro transcription (IVT). SPS is a chemical method for assembling RNA oligonucleotides on a solid support, typically polystyrene beads. The synthesis proceeds in the 3' to 5' direction using

phosphoramidite chemistry. Each cycle involves deprotection of the 5' hydroxyl group, coupling of a protected ribonucleotide, capping of unreacted sites, and oxidation of the phosphate tri-ester to a stable phosphate linkage. After the final chain elongation, the RNA is cleaved from the support and deprotected.[69] **Figure 6** shows the reaction cycle of SPS. SPS offers high sequence fidelity and allows for the incorporation of the full pallet of chemical modifications such as 2' substitution, locked nucleic acids (LNAs), Glycol nucleic acids (GNAs) fluorescence labeling, 5' vinylphosphonates and phosphorothioate linkages.[62,68] Despite there is no International Council for Harmonization of Technical Requirements for Pharmaceuticals for Human Use (ICH) or FDA guideline which addresses manufacturing of oligonucleotide based drugs good manufacturing

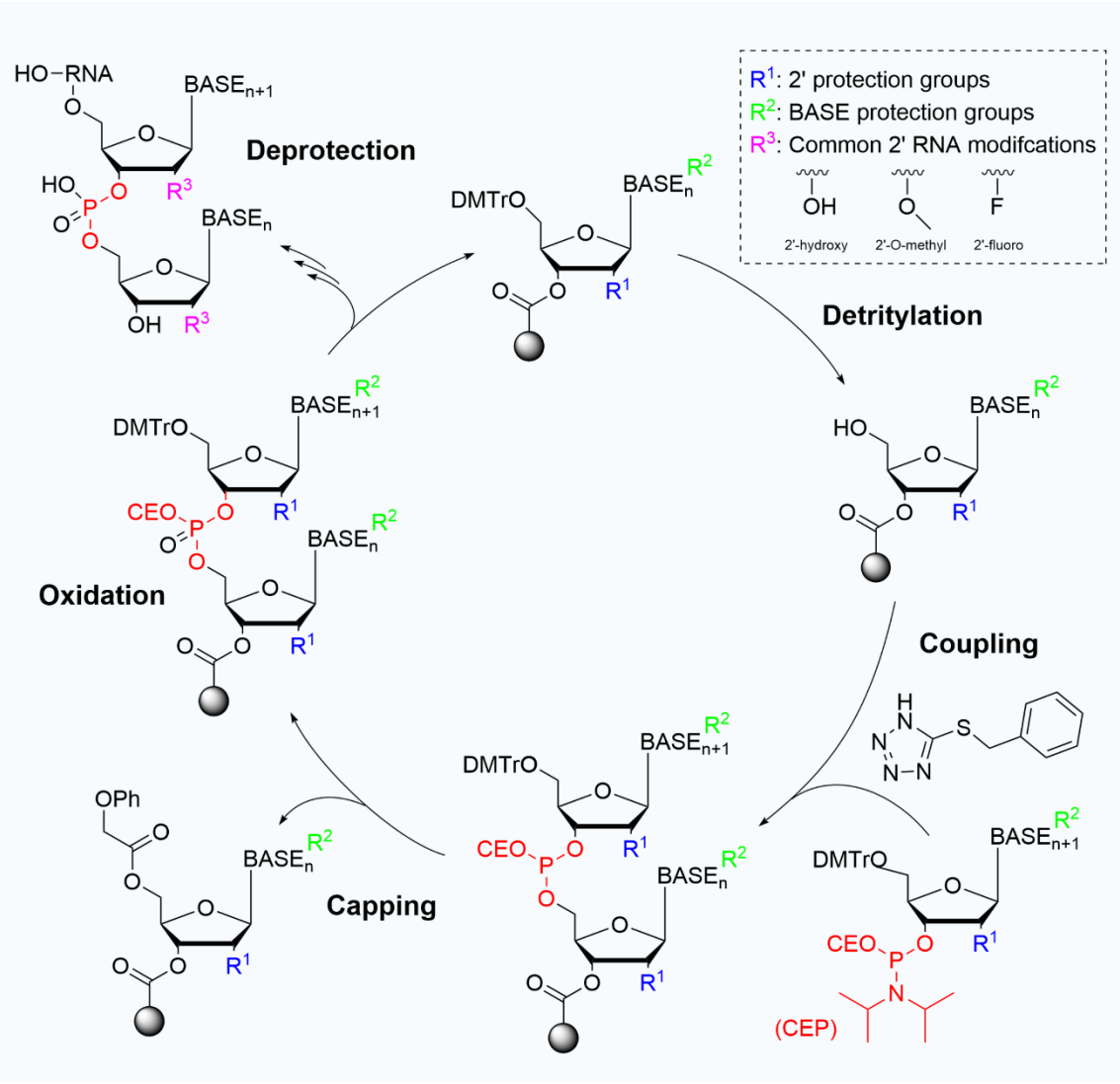

Figure 6 Reaction mechanism of the RNA solid-phase synthesis cycle. *The 3' immobilized nucleotides 5' oxigen gets deprotected by detritylation. This enables the selective 5' coupling with a phosphamidite of the next nucleotide. Not reacted strands are capped to prevent synthesis of unwanted byproducts. After capping the phosphate triesters are oxidized to protected phosphate linkages. Deprotection of the Phosphate group enables recovery or the start of a new synthesis cycle.*[69]

practice (GMP)-compliant RNA production via SPS is well-established. Especially for short oligonucleotides, including siRNAs and oligonucleotide-based therapies.[70] SPS has been successfully used in the commercial production of therapeutics such as patisiran and nusinersen.[70,71]

In contrast, IVT is the preferred method for synthesizing long RNA molecules (>100 nucleotides), particularly messenger RNA (mRNA). These polymerase based reaction involves a linearized DNA template containing a T7 promoter, a nucleoside triphosphate (NTP) mix and a T7 RNA polymerase.[72] To incorporate modified nucleotides such as 2'-Fluoro modified nucleotides, which improve RNA stability, the Y639F mutant of T7 polymerase is commonly used.[73] Due to its inherent enzymatic nature, IVT cannot incorporate site-specific modifications. From a cost perspective, SPS is significantly more expensive per milligram of synthesized RNA, primarily due to the high cost of phosphoramidites, solvents, and specialized equipment. It is best suited for short sequences (<100 nucleotides), where purity and precise modification are critical. IVT, on the other hand, offers higher yields and lower costs for longer RNAs (>100 nucleotides), which not rely on side specific modifications or phosporothioat linkages. In conclusion, solid-phase synthesis remains the method of choice for GMP-compliant production of short RNA therapeutics, offering unmatched control over sequence and modification. However, IVT using the T7 Y639F mutant provides a more cost-effective alternative especially for synthesis of initial compound candidates. Compound candidates as used in the development of targeted therapies.

3.11 Epidermal Growth Factor Receptor

The target choice is an essential part in the developmental process of targeted therapies. A frequently described target in literature is the epidermal growth factor receptor (EGFR), also known as HER1 or ErbB1. The EGFR is a transmembrane receptor tyrosine kinase that plays a central role in regulating cell proliferation, survival, and differentiation. Upon binding to ligands such as epidermal growth factor (EGF) or transforming growth factor-α (TGF-α), EGFR undergoes dimerization and autophosphorylation of its intracellular tyrosine residues. This activates multiple downstream signalling cascades, including the RAS-RAF-MEK-ERK (MAPK) pathway, which promotes cell cycle progression, and the PI3K-AKT pathway, which enhances cell survival and inhibits apoptosis.[74] Aberrant EGFR signalling is implicated in the pathogenesis of several cancers, and has been associated with poor prognosis in NSCLC, colon adeno carcinoma as well as pancreatic adeno carcinoma.[75] In the past various EGFR targeting therapies, such as antibody drug conjugate (ADCs) have been developed as it shows high overexpression rates through different tumor tissues.[76] With an overexpression rates of 40-89% in NSCLC this is of special interest in context of HSat3 RNA transcription and etoposide sensitivity.[77] Combined with the global incidence from

2022 the development of an EGFR specific siRNA delivery platform could be on average in the interest of 1,6 million lung cancer patients every year.

3.12 EGFR Targeting RNA Aptamers

Besides the choice of the target structure there is an inherent necessity of a targeting ligand. As the EGFR is a popular target there is a big variety of available ligands, ranging from antibodies and small molecules to peptides and aptamers. To streamline the production process of a potential therapeutic candidate this work focuses on RNA aptamer structures as targeting ligand. RNA aptamers are short, single-stranded RNA oligonucleotides that are capable of binding specific targets with high affinity and specificity, much like antibodies bind to antigens. Their three-dimensional structures enable them to recognize a broad variety of molecules, including proteins, small molecules, and even whole cells. The discovery and selection of aptamers are typically accomplished through the SELEX (Systematic Evolution of Ligands by EXponential enrichment) process, which enables the isolation of aptamers that exhibit both, high specificity and affinity for their target molecules. Compared to protein or peptide-based recognition motifs, RNA aptamers are chemically synthesized, generally non-immunogenic, and can be modified to enhance their stability and functional versatility in therapeutic and diagnostic applications.[78] Commonly RNA aptamers are synthesized during SELEX using IVT incorporating 2' Fluoro modifications into the pyrimidine bases (Cytosine and Uracil). The literature describes the two EGFR targeting aptamers CL4 and MinE07.[79,80] The first development approaches described in this work will focus on the use of CL4. In later stages the focus will shift to the use of MinE07.

3.13 HSat3 and Etoposide Resistance - Previous Work

This work is based on previous research published by *Kanne, J. and Hussong M. et al.*, which was performed in the lab of Prof. Schweiger. The mentioned study demonstrates that pericentromeric Satellite III transcripts (SatIII RNA) have a significant role in cellular responses to the topoisomerase II inhibitor etoposide. Under stress conditions, particularly heat stress, SatIII transcription is markedly increased, leading to the formation of nuclear stress bodies in pericentromeric regions. These structures function as molecular hubs that attract various proteins, including TOP2A. Notably, the research establishes that etoposide retains the ability to bind TOP2A, thereby refuting previous suggestions that SatIII obstructs drug binding. Instead, SatIII modifies the spatial distribution of the TOP2A-etoposide complex within the nucleus. By concentrating TOP2A in SatIII-enriched areas, etoposide-induced DNA damage becomes localized to pericentromeric regions, which are structurally resilient and less prone to cytotoxic effects. This

redistribution reduces the overall cellular burden from double-strand breaks, resulting in enhanced cell viability and increased resistance to etoposide.

Furthermore, the authors confirm that this resistance is not confined to cell culture models; it is also observed in PDX, where elevated SatIII expression corresponds with diminished etoposide effectiveness. Mechanistically, epigenetic modifications at the SatIII locus support increased transcription. Importantly, pharmacological intervention using BRD4 inhibitors suppresses SatIII transcription and restores global TOP2A-mediated DNA damage, thereby sensitizing cells to etoposide. In summary, the study presents a robust framework in which non-coding RNAs influence nuclear architecture and the spatial patterning of DNA damage, directly impacting chemoresistance. These insights offer promising directions for therapeutic strategies targeting stress-induced satellite transcripts.

4 Aim of The Work

Cancer is one of the largest burdens of humanity causing more than nine million deaths every year. Lung cancer especially non-small cell lung cancer (NSCLC) accounts for 18,7% of all cancer deaths per year and is a leading cause for cancer related deaths. *Kanne, J. and Hussong, M. et al.* have identified HSat3 RNA as a therapeutic target to reverse therapy resistance against etoposide. As the majority of NSCLCs is overexpressing the epidermal growth factor receptor (EGFR), a siRNA therapy delivering HSat3 siRNA in EGFR overexpressing cancers could improve the prognosis of NSCLC.

As described the development of a targeted siRNA therapy needs to consider many factors like siRNA target, chemical modifications, scalability, costs of the research scale compound, choice of the target structure, choice of the targeting ligand as well es strategies to overcome bottlenecks as the endosomal escape. This underlines not only the complexity of the compound design but also the advanced criteria for compound evaluation and development pipeline.

Therefore, this work aims for two major goals. At first the establishment of a cost and time efficient siRNA-conjugate development platform and secondly the evaluation of initial compound candidates. The first part is aiming for a fluorescence based alternative to common siRNA evaluation platforms to avoid necessity of cost intensive substrates while enabling repetitive measurement of single samples. The second part aims for the development of an RNA-aptamer based siRNA delivery platform for receptor specific gene knock down.

In this pilot project the delivery of an HSat3 targeting compound should be evaluated to specifically revert etoposide therapy resistance in EGFR overexpressing tumours.

5 Zielsetzung der Arbeit

Krebs ist eine der größten Geißeln der Menschheit und verursacht jedes Jahr mehr als neun Millionen Todesfälle. Lungenkrebs, insbesondere nicht-kleinzelliger Lungenkrebs (NSCLC), ist für 18,7 % aller Krebstodesfälle pro Jahr verantwortlich und eine der häufigsten Ursachen für krebsbedingte Todesfälle. *Kanne, J. und Hussong, M. et al.* haben HSat3-RNA als therapeutisches Ziel identifiziert, um die Therapieresistenz gegen Etoposid aufzuheben. Da die Mehrheit der NSCLCs den Epidermalen Wachstumsfaktor Rezeptor (EGFR) überexprimiert, könnte eine gezielte siRNA-Therapie, bei der HSat3-siRNA in EGFR-überexprimierende Krebszellen eingebracht wird, die Prognose von Millionen von Menschen verbessern.

Wie beschrieben, müssen bei der Entwicklung einer gezielten siRNA-Therapie viele Faktoren berücksichtigt werden, darunter die siRNA-Zielsequenz, chemische Modifikationen, die Skalierbarkeit, die Kosten der Prototypen, die Wahl der Zielstruktur, die Wahl des Ziel-Liganden sowie Strategien zur Überwindung von Engpässen wie dem Endosomen-Escape. Dies unterstreicht nicht nur die Komplexität des Wirkstoffdesigns, sondern auch die anspruchsvollen Kriterien für die Bewertung von Wirkstoffkandidaten und an die Entwicklungspipeline.

Daher verfolgt diese Arbeit zwei Hauptziele. Zum einen die Etablierung einer kosten- und zeiteffizienten Plattform zur Entwicklung von siRNA-Konjugaten und zum anderen die Bewertung erster Wirkstoffkandidaten. Der erste Teil zielt auf eine fluoreszenzbasierte Alternative zu gängigen siRNA-Bewertungsplattformen ab, um die Notwendigkeit kostenintensiver Substrate zu vermeiden und gleichzeitig wiederholbare Messungen einzelner Proben zu ermöglichen. Der zweite Teil zielt auf die Entwicklung einer RNA-Aptamer-basierten siRNA-Verabreichungsplattform für den rezeptorspezifischen Gen-Knockdown ab.

In diesem Pilotprojekt soll die Verabreichung eines HSat3-gerichteten Wirkstoffs evaluiert werden, um die Resistenz gegen eine Etoposid-Therapie bei EGFR-überexprimierenden Tumoren gezielt aufzuheben.

6 Results – Development of a NA-Therapy Screening Platform

As a developmental process can only be as good as the developmental platform the first section of this work focuses on the establishment and implementation of a new screening platform for nucleic acid-based therapeutics. A central information, necessary especially in the developmental process of RNAi based drugs, is the quantity and functionality of RNAs delivered to the cytoplasm. When starting this work a variety of endpoint measurements could provide this information. Considering the available options, the luciferase assay method was selected as the preferred method because it is highly sensitive and is therefore considered an established method for detecting RNAi in scientific literature. In detail the psiCheck™-2 plasmid (**Figure S 1**) and the Dual-Glo® luciferase assay from Promega was chosen as a starting point. The developmental process of the FluoroDetect system was published 2025 in Mol. Ther. Nucl. Ac. by *Hess et al.*.

6.1 HSat3 Luciferase Assay

As outlined in the introduction the primary target of the project is the development of an siRNA targeting HSat3 RNA. Therefore, a C-rich target motif was cloned into the multiple cloning side (MCS) of the psiCheck™-2 plasmid (**Figure S 1**) which was digested with XhoI and NotI. The new plasmid was called psiCheck HSat3 (**Figure S 2**). The psiCheck™-2 assay is designed as a two-signal ratio metric, containing a reporter and a reference signal for normalization. This can increase the precision of the measurements by overcoming inaccuracies caused through different transfection efficiencies or stress related signal fluctuations. A schematic of the mechanism is shown in **Figure 7**. In this special case the HSat3 target motif (red) was inserted into the 3'UTR of the *Renilla* luciferase (hRluc, green) reporter gene. In presence of a HSat3 targeting siRNA (red) the hRluc mRNA is degraded by RNAi causing a reduction of hRluc protein inside the transfected cells. The *Firefly* luciferase (hluc+, blue) reference gene contains no HSat3 siRNA target and thereby should not be affected by the RNAi, providing a reference point for correcting inaccuracies through normalization.

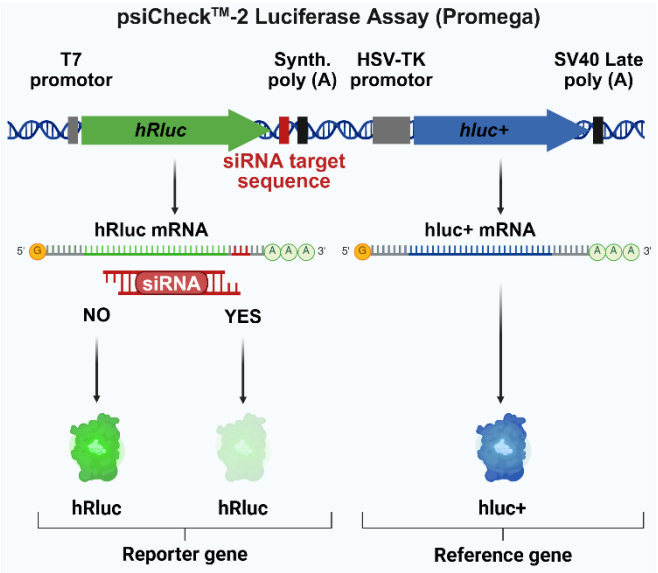

Figure 7 Schematics of the psiCheck HSat3 luciferase assay. *The mRNA of Renilla luciferase (hRluc, green) reporter gene can be downregulated by HSat3 siRNA while the Firefly luciferase (hluc+, blue) mRNA remains untouched.*

By constructing this assay setup, it should be possible to quantify the RNAi effect mediated by HSat3-targeting siRNA in a robust and reproducible fashion. The normalization of the hRluc signal to the hluc+ signal provided a reliable proxy for the functional delivery of siRNA into the cytoplasm, enabling precise assessment of compound efficacy and cellular uptake. To proof the functionality of the assay a first pilot experiment was performed twice testing the psiCheck HSat3 in the two cell lines SW480 and SW620 (**Figure 8**). Both cell line showed no reduction of relative luminescence units (RLU) when exposed to siRNA without a transfection reagent (siHSat3 and siCo). When exposed to siRNAs formulated with Lipofectamin RNAiMAX the cells showed a reduction of RLU when HSat3 targeting siRNA was present (siHSat3 RNAiMAX). No signal reduction could be observed upon exposure with a non-targeting siRNA pool (siCo) (siCo RNAiMAX). This indicated the functionality of the psiCheck HSat3 luciferase assay (**Figure 8**).

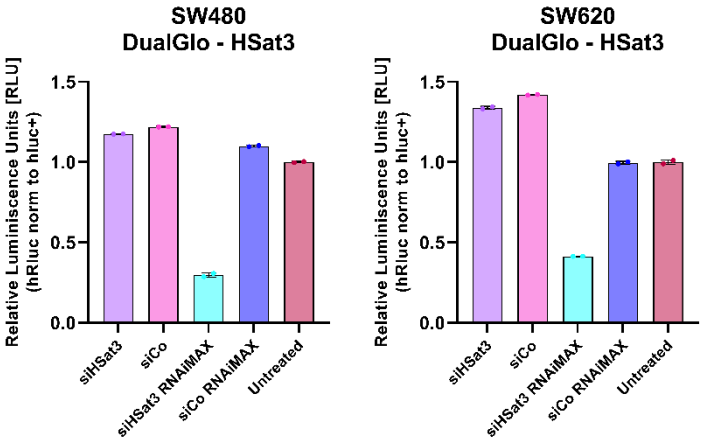

Figure 8 Validation of the psiCheck HSat3 Dual-Glo luciferase assay setup. *Samples were exposed to siRNA or siRNA transfection mix (RNAiMAX) for 48 h. All cells were treated as indicated 24 h after transfecting the psiCheck HSat3 assay plasmid. Diagrams show the median ± 95% confidence interval.*

6.2 Thought Experiment - Continuous Measurements

Despite its high precision, luciferase assays as the psiCheck-2 Dual-Glo assay system suffer from their lytic nature, as they are designed as an endpoint measurement. In other words, the sample needs to be destroyed for the measurement. Moreover, these enzymatic assays need expensive substrates with a limited shelf life. What sounds as a perfect business case suffers in praxis from an error prawn setup when it comes to manual pipetting. Summing this up, luciferase assays are an incredibly precise but if not well-established error prawn and expensive method to measure RNAi. So, if not fine tuning the efficiency of an siRNA this measurement is too expensive in relation to its benefits. Additionally, its endpoint nature, limits the ability to observe dynamic processes. In a thought experiment investigating a dynamic process under three different conditions at three different time points. This makes a total of nine data points equal to nine samples when using an endpoint measurement. In comparison it would just need three samples if using a non-destructive measurement. In conclusion the non destructive measurement leads to a higher data coherence while reducing the material cost. Wrapping this up, there is a need for

the development of a non-destructive, user-friendly and cost-effective platform for siRNA therapy development.

In a next step an assay using fluorescence protein instead of luciferases was designed. An important advantage of fluorescence measurements is that the quantification can be done without lysing cells and without an expensive substrate. As previously demonstrated by *Kojima et al.* fluorescence reporter assays are effective for detecting siRNAs in both bulk samples and single-cell analyses[81]. Furthermore, fluorescence assays employing the red fluorescent protein mCherry and enhanced green fluorescent protein (eGFP) have been developed to facilitate the analysis of dynamic intracellular receptor-ligand interactions[82]. Thus, the development of the dual fluorescence assay called FluoroDetect was started.

6.3 Design of The FluoroDetect Assay

Similar to the psiCheck-2 the FluoroDetect assay system is dual signal system. Containing a reporter and a reference signal, the FluoroDetect assey aims to be more precise than a single signal-based assay. In addition, the reporter gene is under the control of a TET-OFF promotor system inhibited by doxycycline. This should serve as an additional internal control in advanced experimental setups. The schematic mechanism of the FluoroDetect is shown in **Figure 9**. The red fluorescence protein mCherry (red) works as a reporter gene. The 3' untranslated region (UTR) of the reporter gene contains three identical siRNA target motifs, to enhance the sensitivity of the assay. Addition of doxycycline or a targeting siRNA eliminates the reporter signal. The green eGFP reference signal (green) should be unaffected and serves as an internal reference. The assay plasmid was created with a hot fusion cloning protocol starting from the pCW57.1-MCU-Flag TET-OFF plasmid (**Figure S 3**) [83]. The target side of the assay was designed to be flanked by two individual restriction sites (AsiSI & NsiI) for easy and fast modification of the assay (**Figure 10**). The HSat3 sequence was chosen as a target motif. The FluoroDetect HSat3 assay was used in the second section of this work as a platform for the development of HSat3 RNA targeting therapies. As shown by *Valgardsdottir et al.* C-rich and a G-rich lncRNAs of HSat3 are transcribed

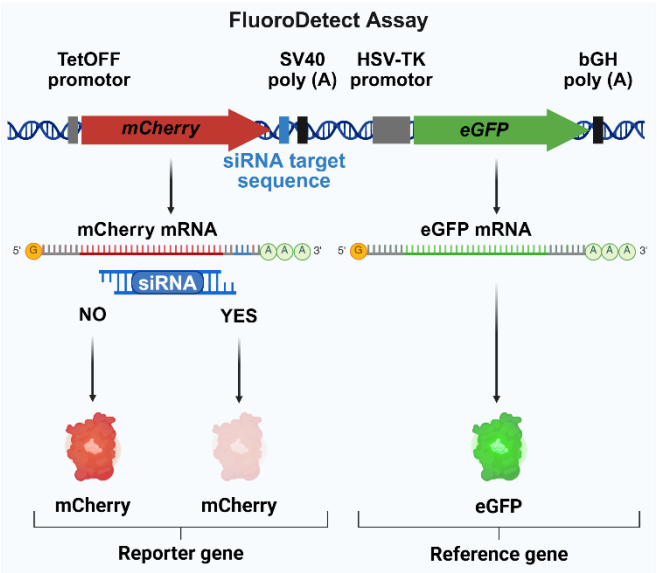

Figure 9 Schematic figure of the FluorDetect assay. *The mRNA of mCherry (red) reporter gene can be downregulated by siRNA while the eGFP (green)reference gene mRNA remains untouched. (Hess et al., Mol. Ther. Nucl. Ac., 2025)[86]*

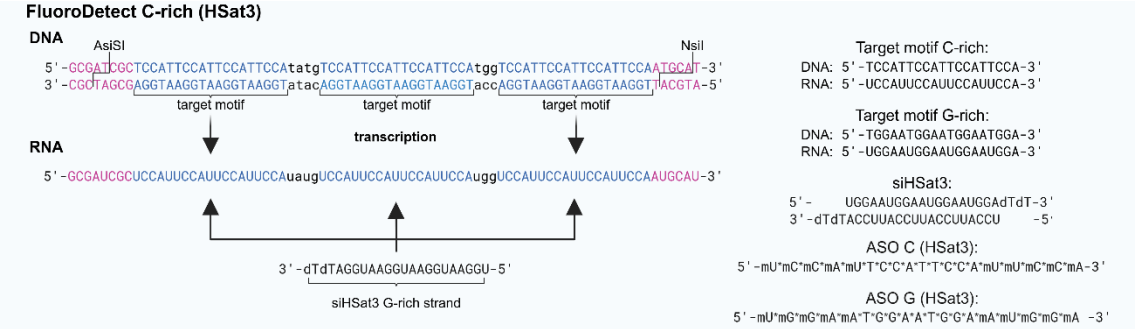

Figure 10 Schematic figure of the DNA and mRNA sequence target motif used in the FluoroDetect C-rich (HSat3) assay. *The flanking enzymatic cutting sites (pink) and siRNA-binding sites (blue). Additionally, the G-rich target motif, the siRNA/ASO sequences used in this work are shown (m: 2' MeO modification, ⁎: phosporothioate modification). (Hess et al., Mol. Ther. Nucl. Ac., 2025)[86]*

under stress conditions.[36] Therefore, assays using the C-rich target motif as well as the G-rich target motif were designed to simulate both species as a target. An example of the DNA target motif which is transcribed into the mRNA target sequence is given in **Figure 10**. The sequences of the C-rich and G-rich target motif as well as the used siRNA and ASO sequences are shown in **Figure 10**. To proof the functionality of the assays a first pilot experiment was performed and evaluated using fluorescence microscopy. For this, HeLa cells were cotransfected with the assay plasmids as well as an HSat3 targeting siRNA (siHSat3). After 48 h of incubation the fluorescence signals were measured with fluorescence microscopy. In both assays a specific reduction of the red fluorescence signal could be observed compared to the untreated control sample (**Figure 11**). Moreover, the samples exposed to siCo did not show a significant reduction of red fluorescence signal. In all samples of the C-rich as well as in the G-rich assay the green fluorescence signal was maintained constant (**Figure 11**). This first proof of concept demonstrates the functionality of the FluoroDetect assay. After the initial positive results with fluorescence microscopy, the assay was adapted to a plate reader system for easier quantification of both fluorescence signals.

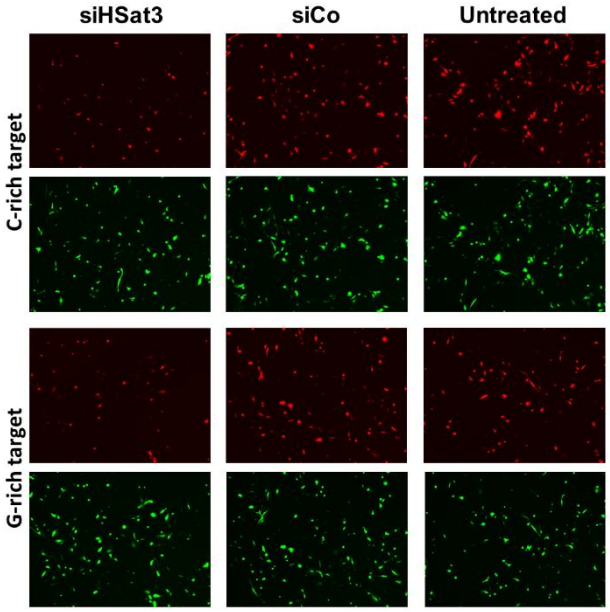

Figure 11 Proof of concept using HeLa cells. *Fluorescence microscope images showing green and red fluorescence signal in samples treated with targeting siRNA (siHSat3), untargeted siRNA control pool (siCo), and an untreated control. Images were taken 48 h after transfection. (Hess et al., Mol. Ther. Nucl. Ac., 2025)[86]*

6.4 Plate Reader Analysis of RNAi Mediated Gene Silencing

In establishing the FluoroDetect assay within a plate-reading system, the excitation and emission wavelengths for eGFP (Ex: 475 nm, Em: 510/20 nm) and mCherry (Ex: 575 nm, Em: 610/20 nm) were selected based on the findings reported in the literature (**Figure S 4 A**) [84,85]. The window of detection should show a linear relationship between cell number and fluorescence intensity. Therefore, the normalized signal (ratio of reporter to reference) is expected to remain stable across all data points without siRNA treatment (**Figure S 4 B,C**)[86] .

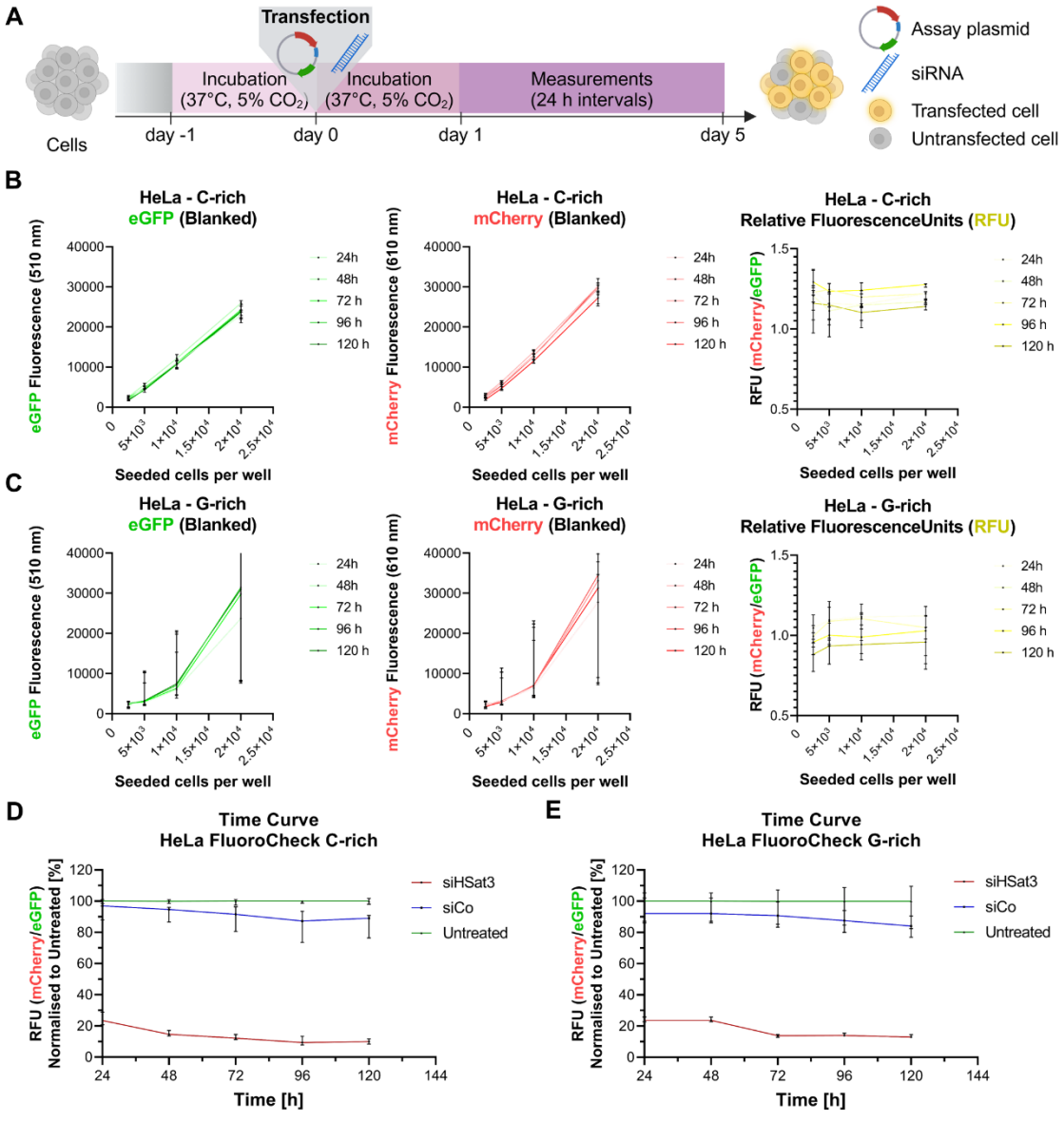

Figure 12 Dynamic measurement of RNAi in transient transfected cells. A: *The schematic diagram illustrates the experimental design, detailing the transfection protocol and subsequent measurement procedures. Transfection efficiency was monitored via fluorescence microscopy, and quantitative fluorescence readings were obtained using a plate reader system.* ***B,C:*** *Plotting of eGFP (green) signal and mCherry (red) signal over the number of seeded HeLa cells per well. Normalizing the mCherry to the eGFP fluorescence gives the relative fluorescence units (RFUs). Plotting of RFU (yellow) in dependence of HeLa cells seeded per well.* ***D,E:*** *Time curve of FluoroDetect transfected HeLa cells measured in 24 h intervals. Diagrams comparing the relative fluorescence units of untreated (green), siCo-treated (blue), and siHSat3-treated (red) cell population (all graphs showing the median ± 95% confidence interval [CI]). (Hess et al., Mol. Ther. Nucl. Ac., 2025)[86]*

In all transient experiments, $2x10^5$ cells were initially seeded in a 6-well plate and transfected after 24 h of incubation. The transfected cells were transferred to a 96-well white-bottom tissue culture-coated plate after 24 h of incubation (**Figure 12 A**). To evaluate the optimal number of cells to start plate reader experiments, different number of cells were seeded in a 96 well plate. This dilution series were performed with three different cell lines (HeLa, SW480 and SW620) in a range of 2.500-20.000 cells per well. Cell measurements were conducted at 24-hour intervals to examine temporal changes (**Figure 12 B,C; Figure S 5 A,B; Figure S 6 A,B**). The signal was most stable within the range of 10,000–20,000 cells per well. After cotransfecting target-specific siRNAs, both C-rich and G-rich assays showed a target-specific knockdown of the mCherry signal lasting up to 120 hours. Control samples showed no effect. Minor differences among controls likely resulted from growth rate variabilities and nonspecific effects of the siCo pool (**Figure 12 D,E; Figure S 5 C,D**; **Figure S 6 C,D**).

To assess the performance of the assay and to confirm the endogenous target knockdown at the mRNA level, RT-qPCR was used to measure HSat3 RNAs. HSat3 expression was induced by a 1-hour heat shock at 44 °C. RNA samples were collected six hours after HS. Because the double-stranded siRNA contains both a G-rich strand and a C-rich strand, the RT-qPCR results (**Figure S 7 A**) were compared with the FluoroDetect C-rich HSat3 (**Figure S 7 B**) and the FluoroDetect G-rich HSat3 (**Figure S 7 C**). The knock down intensity of both experiments showed high similarity.

6.5 Measuring Strand Specificity Using Antisense Oligonucleotides

Given the double-stranded structure of siRNAs, it is pertinent to assess whether the FluoroDetect assay can selectively identify one strand without interference from its complement. This specificity provides valuable insights into guide strand selection and preference. Typically, the RISC complex favours the strand with a less thermodynamically stable 5’ end. [87,88] Particularly in the development and evaluation of siRNA and siRNA conjugates, distinguishing between the guide and passenger strands provides critical insights for optimizing delivery modifications. This differentiation enables precise optimization of efficacy while minimizing unintended off-target effects. Additionally, the ability to detect single-stranded ASOs broadens the range of applications, allowing the assay to identify both RISC-mediated silencing and RISC independent silencing like intracellular microRNA-mediated gene silencing.

Strand specificity was assessed by designing single-stranded ASOs that matched the sequences of the individual strands of the HSat3-targeting siRNA. These ASOs were structured as gapmers with RNA-like sequences flanking the DNA oligonucleotide and included 2’-oxymethyl and phosporothioate backbone modifications intended to enhance stability and efficacy (Error! Reference source not found.).[62,89] Hybridization between the DNA bases of the ASO and the mRNA

target site creates a DNA/RNA hybrid double strand, which recruits RNaseH and results in degradation of the mRNA.[90-92]

Cells were exposed to siRNAs or ASOs 24 hours after FluoroDetect assay plasmid transfection. Fluorescence was assessed by microscopy 24, 48, 72, and 96 hours after transfection. In HeLa cells transfected with the G-rich assay, a knockdown of the mCherry reporter signal was observed in the samples treated with siHSat3 and ASO C upon 48 h after transfection of the RNAs. In the untreated control samples as well as in the not-matching ASO G treated sample no reduction of the mCherry signal could be observed (**Figure 13 A; Figure S 8 A,B**). As expected, the base pairing nature of RNAi implies the interaction of G-rich and C-rich complementary sequences. A quantification of the experiment with plat reader confirmed the microscopic observation and underlined the strand-specific mode of action (**Figure 13 B,C; Figure S 8 C,D**).

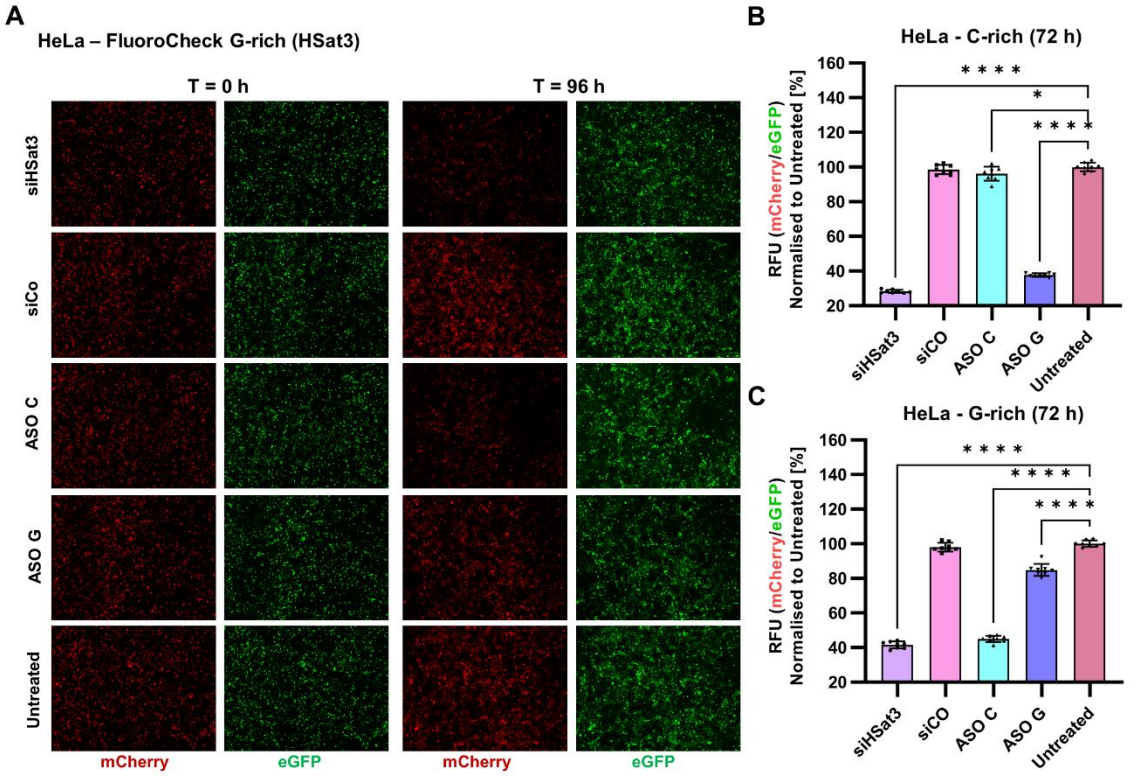

Figure 13 Confirming the strand specific mode of action. A: *Fluorescence microscopy images display HeLa cells transfected with the FluoroDetect G-rich (HSat3) assay at two time points: prior to treatment (t = 0 h) and 96 hours post-treatment (t = 96 h) with siRNA or ASO. Shown cell populations include those treated with siHSat3, siCo, ASO C, and ASO G. For reference, an untreated control group is also presented.* ***B,C:*** *Relative fluorescence units (RFUs) were measured in HeLa cells transfected with either FluoroDetect C-rich (HSat3) or FluoroDetect G-rich (HSat3) constructs, 72 hours following siRNA/ASO treatment as specified below the diagram (All graphs showing the median ± 95% confidence interval [CI]). Only significant comparisons are shown with p value denoted as follows: ∗ p < 0.05; ∗∗ p < 0.01; ∗∗∗ p < 0.001, ∗∗∗∗ p < 0.0001. (Hess et al., Mol. Ther. Nucl. Ac., 2025)[86]*

6.6 The Limit of Detection and The Limit of Quantification

The limit of detection (LOD) and limit of quantification (LOQ) are critical parameters in analytical methodologies. These values are determined by multiplying the standard deviation of the response by an expansion factor and dividing the result by the slope of the linear regression (**Figure S 9 A**). [93,94]

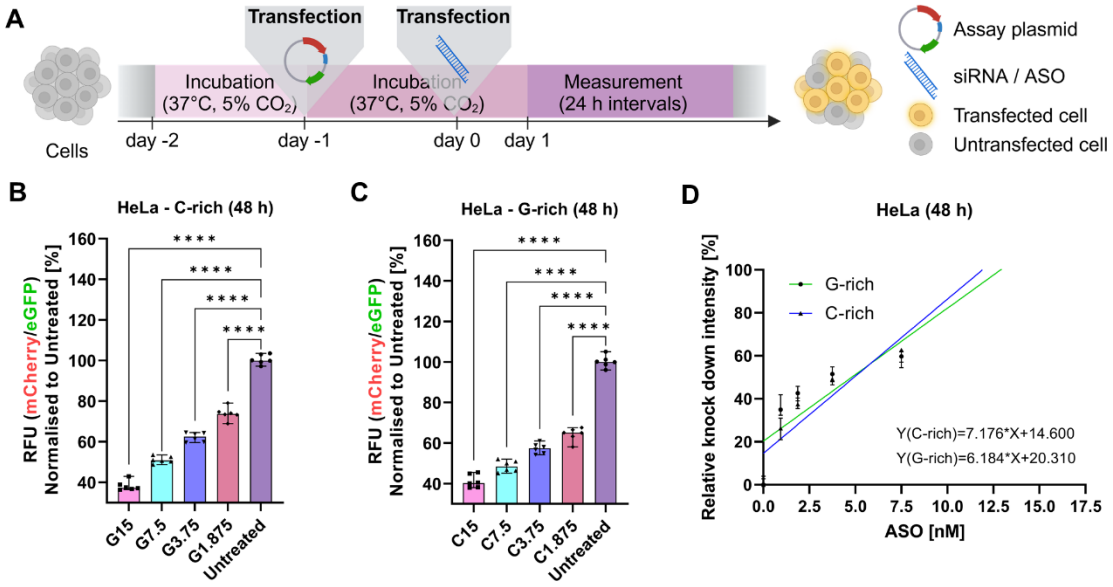

Figure 14 Assessment of assay detection limits. A: *Schematic workflow of transfection. Fluorescence microscopy was used to control transfection efficacy. Changes in red and green fluorescence were measured using a plate reading system.* ***B,C:*** *Knock down intensity was determined as RFU in HeLa cells transfected with FluorDetect C-rich (Hsat3) and FluoroDetect G-rich (HSat3). Measurement was performed 48 h after transfection of different amounts of targeting AOSs (absolute amount: 15; 7,5; 3,75 and 1,875 pmol).* ***D:*** *(All graphs showing the median ± 95% confidence interval [CI]). Only significant comparisons are shown with p value denoted as follows: ∗p < 0.05; ∗∗p < 0.01; ∗∗∗p < 0.001, ∗∗∗∗ p < 0.0001. (Hess et al., Mol. Ther. Nucl. Ac., 2025)[86]*

In this methodology, the distinction between LOD and LOQ arises from the varying tolerances for alpha and beta errors when determining the expansion factor. Calculation of LOD and LOQ was conducted through a dilution series of the C-rich and G-rich ASOs. A total concentration of 30 nM ASOs was maintained, by mixing C-rich and G-rich ASOs, in each transfection reaction to ensure consistent transfection conditions. Measurements were conducted using a plate reader 48 h after transfection of ASOs (**Figure 14 A**). The generated dataset was utilized to conduct a linear regression, which functions as a calibration curve for calculating the LOD and LOQ (**Figure 14 B-D, Figure S 9 B-G**). If the y-intercept of the calibration curve exceeds the standard deviation, it can be used in place of the standard deviation of the response. The y-intercept indicates the response corresponding to zero analyte concentration. When the y-intercept is much greater than the standard deviation, it suggests that baseline noise is low meaning the measurements are more dependable. In conclusion using the y-interceptor instead of the standard deviation improves the reliability of the calculated LOD and LOQ as it accounts for systematic errors and background signals associated within the experimental setup. The LOD and LOQ for both the C-

rich and G-rich assays were determined using three different cell lines. The overall LOD and LOQ values were calculated as the median from the results obtained with HeLa, SW480, and SW620 cell lines. The C-rich assay demonstrated marginally higher sensitivity, exhibiting a median LOD of 6.714 nM, whereas the G-rich assay presented a LOD of 8.555 nM (**Figure 14**, **Figure S 9**, **Table 1**).

Table 1: Values for calculating detection and quantification limits. *(Hess et al., Mol. Ther. Nucl. Ac., 2025)*[86]

Cell line	C-rich			G-rich		
	HeLa	SW480	SW620	HeLa	SW480	SW620
Slope	7,176	4,958	4,328	6,184	5,778	4,548
Y-interceptor	14,600	12,010	6,476	20,310	7,704	11,790
LOD [nM]	6,714	7,994	4,938	10,838	4,400	8,555
LOQ [nM]	20,346	24,223	14,963	32,843	13,333	25,923
Median LOD ± SD [nM]	**6,714 ± 1,535**			**8,555 ± 3,264**		
Median LOD ± SD [nM]	**20,346 ± 4,651**			**25,923 ± 9,891**		

6.7 Stable Cell Lines for Screening or Repetitive Measurements

Given that the long-term objective of this project is to establish a platform for screening and developing nucleic acid therapies, in a next step, stable reporter cell lines were established. To address this, two widely utilized methods in molecular biology are lentiviral transduction and transposase-based genome modification. While both approaches present distinct advantages and disadvantages, their principal difference lies in the delivery vector. The plasmid-based transposase system relies on transfection reagents rather than lentiviruses, making its use very convenient. However, it is ineffective in cell lines that are difficult to transfect. On the other hand lentiviral systems are less convenient, but their broad tropism makes them much more

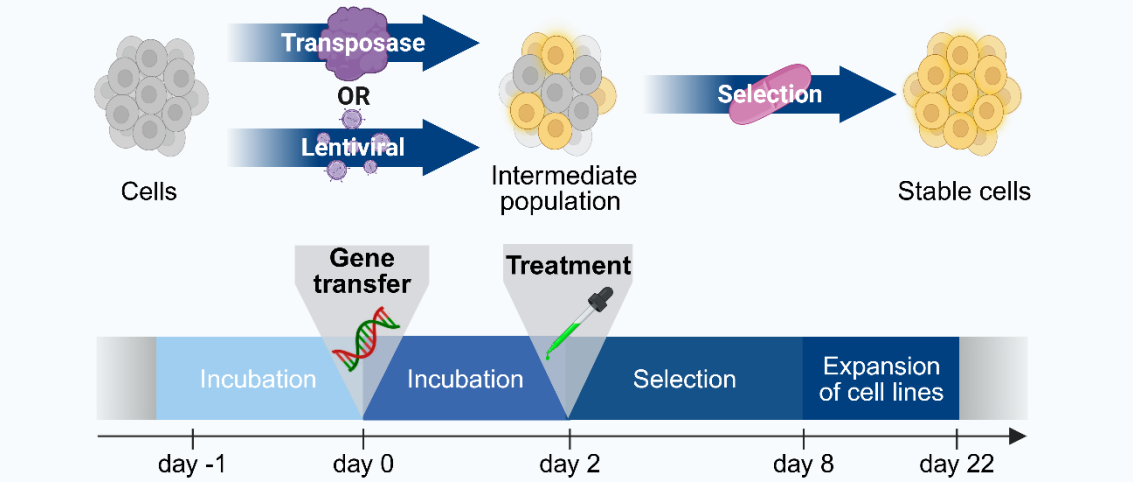

Figure 15 Schematic workflow of stable cell line production*. FluorDetect assay can be integrated into the genome using Transposase based systems or lentiviral systems. The resulting intermediate population can be expanded by Puromycin selection to grow out a polyclonal reporter cell line. Selection should start two days after gene transfer and last two rounds of three days.*

efficient across most eukaryotic cell lines. To provide both systems for future experiments I established the FluorDetect assay for both systems - as a PiggyBac transposase system and as lentiviral system. **Figure 15** shows a schematic workflow of how to produce stable cell lines using the mentioned methods.

To produce stable cell lines using viral transduction, HEK 293 FT cells underwent transfection with packaging, envelope, and transfer plasmids to generate lentiviruses for either the reference or reporter gene. Various cell lines (HeLa, MDA MB 231, SW480, and PC9) were co-transduced with both constructs to establish C-rich and G-rich stable reporter cell lines (**Figure 16 A**).

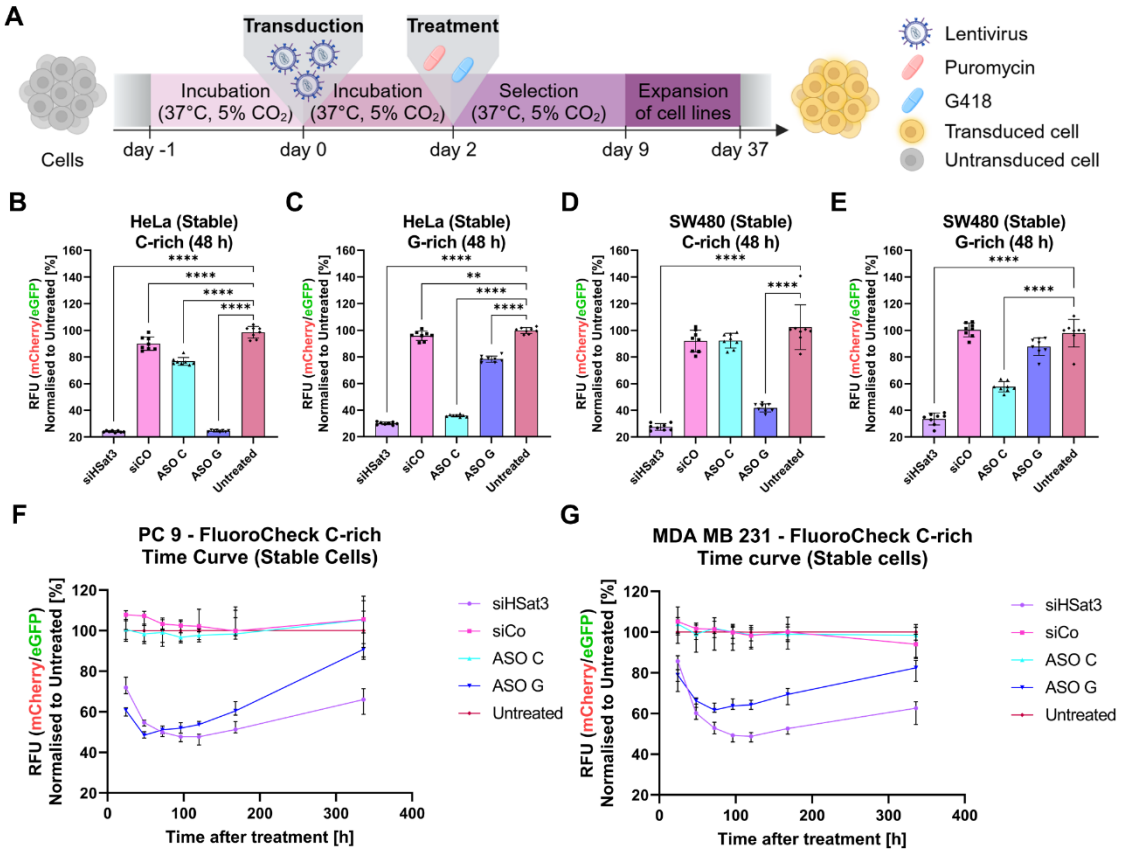

Figure 16 Assessment of stable reporter cell lines. A: *Design of lentiviral transduction experiment and process for selection of stably transduced reporter cells.* ***B-E:*** *RFUs of HeLa and SW480 cells stably expressing FluoroDetect C-rich or G-rich (HSat3) were measured 48 hours after siRNA/ASO treatment.* ***F,G:*** *Time curves demonstrate the RNA interference (RNAi) dynamics in stable transduced reporter cell lines (PC9 FluoroDetect C-rich (HSat3), MDA MB 231 FluoroDetect C-rich (HSat3)), as measured by relative fluorescence units over a time period of up to 336 hours following treatment. (All graphs showing the median ± 95% confidence interval [CI]). Only significant comparisons are shown with p value denoted as follows: ∗p < 0.05; ∗∗p < 0.01; ∗∗∗p < 0.001, ∗∗∗∗p < 0.0001. . (Hess et al., Mol. Ther. Nucl. Ac., 2025)*[86]

After Puromycin selection and polyclonal expansion reporter cells were examined using a fluorescence microscope (**Figure S 10**). Following the microscopic inspection cells were seeded to assess their functionality. Fluorescence of reporter cells was measured 48 h after transfection of siRNAs/ASOs. All cell lines responded to both the siRNA and the corresponding ASO (**Figure 16 B-E**). Long term repetitive measurements showed siRNA knockdowns are stable for up to two

weeks. Furthermore, the response to ASOs was observed to be marginally more rapid than to siRNA, although the effect of siRNA persisted for a somewhat longer duration (**Figure 16 F,G**). For cytometer analysis, stable cells were transfected with either siHSat3 or a control siRNA pool (siCo), alongside untransfected reporter cells as a negative control. The experiment used MDA MB 231 C-rich, MDA MB 231 G-rich, PC9 C-rich, and PC9 G-rich cell lines. Flow cytometry was performed 72 h after siRNA transfection (**Figure 17 A**).

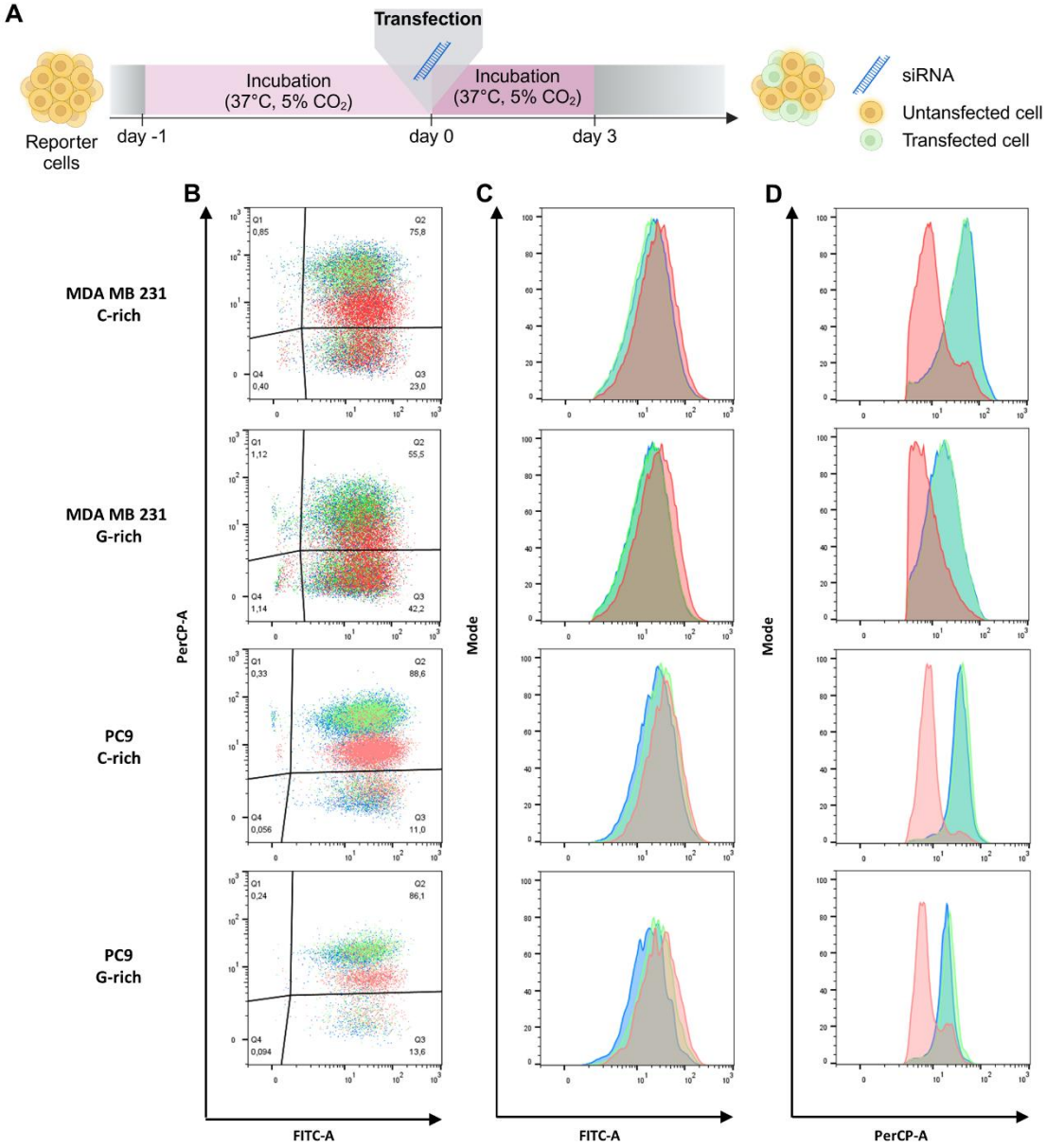

Figure 17 Flow cytometric analysis of the FluoroDetect assay. A: *The illustration depicts the experimental setup for the flow cytometer-based analysis of the FluoroDetect assay system. The fluorescence of transduced reporter cell lines (MDA MB 231 C-rich & G-rich, PC9 C-rich & G-rich) was controlled utilizing fluorescence microscopy before starting flow cytometry.**B:*** *Scatter plots display mCherry (PerCP-A) and eGFP (FITC-A) fluorescence in single cells. Samples include siHSat3-treated (red), siCo-treated (blue), and untreated (green). Gates indicate Q1–Q4: Q1 (mCherry+), Q2 (mCherry+ & eGFP+), Q3 (eGFP+), Q4 (negative for both).* ***C:*** *eGFP fluorescence (FITC-A channel) histograms of gate Q2.* ***D:*** *mCherry fluorescence (PerCP-A channel) histograms of gate Q2. (Hess et al., Mol. Ther. Nucl. Ac., 2025)[86]*

A population referred to as "cells" was initially defined using forward scatter height (FSC-H) versus sideward scatter height (SSC-H) to exclude particles that did not meet the appropriate size

criteria. Subsequently, cell doublets were excluded using the forward scatter area (FSC-A) versus FSC-H channel. Dead cells were excluded based on elevated VioBlue channel signal, utilizing DAPI staining as a viability indicator (**Figure S 12 A-C**). Gating was finalized by setting green and red fluorescence gates using a negative sample as well as cells expressing eGFP or mCherry (**Figure S 12 D**). Across all cell lines, green fluorescence detected via the FITC-A channel remained consistent (**Figure 17**). Nonetheless, a minor population of cells exhibited a loss of green fluorescence. The red mCherry signal was stable in both untreated and siCo-treated groups, but showed a decrease in siHSat3-treated samples. These findings suggest that HSat3-targeting siRNA efficiently suppresses expression of the intended gene, resulting in a diminished mCherry signal in transfected cells (**Figure 17**).

6.8 Exclude Read Through Transcription

As the assay design included the risk of unwanted truncated, elongated, or fused mCherry and eGFP variants, a Western blot was performed. Using a FLAG antibody as well as a GFP antibody mCherry and eGFP were detected (**Figure 18 A**). A Histone H3-targeting antibody served as loading control. All three antibody blotting's could detect bands of the expected size (**Figure 18 A**). This indicates that no unwanted byproducts are expressed, which could interfere with the assay measurement. Additionally, the presence of fusion proteins could be erased as the mChery and the eGFP are coded in different reading frames.

Moreover, it was important to exclude the presence of unwanted fused mRNA transcripts, as this could cause an internal control failure. Therefore, a quantitative reverse-transcription PCR (RT-qPCR) experiment was performed. The mRNA levels of mCherry and EGFP were measured under different conditions (siHSat3, siCo, and untreated) in HeLa cells. The cells showed a specific reduction of mCherry mRNA in the presence of HSat3 siRNA, whereas the eGFP mRNA level remained unaffected. The untreated control samples as well as the siCo treated negative control showed no significant change of mCherry or eGFP mRNA. The finding described was independent of the C-rich or G-rich assay (**Figure 18 B**). To establish an eGFP and mCherry qPCR measurement, primer performance was evaluated using a dilution series of the assay plasmids. Both qPCR primer pairs showed high performance (**Figure 18 C**). The FluoroDetect assay was integrated in the genome of the tested cells using a PiggyBac transposase system. In conclusion the Western blot not only erased the presence of unwanted by products but also demonstrates the functionality of the transposase-based production of stable reporter cell lines (**Figure 18**).

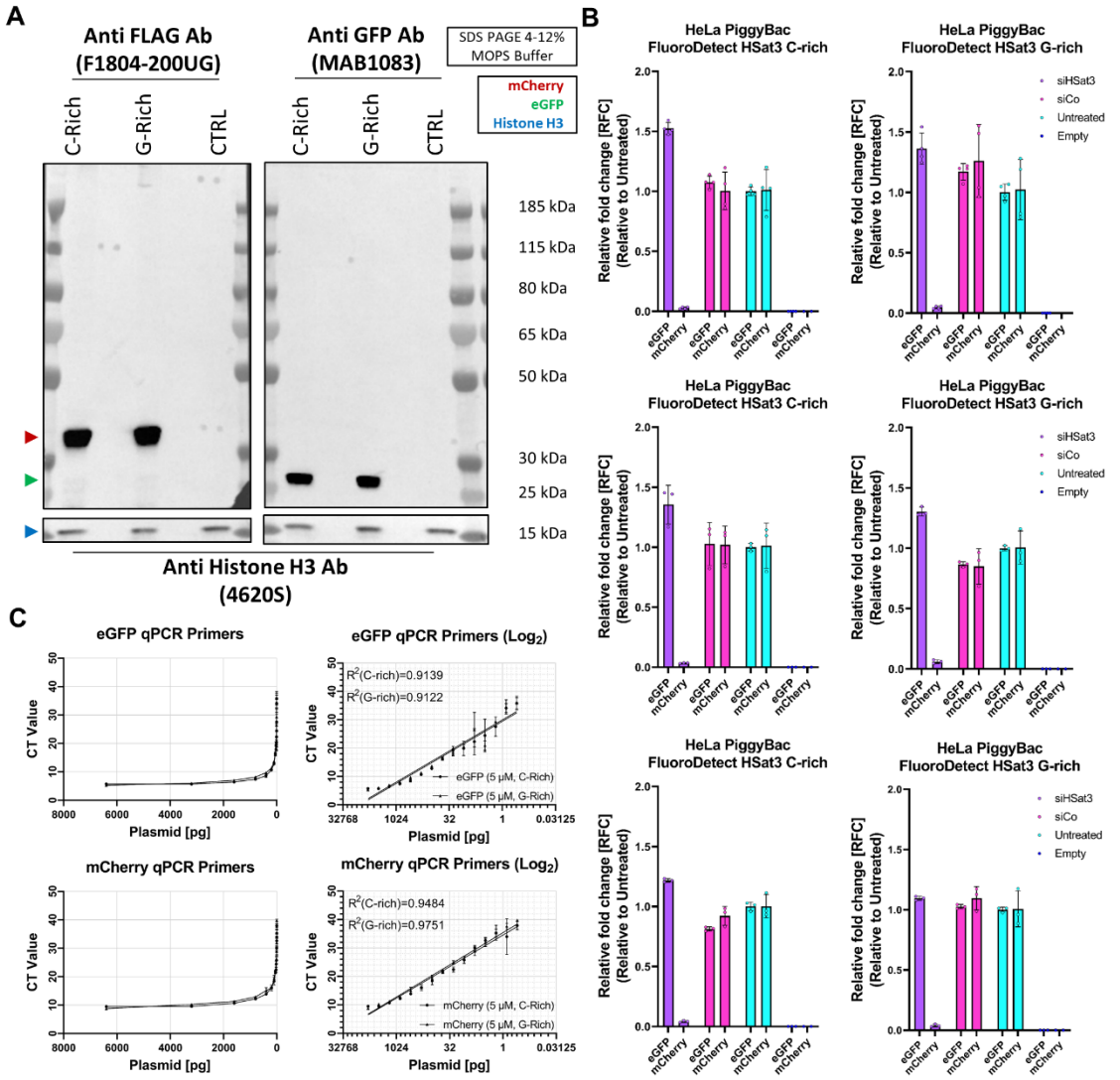

Figure 18 Independec of eGFP and mCherry reading frame and tranbscripts. A: *Western blot of stable reporter cell lines HeLa C-rich HSat3 (C-Rich) and HeLa G-rich HSat3 (G-Rich). A wild type HeLa population was used as negative controle (CTRL). The N-terminal FLAG Taged mCherry protein was labelled using a FLAg specific antibbody. The refeenc gene eGFP was labelded usaing a GFP specific antibody. The loding control was performed using an antibody labeling Histone H3.* ***B:*** *Indipendenc of mCherry and eGFP transcripts was demostrated using RT-qPCR. The mRNA levels of eGFP and mCherry were determined in samples exposed to siHSat3 and siCo. Results were compared with an untreated population as well as with and wild type population.* ***C:*** *Dilution series of FluoroDetect plasmid DNA was used to determine the prtimer performance of eGFP and mCherry qPCR primers. (All graphs showing the median ± 95% confidence interval [CI]). (Hess et al., Mol. Ther. Nucl. Ac., 2025)*[86]

6.9 Testing Additional Target Motives

To prove the adaptability of the assay, additional assays, using different target motifs were generated: one assay contained a Heat Shock Factor 1 (HSF1) mRNA target motif and one assay contained an Epidermal Growth Factor Receptor (EGFR) target motif. The target sequences of both assays were created with overlapping exon junctions to increase specificity and reduce off-target effects (**Figure 19 A**). A strong sequence-specific knock-down could be observed in both assays using Fluorescence microscopy as well as plate reading (**Figure 19 B,C**).

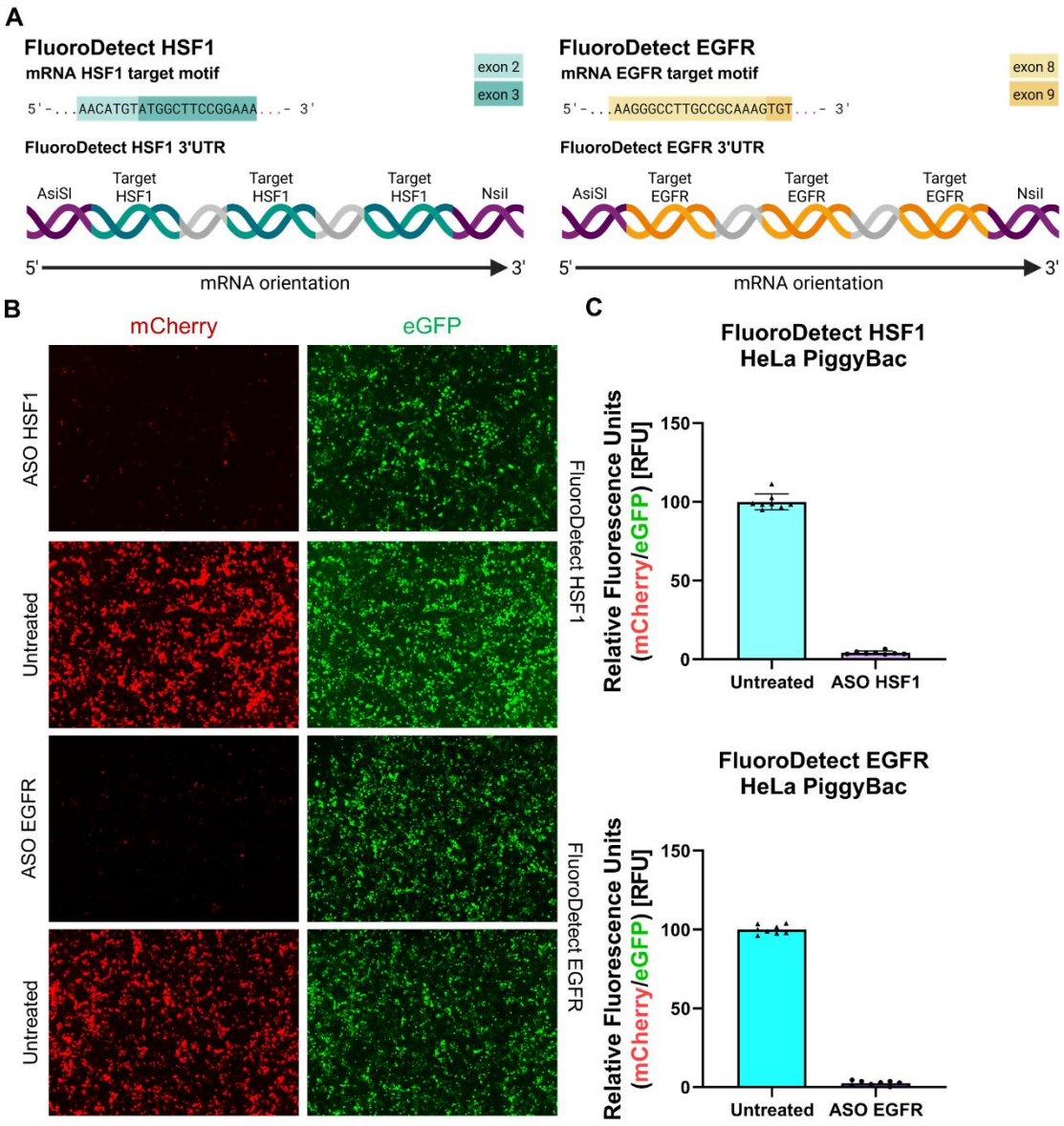

Figure 19 Demonstration of FluoroDetect adaptability testing additional target motifs. A: *Illustration showing the target sequences as well as the target structure in the 3'UTR of the FluoroDetect HSF1 and EGFR. B: Transfection experiment of the FluoroDetect HSF1 and EGFR inspected using fluorescence microscopy. Comparison of Untreated and targeting ASO treated populations.* ***C:*** *Quantification of the knock down efficiency in both assays using plate reading. Comparison of Untreated and targeting ASO treated populations. (All graphs showing the median ± 95% confidence interval [CI]). (Hess et al., Mol. Ther. Nucl. Ac., 2025)*[86]

6.10 Knock Out of The EGFR Using Prime Editing

As previously outlined, a pivotal piece of information, particularly pertinent to the development of RNAi-based pharmaceuticals, involves the quantity and functionality of RNAs that are delivered to the cytoplasm. In addition to the previously mentioned information, the second key point of the developmental platform is the control of the delivery route to precisely investigate targeting approaches. Control of the delivery route can be assessed by genetically engineering of model organisms. As outlined in the introduction this work aims for the tissue specific delivery of siRNAs via the EGFR. So, in the bigger context of this work, control of the delivery rout, in

detail the EGFR, can be given by comparing EGFR positive and EGFR knock out populations. Knocking out the EGFR receptor can be assessed by genome editing technologies like CRISPR Cas9. A novel genome editing technology called PrimeEditing enables precise and versatile genetic modifications without inducing double-strand breaks (DSBs) or requiring donor DNA templates. Developed as an advancement over CRISPR-Cas9 and base editing systems, prime editing combines a catalytically impaired Cas9 nickase with a reverse transcriptase (RT) enzyme, guided by a prime editing guide RNA (pegRNA) to install targeted edits directly into the genome. An example of the pegRNA design is shown in **Figure 20**. In the example the correction of a point mutation causing the R337H mutation in p53 is desired.

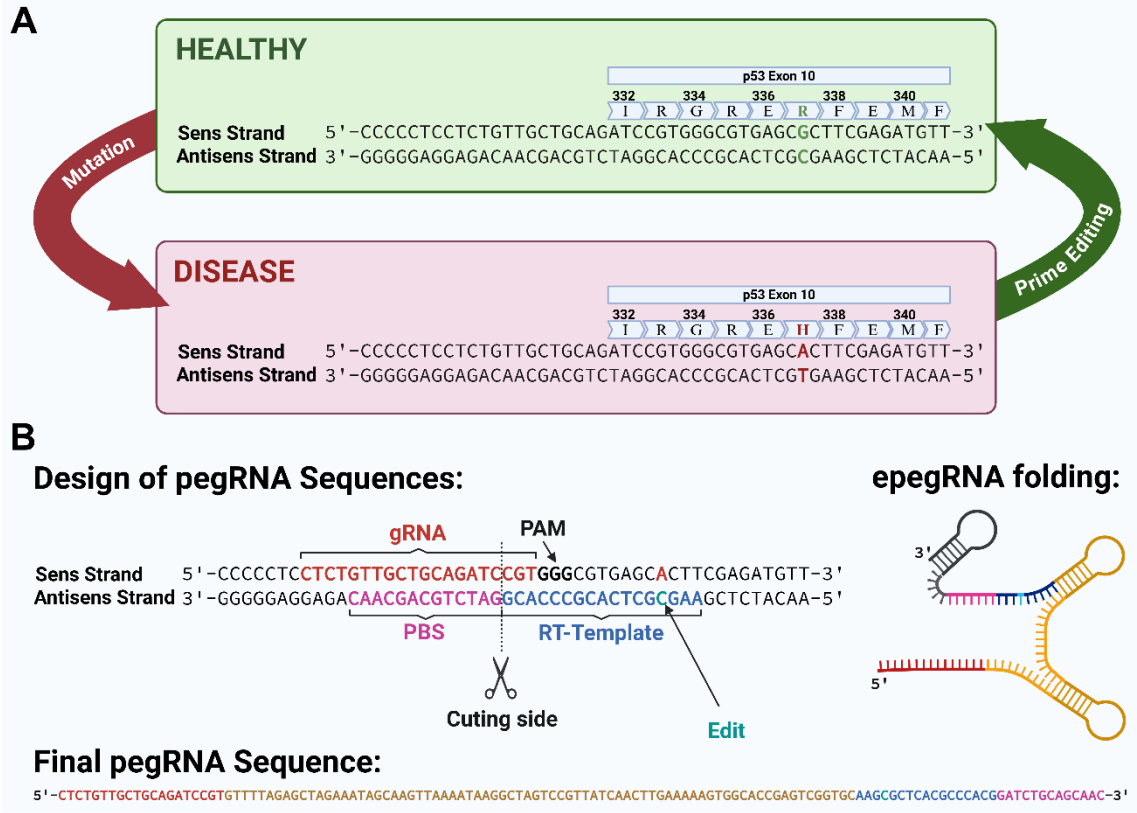

Figure 20 Schematic figure showing the design of a prime editing guide RNA (pegRNA). ***A:*** *Example of prime editing as therapy for disease caused by single gene mutations. p53 R337H a common driver mutation in cancer could be corrected using prime editing.* ***B:*** *Example of pegRNA design to correct the p53 R337H mutation. Structurally the pegRNA consists of four elements from 5' to 3': the guide RNA (gRNA,red), the Cas9 binding scaffold (yellow), the reverse transcription template (RT-Template, blue) and the primer binding site (PBS, pink). The pegRNA can be stabilized by adding an additional "tevopreQ1" loop (gray) to the 3' end.*

The prime editor 2 (PE2) system, the most widely used variant, consists of a Cas9 nickase (H840A mutation) fused to a pentamutant Moloney murine leukemia virus (M-MLV) RT. The pegRNA directs the complex to the target site with its guide RNA (gRNA) component and encodes both the primer binding site (PBS) and the RT template for the desired edit. Upon nicking the DNA, the RT uses the RT template to synthesize the edited strand *in situ*, which is then incorporated into the genome through cellular repair mechanisms.[95] The expression of a dominant negative

MLH1 mutant (hMLH1dn) is used to decrease the mismatch repair (MMR) and increase the prime editing efficacy in the prime editor 4 (PE4) system.[96]

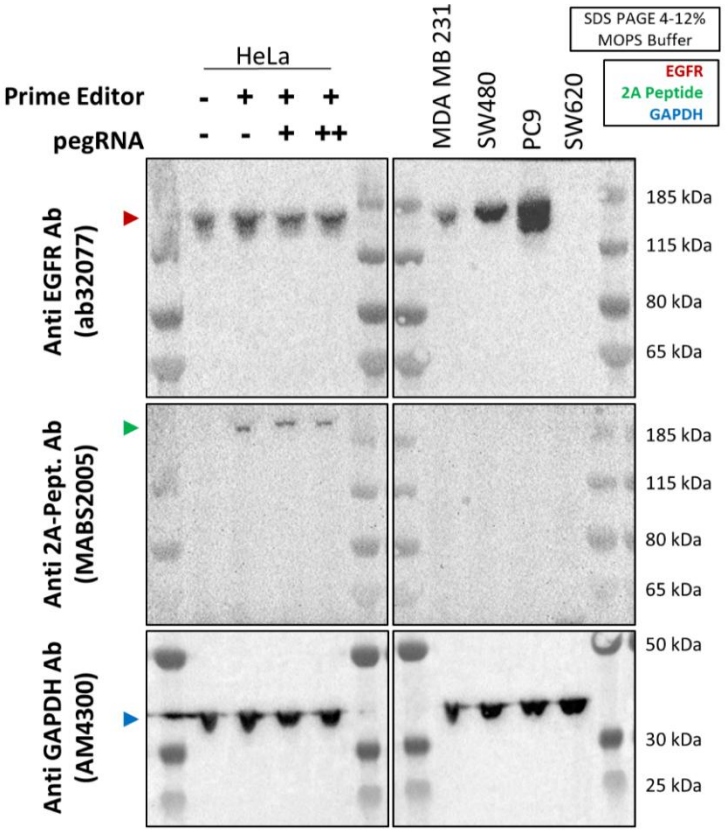

Figure 21 Expression control of EGFR and Prime Editor. *Western blot of Hela,MDA MB 231, SW480 PC9 and SW620 cells. A EGFR antibody for detection of EGFR (red) and a 2A antibody to label the Prime Editor(green) was used. GAPDH targeting antibody was used for loading control (blue). Prime editing was tested in HeLa cells using different conditions, as indicated.*

To perform prime editing and knock out the EGFR in various cell lines an indicial experiment was performed using a PE4 system. For this purpose, the prime editing plasmid pCMV-PEmax-P2A-hMLH1dn [97] (**Figure S 11**) as well as a pegRNA were transfected into HeLa cells. The pegRNA contained the commercial Alt-R gRNA modification pattern provided by Integrated DNA Technologies Inc. (IDT) to enhance RNA stability (**Table S 1**). To knock down the EGFR expression, a L41* stop codon insertion by point mutation was intended. Prime editing efficacy was monitored using sequencing of gDNA as well as Western blotting. As the prime editor is expressed from a bicistronic reading frame its C term contains a 2A protein sequence which can be used as protein tag in Western blot. Cells were harvested 72 h after genome editing. HeLa cells only transfected with the prime editor as well as HeLa cells cotransfected with pegRNA (+: 1,2 µg; ++: 2,4 µg) showed no reduction of EGFR signal on the Western blot, compared to the non-edited control. 2A protein could be detected in all samples transfected with prime editor plasmid. As the prime editor and the hMLH1dn are expressed bicistronic this proofed successful transfection as well as expression of the prime editor. The EGFR status of the cell lines (MDA MB 231, SW480, PC9 and SW620) showed that, the cell line SW620 was indeed negative for EGFR expression. All loading controls (GAPDH) showed equal loading (**Figure 21**). Sanger sequencing was unremarkable and showed no mutations in the target region.

6.11 Knock Out of The EGFR Using CRISPR Cas9

After the initial applications of PrimeEditing, a modification was made to the strategy for genetic engineering. PrimeEditing is an advanced tool that facilitates gene editing in living organisms with a high degree of precision. However, its complex setup and comparable low efficiency when achieving knockout results highlight potential areas for improvement. Consequently, the prevailing methodology for the creation of cell lines with an EGFR knockout was the application of classic Cas9-based CRISPR gene editing. Therefore HeLa, MDA MB 231, SW480 and PC9 cells were electroporated in presence of a ribonucleoprotein (RNP) mix which contained gRNA (**Table S 2)**, Cas9 Nuclease and poly-L-glutamic acid. After an appropriate period of time during which the genetically modified cell population could expand, a flow cytometry analysis was executed. Gating was performed using wild type cells as described in the following. Cell debris and particles with aberrant size were excluded by gating the major cell fraction in the FSC-H over SSC-H density plot. To exclude duplets in the previously defined population a population called single cells was gated in a density plot of FSC-H over FSC-A. Dead cells were excluded by DAPI staining and stringent gating in the DAPI channel. The cell population was labelled with an APC Fire™ 750 tagged EGFR specific antibody prior to the measurement. APC Fire™ 750 labelling assessed detection of receptor expression in the Cy5 channel of the cytometer. An isotype control was performed showing effect size of unspecific antibody cell interaction.

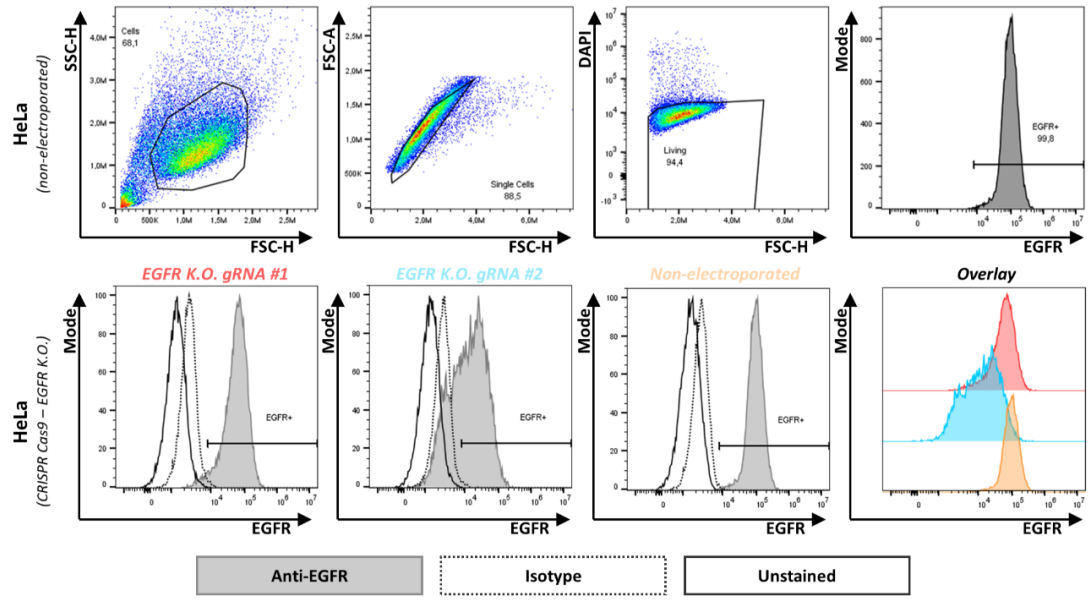

Figure 22 Flow cytometry analysis of CRISPR Cas9 EGFR knock out in HeLa cells. Upper Row: *Gating strategy to assess EGFR knock down. Population called "cells" was defined in a FSC-H versus SSC-H scatterplot. Subpopulation of "single cells" was defined in a FSC-H versus FSC-A scatter plot. Living cell population was gated by excluding cells exhibiting enhanced fluorescence in the DAPI channel. WT population (gray) stained with EGFR specific antibody was used to define EGFR+ gate.* ***Lower Row:*** *Isotype control (dotted line) defined unspecific antibody interaction. Unstained population (continuous line) was included to evaluate autofluorescence. Gene editing efficiency was evaluated comparing the edited populations EGFR K.O. gRNA#1 (red) and EGFR K.O. gRNA#2 (blue) with a non-electroporated wildtype sample(orang).*

In all cell lines the control samples showed the expected response. As already shown in Western blot analysis, EGFR expression could be detected in all cell lines when using EGFR specific antibody. The performance of gRNA #1 was very unequal across all cell lines Flow cytometric analysis showed intermediate to high knock out rate when gRNA #2 was used across all cell lines (HeLa, MDA MB 231, SW480 and PC9) (**Figure 22**,**Figure S 13**, **Figure S 14**, **Figure S 15**). Following the CRISPR Cas 9 knockdown EGFR negative cell populations were sorted into cell culture vessel and expanded to establish EGFR knock out cell lines. In follow up experiments the engineered EGFR knock out cell lines were used to create EGFR negative FluoroDetect reporter cell lines. A list of generated cell lines can be found in the appendix of this work (**Table S 3**). Establishing the FluoroDetect based compound development platform in the generated EGFR K.O. cell lines enhanced the platform capacity evaluation of receptor specific uptake. Integrating this essential aspect represents the final improvement of the FluoroDetect platform to create ideal conditions for the development of EGFR targeting RNA conjugates.

7 Results – Development of a Delivery System

As stated in the introduction, there is a significant clinical need for receptor-specific nucleic acid delivery systems, capable of targeting tissues outside the liver. These delivery systems could give new therapy perspectives in neurodegenerative disease, infectious disease as well as in oncology. An example which is followed up on in HSat3 RNA which is associated with etoposide resistance in lung cancer. Therefore, the second section of this work focuses on the development of an EGFR specific aptamer-RNA conjugate (ARC) targeting HSat3 RNA utilizing solid-phase synthesis, in vitro transcription and hybrid approaches.

7.1 Development Process

The development of RNA conjugates cannot be streamlined as a linear process. It rather can be seen as a cycling process of trial and error. In the first phase the drug candidate is designed *in silico* and synthesized. In a second phase the compound is evaluated based on an efficient development platform. In a third phase the experimental data is analysed, compared to scientific literature and the information gained are involved in the design of the next cycle. Each of these cycles can be considered as a generation improving the compound candidate each generation (**Figure 23**). The following chapters show the first five generations of the developmental process designing an EGFR specific HSat3 targeting ARC.

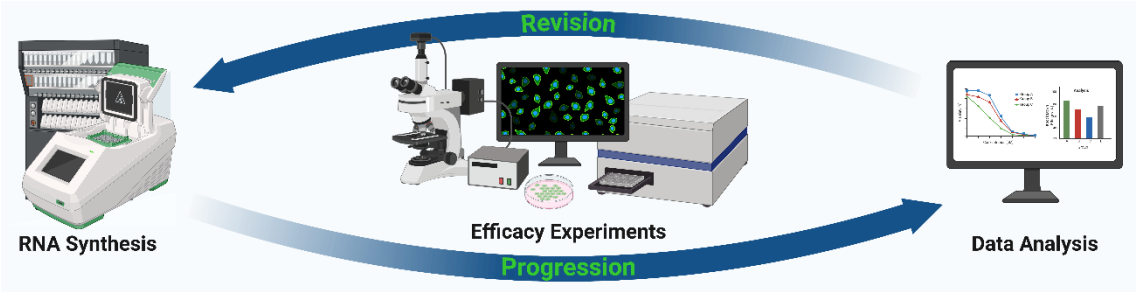

Figure 23 Schematic figure of the general workflow in Aptamer-RNA conjugate development. *The three-step circular development process of Aptamer siRNA conjugates is divided in: Phase 1 – Design and RNA Synthesis; Phase 2 – Experimental evaluation and Phase 3 – Data analysis.*

7.2 RNA Conjugates 1st Generation (Cleavable + Click Reaction)

With the initial idea to develop an ARC delivering a HSat3 specific ASO and targeting the EGFR the drug developmental process was started. Considering the whole process of preclinical and clinical development an RNA aptamer (CL4) was chosen as EGFR targeting ligand, to keep synthesis and drug approval as simple as possible. Evolved by *Esposito et al.* the RNA aptamer CL4 binds NSCLC cell lines with a dissociation constant of 10 nM. This makes it a promising candidate

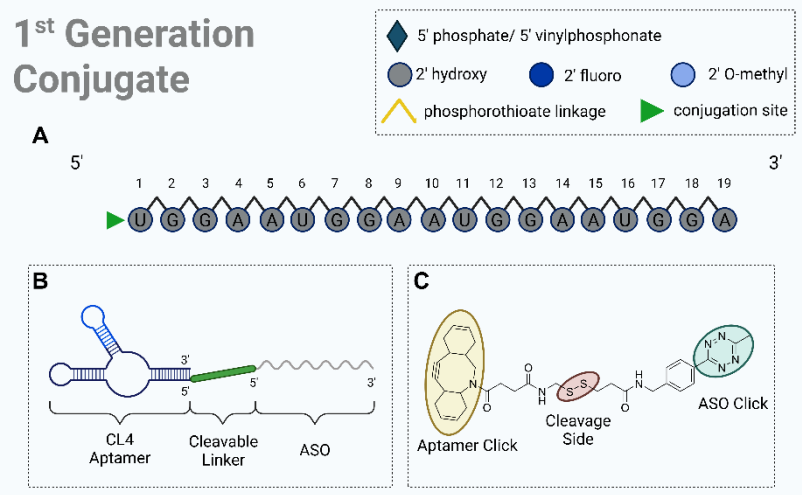

Figure 24 Schematic figure of the 1st generation RNA conjugates. A: *5' modified HSat3 targeting antisense oligo nucleotide.* ***B:*** *Schematic structure of the assembled aptamer antisense oligonucleotide conjugate.* ***C:*** *Linker molecule indicating the reactive groups for assembly and disulfide bond for selective intracellular cleavage.*

for targeted RNA delivery. Moreover, it could be shown that CL4 is internalized into EGFR positive cells. In addition, CL4 can selectively cause apoptosis in EGFR overexpressing cell lines, possibly enhancing the efficacy of a potential drug candidate. With the choice of a targeting ligand and HSat3 RNA as a siRNA target the missing piece for drafting a first prototype was the linkage of aptamer and ASO. To release ASO after endocytosis a glutathione instable linker molecule (**Figure 24**) was designed, synthesized and provided by the research group of Prof. Kath-Schorr. As the glutathione concentration increases inside eukaryotic cells, the cleavage of the integrated disulfide bond should release the ASO into the cytoplasm upon endocytosis (**Figure S 16**).[98] As an assembly strategy the 5' azido-polyethylene glycol4 (PEG4) modified aptamer (**Figure S 17**) was covalently bound to the dibenzocyclooctyne (DBCO) group of the linker using a strand promoted azide-alkine cycloaddition (SPAAC)(**Figure S 18**). The product received was loaded with the 5' trans-cyclooctene (TCO)-PEG4 (**Figure S 19**) modified ASO by an inverse electron demand Diels-Alder reaction (IEDDA)(**Figure S 20**) to the group of the linker. The assembly as well as the quality

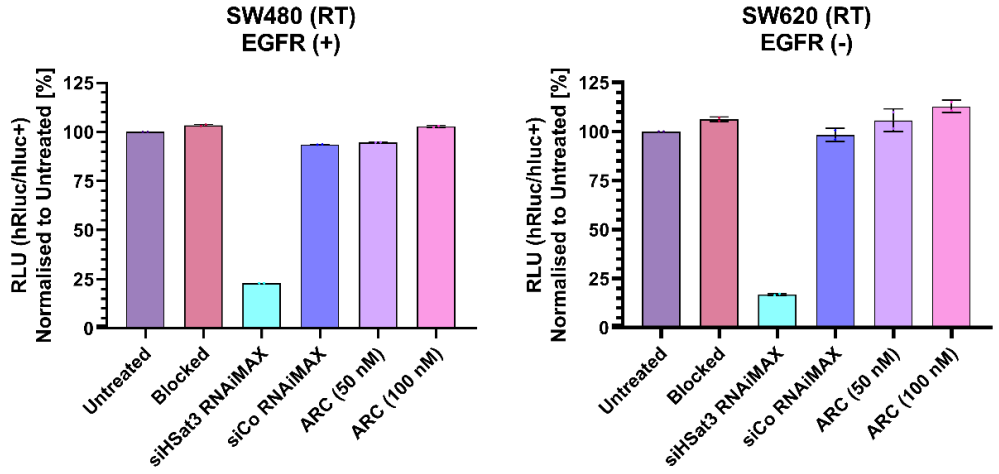

Figure 25 Evaluation of 1st generation compound candidates at RT using psiCheck2 HSat3 Luciferase assay. *EGFR positive SW480 and EGFR negative SW620 cells expressing the psiCheck2 HSat3 assay treated with 100 nM and 50 nM concentration of 1st gen. ARC. Bioluminescence was measured at the indicated time points after treatment with the compound. Single value displayed are independent technical replicates normalized to an untreated sample. (All graphs showing the median ± 95% confidence interval [CI])*

control was performed in the lab of Prof. Kath-Schorr. A schematic figure, the used RNA modifications, as well as the ASO sequence of 1st generation compound can be found in **Figure 24**.

The present study set out to investigate the internalisation rate of a 1st generation ARC compound candidate. To this end, the assay was tested in two different cell lines, SW480 (EGFR positive) and SW620 (EGFR negative), both of which expressed the psiCheck2 HSat3 (**Figure S 2**) assay (**Figure 25**). To prevent receptor internalization a control experiment was performed at 4°C (**Figure 26**).[99] To saturate unspecific binding sites cells were blocked 30 minutes prior treatment using a nucleic acid blocking solution which contained shredded salmon sperm DNA (sssDNA). Treatment was performed 10 minutes in binding buffer to prevent compound degradation in the cell culture medium. After treatment cells were washed twice with PBS and cultured in cell culture medium for 48 hours. Independent of the temperature or the EGFR expression status a slight decrees of RLU when exposed to 50 nM concentration of the compound was observed. Upon a 100 nM concentration of the compound no significant reduction of RLU could be detected. In all positive controls transfected with siHSat3 Lipofectamine RNAiMAX lipoplexes, a strong reduction of RLU could be observed. All negative controls transfected with an untargeted siCo pool lipoplexes as well as those treated only with blocking buffer showed no significant reduction compared to the untreated control samples.

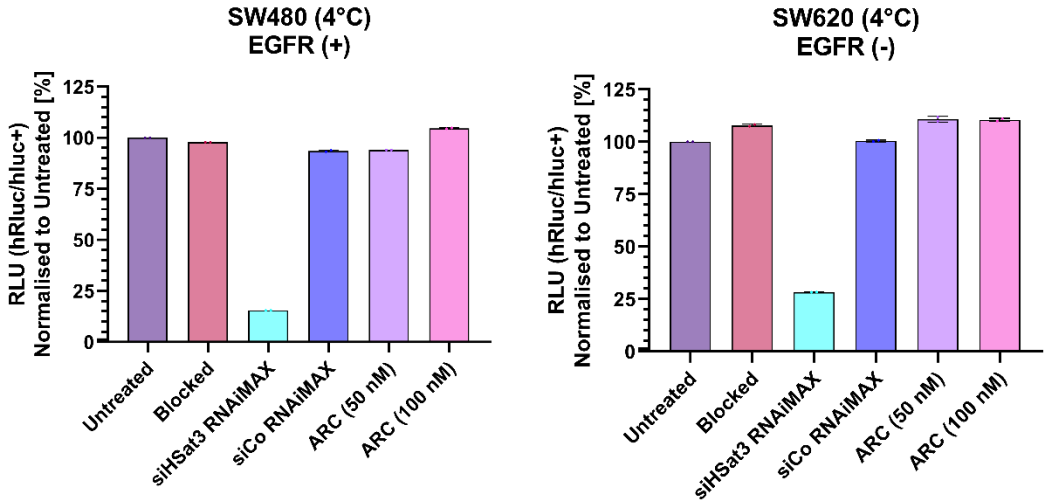

Figure 26 Evaluation of 1st generation compound candidates at 4°C using psiCheck2 HSat3 Luciferase assay. *EGFR positive SW480 and EGFR negative SW620 cells expressing the psiCheck2 HSat3 assay treated with 100 nM and 50 nM concentration of 1st generation ARC. Bioluminescence was measured at the indicated time points after treatment with the compound. Single value displayed are independent technical replicates normalized to an untreated sample. (All graphs showing the median ± 95% confidence interval [CI])*

As all samples were only responding to the lower compound concentration, the compound concentration was reduced for follow up experiments. To evaluate the connection of treatment duration and knock down efficiency the compound exposure time was varied. Chosen treatment durations were 10 minutes, 4 hours and 48 hours. As cells could not be cultured for 4 hours and 48 hours in aptamer binding buffer, treatment was performed in cell culture medium 30 minutes

after blocking. In all samples treated with 25 nM and 50 nM of the compound a marginal reduction in RLU could be observed upon a 10-minute treatment. Upon 4 hours exposure to the compound samples showed various responses, reaching from upregulation towards slight downregulation. Surprisingly, all cell lines showed strong knock down after 48 hours of treatment independent of their EGFR status. All positive and negative controls exhibited the expected response. (**Figure 27**)

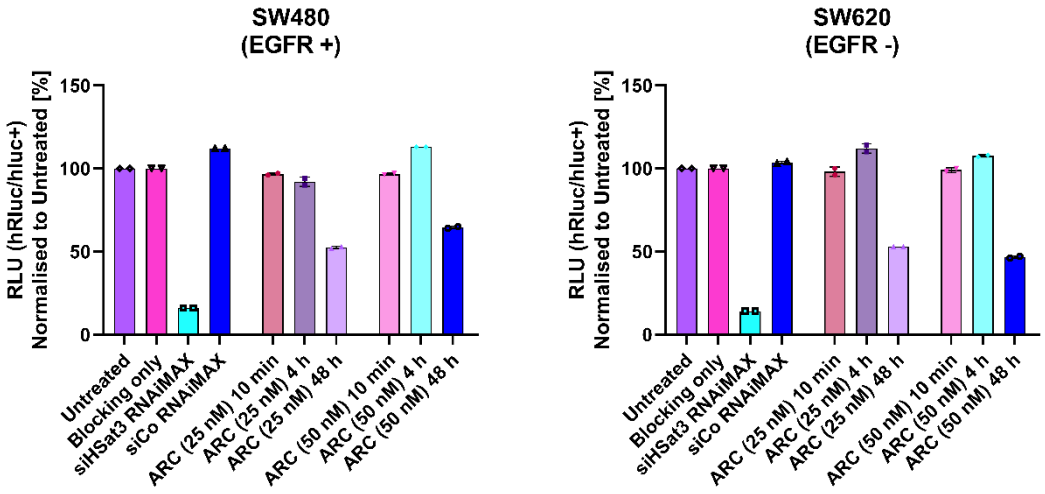

Figure 27 Different treatment time duration of 1st generation ARC. *EGFR positive SW480 and EGFR negative SW620 cells expressing the psiCheck2 HSat3 assay were treated at RT with 50 nM and 25 nM concentration of 1st generation ARC. Bioluminescence was measured at the indicated time points after treatment with the compound. Control samples were treated for 48 h as indicated. Single value displayed are independent technical replicates normalized to an untreated sample. (All graphs showing the median ± 95% confidence interval [CI])*

7.3 RNA Conjugates 2nd Generation (Non-Cleavable + Click Reaction)

After completing the first developmental cycle the compound design was reevaluated and modified. To reduce the strong EGFR unspecific knock down observed in the 1st generation compounds the linker molecule was modified. The thiol mediated uptake is important for various drug delivery strategies (e.g. Spinraza®), it can be a challenging competitor in receptor specific delivery.[100] As not much is known about the exact mechanism dynamic covalent sulphur exchange

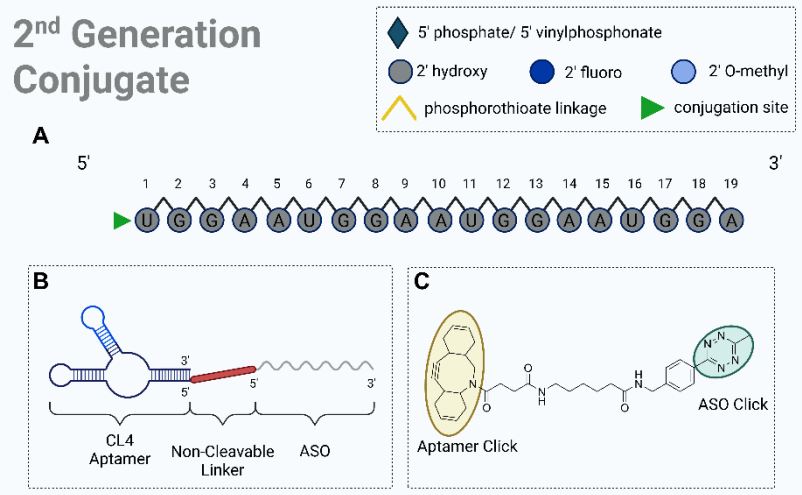

Figure 28 Schematic figure of the 2nd generation RNA conjugates. A: *5' modified HSat3 targeting antisense oligo nucleotide.* ***B:*** *Schematic structure of the assembled aptamer antisense oligonucleotide conjugate.* ***C:*** *Linker molecule indicating the reactive groups for assembly.*

cascades seem to play a dominant role in facilitating direct translocation across the plasma membrane into the cytosol, occurring either prior to or during membrane passage.[98] The intention was to guarantee cytoplasmatic release of the ASO upon endocytosis. Therefore, the glutathione cleavable disulfide bond was a central aspect of 1st generation compound design. Unfortunately, its extracellular cleavage increased the risk of the thiol mediated uptake of the cleaved products (**Figure S 16**).[98] Hence, synthesis as well as assembly of 2nd generation linker and ARC was performed similar to 1st generation conjugates in the lab of Prof. Kath-Schorr. A schematic figure, showing the used RNA modifications as well as the ASO sequence of the 2nd generation compound can be found in **Figure 28**. To evaluate the functionality and improved serum stability compared to 1st generation compound the previously defined setup was repeated. Cells were blocked 30 minutes before treatment with an RNA blocking solution. EGFR positive SW480 and EGFR negative SW480 cells, expressing the psiCheck2 HSat3 assay, were treated with 25 nM and 50 nM concentration of the compound for 48 h in cell culture medium. Cells were lysed, luciferase substrates were added, and luminescence was measured using a plate reading system. Samples exposed to 25 nM concentration of the compound showed no reduction of RLU. Upon 50 nM concentration of the compound an EGFR specific reduction of RLU was observed. Despite expectations a HSat3 specific but receptor independent reduction of RLU was observed upon exposed to 50 nM unformulated siHsat3 (without lipofection reagent). This effect could be caused by thiol mediated uptake of phosphorothioate modified siRNA. Control samples showed no irregularities. (**Figure 29**) Compared to the strong response to the siHSat3 lipoplexes, the knock down efficacy using aptamer ASO conjugates showed very limited efficacy. Nevertheless, this result facilitates a first proof of concept.

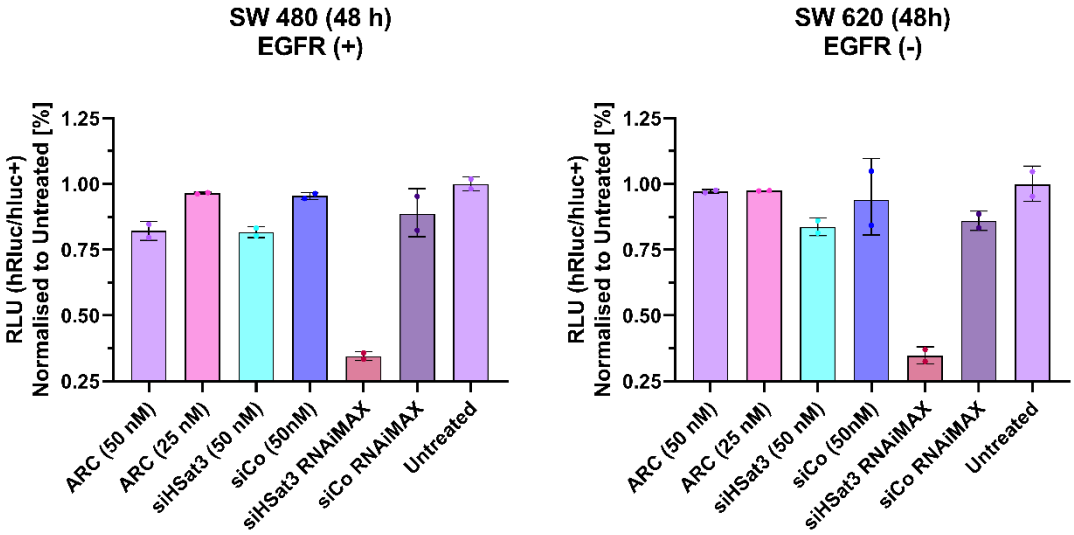

Figure 29 Cell culture evaluation of 2nd generation ARC. *EGFR positive SW480 and EGFR negative SW620 cells expressing the psiCheck2 HSat3 assay treated with 50 nM and 25 nM concentration of 2nd gen ARC. Luciferase assay was performed 48 h after treatment with ARC. Control samples were treated with unformulated siRNAs at a 50 nM concentration as well as with siRNA lipoplexes for efficient transfection. Single value displayed are independent technical replicates normalized to an untreated sample. (All graphs showing the median ± 95% confidence interval [CI])*

7.4 siRNA Conjugates 3rd Generation (Non-Cleavable + C3 Spacer)

The 2nd generation compounds included no 2'-RNA modifications to increase RNase resistance. Therefore, serum stability was estimated to be less than ideal. Additionally, metabolic stability and immunogenicity need to be considered in the context of drug development. Unmodified RNAs are degraded within minutes under physiological conditions and double stranded RNAs trigger innate immune response.[101] Consequently, RNA modifications were integrated to increase efficacy and reduce immunogenicity compared to previous compound generations. To meet state of the art modification requirements a fully 2'-OMe modified configuration of RNA was assessed. To Increase exonuclease resistance two phosporothioate modifications were integrated at all terminal 5' and 3' ends of the used RNA strands. As basic design was shifted from a cleavable linker using a non-cleavable linker, the payload release strategy needed to be re-evaluated. In combination with the drafted design the delivery of a siRNA was preferred over the delivery of an ASO. This was due to several benefits regarding knock down efficacy and durability shown in literature.[60,62] As conjugation of the ASO using SPAAC and IEDDA was challenging and reduced the yield significantly synthesis strategy and linker were modified. To reduce the synthesis complexity the aptamer, linker and passenger strand were synthesized as one strand using SPS. A linker sequence of five C3-Spacers was integrated between aptamer and passenger strand as demonstrated by *Yoon S. and Huang K.-W. et al.*.[102] To increase RISC loading of the guide strand a 5' phosphate modification was attached to its 5' end.[66] A schematic figure, showing the used RNA modifications as well as the siRNA sequence of 3rd generation compounds can be found in **Figure 30**. Here and in the following the aptamer modified passenger strand will be referred to as the 'vehicle'. As the cargo of the 5' phosphorylated biological active guide strand is intended by the vehicle, the pharmaceutical compound will be referred to as the 'payload'. Vehicles, as well as payload were synthesized in the lab of Prof. Kath-Schorr. To assemble a functional aptamer and promote duplex formation

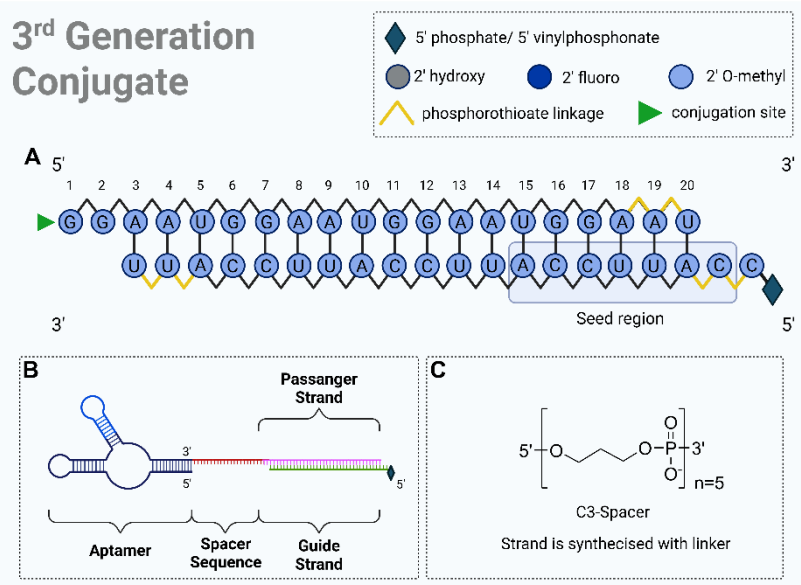

Figure 30 Schematic figure of the 3rd generation RNA conjugates. A: *5' passenger conjugated HSat3 targeting siRNA containing an advanced modification pattern.* ***B:*** *Schematic structure of the assembled aptamer siRNA conjugate.* ***C:*** *Structure of a C3-spacer element for SPS integrated linker integration.*

of the siRNA subunit an annealing protocol needed to be established prior to cell culture treatment. Hence payload and vehicle were mixed in a 1:1 molar ratio in an annealing buffer. Following this step, the hybridization mix was heated up to denature the single strands and slowly cooled down to 4 °C to support aptamer folding and siRNA formation. To proof formation of aptamer siRNA conjugate a Urea PAGE was performed. As a control for the electro mobility shift non-annealed sample of payload and vehicle strand were loaded. Following the electrophoresis, the polyacrylamide gel was stained using SYBER Gold dye. For size comparison ssDNA ladders were loaded. The 20 nucleotide short payload strand could not be detected upon staining. The 69 nucleotide long vehicle strand could be detected slightly shifted compared to the ssDNA ladder, running at a size of 80 nt. Upon annealing of vehicle and payload two species could be detected. One running at the same size as the vehicle strand and a second one showing lower electro mobility running at a size of 90 nt compared to the ssDNA ladder. All lanes loaded with vehicle strand showed weak pattern of RNA degradation. (**Figure 31**) The higher intensity of the second band indicates that the assembly of the aptamer siRNA conjugate worked. Consequently, follow-up experiments were performed investigating the functionality of the ARC. As described in section one in parallel to the compound development, the FluoroDetect system has been developed and established. Evaluation of the 3rd generation compounds therefore was assessed using a transient setup of the FluoroDetect assay system. Moreover, the target sequence needed to be modified to be capable of detecting the C-rich payload strand instead of the G-rich ASO used in 1st and 2nd generation compounds. To identify a sufficient concentration of ARC necessary to facilitate a strong knock down a dilution series ranging from 750 nM to 10,156 nM concentration was performed. EGFR positive HeLa and SW480 cells as well as EGFR negative SW620 cells expressing the FluoroDetect G-rich assay system were treated with the indicated compound concentration for 72 h. Afterwards, the fluorescence signals of the FluoroDetect assay were measured. To control functionality of the siRNA

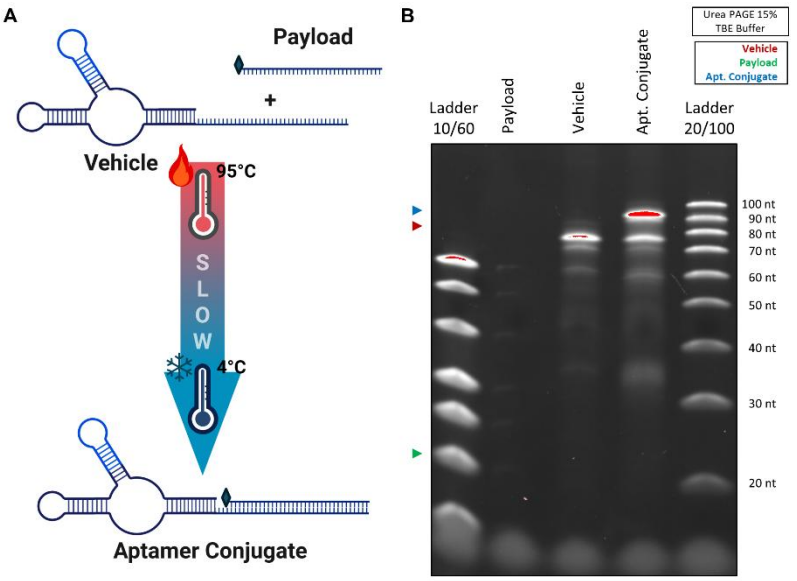

Figure 31 Proof of concept - Hybridisation of vehicle and payload strand. A: *Schematic protocol of ARC assembly.* ***B:*** *Urea PAGE loaded with 20 pmol of indicated species, showing electromobility shift upon assembly. 10/60 and 20/100 ssDNA ladder for comparison. Gel stained with SYBER Gold.*

subunit of the ARC control samples were exposed to ARC lipoplexes. Upon exposure the RFU in the samples was decreased by 30-40% indicating a functional but low performing siRNA compared to the siHSat3 positive control. HeLa and SW480 cells showed no response to the non-targeting siCo lipoplexes. In contrast the SW620 cell line showed a strong response to the negative control limiting the data interpretation. Nevertheless, no significant reduction of RFU could be observed in the cell lines independent of the compound concentration. (**Figure 32**)

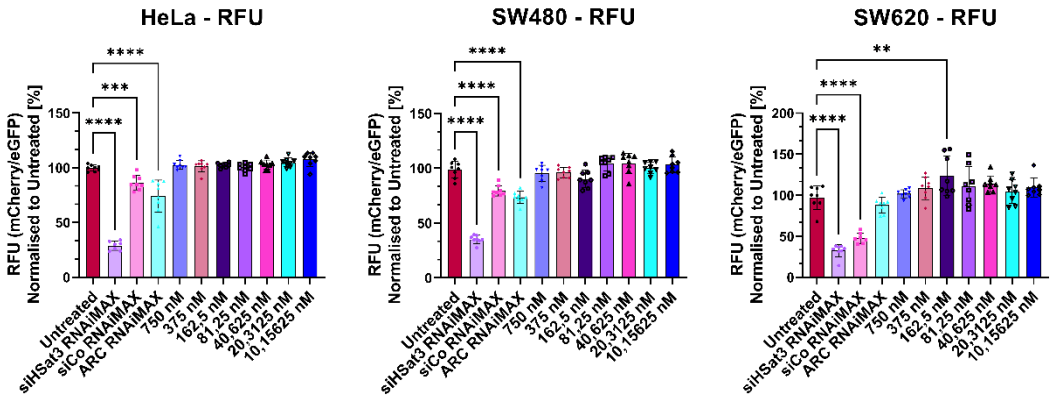

Figure 32 Dose escalation experiment of the 3rd generation ARC. *EGFR EGFR positive HeLa and SW480 as well as EGFR negative SW620 cells expressing the FluoroDetect HSat3 G-rich assay treated with different concentrations of 3rd gen. ARC. Fluorescence was measured 72 h treatment with the compound. Control samples were treated with siRNA lipoplexes as indicated. Single value displayed are independent technical replicates normalized to a untreated sample (All graphs showing the median ± 95% confidence interval [CI]).*

7.5 In Silico Design of 4th Generation Conjugates

Finishing the 3rd generation of aptamer siRNA conjugates showing sufficient knock down efficiency upon transfection could prove the functionality of siRNA conjugated with a targeting RNA aptamer. Nevertheless, independent of the concentration, no sufficient delivery of the 3rd gen. ARC could be detected. Thus, the functionality of the RNA aptamer was in the focus of the project. Therefor detailed consideration of the RNA aptamers selection during SELEX was necessary. To increase RNA stability during most RNA SELEX screenings the mutant T7 RNA polymerase Y639F, developed by *Sousa, R. and Padilla, R.*, is used to integrate 2'F modified pyrimidine nucleotides into the RNA.[103] These 2'-F modifications can be of central importance for the folding and binding affinity of the RNA aptamer.[104] Moreover, re-evaluating the choice of targeting aptamer, the work of *Kelly, L., Maier, K.E., Yan, A.et al.* comparing different cell surface targeting aptamers, became of interest for this project. *Kelly, L., Maier, K.E., Yan, A.et al.* could show much higher EGFR internalization of the RNA aptamer MinE07 in comparison to CL4, which was used in the 1st-3rd generation of RNA aptamer conjugates.[105] In addition *Thomas, Brian J. et al.* could show cellular uptake of a 3' elongated MinE07 hybridized with a fluorescent labelled DNA probe. In a result MinE07 was used as aptamer part for the design of 4th generation conjugates. Despite *Thomas, Brian J. et al.* already proofed the uptake of this aptamer conjugate it is possible that

still does not work, as the correct folding of the aptamer strongly dependents on the sequence added.[80] Furthermore, annealing of a second payload strand could also interfere with the aptamer sequence disrupting its functionality. Therefore, in order to evolve the design of 4th generation ARCs three different RNA prediction algorithms were used to predict aptamer folding and the hybridization of the payload. Two-dimensional energy-based structure modelling of aptamer folding as well as two dimensional cofolding of multiple strands was performed using ViennaRNA WebServer[106,107] and DINAMelt web server[108]. Three dimensional predictions were performed using AlphaFold3 Server provided by GoogleDeepmind.[109] The prediction of MinE07 and MinE07tail (Construct used by *Thomas, Brian J. et al.*[80]) were used to predict the structure of the 4th generation ARC.

The prediction of MinE07 folding using Vienna web server showed the formation of two interior loops as well as one hairpin within the stem loop structure and is shown as dot bracket notation (**Figure 33 A**). Overall, the prediction showed a minimum free energy (MFE) of -9,30 kcal/mol indicating a thermodynamically stable structure.[110]

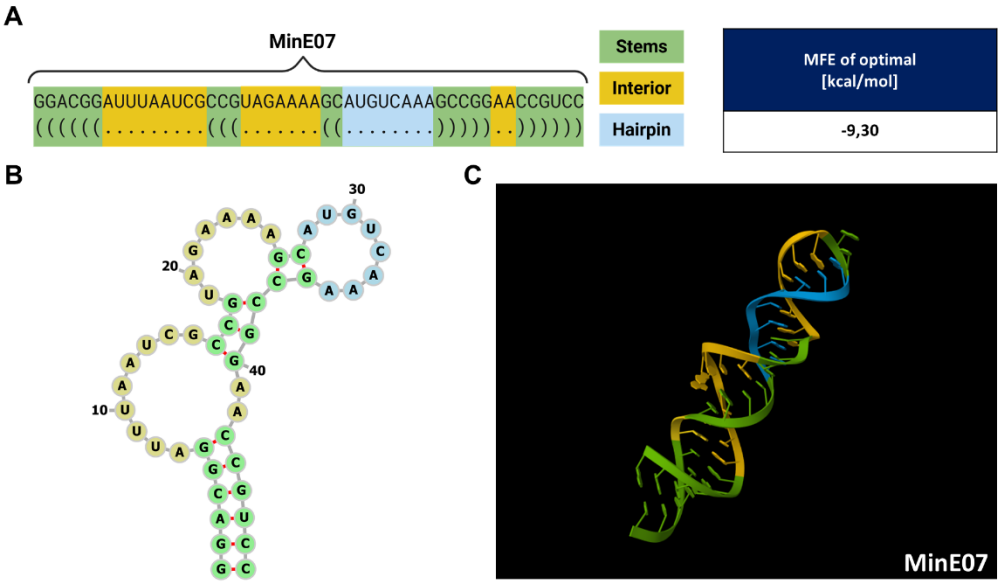

Figure 33 Predicted structure of the RNA aptamer MinE07. A: *Prediction of aptamer folding and structural elements in dot and bracket notation (VRWS). Stems (green) Interior (orange) and Hairpin (blue) loops indicated by colour coding. MFE of the displayed thermodynamically most stable confirmation (optimal).* ***B:*** *Two-dimensional visualization of the MinE07 conformation using the FORNA web tool.* ***C:*** *Three-dimensional folding of MinE07 using AlphaFold3 web server.*

RNA secondary structure visualized using the FORNA web tool showed the same structure as seen in the dot bracket notation (**Figure 33 B**). The predicted stem loop, interior loop and hairpin structure predicted by the ViennaRNA WebServe (VRWS) were included in the three dimensional prediction of AlphaFold3 by colour-coding. In the next step the structure of the conjugate used by *Thomas, Brian J. et al.* was investigated using the mentioned prediction platforms. Upon co-folding using the VRWS the predicted dot bracket notation showed annealing of the tail (blue)

and antitail (blue). Moreover, the two-dimensional base pairing showed a similar assembly of the aptamer part (orange) as the unmodified aptamer. (**Figure 34 A**) Predictions using the AlphaFold3 showed hybridization of the tail and antitail sequences as predicted using the VRWS tool (**Figure 34 B**). Analysis of the cofolding using the DINAMelt web server (DMWS) predicted a melting temperature (T_m) of 88,9 °C for the conjugate. In addition, the cofolded conjugate (AB) showed a low MFE of -52,20 kcal/mol, indicating high thermodynamic stability. The ensemble free energy (EFE) calculated with VRWS of the species AB is as low as -53,960 kcal/mol and indicates high number of thermodynamically stable species in the ensemble of AB. The Concentration plot calculated with DMWS underlines this by predicting high concentration of AB upon denaturation. (**Figure 34 C,D**)

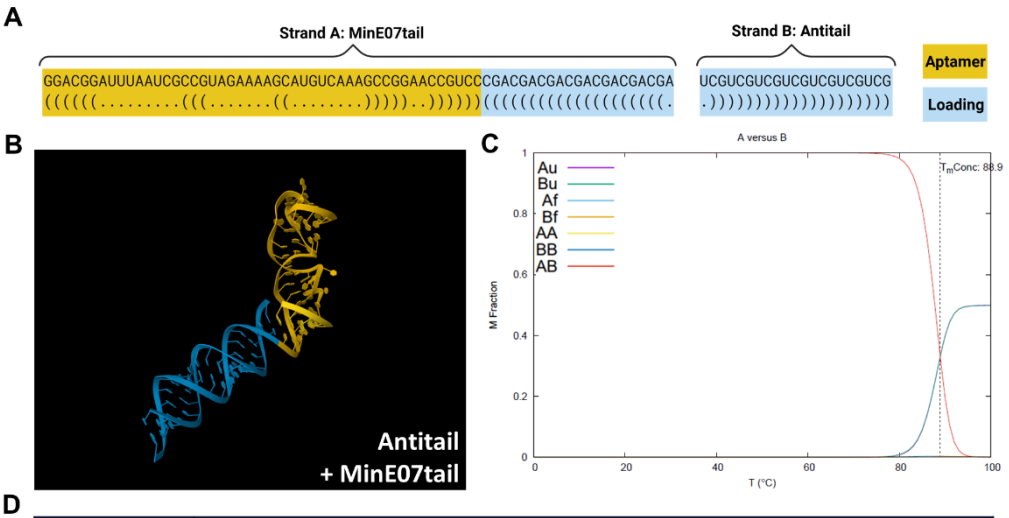

D

MFE of optimal [kcal/mol]	Ensamble free energy [kcal/mol]				
	AB	AA	BB	A Mono	B Mono
-52,20	-53,960	-34,624	-15,168	-13,931	-4,669

Figure 34 Predicted structure of the MinE07 conjugate designed by Thomas, Brian J. et al.. A: *Prediction of aptamer (MinE07tail) cofolding with a fluorescent probe (Antitail). Conjugate in dot and bracket notation (VRWS). The subunits aptamer (orange) and loading (blue) are indicated by colour coding.* ***B:*** *Three-dimensional folding of MinE07 conjugate using AlphaFold3 web server.* ***C:*** *Concentration plot showing the mole fractions of each species as a function of temperature. MinE07tail defined as species A and antitail defined as species B. Melting temperature indicated as dotted line. (DMWS)* ***D:*** *MFE of the displayed thermodynamically most stable cofolded confirmation (optimal). Ensemble free energy of the species AB, AA, BB, A Mono and B Mono calculated using VRWS.*

The prediction of the MinE07tail conjugate was followed by the prediction of the drafted 4th generation design. As recommended by *Tang, Q. and Khvorova, A.* the passenger strand of the siRNA subunit was modified on the 3' end.[62] In conclusion, differing from the conjugate used by *Thomas, Brian J. et al.* the MinE07 was modified at the 5' end.[80] Cofolding with VRWS showed that the vehicle and payload annealed, as indicated by the predicted dot bracket notation. The two-dimensional base pairing also demonstrated that the aptamer region assembled similarly to the unmodified aptamer. (**Figure 35 A**) Results from AlphaFold3 prediction indicated hybridization between the vehicle and payload sequences, consistent with predictions made using

VRWS. (**Figure 35 B**) Analysis of cofolding with the DMWS tool indicates that the conjugate has a melting temperature (Tm) of 82,4 °C.(**Figure 35 C**) In addition, the cofolded conjugate (AB) showed a low MFE of -52,20 kcal/mol, indicating a high thermodynamic stability. The ensemble free energy (EFE) calculated with VRWS of the species AB is as low as -53,960 kcal/mol and indicates a high number of thermodynamically stable species in the ensemble of AB. (**Figure 35 D**) The Concentration plot calculated with DMWS underlines this by predicting high concentration of AB upon denaturation.

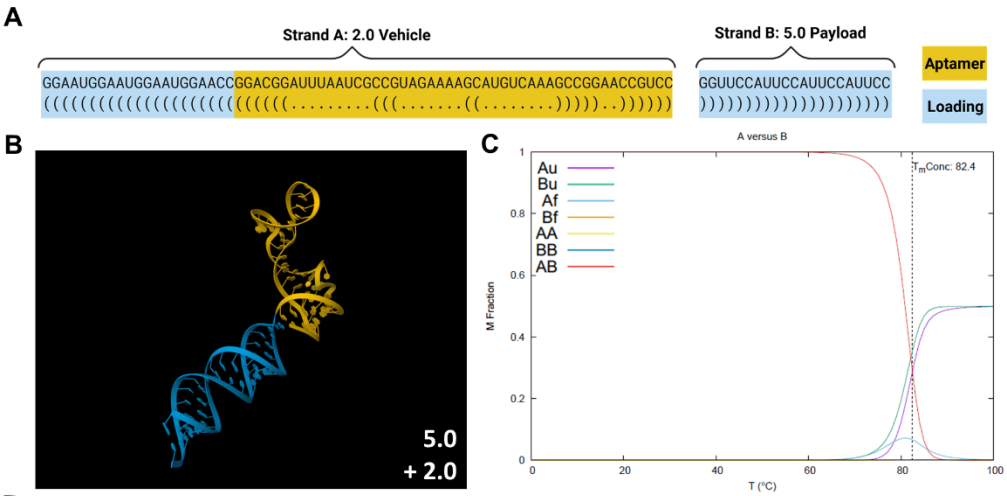

D

MFE of optimal [kcal/mol]	Ensamble free energy [kcal/mol]				
	AB	AA	BB	A Mono	B Mono
-48,70	-49,739	-34, 674	-6,006	-13,866	-0,941

Figure 35 Predicted structure of the 4th generation conjugate. A: *Prediction of aptamer cofolding with siRNA payload. Conjugate in dot and bracket notation (VRWS). The subunits aptamer (orange) and loading (blue) are indicated by colour coding.* ***B:*** *Three-dimensional folding of 4th generation conjugate using AlphaFold3 web server.* ***C:*** *Concentration plot showing the mole fractions of each species as a function of temperature. Vehicle defined as species A and payload defined as species B. Melting temperature indicated as dotted line. (DMWS)* ***D:*** *MFE of the displayed thermodynamically most stable cofolded confirmation (optimal). Ensemble free energy of the species AB, AA, BB, A Mono and B Mono calculated using VRWS.*

As the dot bracket annotation of both conjugates was similar to the prediction of the unmodified aptamer but strongly differing to the structure predicted using AlphaFold 3 further analysis was necessary. Moreover, the colour coding of the dot bracket annotation was not fitting with the structural elements observed in the AlphaFold3 modelling of the unmodified aptamer (**Figure 33 C**). Therefore, the colour coding of the dot bracket annotation was transferred to the AlphaFold3 modelling of both conjugates to compare the fit of the structural elements. Colour coding of structural elements was performed based on dot and bracket notation of MinE07 (**Figure 36 A**). Given the difference in aptamer conjugation (MinE07tail: 5'Aptamer and 3'Probe; 4th

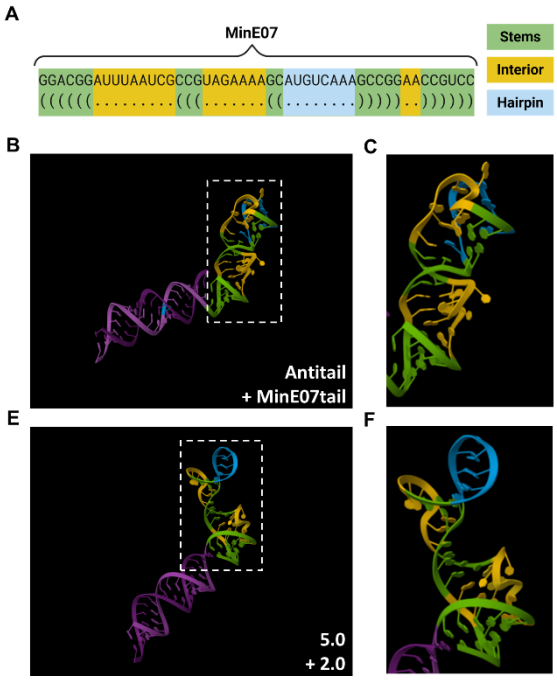

Figure 36 Comparing structural elements predicted in dot and bracket notation with three-dimensional prediction of aptamer folding. A: *Prediction of aptamer folding and structural elements in dot and bracket notation (VRWS). Stems (green) Interior (orange) and Hairpin (blue) loops indicated by colour coding.* ***B,C:*** *Three-dimensional folding of MinE07tail conjugate including colour coding of structural elements.* ***D,E:*** *Three-dimensional folding of 4th generation conjugate including colour coding of structural elements.*

Generation: 5'siRNA and 3' Aptamer) a slightly different angel of the aptamer relative to the loaded double strand was observed comparing both conjugates (**Figure 36 B-E**). Comparing the folding of the aptamer in detail showed base paring in both conjugates as predicted in dot and bracket notation. Moreover, the structural differences predicted in three-dimensional folding seem to occur only in the more flexible interior loops. In conclusion the predicted structure of the 4th generation can be evaluated positive as it is closely comparable with the functional structure used in the work of *Thomas, Brian J. et al.*.[80] Nevertheless, especially the three-dimensional prediction should not be overestimated as none of the prediction models included RNA modifications.

7.6 Establishing an In Vitro Transcription Pipeline

Overall targeted therapy approaches are a rapidly evolving field underlined by the rising clinical relevance of antibody drug conjugates (ADCs). Despite their big potential ADCs suffer from a complex and cost-intensive synthesis. Moreover, low tissue penetrance in solid tumors is a limiting factor mainly due to their large size. Problems which can be overcome developing Nucleic acid based targeted therapy approaches which decreased the molecular size by the power of ten compared to classic ADCs.[111] Moreover, enzymatic based synthesis of nucleic acid-based therapies can reduce the cost of the prototypes as well as fasten the research process as it only needs simple laboratory equipment. Therefore, an in vitro transcription (IVT) based pipeline for the fast prototyping of new aptamer conjugates was established.

As previously mentioned in turn of aptamer re-evaluation the mutant T7 RNA polymerase Y639F is often used to integrate 2'F modified pyrimidine nucleotides into RNA during SELEX. As the MinE07 was also evolved using T7 RNA polymerase Y639F its much likely its functionality is dependent on the 2' F modified pyrimidine bases.[104] Concluding that an IVT synthesized vehicle strand should guarantee targeting function and be much more ribonuclease resistant compared to an unmodified RNA. To establish the IVT different template synthesis methods were evaluated and compared. Of all tested conditions dsDNA template synthesized by SPS showed the highest yield and fidelity.

As the 4th generation conjugate was designed, additional to the vehicle the synthesis of the payload was planed using IVT. Tests showed no sufficient transcription and clean-up of the payload due to small size of the strand. Therefore, synthesis of payload was performed using SPS. This enabled the integration of an advanced RNA modification pattern in the payload strand. Consisting of a 5' phosphate, phosphorothioate backbones as well as 2'-OMe. Every second nucleotide, starting with a modified nucleotide, was 2'-OMe modified (**Figure 38**). In conclusion, follow up compound candidates were synthesized using a hybrid design combining IVT and SPS for rapid assessment of prototypes (**Figure 37**).

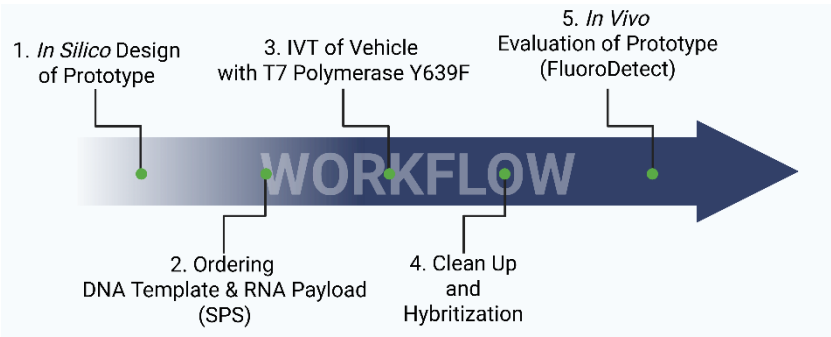

Figure 37 Schematic workflow of hybrid design and rapid assessment (HYDRA) for fast prototyping and evaluation of aptamer siRNA conjugates.

7.7 siRNA Conjugates 4th Generation (IVT Conjugates)

Finishing the *in silico* design of the aptamer conjugate and establishing the hybrid design and rapid assessment (HYDRA) workflow the 4th generation aptamer conjugates were synthesized. As previously described, the vehicle strand contained 2'-F modified pyrimidine bases. Based on the results of *Thomas, Brian J. et al*. no linker sequence was integrated into the design.[80] In consideration of the work from *Tang, Q. and Khvorova, A.* the siRNA passenger strands 3' end was fused to the 5' end of the aptamer.[62] Initial planning of the 4th generation included payload synthesis using IVT. Therefore, two guanines were added to the sequence as this boosts the transcription start and reduces the transcription abortion rate.[112] A schematic figure, showing the used RNA modifications as well as the siRNA & aptamer sequence of 4th generation compound can be found in **Figure 38**.

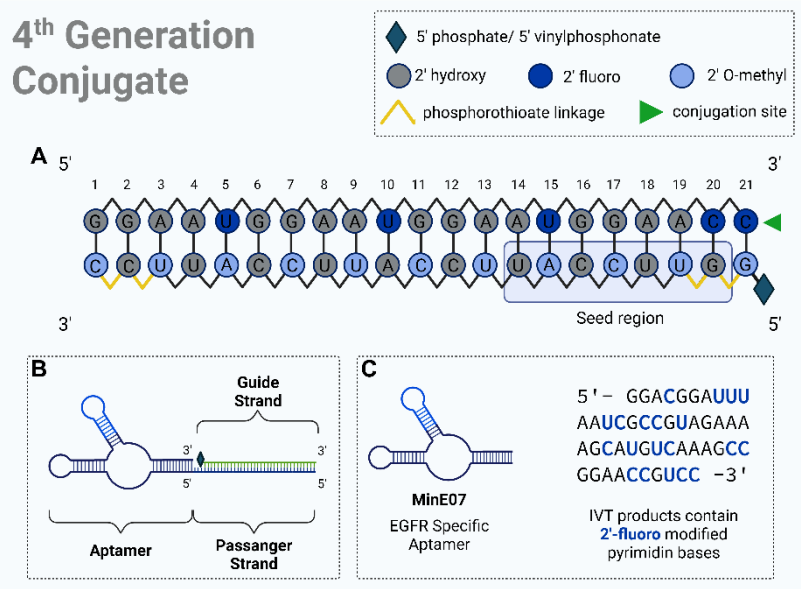

***Figure 38 Schematic figure of the 4th generation RNA conjugates**. 5' passenger conjugated HSat3 targeting siRNA containing an advanced modification pattern. Schematic structure of the assembled aptamer siRNA conjugate. Sequence of MinE07 aptamer indicating the 2'-F modified pyrimidine bases (blue).*

As lipoplexes of used aptamer conjugates were necessary in follow up experiments to proof functionality of the siRNA subunit the transfection conditions of aptamer conjugates were optimized. Therefore, lipoplexes were formulated using different ratios of 4th generation ARC and Lipofectamin RNAiMAX. HeLa reporter cell lines stably expressing the FluoroDetect HSat3 C-rich and G-rich were exposed to the lipoplexes and fluorescence of FluoroDetect assay was measured 72 h later. The eGFP reference signal of samples was observed to evaluate viability of the cells as it corelates with the number of cells per sample. In cells expressing the assay with the C-rich target side a reduction of eGFP fluorescence could be observed compared to the untreated samples. Intensity of eGFP fluorescence was constant through all ARC transfected samples but significantly lower compared to control samples. No significant change of eGFP could be observed comparing the siRNA controls with the untreated sample. Cells expressing the FluoroDetec assay with the G-rich target side showed no intense difference in eGFP fluorescence throughout all samples. (**Figure 39**)

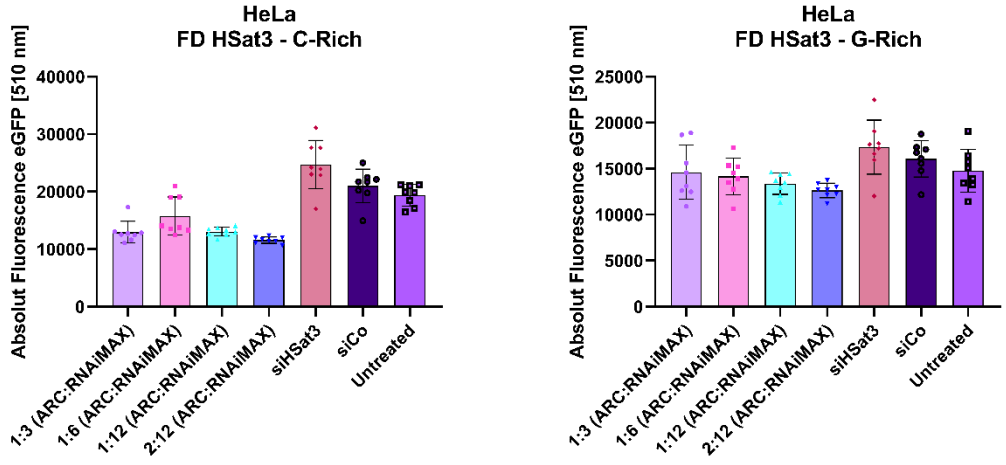

Figure 39 Evaluation of absolute eGFP fluorescence upon ARC transfection. *To optimize transfection of ARC different transfection ratios of Lipofectamin RNAiMAX and ARC have been tested using the FluoroDetect HSat3 assay system. To evaluate the toxicity of the transfection the absolute eGFP fluorescence was compared to the control samples. Single value displayed are independent technical replicates normalized to an untreated sample (All graphs showing the median ± 95% confidence interval [CI]).*

To evaluate the knock down intensity and connect the transfection efficacy the RFU of all samples was analysed. The C-rich as well as the G-rich assay showed equal results underlining the robustness of the FluorDetect assay system. All samples transfected with ARC showed significant knock down intensity compared to the untreated control, exposed to the lipoplexes. No significant difference in transfection efficiency could be observed throughout the tested ratios of ARC to lipofectamine. All control samples behaved as expected proving functionality of the experimental setup. In future experiments a ratio of 1:3 was chosen to transfect ARCs. (**Figure 40**)

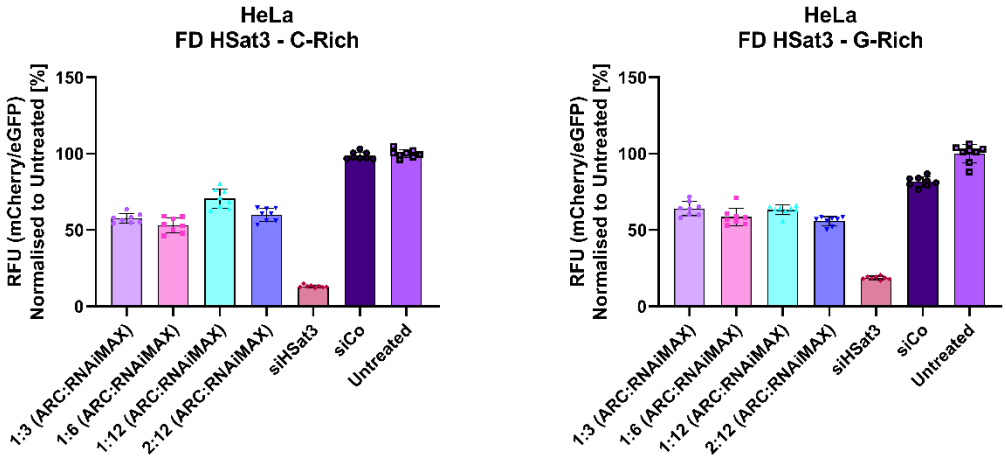

Figure 40 Optimization of ARC transfection conditions. *To optimize transfection of ARC different transfection ratios of Lipofectamin RNAiMAX and ARC have been tested using the FluoroDetect HSat3 assay system. The transfection efficiency the RFUs measured are compared to the control samples. Single value displayed are independent technical replicates normalized to an untreated sample (All graphs showing the median ± 95% confidence interval [CI]).*

Upon optimization of the transfection conditions functionality of 4th generation conjugate was examined using HeLa reporter cell lines stably expressing the FluoroDetect C-rich and G-rich

assay system. Fluorescence of cells was measured at the time points 0 h, 24 h, 48 h, 72 h, 168 h, 192 h after start of the indicated treatment. Results are shown as time curve of the RFU. Samples transfected with the ARC showed low knock down efficacy compared to siHSat3 transfected cell population. In the assay expressing the G-rich target sequence a slight reduction of RFU was measured up on exposure to siCo lipoplexes. It could be observed that cells were recovering RFU to a level of untreated sample by time. Especially in the G-rich assay no significant difference between siCo and ARC could be observed. (**Figure 41**)

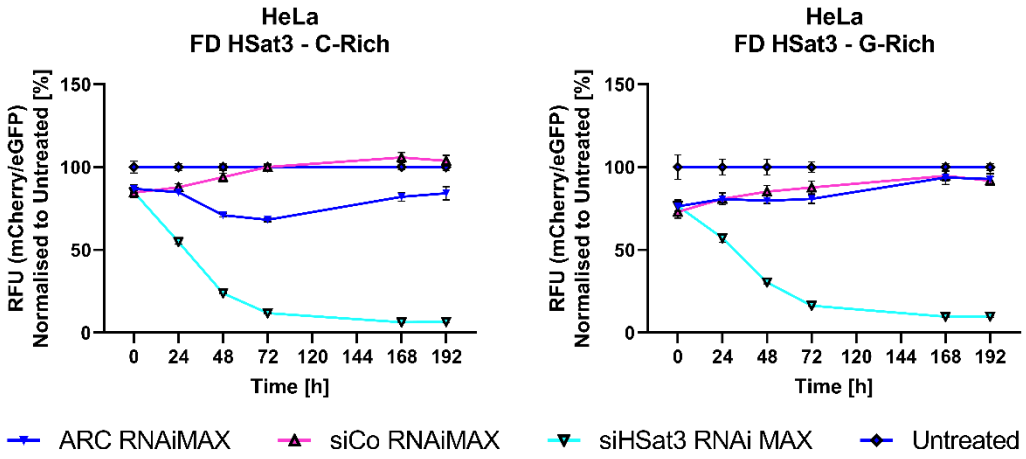

Figure 41 Determination of 4th generation knock down efficiency. Figure showing a dynamic evaluation of the knock down efficiency of the 4th generation ARC. *Using a C-rich and a G-rich target the activity of the payload and vehicle strand was assessed. Value displayed are represent the median of eight technical replicates normalized to an untreated sample (All graphs showing the median ± 95% confidence interval [CI]).*

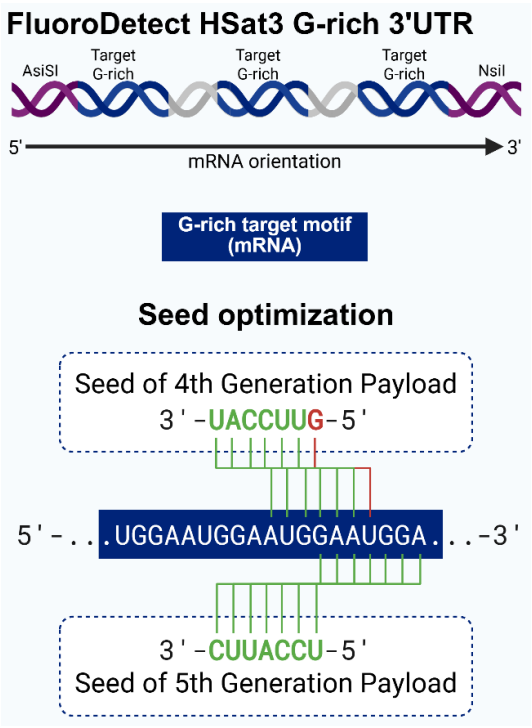

Figure 42 Seed optimization of 4th generation conjugate. *Schematic figure showing the miss match of the 4th generation seed as well as the optimized seed region for 5th generation compounds.*

As the samples transfected with the ARC showed low knock down efficacy, especially samples of the G-rich assay, the sequence of the payload was re-evaluated. Aligning the seed region of the 4th generation payload with the target side of the FluoroDetect G-rich identified a miss match in position 2 of the payload. As this could cause strong limitations in on-target efficacy the sequence of the payload strand needed to be optimized. Therefore, the seed sequence was fitted for the best match with the G-rich target sequence as well as with the sequence of the siHSat3. In conclusion optimization of the seed sequence will guarantee higher detection sensitivity using the FluoroDetect assay system and in addition high targeting efficacy for HSat3 RNA.

Schematic alignment of 4th and 5th generation seed alignment with the assays target side is shown in **Figure 42**.

7.8 Endosomal Escape Enhancer and Endosomolytic Agents

As described by *Steven F. Dowdy*, another factor limiting the effective cytoplasmatic delivery of targeted siRNA therapies is caused by endosomal entrapment. Recent studies suggest that only 0,3% of targeted siRNA compounds can overcome the endosomal escape problem. As such low delivery rates could mask the detection of ARC prototypes the use of endosomal escape enhancing and endosomolytic agents was considered. Despite their clinical intolerable toxicity, these agents could at least prove endosomal uptake of targeted cells under laboratory conditions. For this purpose, the effect of polybrene and nigericin on enhancing the delivery of 4th generation conjugates should be tested.

Polybrene, also known as hexadimethrine bromide, is a synthetic cationic polymer commonly used to enhance viral transduction efficiency in mammalian cells. Its primary mechanism involves neutralizing the electrostatic repulsion between negatively charged viral particles and the negatively charged cell surface, particularly sialic acid residues. This charge neutralization facilitates closer contact between the virus and the cell membrane, thereby promoting viral adsorption and entry (**Figure 43**). In retroviral and lentiviral systems, polybrene can significantly increase transduction efficiency by several orders of magnitude depending on the cell type and experimental conditions.[113] As discussed by *Steven F. Dowdy* the exact mechanism of endosomal escape remains unknown. Nevertheless, it seems to be beneficial reducing membrane repulsion of anionic nucleic acids inside the endosome to enhance endosomal escape. Somehow unconventionally in combination with nucleic acids this experiment should unravel if polybrene could enhance the efficacy of endosomal escape by reduction of membrane repulsion. For this purpose, HeLa cells stably expressing a FluoroDetect HSat3 assay were treated with 4th generation ARC in combination with a 10 mg/mL concentration of polybrene as common in lentiviral transduction experiments. After 144 h of incubation eGFP and mCherry fluorescence of the cells was measured using a plate reading system. To evaluate

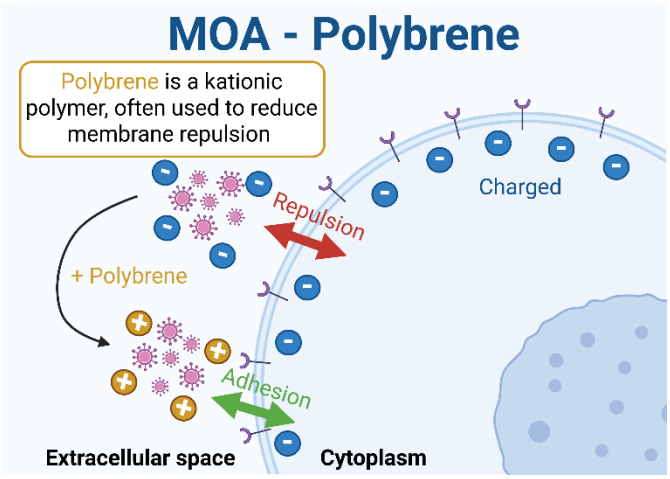

Figure 43 Schematic figure showing the mechanism of action (MOA) of polybrene. *As commonly used in viral transduction adding polybrene neutralizes the negative charge of salic acid residues on cellular surface to reduce membrane repulsion (red arrow). This increases adhesion (green arrow) of virus particles(pink).*

unspecific artefacts caused by polybrene associated cytotoxic stress a sample only treated with polybrene was included. Moreover, to estimate the maximum effect size an additional control was exposed to ARC lipoplexes. In both cell lines (C-rich and G-rich target side) a reduction of 10 percent in RFU was observed when treated with polybrene, independent of the presence of the ARC. When exposed to the ARC lipoplexes cells showed a significant stronger decrease of RFU compared to siCo treated control, indicating active RNAi upon 4th ARC transfection. The siRNA control samples as well as the untreated sample showed no irregularities. (**Figure 44**)

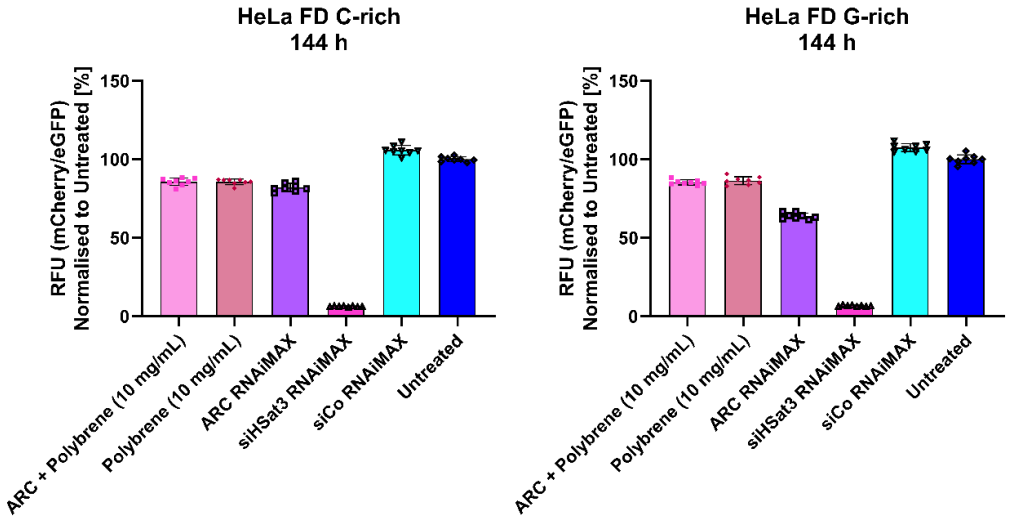

Figure 44 First evaluation of polybrene as bioenhancer to improve endosomal escape. *RFUs of the FluoroDetect HSat3 C-rich and FluoroDetect HSat3 G-rich measured upon 144 h of the indicated treatment. Single value displayed are independent technical replicates normalized to an untreated sample (All graphs showing the median ± 95% confidence interval [CI]).*

In a follow up experiment the unspecific reduction of RFUs upon exposure to polybrene should be investigated to determine a tolerable concentration for future experiments. Therefore, HeLa cells stably expressing a FluoroDetect HSat3 assay were treated with different concentrations of polybrene, ranging from 10 mg/mL to 0,625 mg/mL. Fluorescence was measured 72 h after treatment using a plate reading system. To evaluate measurement artefacts a detailed investigation of the assays raw data seemed to be necessary. For this purpose, the absolute eGFP and mChery values were plotted. As the eGFP signal correlates with the cell number it can give information about cytotoxicity. As the mCherry reporter signal can also be affected by cell toxicity it should mirror eGFP signal if not specifically affected. In both cell lines a fluctuation of eGFP was observed with maximum in RFU reduction around 1,25 mg/mL polybrene. In comparison the mCherry reporter signal showed a slightly stronger reduction but mirrored the eGFP signal indicating a faster reduction of mCherry compared to eGFP or an overestimation of the eGFP signal. (**Figure S 21**) This faster reduction of mCherry lead to dose dependent reduction of RFU in the FluoroDetect HSat3 C-rich as well as G-rich assay system. As both systems were affected

a systematic error caused by cell toxicity can be considered. (**Figure 45**) For future experiments a polybrene concentration below 625 ng/mL sems to be tolerable.

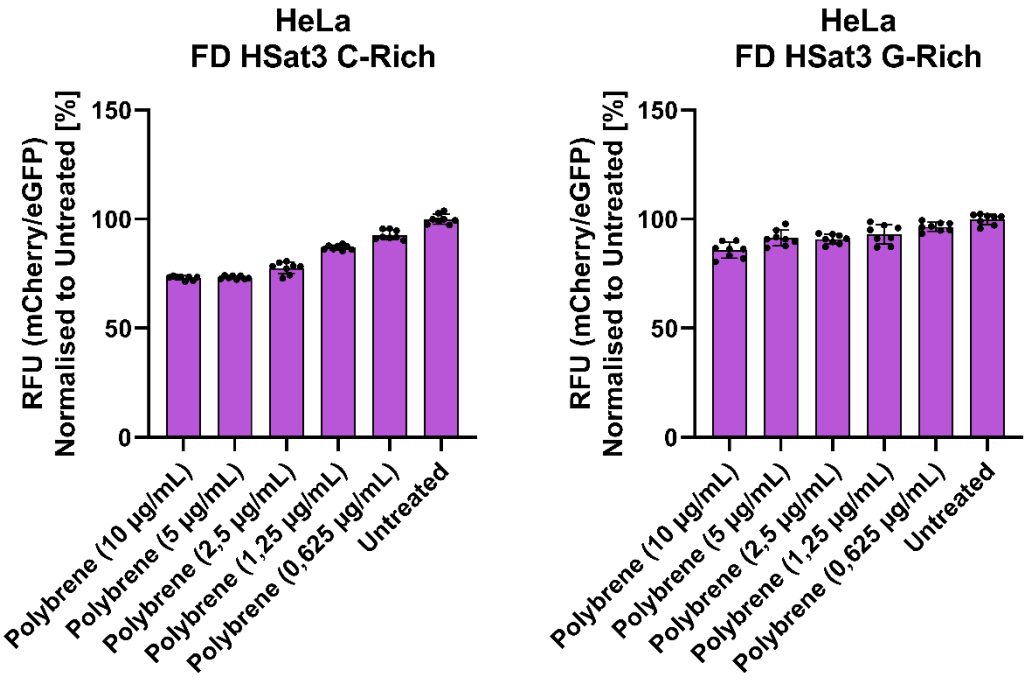

Figure 45 Dilution series of polybrene to evaluate the dose dependent artefact intensity. *HeLa cells stably expressing the FluoroDetect HSat3 assay were treated with indicated concentration of polybrene. RFUs of all samples were compared to an untreated control population. Single value displayed are independent technical replicates normalized to an untreated sample (All graphs showing the median ± 95% confidence interval [CI]).*

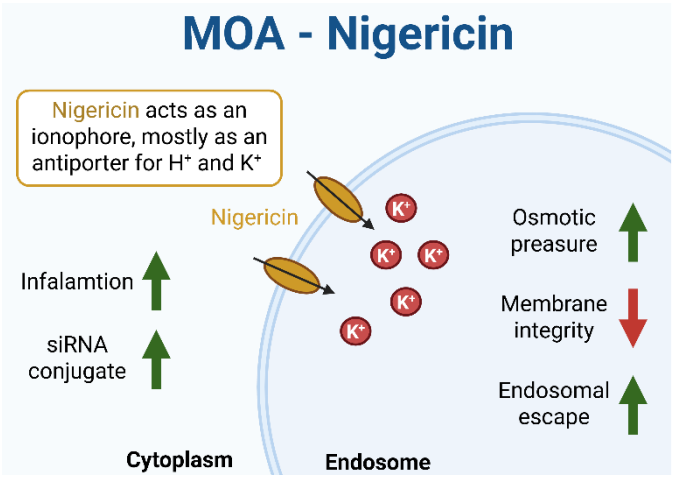

Figure 46 Mechanism of action (MOA) of Nigericin as an ionophore. *In intracellular environment nigericin binds K+ and releases it in the low pH environment of early endosomes as well as in lysosomes. This reduces membrane integrity and enhances endosomal escape of cargo as well as inflammation upon innate immune response.*

Nigericin, a K^+/H^+ ionophore, has emerged as a potent agent for promoting endosomal escape by disrupting ionic gradients across endosomal membranes. Its mechanism involves the exchange of intracellular potassium for protons, leading to cytoplasmic acidification and osmotic swelling of endosomes, which can culminate in membrane destabilization and rupture.[114] Ion exchange activity is particularly effective in early endosomes, where the proton gradient is steep, allowing nigericin to induce rapid changes of ion concentration inside endosomes. These changes compromise membrane integrity by increasing osmotic pressure, facilitating the release of entrapped cargo into the cytosol. As not only cargo but also endosomal proteins are released into cytoplasm the innate immune

response is activated upon exposure to nigericin. (**Figure 46**) In delivery systems such as folate-conjugated siRNA (FolamiRs), nigericin has been shown to significantly enhance cytoplasmic release and gene silencing efficiency without requiring chemical modification of the cargo.[115] For this purpose, HeLa cells stably expressing a FluoroDetect HSat3 assay were treated with 4th generation ARC in combination with nigericin as bioenhancer as showed by *Orellana, Esteban A. et al.*.[116] After 144 hours of incubation, eGFP and mCherry fluorescence of the cells was measured using a plate reader system. To account for potential nonspecific artefacts resulting from nigericin -induced cytotoxic stress, a sample treated solely with nigericin was included. Additionally, to determine the maximum effect size, a separate control was exposed to ARC lipoplexes. In both cell lines (C-rich and G-rich target sites), treatment with nigericin resulted in a 50% reduction in RFU, regardless of ARC presence. Exposure to ARC lipoplexes induced a significantly greater decrease in RFU compared to the siCo-treated control, suggesting active RNA interference following fourth-generation ARC transfection. The siRNA control samples, and untreated samples exhibited no irregularities. (**Figure 47**)

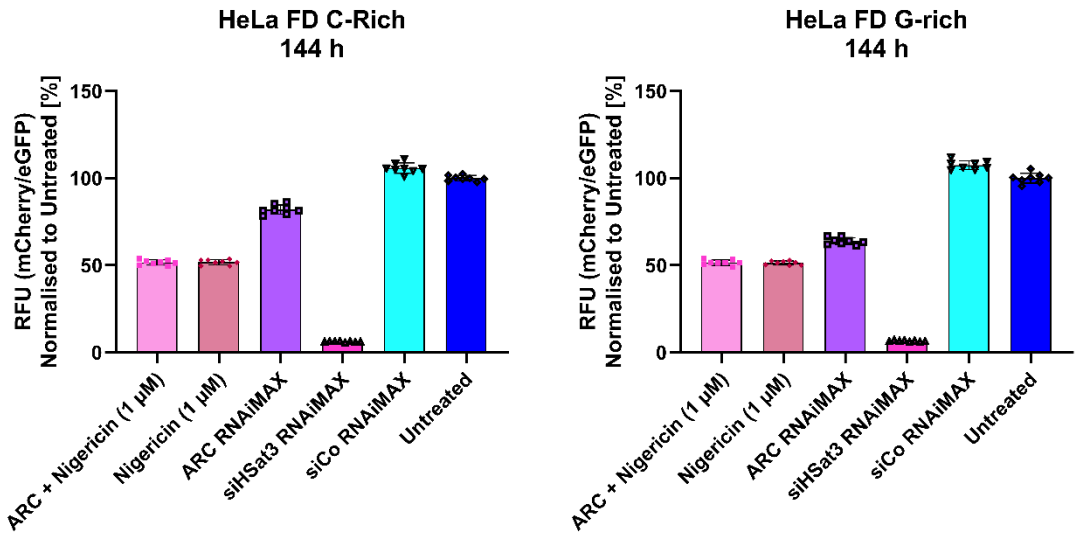

Figure 47 First evaluation of nigericin as bioenhancer to improve endosomal escape. *RFUs of the FluoroDetect HSat3 C-rich and FluoroDetect HSat3 G-rich measured upon 144 h of the indicated treatment. Single value displayed are inde-pendent technical replicates normalized to an untreated sample (All graphs showing the median ± 95% confidence interval [CI]).*

In a follow up experiment the unspecific reduction of RFUs upon exposure to nigericin should be investigated to determine a tolerable concentration for future experiments. Therefore, HeLa cells stably expressing a FluoroDetect HSat3 assay were treated with different concentrations of nigericin, ranging from 1 µM to 62,5 nM. Fluorescence was measured 72 h after treatment using a plate reading system. To evaluate measurement artefacts a detailed investigation of the assays raw data seemed to be necessary. For this purpose, the absolute eGFP and mCherry values were plotted (**Figure S 22**). As the eGFP signal correlates with the cell number it can give information

about cytotoxicity. The mCherry reporter signal can also be affected by cell toxicity but should mirror eGFP signal if not specifically affected. In both cell lines a dose dependent reduction of eGFP and mCherry was observed with maximum in RFU reduction at 1 µM nigericin cocnetration. In comparison to the eGFP signal the mCherry reporter signal showed a slightly stronger reduction but followed the eGFP signal. This indicated a faster reduction of mCherry compared to eGFP or an overestimation of the eGFP signal. (**Figure S 22**) This faster reduction of mCherry lead to dose dependent reduction of RFU in the FluoroDetect HSat3 C-rich as well as G-rich assay system. As both systems were affected a systematic error caused by cell toxicity can be considered. (**Figure 48**) For future experiments a nigericin concentration below 62,5 nM sems to be tolerable.

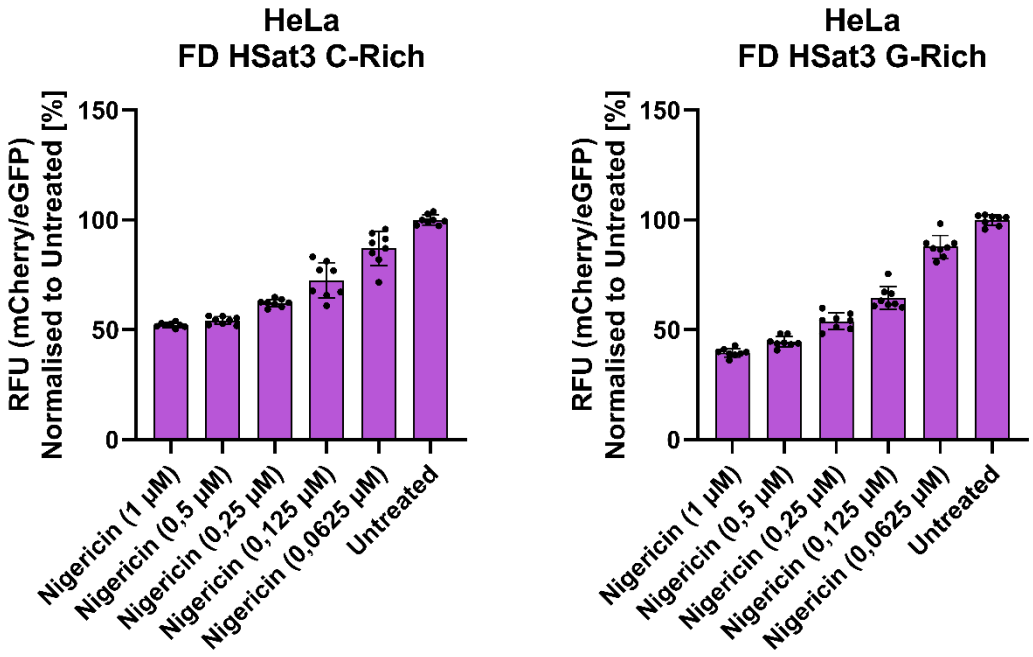

Figure 48 Dilution series of nigericin to evaluate the dose dependent artefact intensity. *HeLa cells stably expressing the FluoroDetect HSat3 assay were treated with indicated concentration of nigericin. RFUs of all samples were compared to an untreated control population. Single value displayed are independent technical replicates normalized to an untreated sample (All graphs showing the median ± 95% confidence interval [CI]).*

7.9 siRNA Conjugate 5th Generation (Optimized IVT Conjugates)

Considering the low RNAi activity of the 4th generation payload strand and the seed optimization, the 5th generation payload strand was modified. As discussed previously this should guarantee a higher targeting affinity and result in higher sensitivity of the FluoroDetect assay. To optimize the hybridization of the 5th generation payload a new vehicle was designed missing the two bases which have been complementary to the two 5' guanines of the 4th generation payload. This caused shortening of the guide strand from 21 nucleotides to a total length of 19 nucleotides. (**Figure 49**) As the new designed 5th generation payload was shortened it should also bind to the 4th generation vehicle strand including a linker sequence of two cytosines. Therefore, two assemblies of the 5th generation were possible. Combining the old vehicle (2.0) with the new payload (5.1) and combining the new vehicle (2.1) with the new payload (5.1). As previously described, the vehicle strand contained 2'-F modified pyrimidine bases. Based on the results of *Thomas, Brian J. et al*. no linker sequence was integrated into the design.[80] In consideration of the work from *Tang, Q. and Khvorova, A.* the siRNA passenger strands 3' end was fused to the 5' end of the aptamer.[62] To estimate if both variants can assemble an *in silico* hybridization and folding prediction was performed using the VRWS DMWS and AlphaFold3. (**Figure 50**, **Figure 51**)

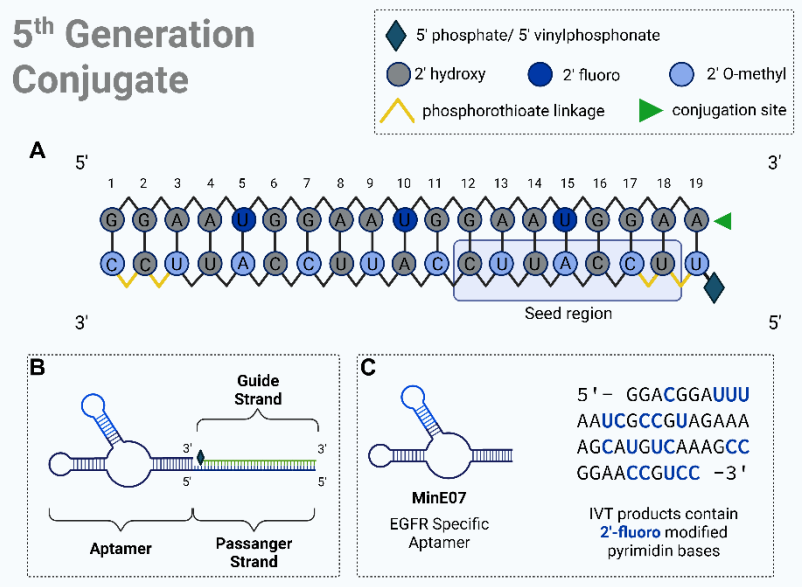

Figure 49 Schematic figure of the 4th generation RNA conjugates. *3' passenger conjugated HSat3 targeting siRNA containing an advanced modification pattern. Including the optimized seed region. Schematic structure of the assembled aptamer siRNA conjugate. Sequence of MinE07 ap-tamer indicating the 2'-F modified pyrimidine bases (blue).*

The assembly using the 2.0 vehicle and the 5.1 payload is called here and in the following ARC 2.0. Accordingly, the assembly of 2.1 vehicle and 5.1 payload is called here and in the following ARC 2.1. Starting with the ARC 2.0 cofolding was performed using the VRWS. Dot bracket notation shows annealing of passenger and guid strand. Moreover, it indicates the two-dimensional base pairing of the aptamer region assembling similarly to the unmodified aptamer. (**Figure 50 A**) Results from AlphaFold3 prediction indicated hybridization between the vehicle and the payload sequences, consistent with predictions made using VRWS. (**Figure 50 B**) Analysis of

cofolding with the DMWS indicated that the conjugate has a melting temperature (Tm) of 79,8°C. (**Figure 50 C**) Additionally, the cofolded conjugate (AB) exhibited a low minimum free energy (MFE) of -41,50 kcal/mol, which suggests thermodynamic stability. The ensemble free energy (EFE) for species AB, calculated using VRWS, was also notably low at -42,828 kcal/mol, indicating the presence of numerous thermodynamically stable conformers within the AB ensemble. (**Figure 50 D**) This observation is further supported by the concentration plot derived from DMWS, which forecasts a high concentration of AB following denaturation.

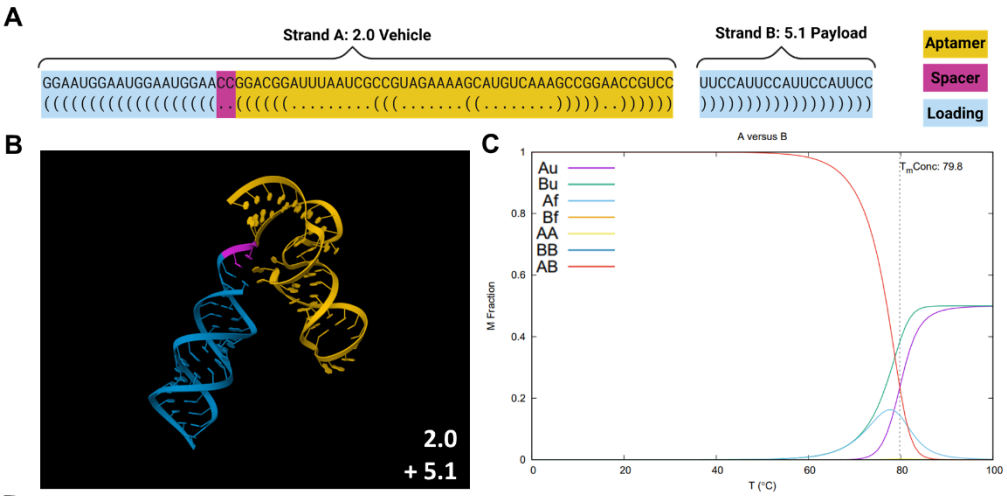

D

MFE of optimal [kcal/mol]	Ensamble free energy [kcal/mol]				
	AB	AA	BB	A Mono	B Mono
-41,50	-42,828	-34,674	1,686	-13,868	-0,002

Figure 50 Predicted structure of 5th generation conjugate 2.0. A: *Prediction of aptamer cofolding with siRNA payload. Conjugate in dot and bracket notation (VRWS). The subunits aptamer (orange) and loading (blue) are indicated by colour coding.* ***B:*** *Three-dimensional folding of 5th generation conjugate using AlphaFold3 web server.* ***C:*** *Concentration plot showing the mole fractions of each species as a function of temperature. Vehicle defined as species A and payload defined as species B. Melting temperature indicated as dotted line. (DMWS)* ***D:*** *MFE of the displayed thermodynamically most stable cofolded confirmation (optimal). Ensemble free energy of the species AB, AA, BB, A Mono and B Mono calculated using VRWS.*

Following the prediction of ARC 2.0 the prediction of ARC 2.1 was performed accordingly. Annealing of the passenger and guide strand (blue) is indicated by predicted structure in dot bracket notation. Furthermore, the two-dimensional base pairing of the aptamer region (orange) assembles in a manner analogous to that of the unmodified aptamer. (**Figure 51 A**) The results from the AlphaFold3 prediction indicated an occurrence of hybridization between the vehicle and the payload sequences. This finding is consistent with predictions made using VRWS. (**Figure 51 B**) A thorough analysis of cofolding with the DMWS revealed that the conjugate has a melting temperature (Tm) of 79.8°C. (**Figure 51 C**) Furthermore, the cofolded conjugate (AB) demonstrated a low minimum free energy (MFE) of -41,70 kcal/mol, indicating thermodynamic stability. The ensemble free energy (EFE) for species AB, calculated using VRWS, was also notably low at -42,926 kcal/mol. (**Figure 51 D**) This finding indicates the presence of numerous

thermodynamically stable conformers within the AB ensemble. This observation is further substantiated by the concentration plot derived from MWS, which forecasts a high concentration of AB following denaturation.

As cofolding of vehicle and payload only predicts hybridization of the siRNA subunit and folding of aptamer, this gives no information about functionality of the siRNA. Functionality that relies on the interaction with the Ago2 protein. As this remains uncertain and is a potential limitation of efficacy an *in silico* protein interaction model was created using AlphaFold3. In the first step unmodified siHSat3 was used to prove the ability of the model to determine siRNA as a functional substrate of the Ago2 protein. To improve clarity of the model a schematic overview shows the structure of siHSat3 as well as a schematic structure of the 5th generation aptamer conjugates. Additionally, the guide/payload (pink) and passenger/vehicle (orange) strand have been colour coded. (**Figure 52**)

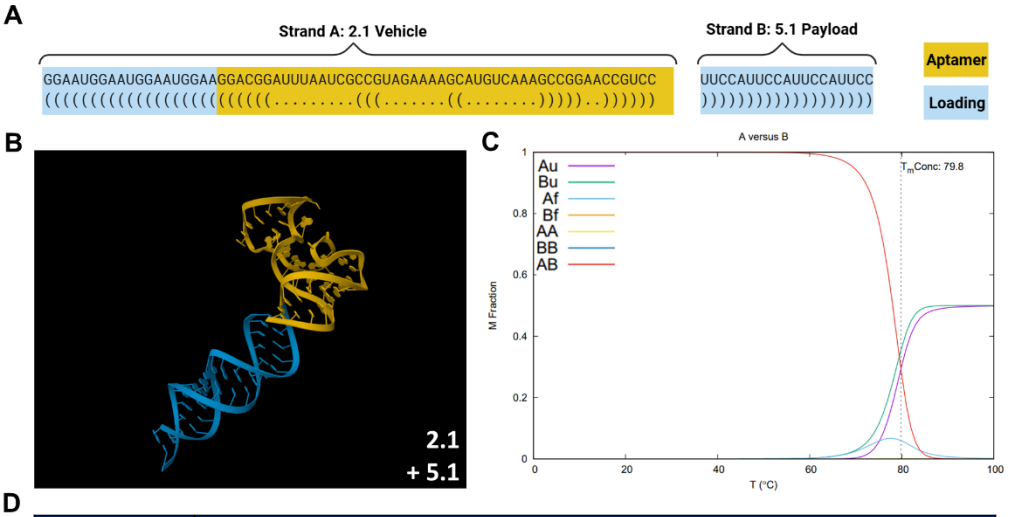

MFE of optimal [kcal/mol]	Ensamble free energy [kcal/mol]				
	AB	AA	BB	A Mono	B Mono
-41,70	-42,926	-28,556	1,686	-12,310	-0,002

Figure 51 Predicted structure of 4th generation conjugate. A: *Prediction of aptamer cofolding with siRNA payload. Conjugate in dot and bracket notation (VRWS). The subunits aptamer (orange) and loading (blue) are indicated by colour coding.* ***B:*** *Three-dimensional folding of 4th generation conjugate using AlphaFold3 web server.* ***C:*** *Concentration plot showing the mole fractions of each species as a function of temperature. Vehicle defined as species A and payload defined as species B. Melting temperature indicated as dotted line. (DMWS)* ***D:*** *MFE of the displayed thermodynamically most stable cofolded confirmation (optimal). Ensemble free energy of the species AB, AA, BB, A Mono and B Mono calculated using VRWS.*

Modelling of Ago2 and siHSat3 shows precise fitting of A-form helix into the internal groove of Ago2 protein. Moreover, prediction showed interaction of the guide strands 5’ end with the middle domain (MID, green) of the Ago2 protein. This is in line with the findings of *M. Sano and M. Sierant et al.*, which showed that elongation of the 3’ end increases the probability of being chosen as guide strand.[117] To prove the ability of the model to distinguish between those two

strands, the siRNA sequence used for modelling was missing the 3' overhang of the passenger strand and is not a representative sequence for the siHSat3 used in other experiments. (**Figure 52 A, B**; **Table S 3**) After evaluation of the model the interaction of the Ago2 protein with the 5th generation aptamer conjugates was predicted. As indicated in the schematic overview the colour coding for vehicle (orang) and payload (pink) was the same as chosen for the siHSat3 example. In both cases a precise fitting of the siRNA subunit into the enzymatic groove of the Ago2 protein could be observed. (**Figure 52 C, D**) As this is in line with the prediction of the siHSat3 Ago2 interaction this can be evaluated as a first positive result. Having a closer look reveals that the strands seem to be exchanged compared to the siHSat3 model. This indicates an interaction of the MID with the better accessible 5' end of the vehicle strand. This observation was similar in both conjugates indicating the optimization potential of the 5th generation conjugates by inverting the structure and modifying the 5' end of the passenger strand.

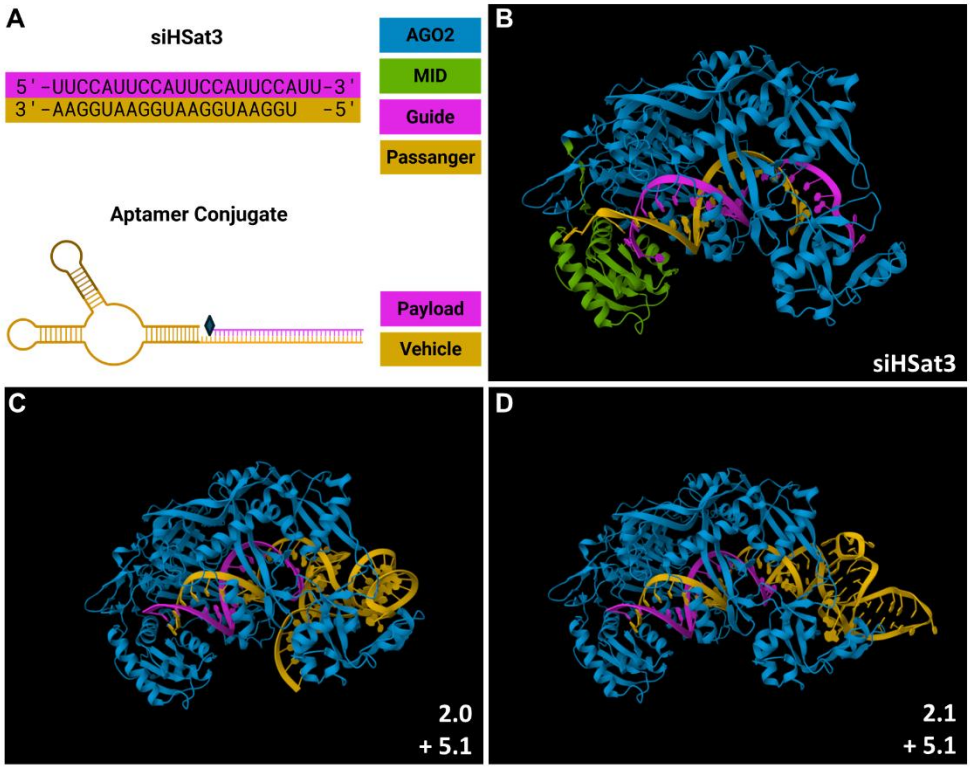

Figure 52 Predicted siRNA Ago2 interaction. A: *Schematic structure of siHSat3 and 5th generation conjugates. Additionally, a colour coded legend shows the colours used in the prediction model.* ***B:*** *Predicted interaction of siHSat3 and Ago2.* ***C:*** *Predicted interaction of ARC 2.0 and Ago2.* ***D:*** *Predicted interaction of ARC 2.1 and Ago2.*

Nevertheless, the probability of the payload strand to be chosen as a guide strand is more likely as the 3' end of the vehicle stand is not accessible for interaction with the PIWI domain of the Ago2 protein. Moreover the 5th generation design is in line with the recommendation of *Tang, Q. and Khvorova, A* and guaranties protection of the 3' end of the passenger strand.[62]

Following the *in silico* evaluation of the 5th generation conjugates, the vehicle and payload strand were synthesized according to the HYDRA workflow. (**Figure 37**) To assemble the functional conjugate both strands were denatured and annealed by heating up to 95°C followed by slow cooling down to 4°C. As described earlier, the 5th generation design enabled two conjugates based on the 2.0 and 2.1 vehicle strand. A schematic structure as well as the sequence are shown in (**Figure 53**). Colour coding identifies the siRNA (green), spacer (pink) and MinE07 aptamer (orange) subunit. Upon hybridization the vehicle strands as well as the annealed conjugates were analysed using a Urea PAGE. 20/100 ssDNA ladder was loaded as length reference. The acrylamide gel was stained using SYBER Gold to visualize the loaded nucleic acids. In both conjugates a change in electromobility was visual upon hybridization. Compared to the ssDNA ladder mobility changed approximately by 10 nucleotides. (**Figure 53 C**) This indicated the annealing of the payload strand to the vehicle strands. In all lanes weak unspecific bands were observed above and below the most intense band.

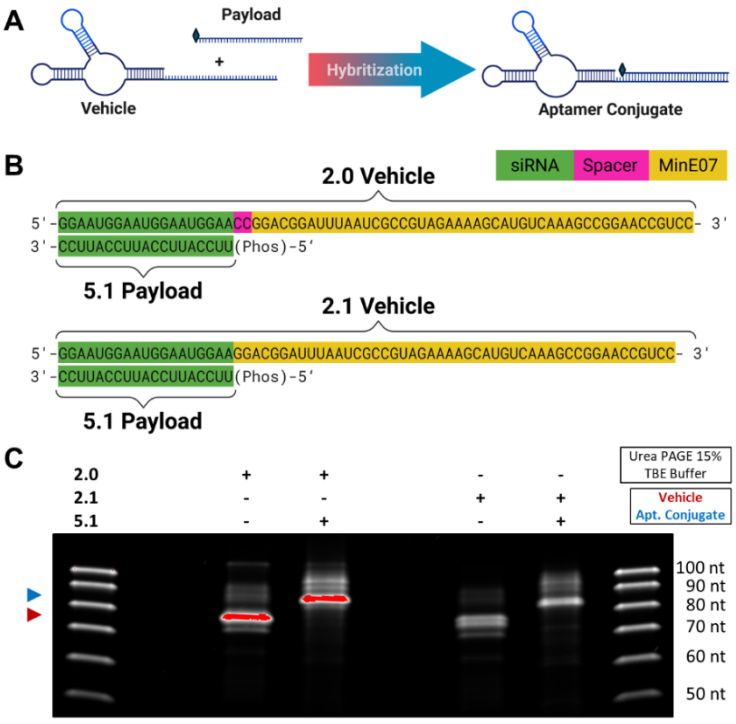

Figure 53 Hybridization of 5th generation vehicle and payload strand. A: *Schematic protocol of ARC assembly. B: Sequences of 2.0 and 2.1 ARC showing the different subunits (colour coded) C: Urea PAGE loaded with 20 pmol of indicated species, showing electromobility shift upon assembly. 20/100 ssDNA ladder for comparison. Gel stained with SYBER Gold to visualize RNA.*

Immediately after hybridization of the conjugates cell culture experiments were performed to assess the functionality of the assembled ARCs. For this purpose, HeLa cells stably expressing the FluorDetect HSat3 C-rich and G-rich assay were used to measure the knock down efficiency of the vehicle (**Figure 54**; **Figure S 23**) and the payload (**Figure 55**; **Figure S 24**) strand. As previously discussed, nigericin can be used to enhance the endosomal escape and increase the assays' sensitivity. Nevertheless, it needs to be used carefully as it can cause cytotoxicity related measurement artefacts. For this purpose, the evaluation of the aptamer conjugates was complete by samples treated with a combination of ARC and nigericin as well as a sample treated only with nigericin to determine the effect size of nigericin induced measurement artefacts. Additionally, a sample was treated with ARC lipoplexes to prove functionality of the ARCs. After treatment started the knock down efficiency was evaluated in 24 h intervals up to a total

duration of 10 days. Upon transfection with the siHSat3 all cell lines exhibited a fast and strong decrease of RFU. In contrast cell lines transfected with the siRNA control pool siCo showed no significant difference compared to the untreated control population. Cells expressing the FluoroDetect HSat3 C-rich assay showed low reduction of RFU starting 24 h after treatment with a maximum knock down intensity after 72 h followed by a recovery of the signal. Comparing the two ARCs 2.0 (**Figure S 23**, **Figure S 24**) and 2.1(**Figure 54**, **Figure 55**), the conjugate without a spacer sequence (2.1) showed stronger knock down intensity. The targeting of the C-rich target indicated a low knock down efficiency of the vehicle strand. In the cell line expressing the FluoroDetect HSat3 G-rich a much stronger reduction of RFU was observed upon treatment with the ARC lipoplexes. Within the first 48 hours after treatment the samples showed no significant difference to the siHSat3 treated positive control. As observed in the cell line expressing the FluoroDetect HSat3 C-rich assy the ARC conjugate mediated knock down reached its maximum after 72 h and started slow RFU recovery after 96 h of transfection. This result underlines the RNAi activity of the payload strand. Cells expressing the FluoroDetect HSat3 C-rich assay showed no response upon treatment with the ARCs. In comparison the cells expressing the G-rich target showed slow but steady decrease of RFU starting upon 48 h to 72 h exposure to the ARC. An enhanced effect could be observed after combination treatment with 50 nM concentration of nigericin.

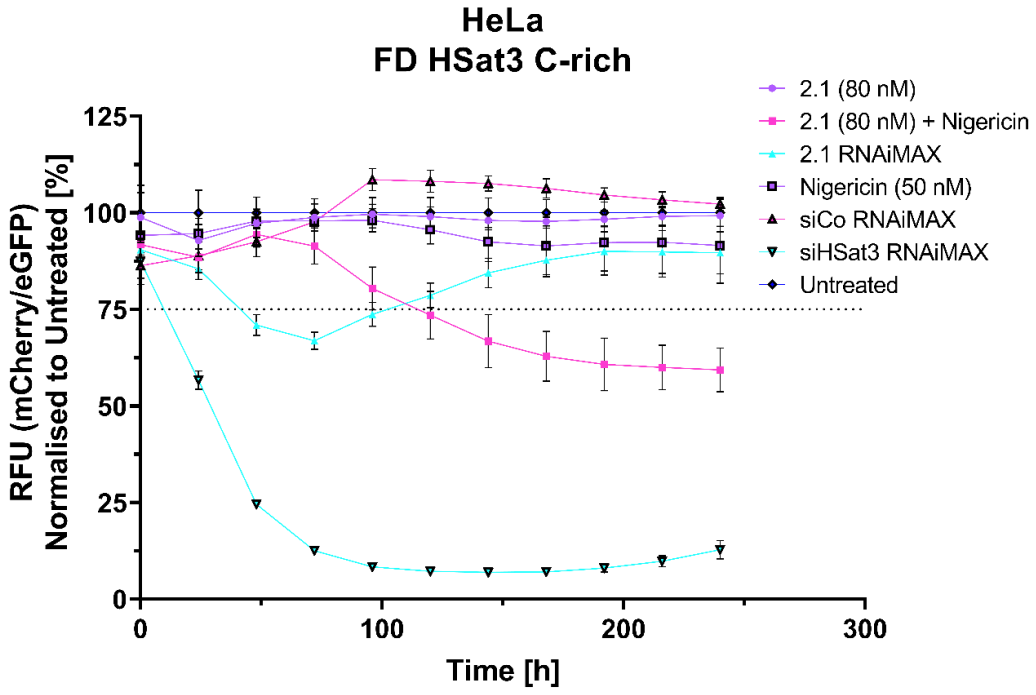

Figure 54 Evaluation of the knock down activity of the 5th generation vehicle strand loaded with 5th generation payload. *Long term experiment showing the RFUs measured in HeLa cells expressing the FluoroDetect Hsat3 C-rich assay. Time period of 0 h to 240 h. Populations are treated as indicated. Value displayed are represent the median of eight technical replicates normalized to an untreated sample (All graphs showing the median ± 95% confidence interval [CI]).*

In contrast the only nigericin treated samples showed no response in the C-rich assay and significant lower response in G-rich assay, when compared to the combination treatment. Overall, this was the first fully functional proof of concept. The EGFR specificity remains uncertain and needs to be evaluated in follow-up experiments using EGFR K.O cells. Moreover, it is of big interest if the effect size and onset can be optimized using higher concentrations of the 5th generation ARC. To exclude measurement artefacts a raw data analysis was performed. Therefore, the blanked fluorescence values of eGFP and mCherry were plotted. (**Figure S 25**-**Figure S 28**)

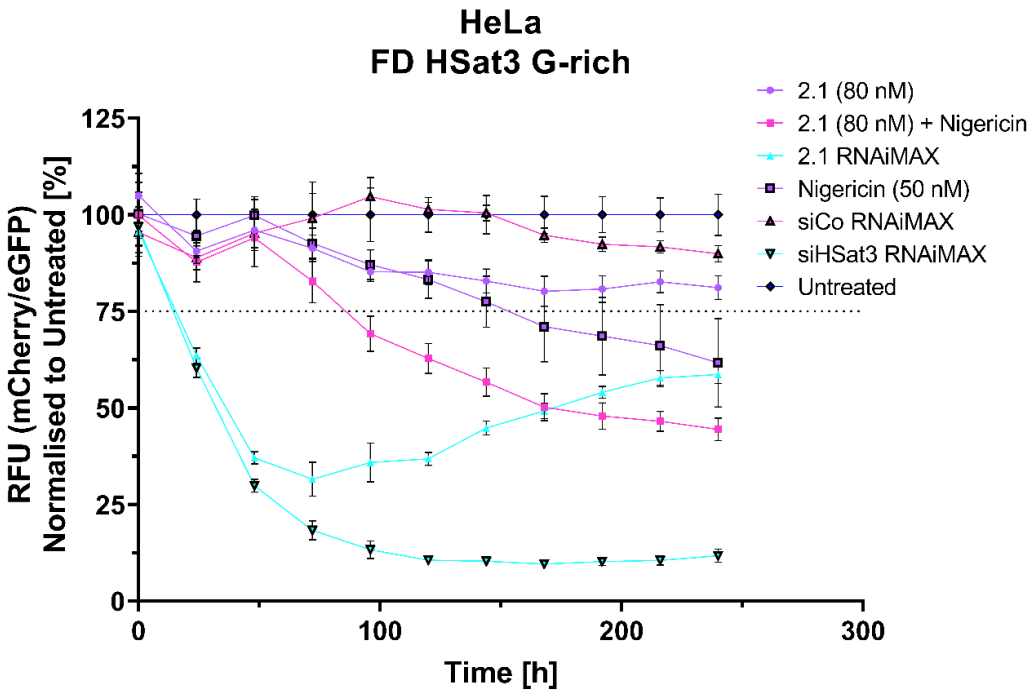

Figure 55 Evaluation of the knock down activity of the 5th generation payload strand carried by the 5th generation vehicle. *Long term experiment showing the RFUs measured in HeLa cells expressing the FluoroDetect Hsat3 G-rich assay. Time period of 0 h to 240 h. Populations are treated as indicated. Value displayed are represent the median of eight technical replicates normalized to an untreated sample (All graphs showing the median ± 95% confidence interval [CI]).*

7.10 siRNA Conjugates and The Endosomal Escape Problem – IF

To evaluate cell ARC interaction and to investigate if the previously observed slow uptake is related to endosomal entrapment described by *Steven F. Dowdy* an immunofluorescence experiment should be performed.[60] For this purpose, a 3' Cy5 modified DNA probe equal to the payload strand sequence was designed. Hybridization of fluorescent probe and ARC was performed as described earlier. Assembly of the vehicle probe conjugate (VPC, **Figure 56 A**) was similar to the 5th generation aptamer conjugates. Annealing was analysed using a Native PAGE. After electrophoresis gel was imaged using a gel doc to evaluate Cy5 fluorescence of the VPC. Following the analysis of the Cy5 fluorescence the gel was stained using SYBER gold to visualize non fluorescent species. Both methods verified the VPC assembly showing a size shifted fluorescent species. (**Figure S 29**, **Figure 56 B**) After assembly of the VPC cells have been treated with the isolated VPC to perform an Immune fluorescence experiment.

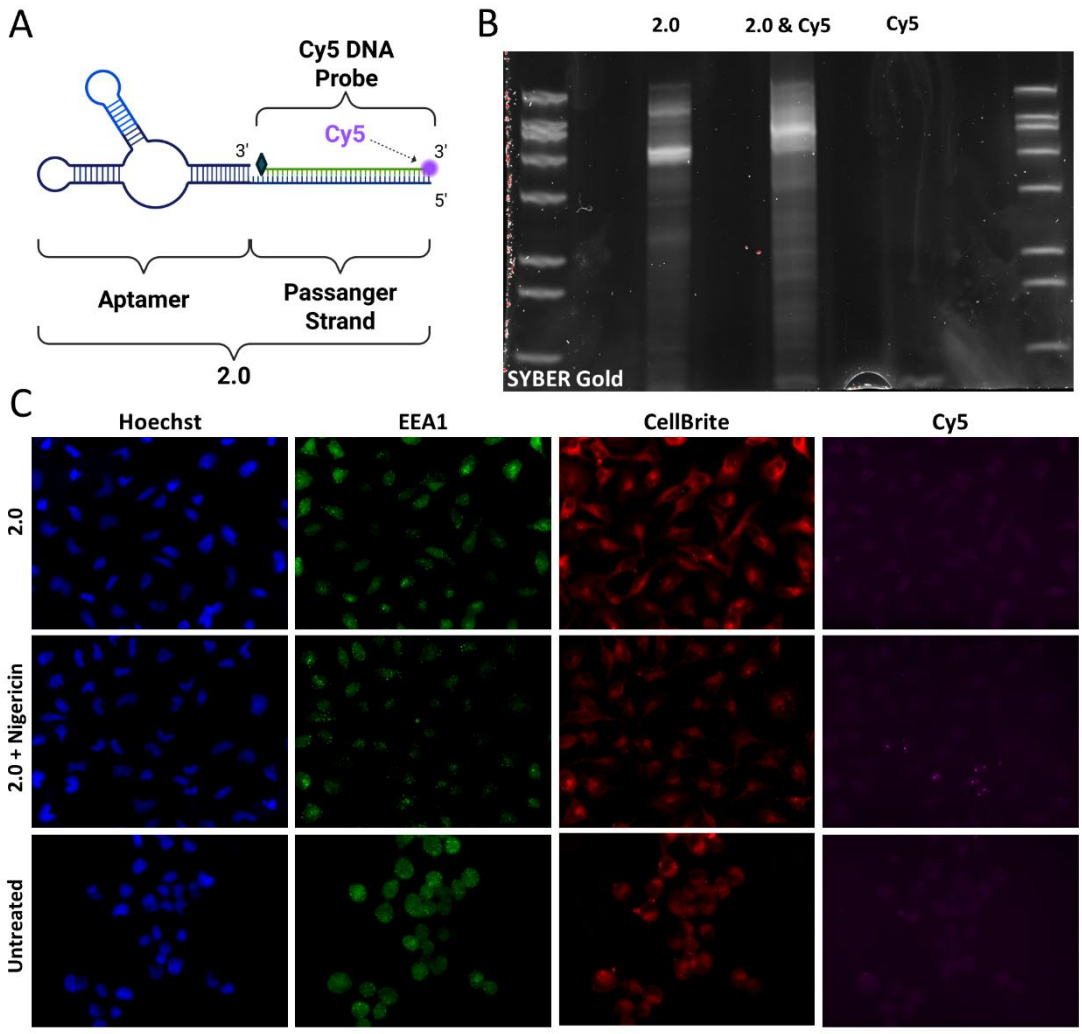

Figure 56 Assembly of Cy5 labelled vehicle probe conjugates and corresponding immune fluorescence images. A: *Schematic figure showing the assembly of the 3' Cy5 labelled VPC.:* ***B:*** *Urea PAGE stained with Syber Gold loaded with 20 pmol of the indicated species.* ***C:*** *Immune fluorescence images of VPC treated cells. Images of the nucleus (blue), early endosomes (green), cell membranes (red) and 5th generation VPCs (purple).*

Therefore, HeLa cells were stained with CellBrite Orange to visualize the cell membrane. Afterwards they have been treated for 45 minutes with the VPC or a combination of VPC and 50 µM of Nigericin. Following the treatment cells were washed and fixed. To investigate endosomal uptake of the VPC, the early endosomal antigen 1 (EEA1) was stained using a specific antibody. Immunofluorescence samples were compared to an untreated sample stained with DAPI, EEA1 antibody and CellBrite. Analysis of the untreated control sample helped determining autofluorescence in the Cy5 fluorescence spectrum. In all VPC treated samples distinct Cy5 foci could be observed. Especially upon a combination treatment of VPC and Nigericin the foci intensity was increasing in a non-defined subpopulation of the cells. Foci were mostly colocalizing with the CellBrite stained membrane but not with the EEA1 staining. In the untreated sample a weak autofluorescence of the cells in the Cy5 spectrum was observed. (**Figure 56 C**) Single staining controls showed no unexpected autofluorescence or spill over. (**Figure S 30**)

8 Discussion – Development of a NA-Therapy Screening Platform

As mentioned in the first section of this work the implementation of a new development platform for nucleic acid-based therapeutics was a major focus of the project as the platform provides critical information for the developmental process of the siRNA compound. The developmental process of the FluoroDetect system was published 2025 in Mol. Ther. Nucl. Ac. by Hess et al.. Starting with the establishing a HSat3 specific luciferase system, based on the psiCheck 2 plasmid, the need for a more cost- and time-efficient solution became clear.

Nevertheless, the generated psiCheck2 HSat3 system was a sensitive and functional platform to measure the RNAi. As the assay creates a ratio metric of two luciferases signals it provides highly sensitive assay mostly suffering from expensive substrates and its sample destructive setup.

As described, this was the starting point for drafting the FluoroDetect assay system. A dual fluorescence-based assay system with eGFP as reference and mCherry as reporter, to create a ratio metric for the knock down efficiency of a specific target sequence included in the 3'UTR of the reporter.

As described by *Valgardsdottir et al.* C-rich and a G-rich lncRNAs of HSat3 are transcribed under stress conditions.[118] Moreover, the evaluation of siRNA-based therapeutics relies on information of knock down activity of both RNA strands as the intended passenger strand can cause undesired off target events. Therefore, assays using the C-rich target motif as well as the G-rich target motif were designed to simulate both HSat3 RNA species as a target.

Upon cloning the first evaluation of FluorDetect HSat3 C-rich and G-rich assay was successful using fluorescent microscopy, as both assay systems showed specific response to the siHSat3 but not to the control samples.

In a next step the quantitative measurement of the fluorescence was assessed using plat reading. In this context the assay parameters for plat reading were defined using three different cell lines. The performance of the assay in combination with a plate reading system was beyond expectation and showed robustness over a broad range of cells per well. Additionally, the first time the non-destructive setup underlined the benefits of the assay as a time curve ranging from 24 h to 120 h could be created using three instead of 12 samples (if compared to a destructive setup).

Furthermore, comparing the FluorDetect assay with RT-qPCR data showed its capability of being representative for the endogenous target. Nevertheless, the on-target efficacy of an ASO or

siRNA needs to be evaluated for every new target as the RNA structure of the endogenous target can be significantly different to the target side in the 3' UTR of the reporter gene (mCherry).

As the strand specificity of the assay needed to be assessed an experimental setup was designed including single stranded ASOs corresponding to the sequences of the single strands of the siH-Sat3. As only one of this ASOs should be capable of targeting the assay this experiment should unravel the vulnerability of the assay to unspecific off target effects as well as its strand specific mode of action. Using fluorescence microscopy as well as plate reading a strand specific response could be observed in all used cell lines.

As the solid mode of action could be demonstrated the assays sensitivity was of major interest as this is an essential parameter for the development of nucleic acid-based therapies. Especially in context of the low endosomal escape rate of nucleic acid conjugates described by *Steven F. Dowdy*.[60] Upon measurement of fluorescence signals in samples exposed to different concentrations of targeting ASOs a linear regression was performed to calculate the limit of detection (LOD) and quantification (LOQ). The determined values of three different cell lines of each target were used to calculate the median LOD and LOQ of the C-rich and G-rich assay system. As demonstrated, the median values are in a low nanomolar concentration range underlining the sensitivity of the assay system.

To assess long time repetitive measurement approaches and to avoid recurring necessity of transfection the assay system was integrated into a lentiviral and a transposase-based system to generate stable reporter cell lines. As the expansion of the intermediate cell population after gene transfer relies on a selection marker, the assay system was supplemented by a puromycin resistance gene. Outlined in the results part the selection process can be performed as a poly or single clonal expansion dependent on the needs of the follow up experiment.

Integration into the lentiviral transduction system allows gen transfer into hard to transfect cell lines broaden the field of application. In a pilot experiment the lentiviral transduced reporter cell lines evaluated using siHSat3 as well as HSat3 targeting ASOs. A strand specific mode of action could be observed in all reporter cell lines. Moreover, the performance of the assay system over an expanded time period was in line with the findings of *Bartlett and Davis* who investigated the kinetics of siRNA-mediated gene silencing using bioluminescence. 27

The larger cargo capacity of PiggyBac transposase-based systems allows it to carry more complex and longer constructs. Secondly, PiggyBac poses a lower risk of insertional mutagenesis, as it tends to integrate into stable regions of the genome. Additionally, the production of PiggyBac transposons is more cost effective and simpler compared to the complex and expensive process

of producing viral vectors. Another significant benefit is the ability of PiggyBac transposons not to rely on host cell factors for integration.

Following up the flow cytometer-based analysis of the FluoroDetect assay was established to expand the field of application. As shown, this additional readout gave information about sub-populations in the sample, which can be particularly useful for pharmacological developments as well as in mixed cell culture experiments. However, for the FluoroDetect assay with eGFP and mCherry, flow cytometers analysis using a violet (405 nm), blue (488 nm), and yellow (561 nm) laser line are recommended to ensure faithful separation of reporter and reference signal in two different laser lines.

To make sure the assay systems robustness and data analysis is not affected by internal control failure, additional parameters regarding the independence of the reporter and reference gene needed to be investigated. Uncertainty regarding unintended fusion proteins could be erased performing a Western blot of PiggyBac transposase generated reporter cell lines. As demonstrated no fusion protein of mCherry or eGFP could be detected using specific antibodies. Moreover, the presence of a fused mRNA could not be validated as a specific mCherry mRNA reduction was observed only in cells treated with siHSat3.

To prove the intended fast adaptability of the assay additional target sequences of EGFR and HSF1 have been designed. Upon gene transfer and selection using the PiggyBac transposase system the reporter cells showed the expected responses upon investigation with Fluorescence microscopy and plate reading.

After development and successfully establishing the assay system the platform design was missing a pivotal information in context of receptor specific delivery. As mentioned earlier the second key point of the platform is control of the delivery rout. For this purpose, a prime editing approach was started do knock out the EGFR by integration of a premature stop codon via point mutation. As demonstrated the cells showed no significant reduction of EGFR receptor upon initial prime editing experiments. Revaluation of the method revealed its undeniable potential as a gene editing therapy but also showed its disproportional workload in laboratory environment when compared to CRISPR Cas9 mediated gene knock out.

Therefore, a CRISPR Cas9 mediated knock out was established in cooperation with the lab of Prof. Stripecke and the Max Plank Institute for Biology of aging. Upon knock out of the EGFR, using two different gRNAs, all cell lines showed a significant reduction of the EGFR. Overall, the performance of gRNA #1 was much better compared to gRNA #2. The resulting intermediate cell

populations was separated using fluorescence associated cell sorting (FACS) to grow out polyclonal EGFR cell lines.

To finish the platform design, the FluoroDetect system was established in the EGFR knock out cell line. This provides a new cost efficient and convenient platform for the development of RNAi based EGFR targeting therapies.

In summary the first section demonstrates how to establish and modify the FluoroDetect assay system for fast evaluation in the developmental process of new targeted therapy approaches. It can be evaluated using fluorescence microscopy, plate reading as well as flow cytometry. Additionally, it can be performed as a transient or stable system depending on the desired experimental setup. In combination with CRISPR Cas9 based genetic engineering of the implemented cell line it represents an even more powerful tool for the development of nucleic acid-based therapies.

9 Discussion – Development of a Delivery System

As the first section of this work was focusing on the development of the FluoroDetect platform design, the second section focused on the implementation of an EGFR specific siHSat3 targeting therapy to reverse HSat3 RNA related etoposide resistance. [44]

As mentioned earlier the process of developing RNA conjugates is an iterative process of trial and error. In the first phase, the drug candidate is designed using *in silico* methods followed by its synthesis. In the second phase, the compound is evaluated using an efficient development platform. In the third phase, the experimental data is analysed and compared to the scientific literature, with the information gained shaping the design of the next cycle. Each cycle can be considered a generation, with each generation improving the compound candidate. This work demonstrated the first five generations of the developmental process.

The first-generation of the compound was started with the draft of an idea to transport an antisense oligonucleotide targeting HSat3 into EGFR positive cells. With this initial idea the targeting of the nuclear long noncoding HSat3 RNA was desired. As the RNAi machinery necessary for siRNA mediated knock down is mostly cytoplasmatic an ASO was chosen to knock down HSat3 RNA. With this decision the functional subunit of the compound was defined. As receptor specific delivery was desired the next essential step was the choice of EGFR targeting ligand. As the field of targeting ligands is broad and includes many different compound categories with a variety of advantages and disadvantages the drug approval process and regulations have been decisive for the choice of ligand. As an example, DNA aptamers are easy to synthesise, cost efficient and more stable compared to unmodified RNA. On the other hand, they need to guarantee long-term safety due to potential genomic integration. Additionally, the use of two different compound categories would need the use of two independent synthesis methods of the compound's subgroups potentially increasing production cost and complexity of quality control. Therefore, an RNA aptamer evolved by *Esposito et al.* was chosen.[79] As the CL4 called aptamer was evolved using NSCLC cells and its dissociation constant was determined to be as low as 10 nM it seemed to be an excellent candidate. Moreover, it does not activate the EGFR, is internalized and causes selective apoptosis. All the mentioned properties supplemented the portfolio of the designed compound candidate. Especially the missing EGFR activation guaranties to maintain the exposure of cell surface exposed EGFR level, as strong over activation can lead to strong downregulation of the receptor within minutes.[99] Last but not least the missing link of the compound was the linker structure connecting aptamer and ASO subunit. To increase the ASO release upon endocytosis a linker molecule containing a glutathione cleavable disulfide bond was designed in cooperation with the research group of Prof. Kath-Schorr.

Since the first and second sections of this work were not chronologically separate from each other, but rather simultaneous the first-generation compound was evaluated using the psiCheck2 HSat3 luciferase assay. As the internalization of the EGFR is an outstanding fast cellular process the treatment duration was chosen to be only 10 minutes. As the internalization rate of the EGFR is disrupted by low temperature a control treatment was performed at 4°C.[99] Moreover, an EGFR negative cell population was used as a second control. Despite all control parameters a temperature and EGFR independent but low response was observed upon treatment with a 50 nM compound concentration. As this concentration exceeded the CL4 dissociation constant by the power of five it should guarantee a sufficient treatment. As the observed effect did not exceed the response measured in the negative control treated with siRNA control (siCo) lipoplexes the result is considered as unspecific background. Especially in context of the slow endosomal escape and entrapment described by *Steven F. Dowdy*. [60]

Nevertheless, follow up experiments were performed evaluating longer incubation times to maintain constant uptake of the ARC. Despite the inconsistent results upon 10 minute and 4 h treatment all cell lines showed a strong response to the compound upon 48 h of treatment. The observed finding was again independent of the EGFR status indicating an EGFR independent cellular uptake. As the exact mechanism remains unclear it was likely to be caused by a degradation product of the compound. Especially if considering the possibly thiol mediated uptake of the cleaved ASO subunit.[100]

To stabilize future compound candidates and to avoid undesired thiol mediated uptake the second generation compound was designed with a non-cleavable linker. To evaluate the compounds functionality the experimental setup of the last experiment was repeated excluding the 10 minute and 4 h treatment condition. Underlining the hypothesis of thiol mediated uptake no unspecific response was observed after 48 h of treatment. On contrary the first time an EGFR specific response was observed after exposure to a 50 nM concentration of the ARC. Despite this first positive evaluation this result needs to be evaluated careful as no significant difference to samples treated with siCo lipoplexes was observed.

Upon the low response observed in the first two generations the general compound design was re-evaluated. Especially in retrospective several disadvantages included in the compound design can be unrevealed. Moreover, the experimental structure was missing a control sample, showing the functionality of the compound upon transfection. Without this crucial information evaluation of compound uptake is highly limited. Nevertheless, the compound design using unmodified RNA probably strongly limited the functionality of the RNA aptamer.[119] Additionally, the serum stability of the ASO subunit can be evaluated as suboptimal based on the work of *Layzer,*

J. M. et al..[119] Furthermore, the structural design of the ASO was limiting its knock down potential as it didn't contain the gapmere design which is essential for the activation of RNaseH. From a synthesis perspective the design involving three different molecules to be combined using two click reactions was disproportional complex in regard of the poor design of the compound. Moreover, *Valgardsdottir et al.* described that the majority of the HSat3 RNA expressed upon stress is the G-rich species.[36] Therefore, planning to target this species with a G-rich ASO sems to be a not really promising strategy.

Facing all the disadvantages of the first two compound generations resulted in a general restructuration when designing the third generation compound. To target the immunogenicity of unmodified RNA as well as its low nuclease resistance a fully 2'-OMe modified RNA configuration was chosen. To achieve even higher exonuclease resistance two phosporothioate modifications were integrated at all terminal 5' and 3' ends of the used RNAs. Longer knock down efficiency should be achieved changing the ASO subunit to an siRNA subunit although this lowers the knock down efficiency of nuclear targets. To lower the synthesis complexity a sequence of five C3 spacers was integrated into the SPS synthesis to enable a single step synthesis of the so called vehicle strand. Functionality of C3 spacers as a linker sequence was demonstrated by *Yoon S. and Huang K.-W. et al..*[102] As described earlier the functional siRNA subunit contained a 5' phosphate to enhance RISC loading according to the work of *Frank, F.; Sonenberg,N. and Nagar, B. et al*.[66]

Following the reconstruction and synthesis the annealing of the payload strand to the vehicle strand could be proved using Urea PAGE. This gave a first positive evaluation regarding the functional assembly of the compound. Nevertheless, minor part of the vehicle strand showed no change in electromobility shift. This could be explained by the desaturating nature of Urea gels and could be overcome by using a native PAGE. Slightly increased degradation could be observed upon hybridization, which could be explained by the temperature profile of the hybridization in combination with a not RNase free environment. To overcome this RNase inhibitor could be added to the hybridization protocol.

As the functionality of the compound should be evaluated a dose escalation experiment was performed exposing the cells to compound concentrations ranging from 750 nM to 10,156 nM. As discussed earlier the experimental setup was supplemented by a sample transfecting the ARC into the cells to evaluate its functionality. In all cell lines a 20-30 % reduction of RFU was observed proving the function of the siRNA subunit. Nevertheless, as described in the work of *Cazuderna F. et al.* a limiting factor in the third generation design is the fully 2'OMe modified payload strand.[120] Additionally, the results of the SW620 cell line need to be considered carefully as they showed a strong response to the non-targeting siCo lipoplexes. Moreover, no cytoplasmatic

aptamer conjugate could be detected independent of the ARC concentration. As discussed earlier the missing 2'-F modification of the pyrimidine bases in the aptamer subunit could possibly strongly affect its EWGFR targeting property. Nevertheless, this result demonstrates that conjugation of the passenger strand is possible without losing the siRNA activity.

Upon this positive result the design of the fourth generation was started. As the cellular uptake of the third generation ARC was far behind the expectation choice of the aptamer was reevaluated based on the work of *Kelly, L., Maier, K.E., Yan, A.et al*..[105] Underlined by the low performance of CL4 in the mentioned study changing the targeting ligand was an important turning point of the project. Moreover, the work of *Thomas, Brian J. et al.* was decisive for choosing MinE07 as a targeting ligand.[80] As the mentioned study proved the internalization of a vehicle probe conjugate (VPC). Moreover, this work served as a solid foundation for *in silico* design as the used conjugate served as a positive control for *in silico* design.

The *in silico* design of the fourth generation conjugates showed high similarity with the VPC designed by *Thomas, Brian J. et al*. allowing a first positive evaluation of targeting capability. Formation of a A-form helix indicated a functional assembly of the siRNA subunit. Nevertheless, it remains unknown if the predicted structures of the ARC represent the actual assembly as there are some major limitations of the prediction models. Especially the missing capability of the used models to integrate 2' modifications into the folding could limit the prediction quality as they directly impact the base pairing energy.

Considering that RNA aptamers are evolved using the T7 RNA polymerase mutant Y639F developed by *Sousa, R. and Padilla, R.* low delivery rates in previous compound generations need to be reevaluated.[103] As described earlier the T7 mutant is used to integrate 2'-F pyrimidine bases int aptamers during SELEX. This significantly increases the stability of the resulting aptamers but can also be decisive for their targeting ability. Therefore, the synthesis pipeline of the aptamer containing strand needs to be redesigned. This was targeted by establishing the hybrid design and rapid assessment (HYDRA) workflow by combining IVT and SPS. Development of the HYDRA workflow significantly improved the project performance and can be considered as a major turning point in the developmental process.

Upon *in silico* design and implementation of the HYDRA workflow the functional evaluation of the compound was assessed. Discussed earlier the ARC lipoplexes are of central interest when evaluating ARC internalization, as they prove activity of the assembled siRNA subunit. For this purpose, the transfection reagent to ARC ratio was optimized. As the ARC is much bigger compared to an siRNA it also exhibits more negative charges which need to be neutralized by the cationic lipids of the transfection reagent to reduce membrane repulsion. Considering the

absolute eGFP fluorescence as a representation of cell count and viability a higher toxicity was observed through all samples treated with ARC lipoplexes.

Especially, in comparison with the siRNA lipoplexes this implies a toxicity of the ARC which could be caused by innate immune response. Nevertheless, all used ratios caused a sufficient knock-down, underlining the activity of the assembled siRNA subunit.

Despite the high performance observed in the transfection optimization experiment the transfection of the ARC showed a much lower performance as expected in repetitive measurement approaches. As the G-rich assay showed less response compared to the C-rich assay this could be explained by multiple factors. As observed in the transfection optimization the cells exhibited signs of cytotoxicity upon ARC transfection. Discussed earlier the expression of a high amount of G-rich HSat3 RNA is a general stress response in human cells.[118] In consequence the mRNA target motif is in competition with the endogenous target sequence, which might affect the FluoroDetect HSat3 assay.

Additionally, this can be explained by the modification of the payloads sequence which was a consequence of planning an IVT synthesis of the short C-rich strand. Respective shifting the seed region of the payload to avoid SPS sems to be a delicate strategy if the intended seed does not start with a guanine. Nevertheless, this is irrelevant as IVT synthesis of short RNA strands showed low efficiency.

As described by *Steven F. Dowdy*, another factor limiting the effective cytoplasmatic delivery of targeted siRNA therapies is caused by endosomal entrapment. Recent studies suggest that only 0,3% of targeted siRNA compounds can overcome the endosomal escape problem.[60] As such low delivery rates could mask the detection of ARC prototypes the use of endosomal escape enhancing and endosomolytic agents was considered. Despite their clinical intolerable toxicity, these agents could at least prove endosomal uptake of targeted cells under laboratory conditions.

Therefore, the two compounds polybrene and nigericin were used to increase endosomal escape of the ARC. As an unspecific reduction of RFU was observed in all samples treated only with the bioenhancer substance this indicated measurement artefacts caused by the treatment itself. In a consequence a follow up experiment aimed to reduce measurement artefacts by titrating the concentration of the bioenhancer. As mentioned, the used bioenhancers exhibit clinical intolerable toxicity which could explain the observed measurement artefacts by cytotoxicity in cell culture. Underlining this theory a dose responsive reduction of eGFP fluorescence was observed in both compounds. As an even higher does dependent decrease of mCherry fluorescence was observed the resulting RFU dropped. This could be caused by overestimating the eGFP

fluorescence upon cellular stress and cytotoxicity as cellular debris and stress granular shows increase of autofluorescence. For this reason, experimental conditions exhibiting high cytotoxicity need to be evaluated carefully and always include a control sample only treated with the bioenhancer.

In consideration of the seed optimization the fifth generation ARC was designed. As the new payload could theoretically be annealed to the 4th generation vehicle this led to two versions of the fifth generation compound. The old vehicle 2.0 with the new payload 5.1 and the new vehicle 2.1 with the new payload 5.1. For clear differentiation between the two constructs the assembled Arc was named as the used vehicle strand. As previously demonstrated the RNA folding prediction can be a powerful tool to predict the formation of the siRNA subunit. Therefore, the assembly of the two conjugates was investigated *in silico*. A high similarity with the VPC designed by *Thomas, Brian J. et al.* was predicted. Hence a first positive evaluation of targeting capability could be made. Formation of a A-form helix indicated a functional assembly of the siRNA subunit.

As the functionality of the siRNA subunit strongly depends on the interaction with the Ago2 protein further in silico experiments were performed. The algorithm's ability to select a preferred guide strand has been successfully tested. As the designed guid strand contained a 3’ overhand it should decrease the 5’ interaction of passenger and MID. Following this first experiment the ARCs 2.0 and 2.1 were tested. As already predicted the A-form helix was fitting into the grove of the Ago2 indicating a functional siRNA subunit. Nevertheless, a stronger prediction of the passenger 5’ and the Ago2 protein was predicted. This can be explained by the diminished accessibility of the payload 5’ caused by the aptamer. Considering this in the next compound generation the 5’ end of the passenger strand should be modified with the aptamer. Independent of the preference of the 5’, the passenger strand is no sufficient Ago2 substrate, as it is much to long to interact with the PIWI domain of the Ago2.

The assembly of the fifth generation conjugates was successful showing the expected electromobility shift upon hybridization of the vehicle and payload strand. The observed unexpected RNA species detected in the Urea PAGE could be explained by different conformations of the RNA strands, unperfect annealing or unspecific elongation during IVT. As they show much lower intensity compared to the main band they can be tolerated in the following experimental setups. Nevertheless, they demonstrate an improved clean-up of the assembled conjugates could be beneficial for future evaluation or large scale synthesis of the ARCs.

Following the assembly of the ARCs the evaluation of the compounds was performed using HeLa FluoroDetect HSat3 C-rich and G-rich reporter cell lines. For the first time in the developmental

process a high performance and payload selective mode of action was measured. Additionally, a slow but steady knock down could be observed when exposing the cells to the ARC over long time periods. Moreover, the uptake could be enhanced by a combination treatment of ARC with 50 nM of nigericin. This underlines the theory of endosomal entrapment of the ARCs. Compared with the lipoplexes the ARCs showed a later onset but longer lasting knock down. This is in line with the endosomal depot effect mentioned by *Steven F. Dowdy*. As the functional analysis was performed in EGFR positive cell lines the EGFR specificity remains uncertain and needs to be evaluated using EGFR knock out cell lines.

Following the functional analysis interaction of cells and ARC was investigated using immune fluorescence. Following the design of *Thomas, Brian J. et al.* a Cy5 labelled DNA prob was annealed to the vehicle to visualize the vehicle. Upon 45 minutes of exposure a cell interaction could be observed, which was even increased in combination with 50 nM of nigericin. This is in line with the previous results of the FluorDetect assay. As there was only low colocalization of VPC and EEA1 this finding also seems to be in line with the findings of *Steven F. Dowdy* as the highest concentration of entrapped RNA therapeutics seems to be localized in processed "Depot Endosmes". Nevertheless, follow up experiments need to be performed to validate this findings and to investigate if the observed effect is EGFR specific. In example by using the generated EGFR knock out cell lines.

In summery this section demonstrated the development of a powerful cost and time efficient pipeline for fast prototyping of aptamer siRNA conjugates. The implementation of *in silico* design evaluation opens the opportunity to integrate new computational tools into the HYDRA workflow. Moreover, it led to the design of a promising compound candidate for EGFR specific delivery of siHSat3 RNA. An overview of the evaluated compounds can be found in Table 2 **Summary of Compound Generations.**

Furthermore, it could be interesting to evaluate the correlation of cell death and HSat3 knock down up on stress conditions using flow cytometry assays.

Table 2 Summary of Compound Generations.

Compound	Aptamer	Linker	Target	Modifications
1st Generation	CL4	Synthetic Disulfide Linker (Cleavable)	HSat3	Unmodified ASO
2nd Generation	CL4	Synthetic Linker (Non-Cleavable)	HSat3	Unmodified ASO
3rd Generation	CL4	C3 Spacer (Non-Cleavable)	HSat3	Full 2'OMe siRNA
4th Generation	MinE07	Without	HSat3 (Shifted)	Hybrid design (2'-OMe, 2'-F and Phosphorotioate)
5th Generation	MinE07	Without	HSat3	Hybrid design (2'-OMe, 2'-F and Phosphorotioate)

10 Outlook

The first section demonstrates how to establish and modify the FluoroDetect assay system for fast evaluation of nucleic acid based compounds in the developmental process of new targeted therapy approaches. In combination with CRISPR Cas9 based genetic engineering of the implemented cell line it represents an even more powerful tool for the development of nucleic acid-based therapies.

A power which could be proved in the second section of this work as the combination of FluoroDetect and hybrid design siRNA conjugates led to the HYDRA workflow. A workflow which could be improved by a second generation of FluoroDetect assays as well as modification of the IVT based synthesis.

As mentioned earlier an *in vivo* transgenic animal model of the FluoroDetect assay could be beneficial for the systematic evaluation of ARC pharmacodynamic and pharmacokinetic properties under physiological conditions. Moreover, a second generation of FluoroDetect assays could be designed using a three signal ratio metric evaluating the performance of guid and passenger strand in single cells. Additionally, the generated EGFR knock out cell lines could be used in cell culture an in a cell line derived xenograft (CDX) model to further demonstrate receptor specificity of the compound candidates.

Demonstrated in the second section the performance of the HYDRA workflow is undeniable and opens a variety of future perspectives. The combination of rapid evaluation and *in silico* compound design could give the opportunity to integrate artificial intelligence for faster design of even more promising compound candidates.

Furthermore, the fast and cost efficient prototyping gives the opportunity for more advanced compound designs. In example a vehicle strand with two or more aptamers targeting different receptors could be designed based on the model of bispecific antibodies. Additionally, longer passenger strands could be evaluated increasing the cargo capacity of the conjugate.

Besides this improving the IVT based on the pioneering work of Craig T. Martin immobilizing T7 polymerases to establish flow through synthesis of the vehicle strands could significantly reduce the cost for large scale synthesis of aptamer siRNA conjugates. In this context evolving T7 polymerases to be capable of integrating additional 2’ RNA modifications for synthesis of fully modified RNA would be invaluable for the whole RNA community.

11 Material and Methodes

11.1 Vector Design

All inserts were designed according to the hot fusion protocol described by C. Fu et al.[83] The plasmid pCW57.1 Empty (N-FLAG, TetOFF) was created inserting a synthetic multiple cloning site (MCS) oligo in the pCW57.1-MCU-Flag-TetOFF (Addgene plasmid #185657, RRID: Addgene 185657) generously provided by Dipayan Chaudhuri. A synthetic sequence of C-rich HSat3 flanked by AsiSI and NsiI restriction side sequences was cloned into the pmCherry-C3 (Clontech) generating pmCherry-C3 (HSat3 C-rich). The eGFP and mCherry (HSat3 C-rich) gene sequences were amplified by PCR from the plasmids peGFP C1 and pmCherry-C3 (HSat3 C-rich). The generated PCR-products were cloned into the pCW57.1 Empty (N-FLAG, TetOFF) generating the pFluoroCheck (C-rich HSat3). Oligos containing the HSat3 G-rich target motive (Ordered from Integrated DNA technologies, Inc. (IDT)) were ligated into the digested pFluoroCheck (C-rich HSat3) to generate pFluoroCheck (G-rich HSat3). For lentiviral transduction single-colour transfer plasmids were used. The transfer plasmids pCW57.1 TET-OFF mCherry (C-rich HSat3) and pCW57.1 TET-OFF mCherry (G-rich HSat3) coding the reporter gene, were generated by cutting the plasmids pFluoroCheck (C-rich HSat3) and pFluoroCheck (G-rich HSat3) to exclude the eGFP. A transfer plasmid coding only eGFP was cloned by inserting an eGFP sequence into the pCDH-3xFLAG-TERT (Addgene plasmid #51631, RRID: Addgene 51631) generously provided by Steven Artandi.[86]

11.2 Molecular Cloning

For In-Fusion cloning primer pairs were designed matching the desired inserts, as described by C. Fu et al. in 2014. Each primer had a 5’ homology overlap of 17-30 bp flanking the insert sites of thr destination backbone. Insert PCR-products were separated on a 1% agarose gel (Carl Roth GmbH + Co. KG, Art. Nr. 3810.3) in TAE buffer, followed by cutting out the band of the desired product size and cleaning up following the manual of the NucleoSpin® Gel and PCR Clean-up Kit (MACHEREY-NAGEL GmbH & Co. KG, REF 740609.50). Linearization/ restriction digest of the acceptor plasmid was performed using the appropriate restriction enzyme. All restriction enzymes were ordered from NEB. In-Fusion was performed in a final volume of 20 µl, in 0,2 M Tris pH 7,5, 0,2 M MgCl2, 2 mM dNTP’s, 0,2 M DTT, 5 % PEG-800, 0,15 U T5 Exonuclease and 1 U Phusion Hot Start Flex DNA Polymerase. For all In-Fusion reactions the molar ratios of 1:1, 1:2 and 1:4 of digested plasmid to insert were tested and a total amount of 200 ng DNA was used. In-Fusion reaction was performed 1 h at 50 °C followed by a ramp down to 20 °C with a ramping speed of 0,1 °C per second. In-Fusion reaction was stored at -20 °C or immediately used for bacterial

transformation. The plasmids were isolated using NucleoSpin® Plasmid, Mini Kit (MACHEREY-NAGEL GmbH & Co. KG, REF 740588.50) or NucleoBond® Plasmid, Xtra Midi EF Kit (MACHEREY-NAGEL GmbH & Co. KG, REF 740420.50). When used for cell culture experiments. All generated plasmids were validated by sequencing Microsynth Seqlab GmbH (Microsynth). All primers and cloning oligos were ordered from Integrated DNA technologies, Inc. (IDT). Maps of generated plasmids can be found in the appendix of this work (**Figure S 1-S 3, S 11, S 31-S 44**). [86]

11.3 Cell Culture

HeLa (RRID: CVCL0030), SW480 (RRID: CVCL_0546), SW620 (RRID: CVCL_0547), MDA MB 231 (RRID: CVCL_0062), HEK 293 FT (RRID: CVCL6911), PC9 (RIDD: CVCL_B260) were used in this study.

The human cervical cancer cell line HeLa, lung cancer cell line PC9 and the colon cancer cell lines SW480 and SW620 were cultured in Dulbecco's Modified Eagles Medium (DMEM) (PAN-Biotech, P04-01500) supplemented with 10% (v/v) fetal calf serum (FCS) (Sigma-Aldrich, F7524), 100 U/mL penicillin, 100 µg/mL streptomycin (Sigma-Aldrich, P4333-100ML) and a final concentration of 2 mM L-Glutamine (Sigma-Aldrich, G7513-100ML). The human embryonic kidney cell line HEK 293 FT was cultured in Dulbecco's Modified Eagles Medium GlutaMAX™ (DMEM GlutaMAX™) (Thermo Scientific, 10569010) supplemented with 10% (v/v) fetal calf serum (FCS) (Sigma-Aldrich, F7524), 100 U/mL penicillin, 100 µg/mL streptomycin (Sigma-Aldrich, P4333-100ML). All cell lines were tested negative for *Mycoplasma* contamination using the Mycoalert Plus *Mycoplasma* detection kit (Lonza, LT07-710). Cell cultures at 37°C, 95% humidity and 5% CO_2. [86]

11.4 Transfection, Reverse Transfection and Lentiviral Transduction

The transfection of the assay plasmids (pFluoroCheck HSat3 C-rich; pFluoroCheck HSat3 G-rich) and cotransfection of plasmids and siRNA/ASOs was performed using Lipofectamine 2000 (Invitrogen Inc., #11668027) according to the manufacturer's recommendations. Medium was changed 24 hours after transfection.

Additionally, single transfections of siRNAs and antisense oligonucleotides were performed using Lipofectamine RNAiMAX reagent (Invitrogen Inc., #13778030) according to the manufacturer's recommendations. The transfected antisense oligonucleotides shared the sequence with the siRNA strands but were chemically modified. The sequences of siRNA/antisense-oligos are provided in **Table S 3**. In the case of antisense oligonucleotide dilution series, it is important to dilute the targeted siRNA/ASO with an untargeted control RNA to minimize systematic errors caused by different strong repulsion rates between the samples.

To prepare reverse transfection the transfection mixes had to be prepared. All transfection mixes were prepared for ten wells (eight replicates and two excess). For transfection of siRNA 1 µL of a 10 µM siRNA solution was mixed with 50 µL OptiMEM (Thermo Scientific, 31985070). For transfection of aptamer siRNA conjugates (ARC) 1,25 µL of a 4 µM ARC solution have been mixed with 50 µL OptiMEM. Per RNA species 3 µL of the transfection reagent Lipofectamine RNAiMAX have been diluted in 50 µL OptiMEM in parallel. The resulting Lipofectamine containing mix has been mixed with one of the RNA mixes in a 1:1 ratio. To form lipoplexes the Transfection mix was incubated 5-10 minutes at RT. Upon incubation the mix was mixed with 400 µL of Medium to a final volume of 500 µL. For reverse transfection 50 µL of the final transfection mix were pipetted into a 96 well. After putting the transfection mix $1{,}0x10^4$ cells were seeded in 50 µL of a medium based cell suspension. Following the transfection, cells were incubated at standard conditions. Follow up measurements were performed as described in the results section.

For viral transductions plasmids psPAX2 (gifted from Didier Trono, Addgene plasmid #12260; http://n2t.net/addgene:12260; RRID: Addgene_12260), pMD2.G (gifted from Didier Trono, Addgene plasmid #12259; http://n2t.net/addgene:12259; RRID: Addgene_12259) were used as packaging plasmid and transfected with PEI MAX® (Polysciences, #24765(1), CAS Number: 49553-93-7). The packaging plasmids were cotransfected with the transfer plasmid pmCherry HSat3 C-rich, pmCherry HSat3 G-rich or pCDH eGFP (Neo). The transfection media was replaced with fresh media after 24 h. The Lentiviruses were harvested 48 hours and 72 hours after transfection. Lentivirus containing media was centrifuged at 500 g for 10 minutes followed by passing through a filter membrane with a 0,45 µm pore size (SARSTEDT, 83.1826). Virus containing medium was stored at -80 °C and supplemented with a final concentration of 8 µg/mL polybrene (Merck, TR-1003-G) directly prior to transduction. Cells were incubated 72 hours with the transduction mix followed by a selection with Puromycin dihydrochloride (5 µg/mL, Sigma Aldrich, P8833-25MG) and G418 (400 µg/mL, InvivoGen, ant-gn-1). Selection medium was changed in 96 hours intervals. [86]

11.5 Luciferase Assay

For luciferase assay $7{,}5x10^4$ cells were seeded in a 24 well plate and incubated at 37 °C, 90% humidity and 5% CO_2 overnight. The next day cells were transfected with the psiCheck2 HSat3 plasmid using Lipofectamine 2000 as described. After 24h of incubation cells were treated as indicated in the result section. Luciferase assay was performed using the Dual-Glo® Luciferase assay system (Promega Corporation Prod. No.: E2920). After an appropriate incubation time medium was reduced to 100 µL and cells were lysed using 100 µL of the Dual-Glo® luciferase reagent. After 10 minutes of incubation at RT in the dark, the sample was transferred to a white

96 well plate for measurement. Each sample was divided into two technical replicates with a volume of 90 µL. Bioluminescence of *Firefly* luciferase was determined using a TECAN plate reader. Upon measuring *Firefly* luminescence each well was supplemented with 45 µL Dual-Glo® Stop & Glo® reagent and incubated 10 minutes at RT in the dark. Bioluminescence of *Renilla* luciferase was measured using a TECAN plate reader. Relative fluorescence units were calculated by normalization of *Renilla* luminescence to *Firefly* luminescence.

11.6 FluoroDetect Assay and Plate Reading

The cells were seeded and incubated for 24 hours at 37 °C, 95% humidity and 5% CO_2. Cells were transfected as described above and incubated for 24 hours. For measurement with the Tecan Infinite 200 PRO Micro plate reader (Tecan Germany GmbH). Cells needed to be transferred to a tissue culture coated 96 well flat bottom assay microplate (Falcon®, REF: 53296). Therefore, cells were washed once with 1 mL PBS and trypsinized. Indicated number of cells was seeded in 100 µL cell culture medium per well in a 96 well flat bottom assay microplate.[86]

11.7 Flow Cytometry

For flow analysis of the FluoroDetect assay the cells were seeded and incubated for 24 hours at 37 °C in a humidified incubator with 5% CO_2. Cells were transfected as described above. For measurement with the MACSQuant Analyzer16 Flow Cytometer (Miltenyi Biotec B.V. & Co. KG) cells were suspended into FACS buffer (2 % FCS, 1 mM Ethylene glycol-bis-(2-aminoethyl)-tetra-acetic-acid (EGTA, Carl Roth, Product No.: 3054.3), 4 mM Ethylenediamine tetra-acetic acid (EDTA, Carl Roth, Product No.:8040.2) in PBS). For this purpose, adherent cells were washed once with PBS followed by 10 minutes incubation at 37 °C with 500 µL FACS Buffer per well. The detached cell suspension was passed through a CellTrics™ 30 µm cell strainer (Sysmex, REF: 04-0004-2326) in a 5mL Polystyrene Round-Bottom Tube (Falcon®, REF: 352054) to isolate single cells. The cells were chilled on ice till analysis. Right before measurement cells were incubated with a final concentration of 10 ng/mL 4',6-Diamidino-2-Phenylindole (DAPI, Thermo Fisher Scientific Inc, REF: 62248) to stain dead cells.

11.8 RT-qPCR

RNA was isolated using the NucleoSpin® RNA Kit (MACHEREY-NAGEL GmbH & Co. KG, REF: 740955). Subsequently the cDNA was synthesized using SuperScript™IV reverse transcriptase (Thermo Fisher Scientific Inc., REF: 18090200) with random hexamers (Metabion, Customized) and HSat3 specific primer pairs as described form *Valgardsdottir et al.*.11 All cDNA reaction were incubated with RNase H (New England Biolabs GmbH, REF: M0297L) to degrade remaining RNA templates. Each qPCR reaction contained 5 ng of cDNA, 300 nM gene specific qPCR primers and

was performed in 1x GoTaq® qPCR MasterMix (Promega GmbH, REF: A6002) at a final volume of 10 µL. Cycling parameters were chosen according to the manufacturer's protocol. qPCR was performed using QuantStudio5 (Thermo Fisher Scientific Inc.). For all samples a RT-minus control sample was measured to exclude DNA contamination. The cDNA and qPCR primer sequences are provided in **Table S 4**. Primers were ordered from Integrated DNA technologies, Inc. (IDT). [86]

11.9 Western Blotting

Lysis of cells was performed using Pierce lysis buffer (25 mM Tris–HCl pH 7.4, 150 mM NaCl, 1 mM EDTA, 1% NP-40, and 5% glycerol) containing a protease inhibitor cocktail (cOmplete™, Roche Diagnostics, REF: 11836170001). The proteins were separated by SDS-PAGE using a pre-cast polyacrylamide gel (mPAGE® 4-12% Bis-Tris, Merck KGaA, REF: MP41G15) with a MOPS SDS running buffer (Merck KGaA, REF: MPM0PS) at 200 V for 36 min. Transfer on nitrocellulose membrane was performed in mPAGE® transfer buffer (Merck KGaA, REF: MPTRB) at 70 V for 2 h and 4 °C. Afterwards the membrane was blocked in 5% skim milk-TBST for 1 h at RT. Incubation with primary antibodies (ANTI-FLAG® M2, Merck KGaA, REF: F1804, RRID: AB_262044; Anti-GFP-Antibody Clone 3F8.2, Merck KGaA MAB1083, RRID: AB_1587098, Anti-Histone H3 Clone D2B12 XP®, Cell Signaling Technology, Inc., REF: 4620S, RRID: AB_1904005) was performed at 4 °C over night. Subsequently the membrane was washed three times (10 min each with TBS-0.1% Tween (Tween® 20, Carl Roth GmbH + Co. KG, REF: 9127.1)(TBS-T)) and incubated with the horseradish peroxidase-conjugated secondary antibody (Anti mouse IgG, Cell Signaling Technology, Inc., REF: 7076, RRID: AB_330924; Anti rabbit IgG, Cell Signaling Technology, Inc., REF: 7074, RRID: AB_2099233) for 1 h at RT. Chemiluminescence was performed using Western Lightning Plus-ECL Substrate (Perkin Elmar LAS, REF: NEL104001EA). Used protein ladder was ordered from Thermo Fisher Scientific Inc. (REF: 26620). [86]

11.10 Fluorescence Microscopy

For fluorescence imaging the cells were transferred to the microscope at the indicated time point in a transparent bottom and tissue culture coated 6 Well plate (TPP Techno Plastic Products AG, Prod. No.: 92006). Imaging times were tried to be as short as possible to avoid irregularities in culture conditions. All fluorescence images of transiently transfected cell lines were taken by Keyence BZ-X800E/BZ-X810 (Keyence Deutschland GmbH) and the CFI Plan Apo λ4x objective (NA0.20 WD20.00 mm) (Keyence, 972030). Fluorescence filter sets were BZ-X filter GFP (Ex.:470/40, Em.:525/50) (Keyence, OP-87763) for green channel and BZ-X filter TRITC (Ex.:545/25, Em.:605/70) (Keyence, OP-87764) for the red channel.

All fluorescence pictures of cells in Biosafety Level 2 (S2) were taken by using the Nikon eclipse fluorescence microscope.[86]

11.11 Immune Fluorescence

Upon seeding 7,5x10^4 cells per well on coverslips in a 24-well plate, cells were cultured using standard cell culture conditions for 24 h. Living cells were incubated with 500 µL of membrane staining medium (5 µL CellBrite Orange Cytoplasmic Membrane Dye (Biotium Inc., #30022) and 4 mL of cell culture medium) per well for 30 minutes at 37 °C. Following incubation, cells were washed twice with prewarmed Dulbecco's phosphate-buffered saline (DPBS, Sigma-Aldrich, D8537-500ML). Subsequently, 500 µL of vehicle probe conjugate (VPC) staining solution was added to each well, and the plate was incubated for 45 minutes at 37 °C. A 3'-Cy5 labelled DNA probe was hybridized to the 4th and 5th generation RNA vehicle using the hybridization protocol. VPC assembly was controlled using PAGE. The staining concentration of VPC was 150 nM. After staining, cells were washed twice with DPBS. To fix the cells, 500 µL of 4% formaldehyde (Low MeOH, Carl Roth GmbH + Co. KG, Product No.: 6742.1) in DPBS was added per well, and the plate was incubated for 10 minutes at 4 °C. Cells were then washed once with DPBS. Permeabilization was performed by adding 500 µL of 0.1% Triton X-100 (Sigma-Aldrich, X100-500ML) in DPBS per well and incubating for 5 minutes at room temperature (RT). Blocking was carried out by incubating the cells for 1 hour at RT with 1% bovine serum albumin (BSA, PanReac AppliChem, Product No.: A6588 – 50 g) in 0.1% DPBS Tween-20 (Tween® 20, Carl Roth GmbH + Co. KG, REF: 9127.1). After blocking, the plate was transferred to a humidified chamber. Cells were incubated overnight at 4 °C with 50 µL per well of a 1:1000 dilution of Early Endosome Antigen 1 (EEA1) antibody (Abcam Limited, ab70521; mouse monoclonal, stock concentration 1 µg/µL,) prepared in 1% BSA and 0.1% DPBS Tween-20. The following day, samples were washed three times with DPBS. Secondary antibody staining was performed by incubating the cells for 1 hour at RT in the dark with 50 µL per well of a 1:1000 dilution of Alexa Fluor 488 anti-mouse antibody (A11029; goat polyclonal, stock concentration 2 µg/µL,) in 0.2% BSA DPBS. Samples were again washed three times with DPBS. For nuclear counterstaining, Hoechst 33342 (PromoKine, Cat: PK-CA707-4044) was diluted 1:5000 in DPBS and applied to the samples for 5 minutes at RT in the dark. After staining, cells were washed three times with DPBS. Finally, samples were mounted bottom up on microscope slides using ProLong™ Gold Antifade Mountant (Thermo Fisher Scientific Inc., P10144) for imaging. All DNA probes were ordered from Integrated DNA technologies, Inc. (IDT).

11.12 In Vitro Transcription

After *in silico* design of the aptamer siRNA conjugate the DNA template for the vehicle strand needed to be designed. The double stranded template needed to be designed containing a T7 promotor sequence upstream of the template sequence. An example is shown in **Table 3**:

Table 3 Guid for IVT dsDNA template design. *T7 promotor sequence is highlighted in yellow.*

T7 Promotor Primer (FW) and DNA Template (RV)	
(#) Template FW:	5’ –TAATACGACTCACTATAGGNNNNNNNNNNNNNNNNN– 3’
(#) Template RV:	3’ –ATTATGCTGAGTGATATCCNNNNNNNNNNNNNNNNN– 5’

The template strand is shown in 3’-5’ orientation. To order from IDT 5’-3’ orientation was essential. Upon receiving the DNA templates have been diluted to a final concertation of 1 µg/µL. For long time storage aliquots à 2 µL were stored at -20 °C. As the forward and reverse DNA strand of the template have been ordered separate they needed to be annealed for the IVT reaction. Therefore, the 2 µL forward template and 2 µL reverse template have been mixed in 10 µL H2O. The mixture was heated up to 98 °C for 3 minutes followed by a slow cool down to 4 °C with a ramp rate of -0,1 °C/s. Upon annealing the double stranded template was used for IVT reaction. The 4th generation vehicle strands were synthesized using the Apt-Get 2’F T7 transcription kit (Roboklon, E0905-02) for IVT reactions. Therefore, 14 µL of the annealed template have been mixed with 3 µL of a 2’-F pyrimidine base NTP-Mix (25 mM per NTP), 10 µL reaction buffer (5x), 2 µL Apt-Get 2’-F T7 RNA Polymerase and 1 µL Ribonuclease Inhibitor (Thermo Fisher Scientific Inc., R1158-10KU). The mixture has filled up with 20 µL RNase free H_2O to a total volume of 50 µL. The 5th generation vehicle strands were synthesized using T7 R&DNA Polymerase (Biosearch, D7P9205K) for IVT reactions. The kit did not provide a 2’-F pyrimidine base NTP-Mix. Therefore, the four nucleoside triphosphates ATP (Thermo Fisher Scientific Inc., R0441), 2’-F-CTP (Jena Bioscience GmbH, NU-1214S), GTP (Thermo Fisher Scientific Inc., R0461) and 2’-F-UTP (Jena Bioscience GmbH, NU-1215S) were mixed in an equal molar ratio. The resulting mix had an NTP concentration of 25 mM. To prepare the IVT reaction 14 µL of the annealed template have been mixed with 3 µL of a 2’-F pyrimidine base NTP-Mix (25 mM per NTP), 10 µL reaction buffer (5x), 1 µL T7 R&DNA Polymerase (50 U/µL) and 1 µL Ribonuclease Inhibitor (Thermo Fisher Scientific Inc., R1158-10KU). The mixture has filled up with 21 µL RNase free H_2O to a total volume of 50 µL. The IVT reaction was performed at 37 °C for 12 h as an over night reaction. Reaction mix was stored at 4 °C. Upon IVT reaction the mixture was incubated for 10 minutes at 37 °C with 5 µL of a 1:10 diluted rDNase (MACHEREY-NAGEL GmbH & Co. KG, REF: 740963). Clean-up of the IVT product was performed using Amersham™ MicroSpin G-25 columns (Cytiva, 27532501) according to the manufacturer’s manual. The RNA concentration of the eluted product was measured

using NanoDrop Lite Plus spectrophotometer (Thermo Fisher Scientific Inc.). Size and quality of the product was evaluated using native or urea polyacrylamide gel electrophoresis (PAGE). RNA was prepared immediately before the experiment and stored at 4 °C. Sequences of all templates can be found in **Table S 5**.

11.13 Hybridization of Aptamer-siRNA Conjugates

To prepare hybridisation of the vehicle strands with the payload strand, 300 pmol of each species were mixed in 75 µL of a hybridization buffer (5 mM MgCl2 in DPBS pH 7,4). To perform the annealing the mix was desaturated at 95 °C for 2 minutes. After denaturation the mix was cooled down to 55°C with a ramp rate of 0,1 °C/s. The mix was incubated 30 minutes at 55°C to increase hybridization probability. In a final step the mix was cooled down to 4 °C with a ramp rate of 0,1 °C/s. Annealed samples were stored at 4 °C till treatment. Annealing is always performed immediately before treatment of cell cultures.

11.14 Polyacrylamide Gel Electrophoresis

Before starting electrophoresis, the samples have been prepared as shown in **Table 4**. For denaturing Urea-PAGE the Gel Loading Buffer II (Thermo Fisher Scientific Inc., AM8546G) was used. For Native PAGE the Gel Loading Dye, Purple (New England Biolabs, B7024S) was used. Single stranded samples have been desaturated for 5 minutes at 95 °C prior to loading.

Table 4 Composition of PAGE samples, empty pockets and ladder.

Sample preparation for PAGE			
Name	**RNA or DNA**	**Gel Loading Buffer**	**Water**
Sample	10 µl (20 pMol)	10 µL	-
Empty	-	10 µL	10 µL
Ladder	4 µL	10 µL	6 µL

The Polyacrylamide gel electrophoresis (PAGE) was performed using urea (Novex™ TBE-Urea Gels, 15%, Thermo Fisher Scientific Inc., EC6885BOX) or native (Novex™ TBE Gels, 10%, Thermo Fisher Scientific Inc., EC62752BOX) precast gels depending on the experiment. Electrophoresis was performed using XCell Sure Lock™ Mini-Cell electrophoresis chamber (Thermo Fisher Scientific Inc.) and TBE Running buffer (Thermo Fisher Scientific Inc., LC6675). Before loading the samples, all pockets have been flushed twice using a syringe and TBE buffer. All pockets were loaded with 20 µL of prepared sample. Electrophoresis ran 60-80 minutes with 210 V at room temperature. Gels were stained using a SYBR™ Gold (Thermo Fisher Scientific Inc., S11494) containing solution (1:10.000 in MilliQ H_2O). Gels were Imaged using a ChemiDoc imaging system (Bio-Rad Laboratories, Inc.).

11.15 Prime Editing

The prime editing experiments were performed using a PE4 system as described by (SOURCE). To prepare prime editing pegRNAs were designed to insert a L41* stop codon mutation. The designed pegRNAs have been ordered from Integrated DNA Technologies Inc. (IDT) containing the provided Alt-R gRNA modification pattern (**Table S 1**). The prime editor coding plasmid pCMV-PEmax-P2A-hMLH1dn (**Figure S 11**) was a gift from David R. Liu (Addgene plasmid #174828; http://n2t.net/addgene:174828; RRID: Addgene_174828).[96,97] 1 µg of plasmid coding the prime editor and pegRNA (1,2 µg or 2,4 µg) were cotransfected using Lipofectamine 2000 as described previous. Cells were cultivated using standard conditions for 72h upon transfection. Prime editing was validated using Western blot and sanger sequencing of gDNA.

11.16 CRISPR Cas9

Initial of the CRISPR Cas9 experiment cells needed to be split 24 h before electroporation to keep cells in growth phase. To prepare cell suspension cells were harvested using trypsinization (Trypsin-EDTA Solution, Sigma-Aldrich, T4174-100ML) and were washed once with DPBS (DPBS, Sigma-Aldrich, D8537-500ML). Following up $6x10^6$ cells were transferred to a 15 mL Falcon tube and spined down with 500 rpm. Supernatant was discarded and cells were resuspended in 50 µL TexMACS Medium (Miltenyi Biotec, 130-097-196). Final volume of cell suspension was measured using reverse pipetting and filed up to a total volume of 150 µL. In parallel the ribonucleoprotein (RNP) mix for gene editing was prepared. Therefore 1,5 µL gRNA (100 µM), 2,4 µL of poly-L-glutamic acid (PGA, Sigma-Aldrich, P4761-25MG) in H_2O as well as 0,82 µL Alt-R™ S.p. Cas9 Nuclease V3 (10 µg/µL, 61µM, Integrated DNA technologies, Inc., 1081058) were mixed and incubated for 30 minutes at RT. For electroporation 50 µL of cell suspension and 4,7 µL of RNP mix are combined in an electroporation cuvette and electroporated following the ssEP SOP v12 of the ExPERT ATx electroporation device (MaxCyte). Upon electroporation cells are transferred to a pre warmed 96 well plate (50 µL DMEM per well) and recovered for 30 minutes. For expansion cells are transferred to a prewarmed 12 well plate containing 2 mL of DMEM per well. Cells were incubated and expanded at 37 °C in a humidified incubator with 5% CO_2. For flow cytometry and fluorescence associated cell sorting (FACS) cells were prepared as described previously. Cells were sorted into a 12 well plate containing 1 mL of DMEM per well. For determination of EGFR status of cell populations cells were incubated with an APC Fire labelled EGFR specific antibody (APC/Fire™ 750 anti-human EGFR Antibody (BioLegend,Inc., REF: 352925)). Isotype CTRLS were stained with an Isotype antibody (APC/Fire™ 750 Mouse IgG1, κ Isotype Ctrl Antibody (BioLegend,Inc., REF: 400195)). Sorted polyclonal populations were incubated and expanded at 37 °C in a humidified incubator with 5% CO_2.

11.17 In Silico Prediction Models

All in silico prediction tools were used as described on the respective website. Cofolding prediction was performed using ViennaRNA web server (VRWS), DINAMelt web server (DMWS) and AlphaFold 3.

11.18 Statistical Analysis

Statistical analyses were performed with the software package GraphPad Prism 9 (GraphPad Software, RRID:SCR_002798). The type of statistical analyses, parameters, and the number of replicates is indicated in the figure legends. For all tests, p value significance was defined as follows: not significant (n.s.) $p > 0.05$; * $p < 0.05$; ** $p < 0.01$; *** $p < 0.001$, **** $p < 0.0001$.

11.19 Figure Design

All schematic figures were created with BioRender.

List of Material

2'-F-CTP (Jena Bioscience GmbH, NU-1214S)

2'-F-UTP (Jena Bioscience GmbH, NU-1215S)

4% formaldehyde (Low MeOH, Carl Roth GmbH + Co. KG, Product No.: 6742.1)

4',6-Diamidino-2-Phenylindole (DAPI, Thermo Fisher Scientific Inc, REF: 62248)

5 mL Polystyrene Round-Bottom Tube (Falcon®, REF: 352054

6 well plate (TPP Techno Plastic Products AG, Prod. No.: 92006)

12 well plate (TPP Techno Plastic Products AG, Prod. No.: 92012)

24 well plate (TPP Techno Plastic Products AG, Prod. No.: 92024)

96 well flat bottom assay microplate (Falcon®, REF: 53296).

96 well plate (TPP Techno Plastic Products AG, Prod. No.: 92096)

APC/Fire™ 750 anti-human EGFR Antibody (BioLegend,Inc., REF: 352925)

APC/Fire™ 750 Mouse IgG1, κ Isotype Ctrl Antibody (BioLegend,Inc., REF: 400195)

Agarose (Carl Roth GmbH + Co. KG, Art. Nr. 3810.3)

Alt-R™ S.p. Cas9 Nuclease V3 (10 µg/µL, 61µM, Integrated DNA technologies, Inc., 1081058)

Amersham™ MicroSpin G-25 columns (Cytiva, 27532501)

ANTI-FLAG® M2 (Merck KGaA, REF: F1804, RRID: AB_262044)

Anti mouse IgG (Cell Signaling Technology, Inc., REF: 7076, RRID: AB_330924)

Anti rabbit IgG (Cell Signaling Technology, Inc., REF: 7074, RRID: AB_2099233)

Anti-GFP-Antibody Clone 3F8.2 (Merck KGaA, MAB1083, RRID: AB_1587098)

Anti-Histone H3 Clone D2B12 XP® (Cell Signaling Technology, Inc., REF: 4620S, RRID: AB_1904005)

Apt-Get 2'F T7 transcription kit (Roboklon, E0905-02)

ATP (Thermo Fisher Scientific Inc., R0441)

Bovine serum albumin (BSA, PanReac AppliChem, Product No.: A6588 – 50 g)

CellBrite Orange Cytoplasmic Membrane Dye (Biotium Inc., #30022)

CellTrics™ 30 µm cell strainer (Sysmex, REF: 04-0004-2326)

Dual-Glo® Luciferase assay system (Promega Corporation Prod. No.: E2920)

Dulbecco's Modified Eagles Medium (DMEM) (PAN-Biotech, P04-01500)

Dulbecco's Modified Eagles Medium GlutaMAX™ (DMEM GlutaMAX™, Thermo Scientific, 10569010)

Dulbecco's phosphate-buffered saline (DPBS, Sigma-Aldrich, D8537-500ML)

Early Endosome Antigen 1 (EEA1) antibody (Abcam Limited, ab70521; mouse monoclonal, stock concentration 1 µg/µL,)

Ethylene glycol-bis-(2-aminoethyl)-tetra-acetic-acid (EGTA, Carl Roth, Product No.: 3054.3)

Ethylenediamine tetra-acetic acid (EDTA, Carl Roth, Product No.:8040.2

Fetal calf serum (FCS) (Sigma-Aldrich, F7524)

G418 (400 µg/mL, InvivoGen, Prod. No.: ant-gn-1)

Gel Loading Buffer II (Thermo Fisher Scientific Inc., AM8546G)

Gel Loading Dye, Purple (New England Biolabs, B7024S)

GoTaq® qPCR MasterMix (Promega GmbH, REF: A6002)

GTP (Thermo Fisher Scientific Inc., R0461)

Hoechst 33342 (PromoKine, Cat: PK-CA707-4044)

L-Glutamine (Sigma-Aldrich, G7513-100ML)

Lipofectamine 2000 (Invitrogen Inc., #11668027)

Lipofectamine RNAiMAX (Invitrogen Inc., #13778030)

MOPS SDS running buffer (Merck KGaA, REF: MPM0PS)

Mycoalert Plus Mycoplasma detection kit (Lonza, LT07-710)

Novex™ TBE Gels, 10%, (Thermo Fisher Scientific Inc., EC62752BOX)

Novex™ TBE-Urea Gels, 15% (Thermo Fisher Scientific Inc., EC6885BOX)

NucleoBond® Plasmid, Xtra Midi EF Kit (MACHEREY NAGEL GmbH & Co. KG, REF 740420.50)

NucleoSpin® Gel and PCR Clean-up Kit (MACHEREY NAGEL GmbH & Co. KG, REF 740609.50)

NucleoSpin® Plasmid, Mini Kit (MACHEREY NAGEL GmbH & Co. KG, REF 740588.50)

NucleoSpin® RNA Kit (MACHEREY-NAGEL GmbH & Co. KG, REF: 740955)

Opti-Minimal Essential Medium (Opti-MEM™, Thermo Scientific, 31985070)

PEI MAX® (Polysciences, #24765(1), CAS Number: 49553-93-7

Penicillin and streptomycin (Sigma-Aldrich, P4333-100ML)

Phusion™ Hot Start Flex DNA Polymerase (New England Biolabs, M0535S)

Poly-L-glutamic acid (PGA, Sigma-Aldrich, P4761-25MG)

Polybrene (Merck, TR-1003-G)

ProLong™ Gold Antifade Mountant (Thermo Fisher Scientific Inc., P10144)

Protease inhibitor cocktail (cOmplete™, Roche Diagnostics, REF: 11836170001)

Protein ladder (Thermo Fisher Scientific Inc., REF: 26620)

Puromycin dihydrochloride (5 µg/mL, Sigma Aldrich, Prod. No.: P8833-25MG)

rDNase (MACHEREY-NAGEL GmbH & Co. KG, REF: 740963)

Ribonuclease Inhibitor (Thermo Fisher Scientific Inc., R1158-10KU)

RNase H (New England Biolabs GmbH, REF: M0297L)

SDS-PAGE using a precast polyacrylamide gel (mPAGE® 4-12% Bis-Tris, Merck KGaA, REF: MP41G15)

SuperScript™IV reverse transcriptase (Thermo Fisher Scientific Inc., REF: 18090200)

Syringe filter 0,45 µm pore size (SARSTEDT, 83.1826)

T7 R&DNA Polymerase (Biosearch, D7P9205K)

TBE Running buffer (Thermo Fisher Scientific Inc., LC6675)

TexMACS Medium (Miltenyi Biotec, 130-097-196)

Triton X-100 (Sigma-Aldrich, X100-500ML)

Trypsin (Trypsin-EDTA Solution, Sigma-Aldrich, T4174-100ML)

Tween (Tween® 20, Carl Roth GmbH + Co. KG, REF: 9127.1)

Western Lightning Plus-ECL Substrate (Perkin Elmar LAS, REF: NEL104001EA)

List of Abbreviations

2’-F: 2’-fluoro

2’-OMe: 2’-O-methyl

3’ UTR: 3’ untranslated region

ADCs: antibody drug conjugate

Ago2: argonaute 2

ARC: aptamer-RNA conjugate

ASGPR: asialoglycoprotein receptor

ASOs: antisense oligonucleotides

CI: confidence interval

cDNA: coding DNA

CL4: EGFR targeting aptamer

CNS: central nervous system

CO_2: carbon dioxide

Cy5: cyanine 5

DBCO: Dibenzocyclooctyne

DMEM: Dulbecco’s Modified Eagles Medium

DMEM GlutaMAX™: Dulbecco’s Modified Eagles Medium GlutaMAX™

DMWS: DINAMelt web server

DNA: deoxyribonucleic acid

DPBS: Dulbecco’s phosphate-buffered saline

DSBs: double-strand breaks

eGFP: green fluorescent protein

EFE: ensemble free energy

EGF: epidermal growth factor

EGFR: epidermal growth factor receptor

Em.: emmission

Ex.: excitation

FDA: Food and Drug Administration

FCS: fetal calf serum

FolamiRs: folate-conjugated siRNA

GalNAc: N-acetylgalactosamine

GNAs: glycol nucleic acids

GMP: good manufacturing practice

gRNA: guide RNA

H_2O: water

hluc+: *Firefly* luciferase

HSat3: satellite repeats III

HSat3 RNA: satellite III non-coding RNA

HSF1: heat shock factor 1

HSR: heat shock response

HYDRA: hybrid design and rapid assessment

ICH: International Council for Harmonizatio of Technical Requirements for Pharmaceuticals for Human Use

IDT: Integrated DNA technologies, Inc.

IEDDA: inverse electron demand Diels-Alder reaction

IVT: in vitro transcription

LNAs: locked nucleic acids

LNPs: lipid nanoparticles

LOD: limit of detection

LOQ: limit of quantification

lncRNAs: long non-coding RNAs

M-MLV: moloney murine leukemia virus

MCS: multiple cloning side

MFE: minimum free energy

mCherry: red fluorescent protein

MID: middle domain

miRNAs: microRNAs

MinE07: EGFR targeting aptamer

mRNA: messenger RNA

nSBs: nuclear stress bodies N-FLAG: N-terminal FLAG tagged

NMD: nonsense-mediated decay

NSCLC: non-small cell lung cancer

NTP: nucleoside triphosphate

PAGE: polyacrylamide gel electrophoresis

PBS: primer binding site

PCR: Polymerase chain reaction

PDX: patients derived xenograft

PE2: prime editor 2

PE4: prime editor 4

PEG4: polyethylene glycol

pegRNA: prime editing guide RNA

pre-miRNAs: precursor miRNAs

pri-miRNAs: primary miRNA transcripts

PS: phosphorothioate

PSR: proteotoxic stress response

RFU: relative fluorescence units

RISC: RNA-induced silencing complex

RLU: relative luminescence units

RNA: ribonucleic acid

RNAi: RNA interference

RNase H1: ribonucleases hybrid 1

RNP: ribonucleoprotein

RT: reverse transcriptase

RT-qPCR: quantitative reverse-transcription PCR

satDNA: satellite DNA

SDS: sodium dodecyl sulphate

SELEX: Systematic Evolution of Ligands by EXponential enrichment

siCo: siRNA control pool

siHSat3: HSat3 targeting siRNA

siRNAs: small interfering RNAs

SPAAC: strand promoted azide-alkine cycloaddition

SPS: solid-phase synthesis

sssDNA: shredded salmon sperm DNA

T2T: Telomere-to-Telomere

TBS: tris-buffered saline

TBS-T: TBS with Tween 20

TCO: trans-cyclooctene

TetOFF: tetracycline deducible system

TGF-α: transforming growth factor-α

TLRs: toll-like receptors

TOP2A: topoisomerase 2a

UTR: untranslated region

VPC: vehicle probe conjugate

VP: vinyl phosphonate

VRWS: ViennaRNA WebServe

WHO: world health organization

XPO5: exportin-5

Literature

1. Sung, H., Ferlay, J., Siegel, R.L., Laversanne, M., Soerjomataram, I., Jemal, A., and Bray, F. (2021). Global Cancer Statistics 2020: GLOBOCAN Estimates of Incidence and Mortality Worldwide for 36 Cancers in 185 Countries. CA Cancer J Clin *71*, 209-249. 10.3322/caac.21660.
2. Ferlay, J., Colombet, M., Soerjomataram, I., Parkin, D.M., Pineros, M., Znaor, A., and Bray, F. (2021). Cancer statistics for the year 2020: An overview. Int J Cancer. 10.1002/ijc.33588.
3. <WHO COVID-19 deaths _ WHO COVID-19 dashboard.pdf>. https://data.who.int/dashboards/covid19/deaths.
4. AUSTRIA, S. <Population Statistics Austria 2025.pdf>. https://www.statistik.at/statistiken/bevoelkerung-und-soziales/bevoelkerung/bevoelkerungsstand/bevoelkerung-zu-jahres-/-quartalsanfang.
5. <WHO-estimated-deaths-from-2022-to-2050-both-sexes-age-0-85-all-cancers.pdf>. https://gco.iarc.who.int/tomorrow/en/dataviz/bubbles?multiple_populations=1&sexes=0&populations=900&types=1&age_end=17&age_start=0&group_populations=1&years=2050.
6. <WHO-estimated-new-cases-from-2022-to-2050-both-sexes-age-0-85-all-cancers.pdf>. https://gco.iarc.who.int/tomorrow/en/dataviz/bubbles?multiple_populations=1&sexes=0&populations=900&types=0&age_end=17&age_start=0&group_populations=1&years=2050.
7. <Population Statistics Netherlands 2025.pdf>. https://opendata.cbs.nl/statline/#/CBS/en/dataset/83474ENG/table?ts=1619463313751.
8. Chen, S., Cao, Z., Prettner, K., Kuhn, M., Yang, J., Jiao, L., Wang, Z., Li, W., Geldsetzer, P., Barnighausen, T., et al. (2023). Estimates and Projections of the Global Economic Cost of 29 Cancers in 204 Countries and Territories From 2020 to 2050. JAMA Oncol *9*, 465-472. 10.1001/jamaoncol.2022.7826.
9. F., K. (07.03.2023). Cancer will cost the world $25 trillion over next 30 years. https://www.nature.com/articles/d41586-023-00634-9.
10. Hanahan, D., and Weinberg, R.A. (2011). Hallmarks of cancer: the next generation. Cell *144*, 646-674. 10.1016/j.cell.2011.02.013.
11. Hendrik Lehnert , H.K., Ina Kirmes , Ralf Dahm (2018). Epigenetik – Grundlagen und klinische Bedeutung; Aus der Vortragsreihe der Medizinischen Gesellschaft Mainz e.V. Springer Berlin, Heidelberg.
12. Darwiche, N. (2020). Epigenetic mechanisms and the hallmarks of cancer: an intimate affair. Am J Cancer Res *10*, 1954-1978.
13. Virani, S., Colacino, J.A., Kim, J.H., and Rozek, L.S. (2012). Cancer epigenetics: a brief review. ILAR J *53*, 359-369. 10.1093/ilar.53.3-4.359.
14. Latest advances in treatment for non-small cell lung cancer. (2024). https://www.thelancet.com/pb-assets/Lancet/infographics/nsclc/image.pdf.
15. Zhou, C., Wu, Y.L., Chen, G., Feng, J., Liu, X.Q., Wang, C., Zhang, S., Wang, J., Zhou, S., Ren, S., et al. (2011). Erlotinib versus chemotherapy as first-line treatment for patients with advanced EGFR mutation-positive non-small-cell lung cancer (OPTIMAL, CTONG-0802): a multicentre, open-label, randomised, phase 3 study. Lancet Oncol *12*, 735-742. 10.1016/S1470-2045(11)70184-X.
16. Min, H.Y., and Lee, H.Y. (2021). Mechanisms of resistance to chemotherapy in non-small cell lung cancer. Arch Pharm Res *44*, 146-164. 10.1007/s12272-021-01312-y.
17. <Lung Cancer Survival Rates _ 5-Year Survival Rates for Lung Cancer _ American Cancer Society.pdf>. https://www.cancer.org/cancer/types/lung-cancer/detection-diagnosis-staging/survival-rates.html.

18. Zhang, Q., Yang, J., Bai, J., and Ren, J. (2018). Reverse of non-small cell lung cancer drug resistance induced by cancer-associated fibroblasts via a paracrine pathway. Cancer Sci *109*, 944-955. 10.1111/cas.13520.
19. Lu, Q., Hu, Y., Sun, J., Cheng, Y., Cheung, K.H., and Zhao, H. (2015). A statistical framework to predict functional non-coding regions in the human genome through integrated analysis of annotation data. Sci Rep *5*, 10576. 10.1038/srep10576.
20. Lu, S., Zhang, J., Lian, X., Sun, L., Meng, K., Chen, Y., Sun, Z., Yin, X., Li, Y., Zhao, J., et al. (2019). A hidden human proteome encoded by 'non-coding' genes. Nucleic Acids Res *47*, 8111-8125. 10.1093/nar/gkz646.
21. Liao, X., Hu, K., Salhi, A., Zou, Y., Wang, J., and Gao, X. (2022). msRepDB: a comprehensive repetitive sequence database of over 80 000 species. Nucleic Acids Res *50*, D236-D245. 10.1093/nar/gkab1089.
22. Richard, G.F., Kerrest, A., and Dujon, B. (2008). Comparative genomics and molecular dynamics of DNA repeats in eukaryotes. Microbiol Mol Biol Rev *72*, 686-727. 10.1128/MMBR.00011-08.
23. Ganten, D.R., K. (2005). Human Repetetive DNA. Enceclopedic Reference of Genomics and Proteomics in Molecular Medicine. Springer.
24. repetitive DNA. https://www.spektrum.de/lexikon/biologie/repetitive-dna/56264.
25. Liao, X., Zhu, W., Zhou, J., Li, H., Xu, X., Zhang, B., and Gao, X. (2023). Repetitive DNA sequence detection and its role in the human genome. Commun Biol *6*, 954. 10.1038/s42003-023-05322-y.
26. Altemose, N. (2022). A classical revival: Human satellite DNAs enter the genomics era. Semin Cell Dev Biol *128*, 2-14. 10.1016/j.semcdb.2022.04.012.
27. Nurk, S., Koren, S., Rhie, A., Rautiainen, M., Bzikadze, A.V., Mikheenko, A., Vollger, M.R., Altemose, N., Uralsky, L., Gershman, A., et al. (2022). The complete sequence of a human genome. Science *376*, 44-53. 10.1126/science.abj6987.
28. Satelliten-DNA. https://www.spektrum.de/lexikon/biologie/satelliten-dna/58635.
29. Charlesworth, B., Sniegowski, P., and Stephan, W. (1994). The evolutionary dynamics of repetitive DNA in eukaryotes. Nature *371*, 215-220. 10.1038/371215a0.
30. Schueler, M.G., Higgins, A.W., Rudd, M.K., Gustashaw, K., and Willard, H.F. (2001). Genomic and genetic definition of a functional human centromere. Science *294*, 109-115. 10.1126/science.1065042.
31. Prosser, J., Frommer, M., Paul, C., and Vincent, P.C. (1986). Sequence relationships of three human satellite DNAs. J Mol Biol *187*, 145-155. 10.1016/0022-2836(86)90224-x.
32. Plohl, M., Mestrovic, N., and Mravinac, B. (2012). Satellite DNA evolution. Genome Dyn *7*, 126-152. 10.1159/000337122.
33. Plohl, M., Mestrovic, N., and Mravinac, B. (2014). Centromere identity from the DNA point of view. Chromosoma *123*, 313-325. 10.1007/s00412-014-0462-0.
34. Pezer, Z., Brajkovic, J., Feliciello, I., and Ugarkovc, D. (2012). Satellite DNA-mediated effects on genome regulation. Genome Dyn *7*, 153-169. 10.1159/000337116.
35. Grenfell, A.W., Strzelecka, M., and Heald, R. (2017). Transcription brings the complex(ity) to the centromere. Cell Cycle *16*, 235-236. 10.1080/15384101.2016.1242962.
36. Valgardsdottir, R., Chiodi, I., Giordano, M., Rossi, A., Bazzini, S., Ghigna, C., Riva, S., and Biamonti, G. (2008). Transcription of Satellite III non-coding RNAs is a general stress response in human cells. Nucleic Acids Res *36*, 423-434. 10.1093/nar/gkm1056.
37. Zhang, H., Shao, S., Zeng, Y., Wang, X., Qin, Y., Ren, Q., Xiang, S., Wang, Y., Xiao, J., and Sun, Y. (2022). Reversible phase separation of HSF1 is required for an acute transcriptional response during heat shock. Nat Cell Biol *24*, 340-352. 10.1038/s41556-022-00846-7.
38. Biamonti, G., and Vourc'h, C. (2010). Nuclear stress bodies. Cold Spring Harb Perspect Biol *2*, a000695. 10.1101/cshperspect.a000695.

39. Erhardt, S., and Stoecklin, G. (2020). The heat's on: nuclear stress bodies signal intron retention. EMBO J *39*, e104154. 10.15252/embj.2019104154.
40. Ninomiya, K., Adachi, S., Natsume, T., Iwakiri, J., Terai, G., Asai, K., and Hirose, T. (2020). LncRNA-dependent nuclear stress bodies promote intron retention through SR protein phosphorylation. EMBO J *39*, e102729. 10.15252/embj.2019102729.
41. Hussong, M., Kaehler, C., Kerick, M., Grimm, C., Franz, A., Timmermann, B., Welzel, F., Isensee, J., Hucho, T., Krobitsch, S., and Schweiger, M.R. (2017). The bromodomain protein BRD4 regulates splicing during heat shock. Nucleic Acids Res *45*, 382-394. 10.1093/nar/gkw729.
42. Dai, C., Dai, S., and Cao, J. (2012). Proteotoxic stress of cancer: implication of the heat-shock response in oncogenesis. J Cell Physiol *227*, 2982-2987. 10.1002/jcp.24017.
43. Ehrlich, M. (2009). DNA hypomethylation in cancer cells. Epigenomics *1*, 239-259. 10.2217/epi.09.33.
44. Kanne, J., Hussong, M., Isensee, J., Munoz-Lopez, A., Wolffgramm, J., Hess, F., Grimm, C., Bessonov, S., Meder, L., Wang, J., et al. (2021). Pericentromeric Satellite III transcripts induce etoposide resistance. Cell Death Dis *12*, 530. 10.1038/s41419-021-03810-9.
45. Lee, Y., Kim, M., Han, J., Yeom, K.H., Lee, S., Baek, S.H., and Kim, V.N. (2004). MicroRNA genes are transcribed by RNA polymerase II. EMBO J *23*, 4051-4060. 10.1038/sj.emboj.7600385.
46. Denli, A.M., Tops, B.B., Plasterk, R.H., Ketting, R.F., and Hannon, G.J. (2004). Processing of primary microRNAs by the Microprocessor complex. Nature *432*, 231-235. 10.1038/nature03049.
47. Yi, R., Qin, Y., Macara, I.G., and Cullen, B.R. (2003). Exportin-5 mediates the nuclear export of pre-microRNAs and short hairpin RNAs. Genes Dev *17*, 3011-3016. 10.1101/gad.1158803.
48. Bernstein, E., Caudy, A.A., Hammond, S.M., and Hannon, G.J. (2001). Role for a bidentate ribonuclease in the initiation step of RNA interference. Nature *409*, 363-366. 10.1038/35053110.
49. Bartel, D.P. (2009). MicroRNAs: target recognition and regulatory functions. Cell *136*, 215-233. 10.1016/j.cell.2009.01.002.
50. Pasquinelli, A.E. (2012). MicroRNAs and their targets: recognition, regulation and an emerging reciprocal relationship. Nat Rev Genet *13*, 271-282. 10.1038/nrg3162.
51. Fabian, M.R., Sonenberg, N., and Filipowicz, W. (2010). Regulation of mRNA translation and stability by microRNAs. Annu Rev Biochem *79*, 351-379. 10.1146/annurev-biochem-060308-103103.
52. He, L., and Hannon, G.J. (2004). MicroRNAs: small RNAs with a big role in gene regulation. Nat Rev Genet *5*, 522-531. 10.1038/nrg1379.
53. Crooke, S.T., Witztum, J.L., Bennett, C.F., and Baker, B.F. (2018). RNA-Targeted Therapeutics. Cell Metab *27*, 714-739. 10.1016/j.cmet.2018.03.004.
54. Bennett, C.F., Krainer, A.R., and Cleveland, D.W. (2019). Antisense Oligonucleotide Therapies for Neurodegenerative Diseases. Annu Rev Neurosci *42*, 385-406. 10.1146/annurev-neuro-070918-050501.
55. Lin, S., and Gregory, R.I. (2015). MicroRNA biogenesis pathways in cancer. Nat Rev Cancer *15*, 321-333. 10.1038/nrc3932.
56. Testa, C.M. (2021). Antisense Oligonucleotide Therapeutics for Neurodegenerative Disorders. Current Geriatrics Reports *11*, 19-32. 10.1007/s13670-020-00341-7.
57. Collotta, D., Bertocchi, I., Chiapello, E., and Collino, M. (2023). Antisense oligonucleotides: a novel Frontier in pharmacological strategy. Front Pharmacol *14*, 1304342. 10.3389/fphar.2023.1304342.
58. Bailey, J.K., Shen, W., Liang, X.H., and Crooke, S.T. (2017). Nucleic acid binding proteins affect the subcellular distribution of phosphorothioate antisense oligonucleotides. Nucleic Acids Res *45*, 10649-10671. 10.1093/nar/gkx709.

59. Q2 2025 Quartaly Data Report. (Q2 2025). Amertican Society of Gene and Cell Therapy (ASGCT). https://www.asgct.org/global/documents/cl-080125report-asgct-citeline-q2-2025-jn7765-fina.aspx.
60. Dowdy, S.F. (2023). Endosomal escape of RNA therapeutics: How do we solve this rate-limiting problem? RNA *29*, 396-401. 10.1261/rna.079507.122.
61. He, C., Migawa, M.T., Chen, K., Weston, T.A., Tanowitz, M., Song, W., Guagliardo, P., Iyer, K.S., Bennett, C.F., Fong, L.G., et al. (2021). High-resolution visualization and quantification of nucleic acid-based therapeutics in cells and tissues using Nanoscale secondary ion mass spectrometry (NanoSIMS). Nucleic Acids Res *49*, 1-14. 10.1093/nar/gkaa1112.
62. Tang, Q., and Khvorova, A. (2024). RNAi-based drug design: considerations and future directions. Nat Rev Drug Discov *23*, 341-364. 10.1038/s41573-024-00912-9.
63. An, G. (2024). Pharmacokinetics and Pharmacodynamics of GalNAc-Conjugated siRNAs. J Clin Pharmacol *64*, 45-57. 10.1002/jcph.2337.
64. Brown, C.R., Gupta, S., Qin, J., Racie, T., He, G., Lentini, S., Malone, R., Yu, M., Matsuda, S., Shulga-Morskaya, S., et al. (2020). Investigating the pharmacodynamic durability of GalNAc-siRNA conjugates. Nucleic Acids Res *48*, 11827-11844. 10.1093/nar/gkaa670.
65. O'Reilly, D., Belgrad, J., Ferguson, C., Summers, A., Sapp, E., McHugh, C., Mathews, E., Boudi, A., Buchwald, J., Ly, S., et al. (2023). Di-valent siRNA-mediated silencing of MSH3 blocks somatic repeat expansion in mouse models of Huntington's disease. Mol Ther *31*, 1661-1674. 10.1016/j.ymthe.2023.05.006.
66. Frank, F., Sonenberg, N., and Nagar, B. (2010). Structural basis for 5'-nucleotide base-specific recognition of guide RNA by human AGO2. Nature *465*, 818-822. 10.1038/nature09039.
67. Prakash, T.P., Lima, W.F., Murray, H.M., Li, W., Kinberger, G.A., Chappell, A.E., Gaus, H., Seth, P.P., Bhat, B., Crooke, S.T., and Swayze, E.E. (2017). Identification of metabolically stable 5′-phosphate analogs that support single-stranded siRNA activity. Nucleic Acids Res *45*, 6994. 10.1093/nar/gkx381.
68. Khvorova, A., and Watts, J.K. (2017). The chemical evolution of oligonucleotide therapies of clinical utility. Nat Biotechnol *35*, 238-248. 10.1038/nbt.3765.
69. Flemmich, L., Bereiter, R., and Micura, R. (2024). Chemical Synthesis of Modified RNA. Angew Chem Int Ed Engl *63*, e202403063. 10.1002/anie.202403063.
70. Zhang, D. (2022). Oligonucleotides: Current Thinking and Analytical Challenges Identified in the NusinersenPSG Development. SBIA 2022: Advancing Generic Drug Development: Translating Science to Approval. U.S. FDA.
71. FDA, U.S. (2022). Draft Guidance of Patisiran Sodium.
72. Xu, L., Li, C., Liao, R., Xiao, Q., Wang, X., Zhao, Z., Zhang, W., Ding, X., Cao, Y., Cai, L., et al. (2025). From Sequence to System: Enhancing IVT mRNA Vaccine Effectiveness through Cutting-Edge Technologies. Mol Pharm *22*, 81-102. 10.1021/acs.molpharmaceut.4c00863.
73. Padilla, R., and Sousa, R. (1999). Efficient synthesis of nucleic acids heavily modified with non-canonical ribose 2'-groups using a mutant T7 RNA polymerase (RNAP). Nucleic Acids Research *27*, 1561-1563. 10.1093/nar/27.6.1561.
74. Yarden, Y., and Sliwkowski, M.X. (2001). Untangling the ErbB signalling network. Nat Rev Mol Cell Biol *2*, 127-137. 10.1038/35052073.
75. Liu, H., Zhang, B., and Sun, Z.A.-O. Spectrum of EGFR aberrations and potential clinical implications: insights from integrative pan-cancer analysis.
76. Genta, I., Chiesa, E., Colzani, B., Modena, T., Conti, B., and Dorati, R. (2017). GE11 Peptide as an Active Targeting Agent in Antitumor Therapy: A Minireview. Pharmaceutics *10*. 10.3390/pharmaceutics10010002.
77. Prabhakar, C.N. (2015). Epidermal growth factor receptor in non-small cell lung cancer. Transl Lung Cancer Res *4*, 110-118. 10.3978/j.issn.2218-6751.2015.01.01.

78. Germer, K., Leonard, M., and Zhang, X. (2013). RNA aptamers and their therapeutic and diagnostic applications. Int J Biochem Mol Biol *4*, 27-40.
79. Esposito, C.L., Passaro, D., Longobardo, I., Condorelli, G., Marotta, P., Affuso, A., de Franciscis, V., and Cerchia, L. (2011). A neutralizing RNA aptamer against EGFR causes selective apoptotic cell death. PLoS One *6*, e24071. 10.1371/journal.pone.0024071.
80. Thomas, B.J., Guldenpfennig, C., Guan, Y., Winkler, C., Beecher, M., Beedy, M., Berendzen, A.F., Ma, L., Daniels, M.A., Burke, D.H., and Porciani, D. (2023). Targeting lung cancer with clinically relevant EGFR mutations using anti-EGFR RNA aptamer. Mol Ther Nucleic Acids *34*, 102046. 10.1016/j.omtn.2023.102046.
81. Kojima, S.-I., and Borisy, G.G. (2014). An image-based, dual fluorescence reporter assay to evaluate the efficacy of shRNA for gene silencing at the single-cell level. F1000Research *3*, 60. 10.12688/f1000research.3-60.v1.
82. Schallmayer, E., and Merk, D. (2023). A Fluorescence-Based Reporter Gene Assay to Characterize Nuclear Receptor Modulators. In (Springer US), pp. 125-135. 10.1007/978-1-0716-3397-7_9.
83. Fu, C., Donovan, W.P., Shikapwashya-Hasser, O., Ye, X., and Cole, R.H. (2014). Hot Fusion: An Efficient Method to Clone Multiple DNA Fragments as Well as Inverted Repeats without Ligase. PLoS ONE *9*, e115318. 10.1371/journal.pone.0115318.
84. Cormack, B.P., Valdivia, R.H., and Falkow, S. (1996). FACS-optimized mutants of the green fluorescent protein (GFP). Gene *173*, 33-38. https://doi.org/10.1016/0378-1119(95)00685-0.
85. Shaner, N.C., Campbell, R.E., Steinbach, P.A., Giepmans, B.N.G., Palmer, A.E., and Tsien, R.Y. (2004). Improved monomeric red, orange and yellow fluorescent proteins derived from Discosoma sp. red fluorescent protein. Nature Biotechnology *22*, 1567-1572. 10.1038/nbt1037.
86. Hess, F., Odenthal, M., Wasserburger-Zichel, E., Grimm, C., and Schweiger, M.R. (2025). A dual fluorescence-based reporter assay for real-time determination of siRNA- and antisense oligonucleotide-mediated knockdown. Mol Ther Nucleic Acids *36*, 102631. 10.1016/j.omtn.2025.102631.
87. Zhang, Y. (2013). RNA-induced Silencing Complex (RISC). In Encyclopedia of Systems Biology, W. Dubitzky, O. Wolkenhauer, K.-H. Cho, and H. Yokota, eds. (Springer New York), pp. 1876-1876. 10.1007/978-1-4419-9863-7_329.
88. Gregory, R.I., Chendrimada, T.P., Cooch, N., and Shiekhattar, R. (2005). Human RISC Couples MicroRNA Biogenesis and Posttranscriptional Gene Silencing. Cell *123*, 631-640. 10.1016/j.cell.2005.10.022.
89. Grunweller, A. (2003). Comparison of different antisense strategies in mammalian cells using locked nucleic acids, 2'-O-methyl RNA, phosphorothioates and small interfering RNA. Nucleic Acids Research *31*, 3185-3193. 10.1093/nar/gkg409.
90. Vickers, T.A., Koo, S., Bennett, C.F., Crooke, S.T., Dean, N.M., and Baker, B.F. (2003). Efficient Reduction of Target RNAs by Small Interfering RNA and RNase H-dependent Antisense Agents: A COMPARATIVE ANALYSIS*. Journal of Biological Chemistry *278*, 7108-7118. https://doi.org/10.1074/jbc.M210326200.
91. Walder, R.Y., and Walder, J.A. (1988). Role of RNase H in hybrid-arrested translation by antisense oligonucleotides. Proceedings of the National Academy of Sciences *85*, 5011-5015. 10.1073/pnas.85.14.5011.
92. Wu, H., Lima, W.F., Zhang, H., Fan, A., Sun, H., and Crooke, S.T. (2004). Determination of the Role of the Human RNase H1 in the Pharmacology of DNA-like Antisense Drugs*. Journal of Biological Chemistry *279*, 17181-17189. https://doi.org/10.1074/jbc.M311683200.
93. (ICH), I.C.o.H. (14 December 2023). ICH Q2(R2) Guideline on validation of analytical procedures. In E.M.A. (EMA), ed.
94. Brunetti B, D.E. (2015). About Estimating the Limit of Detection by the Signal to Noise Approach. Pharmaceutica Analytica Acta *06*. 10.4172/2153-2435.1000355.

95. Murray, J.B., Harrison, P.T., and Scholefield, J. (2025). Prime editing: therapeutic advances and mechanistic insights. Gene Ther *32*, 83-92. 10.1038/s41434-024-00499-1.
96. Doman, J.L., Sousa, A.A., Randolph, P.B., Chen, P.J., and Liu, D.R. (2022). Designing and executing prime editing experiments in mammalian cells. Nat Protoc *17*, 2431-2468. 10.1038/s41596-022-00724-4.
97. Chen, P.J., Hussmann, J.A., Yan, J., Knipping, F., Ravisankar, P., Chen, P.F., Chen, C., Nelson, J.W., Newby, G.A., Sahin, M., et al. (2021). Enhanced prime editing systems by manipulating cellular determinants of editing outcomes. Cell *184*, 5635-5652 e5629. 10.1016/j.cell.2021.09.018.
98. Neves, R.P.P., Fernandes, P.A., and Ramos, M.J. (2017). Mechanistic insights on the reduction of glutathione disulfide by protein disulfide isomerase. Proc Natl Acad Sci U S A *114*, E4724-E4733. 10.1073/pnas.1618985114.
99. Sorkin, A., and Duex, J.E. (2010). Quantitative analysis of endocytosis and turnover of epidermal growth factor (EGF) and EGF receptor. Curr Protoc Cell Biol *Chapter 15*, Unit 15 14. 10.1002/0471143030.cb1514s46.
100. Laurent, Q., Martinent, R., Lim, B., Pham, A.T., Kato, T., Lopez-Andarias, J., Sakai, N., and Matile, S. (2021). Thiol-Mediated Uptake. JACS Au *1*, 710-728. 10.1021/jacsau.1c00128.
101. Bishani, A., and Chernolovskaya, E.L. (2021). Activation of Innate Immunity by Therapeutic Nucleic Acids. Int J Mol Sci *22*. 10.3390/ijms222413360.
102. Yoon, S., Huang, K.W., Andrikakou, P., Vasconcelos, D., Swiderski, P., Reebye, V., Sodergren, M., Habib, N., and Rossi, J.J. (2019). Targeted Delivery of C/EBPalpha-saRNA by RNA Aptamers Shows Anti-tumor Effects in a Mouse Model of Advanced PDAC. Mol Ther Nucleic Acids *18*, 142-154. 10.1016/j.omtn.2019.08.017.
103. Sousa, R., and Padilla, R. (1995). A mutant T7 RNA polymerase as a DNA polymerase. EMBO J *14*, 4609-4621. 10.1002/j.1460-2075.1995.tb00140.x.
104. Bege, M., Ghanem Kattoub, R., and Borbas, A. (2025). The 20th Anniversary of Pegaptanib (MacugenTM), the First Approved Aptamer Medicine: History, Recent Advances and Future Prospects of Aptamers in Therapy. Pharmaceutics *17*. 10.3390/pharmaceutics17030394.
105. Kelly, L., Maier, K.E., Yan, A., and Levy, M. (2021). A comparative analysis of cell surface targeting aptamers. Nat Commun *12*, 6275. 10.1038/s41467-021-26463-w.
106. Gruber, A.R., Lorenz, R., Bernhart, S.H., Neubock, R., and Hofacker, I.L. (2008). The Vienna RNA websuite. Nucleic Acids Res *36*, W70-74. 10.1093/nar/gkn188.
107. Bernhart, S.H., Tafer, H., Muckstein, U., Flamm, C., Stadler, P.F., and Hofacker, I.L. (2006). Partition function and base pairing probabilities of RNA heterodimers. Algorithms Mol Biol *1*, 3. 10.1186/1748-7188-1-3.
108. Markham, N.R., and Zuker, M. (2005). DINAMelt web server for nucleic acid melting prediction. Nucleic Acids Res *33*, W577-581. 10.1093/nar/gki591.
109. Abramson, J., Adler, J., Dunger, J., Evans, R., Green, T., Pritzel, A., Ronneberger, O., Willmore, L., Ballard, A.J., Bambrick, J., et al. (2024). Accurate structure prediction of biomolecular interactions with AlphaFold 3. Nature *630*, 493-500. 10.1038/s41586-024-07487-w.
110. Malysheva, D.O., Dymova, M.A., and Richter, V.A. (2024). Analyzing aptamer structure and interactions: in silico modelling and instrumental methods. Biophys Rev *16*, 685-700. 10.1007/s12551-024-01252-z.
111. Zahedi, A.M., Pirouzbakht, M., Zanganeh, S., and Afgar, A. (2025). Aptamer-Drug Conjugates (ApDCs): Transformative approaches in targeted cancer therapy and precision oncology. Int J Pharm *681*, 125902. 10.1016/j.ijpharm.2025.125902.
112. Sari, Y., Sousa Rosa, S., Jeffries, J., and Marques, M.P.C. (2024). Comprehensive evaluation of T7 promoter for enhanced yield and quality in mRNA production. Sci Rep *14*, 9655. 10.1038/s41598-024-59978-5.

113. Nasiri, F., Muhammadnejad, S., and Rahbarizadeh, F. (2023). Effects of polybrene and retronectin as transduction enhancers on the development and phenotypic characteristics of VHH-based CD19-redirected CAR T cells: a comparative investigation. Clin Exp Med *23*, 2535-2549. 10.1007/s10238-022-00928-8.
114. Budunova, I.V., and Mittelman, L.A. (1992). The effect of K+/H+ antiporter nigericin on gap junction permeability. Cell Biol Toxicol *8*, 63-73. 10.1007/BF00119295.
115. Lonn, P., Kacsinta, A.D., Cui, X.S., Hamil, A.S., Kaulich, M., Gogoi, K., and Dowdy, S.F. (2016). Enhancing Endosomal Escape for Intracellular Delivery of Macromolecular Biologic Therapeutics. Sci Rep *6*, 32301. 10.1038/srep32301.
116. Orellana, E.A., Abdelaal, A.M., Rangasamy, L., Tenneti, S., Myoung, S., Low, P.S., and Kasinski, A.L. (2019). Enhancing MicroRNA Activity through Increased Endosomal Release Mediated by Nigericin. Mol Ther Nucleic Acids *16*, 505-518. 10.1016/j.omtn.2019.04.003.
117. Sano, M., Sierant, M., Miyagishi, M., Nakanishi, M., Takagi, Y., and Sutou, S. (2008). Effect of asymmetric terminal structures of short RNA duplexes on the RNA interference activity and strand selection. Nucleic Acids Res *36*, 5812-5821. 10.1093/nar/gkn584.
118. Valgardsdottir, R., Chiodi, I., Giordano, M., Rossi, A., Bazzini, S., Ghigna, C., Riva, S., and Biamonti, G. (2008). Transcription of Satellite III non-coding RNAs is a general stress response in human cells. Nucleic Acids Research *36*, 423-434. 10.1093/nar/gkm1056.
119. Layzer, J.M., McCaffrey, A.P., Tanner, A.K., Huang, Z., Kay, M.A., and Sullenger, B.A. (2004). In vivo activity of nuclease-resistant siRNAs. RNA *10*, 766-771. 10.1261/rna.5239604.
120. Czauderna, F., Fechtner, M., Dames, S., Aygun, H., Klippel, A., Pronk, G.J., Giese, K., and Kaufmann, J. (2003). Structural variations and stabilising modifications of synthetic siRNAs in mammalian cells. Nucleic Acids Res *31*, 2705-2716. 10.1093/nar/gkg393.

Figure Index

Table Index

APPENDIX

Appendix

Attachments

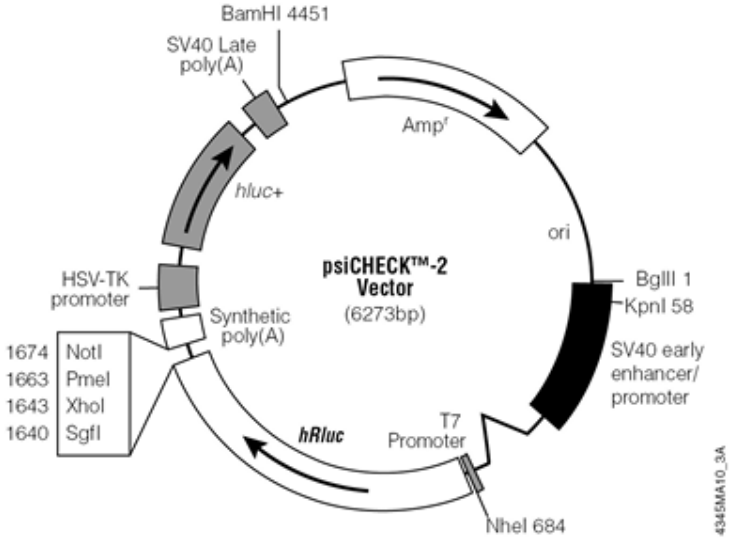

Figure S 1 Plasmid map of psiCheck™-2 empty vector. *Eukaryotic expression plasmid coding a Renilla and a Firefly luciferase. The 3'UTR of the hRluc contains a multiple cloning side (MCS) to insert a RNAi target motif.*

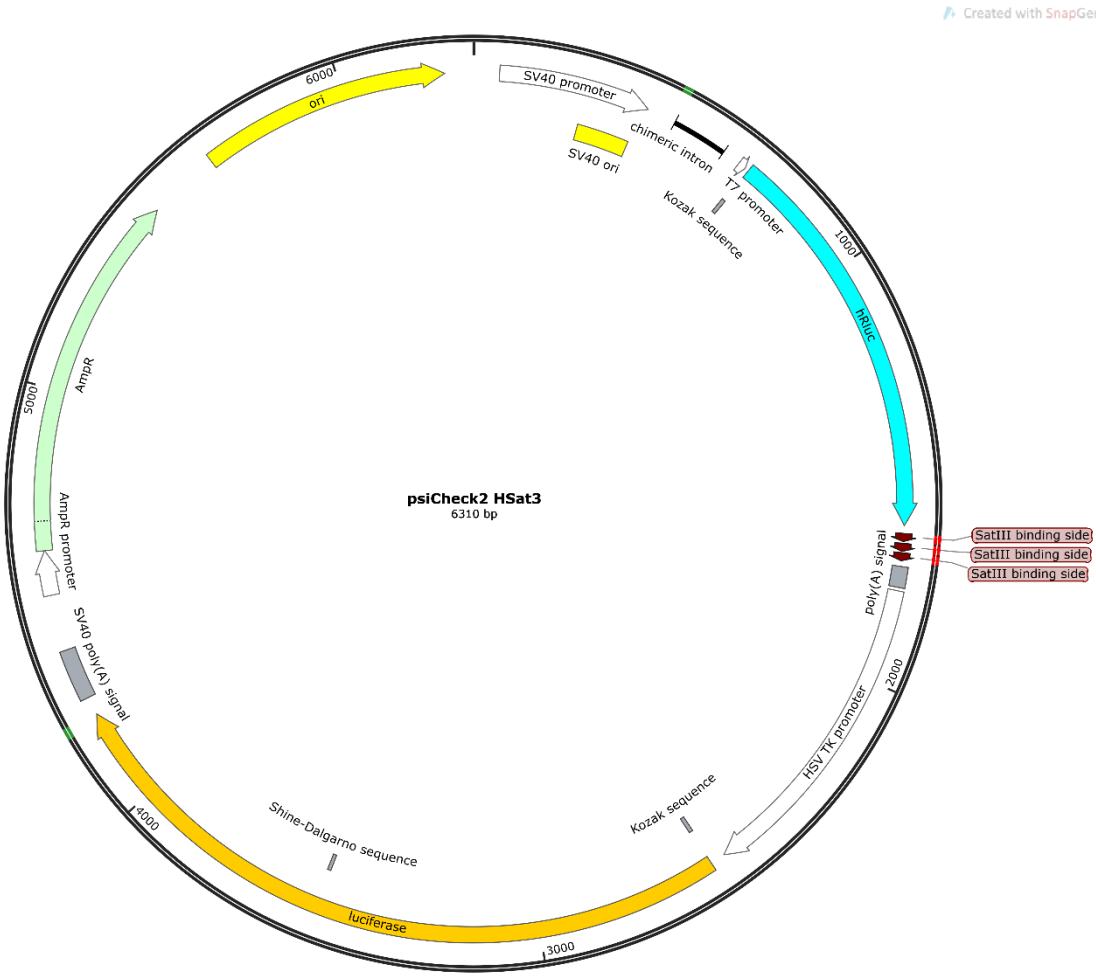

Figure S 2 Plasmid map of psiCheck™-2 HSat3. *Eukaryotic expression plasmid coding a Renilla and a Firefly luciferase. The 3'UTR of the hRluc contains three repeat of a HSat3 Sequence as a RNAi target motif.*

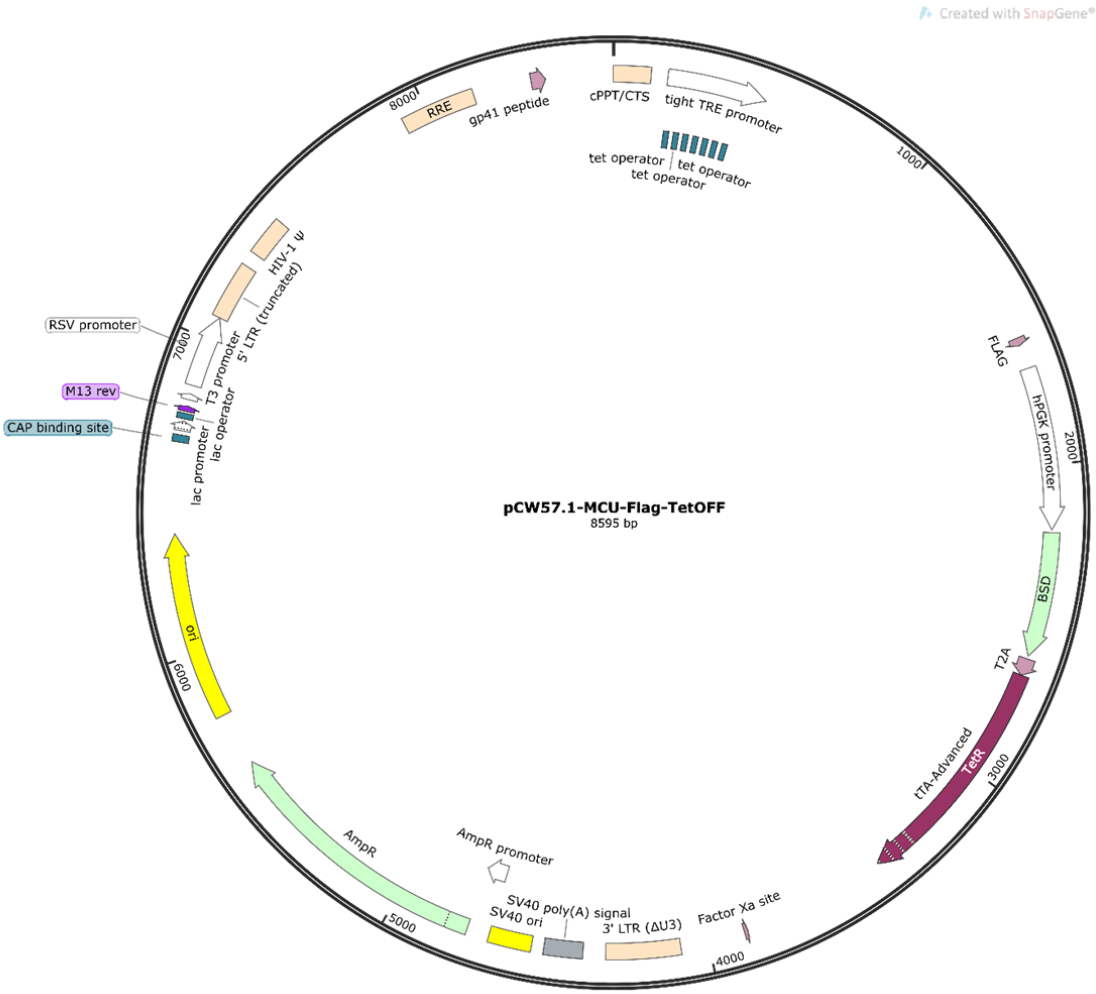

Figure S 3 Plasmid map of pCW57.1-MCU-Flag-TetOFF. *Lentiviral transfer plasmid coding a TetOFF regulated C-term flag tagged MCU.*

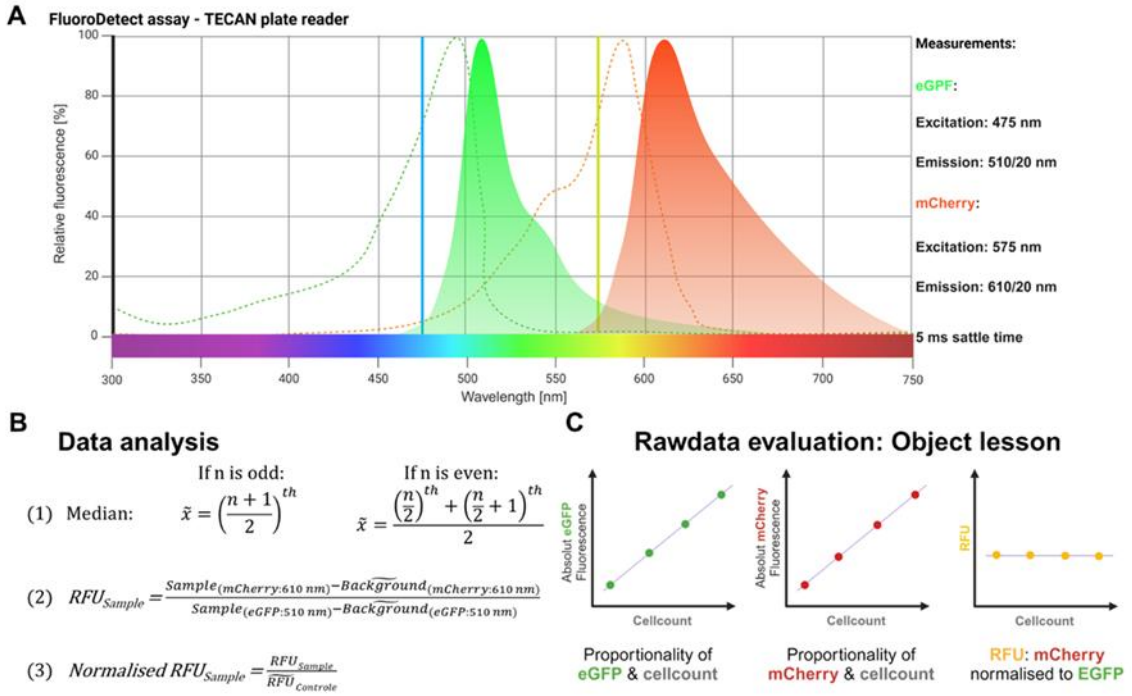

Figure S 4: Setup and data analysis strategy of plate reader measurements. A: *Fluorescence spectrum of eGFP (green) and mCherry (red). On the right side of the spectrum measurement parameters of plate reading approach are shown.* ***B:*** *Data analysis strategy of plate reading experiments. (2) Absolut fluorescence value is blanked by background subtraction of median mCherry and eGFP fluorescence. Relative fluorescence units are defined as quotient of blanked mCherry fluorescence divided by the blanked eGFP fluorescence. (3) Normalization of RFU is performed dividing the RFU of the sample by the RFU of the control sample (e.g. untreated population).* ***C:*** *Object lesson of raw data evaluation showing the correlation of cell number and fluorescence intensity.*

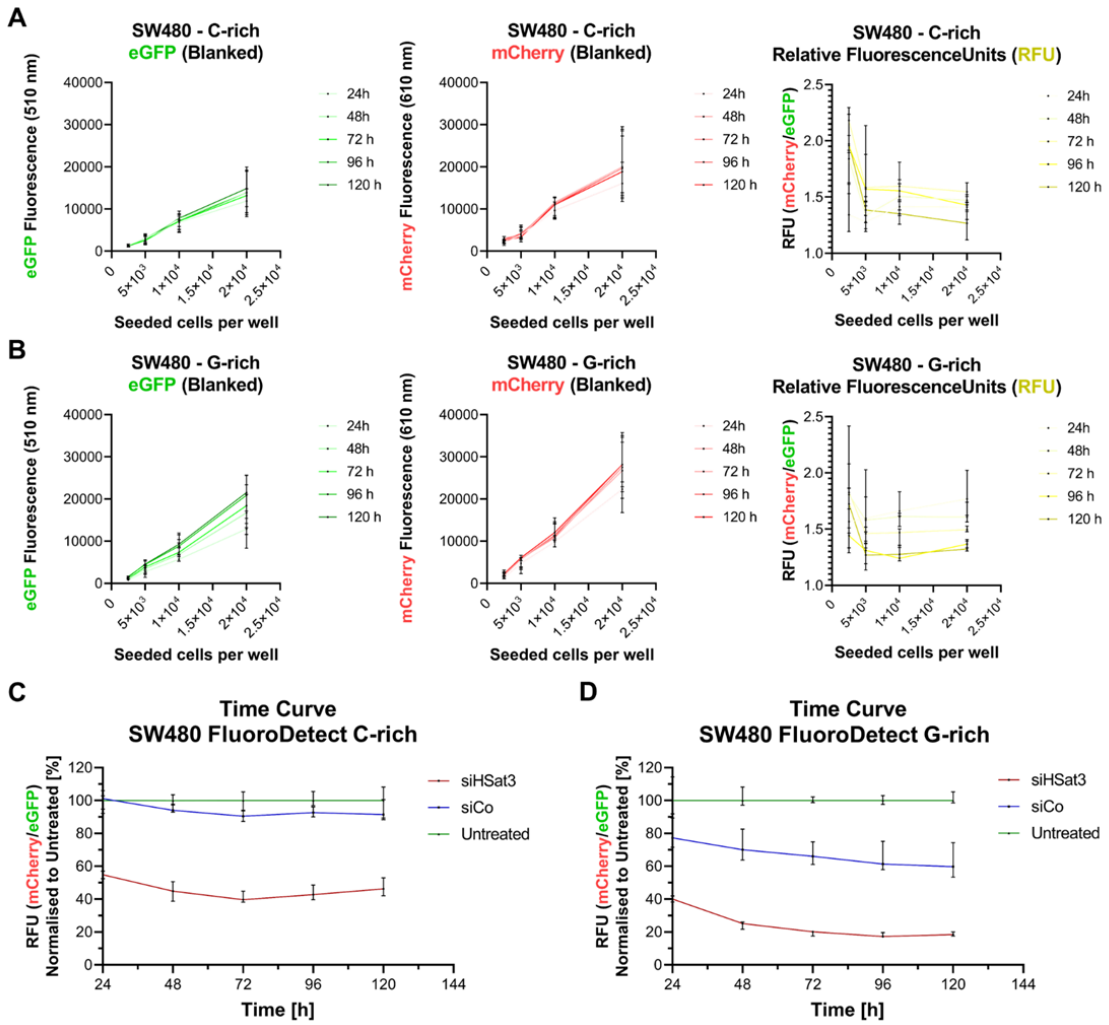

Figure S 5 Additional Time curve of transient transfected FluoroDetect assay performed in SW480 cells. A, B: *Linear regression of eGFP (green) signal and mCherry (red) signal and the number of seeded SW480 cells per well. Determination of relative fluorescence units (RFU) (yellow) in dependence of HeLa cells seeded per well.* ***C, D:*** *Time curve of FluoroDetect transfected HeLa cells measured in 24 h intervals. Diagrams comparing the relative fluorescence units of Untreated (green), siCo treated (blue) and siHSat3 treated (red) cell population. (All graphs showing the median ± CI 95%).*

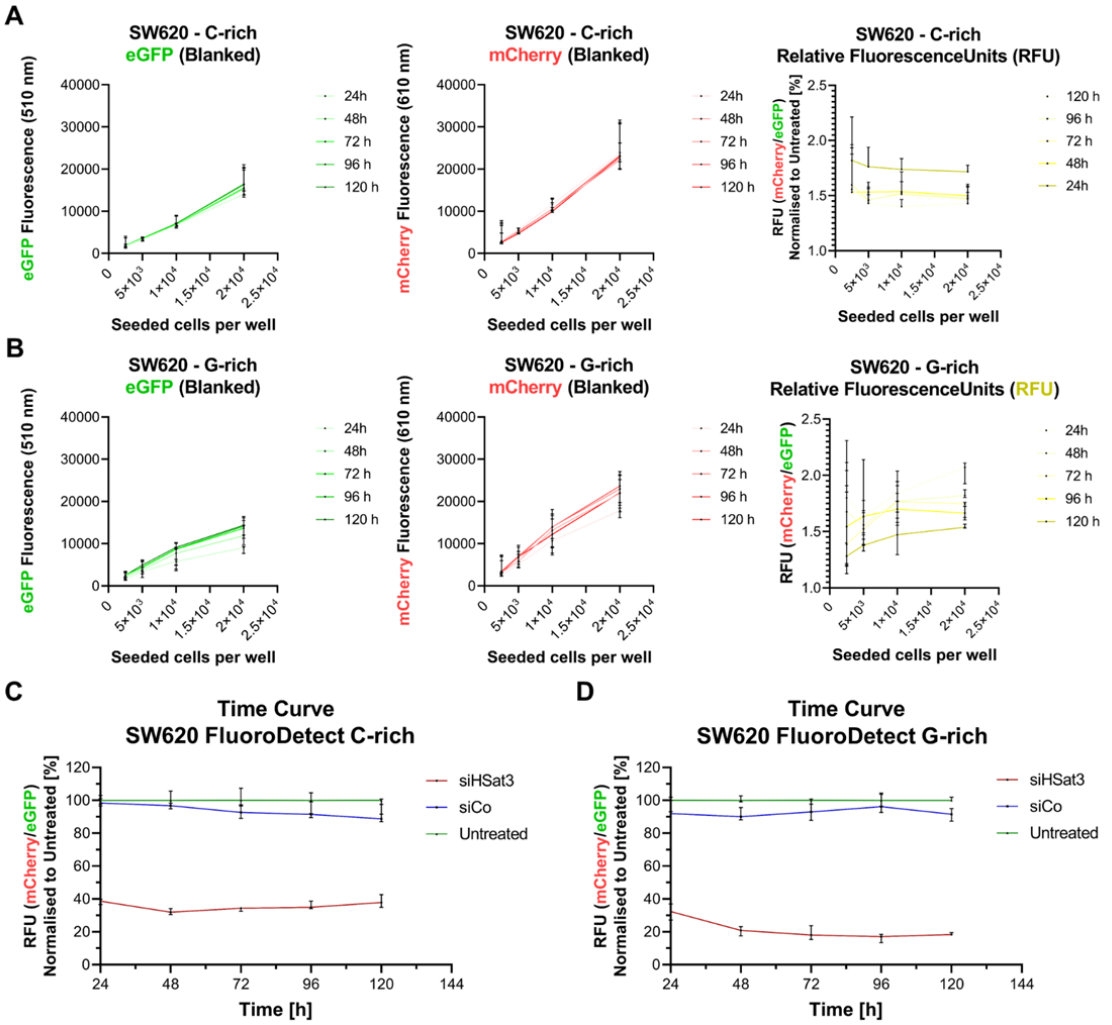

Figure S 6 Additional Time curve of transient transfected FluoroDetect assay performed in SW620 cells. A, B: *Linear regression of eGFP (green) signal and mCherry (red) signal and the number of seeded SW620 cells per well. Determination of relative fluorescence units (RFU) (yellow) in dependence of HeLa cells seeded per well.* ***C, D:*** *Time curve of FluoroDetect transfected HeLa cells measured in 24 h intervals. Diagrams comparing the relative fluorescence units of Untreated (green), siCo treated (blue) and siHSat3 treated (red) cell population. (All graphs showing the median ± CI 95%).*

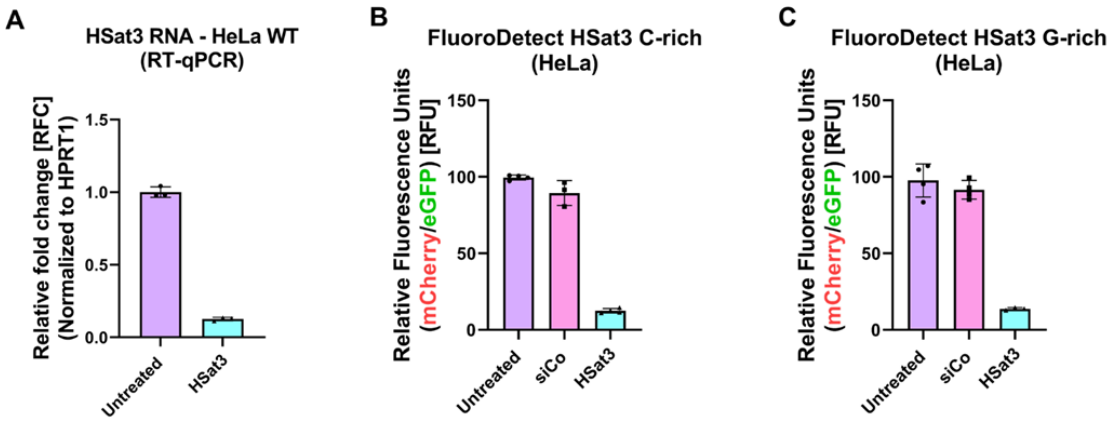

Figure S 7 The knockdown of the endogenous mRNA can be compared to the knock down intensity measured with the FluoroDetect assay. A: *Relative fold change of HSat3 RNA in an untreated and siHSat3 treated sample 6h after heat shock, measured with RT-qPCR. RFC was calculated from delta delta CT values. HPRT served as housekeeping gene.* ***B:*** *Knock down intensity of HSat3 C-rich in untreated, siCo and siHSat3 treated HeLa cells, measured with the FluoroDetect assay.* ***C:*** *Knock down intensity of HSat3 G-rich in untreated, siCo and siHSat3 treated HeLa cells, measured with the FluoroDetect assay. (All graphs showing the median ± CI 95%).*

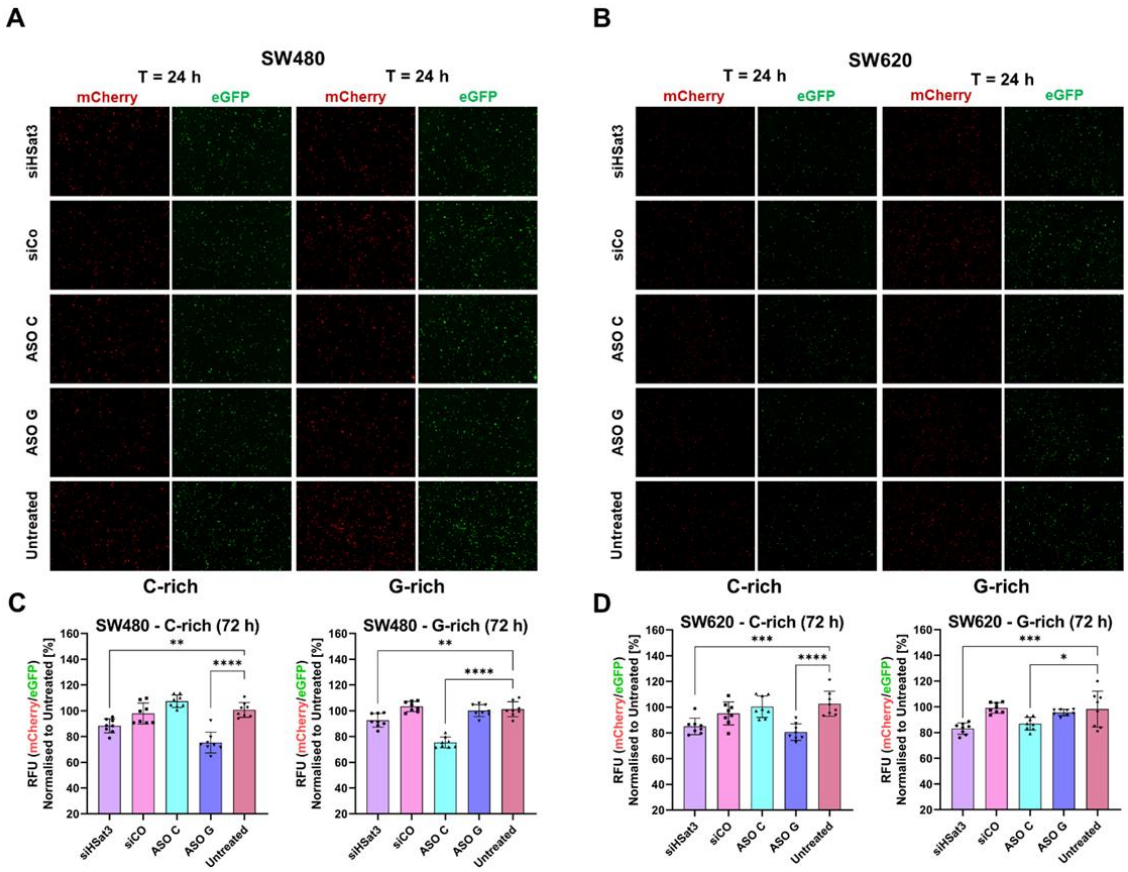

Figure S 8 Additional experiments measuring the strand specific response of the FluoroDetect assay. A, B: *Fluorescence microscope images of SW480 and SW620 cells transfected with the FluoroDetect G-rich and C-rich (HSat3) assay 24 h (T = 24 h) after siRNA/ASO treatment. Populations shown are treated with siHSat3, siCo, ASO C or ASO G. For comparison an additional untreated population is shown.* ***C, D:*** *Relative fluorescence units (RFU) of SW480 and SW620 cells transfected with FluoroDetect C-rich (HSat3) or FluoroDetect G-rich (HSat3) 72 hours after treatment with siRNA/ASO as indicated below the diagram. (All graphs showing the median ± CI 95%).*

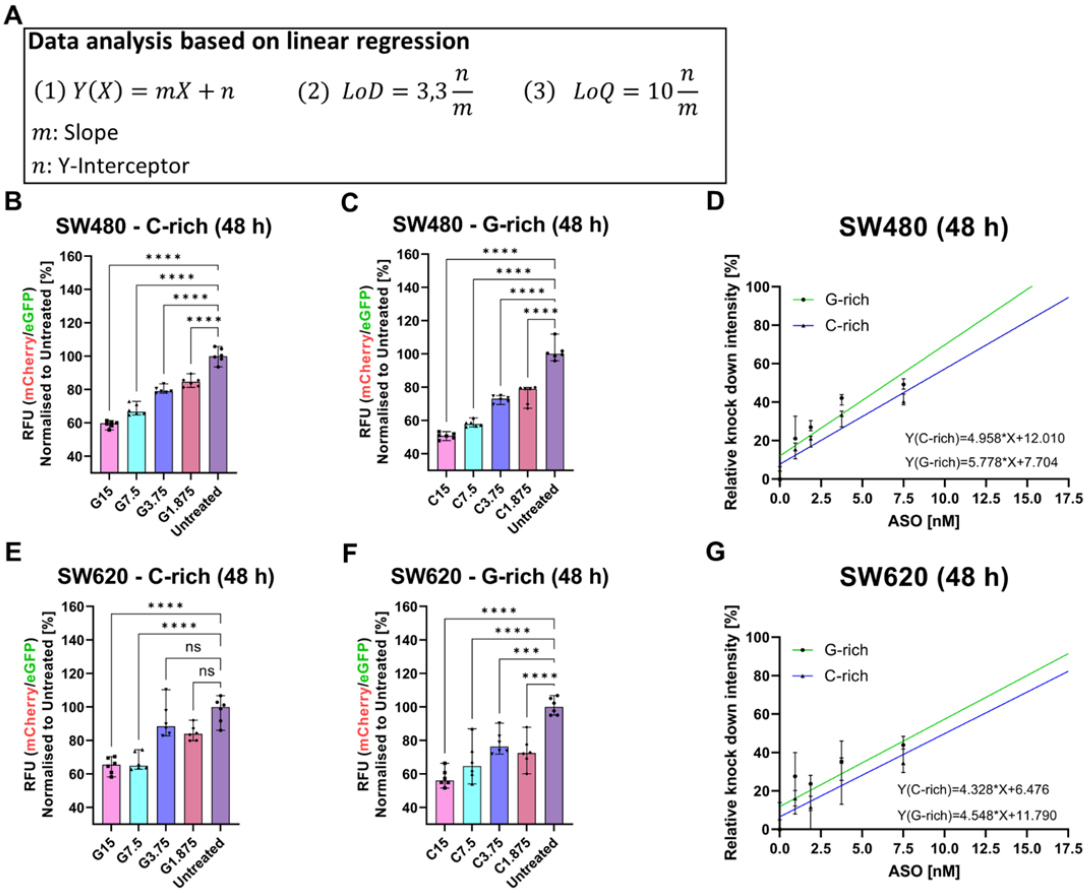

Figure S 9 Additional information and experiments measuring the assays detection boundaries in SW480 and SW620 cells. A: *Determination strategy of limit of detection and limit of quantification.* ***B, C, E, F:*** *Knock down intensity measured as relative fluorescence units (RFU) in HeLa cells 48 hours after treatment with different amounts (Absolut amounts: 15 pmol, 7,5 pmol, 3,75 pmol, 1,875 pmol) of strand specific ASOs.* ***D, G:*** *Linear regression of relative knock down intensity normalised to the untreated control population of FluoroDetect C-rich (HSat3) (blue) and FluoroDetect G-rich (HSat3) (green) 48 hours after treatment. (All graphs showing the median ± CI 95%).*

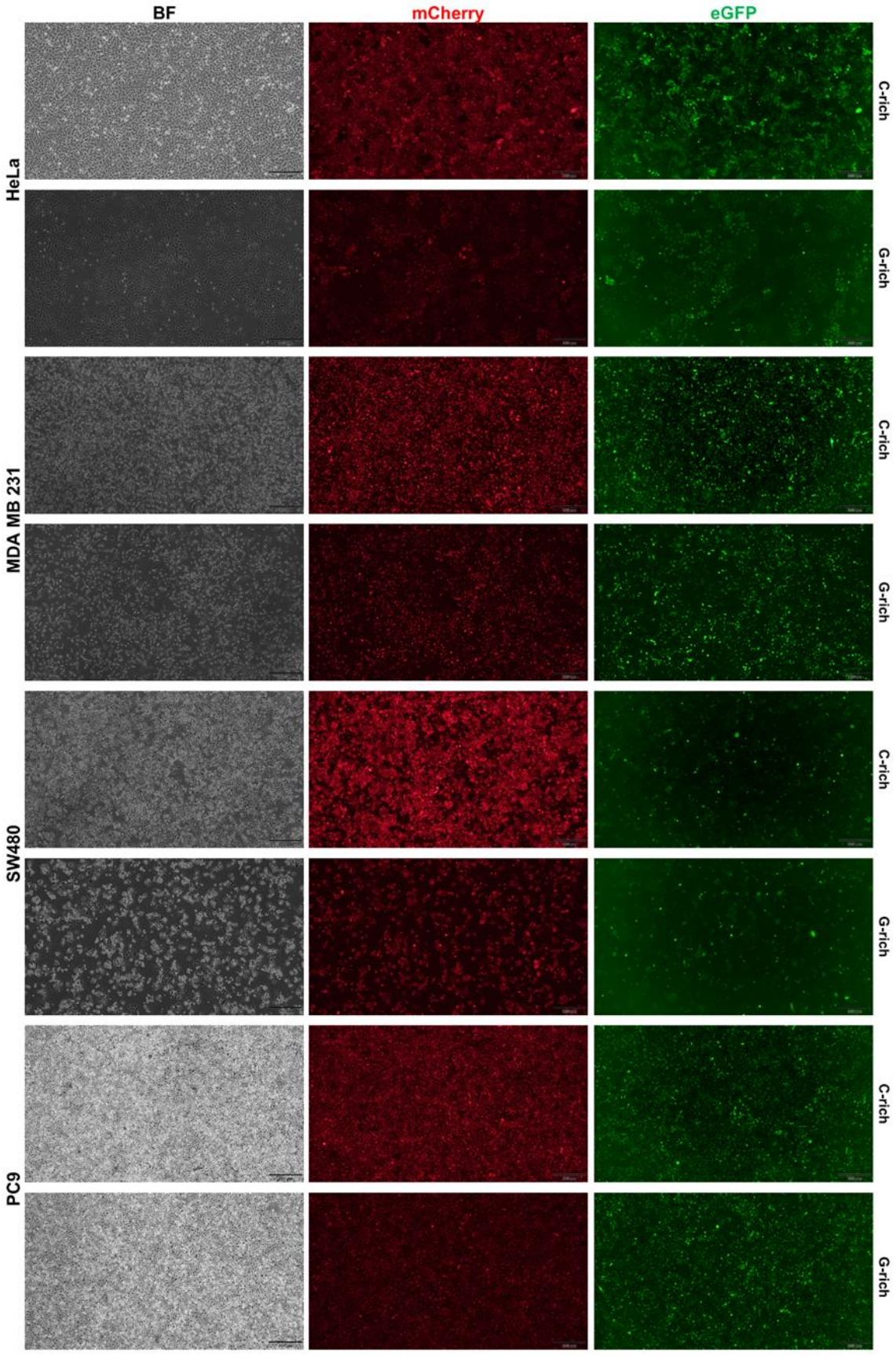

Figure S 10 Lentiviral stable transduced and antibiotic selected polyclonal FluoroDetect reporter cells. *Fluorescence microscopic images of HeLa MDA MB 231, SW480 and PC9 cells in red, green and brightfield channel.*

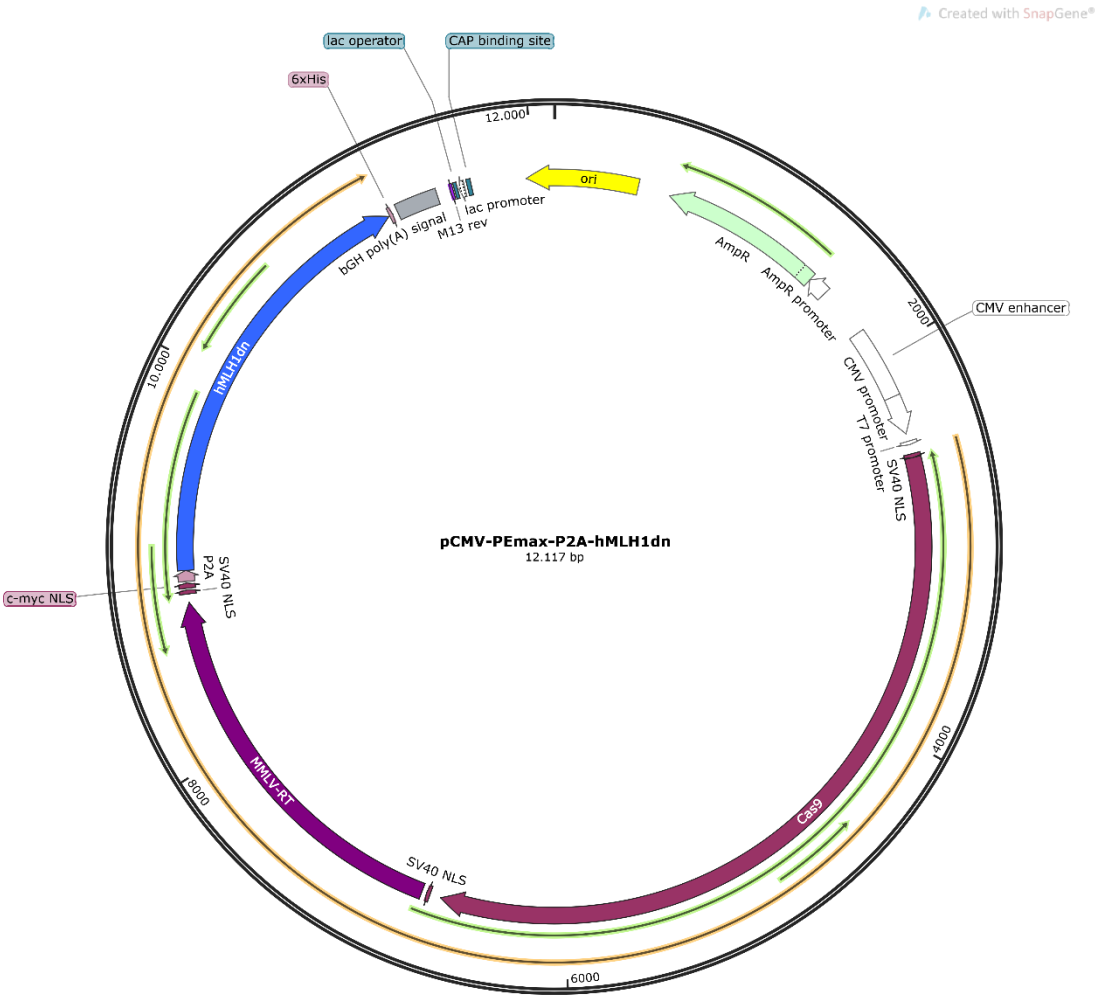

Figure S 11 Plasmid map of pCMV-PEmax-P2A-hMLH1dn. *Eucaryotic expression plasmid coding a bicistronic reading frame of Prime Editor and hMLH1dn.*

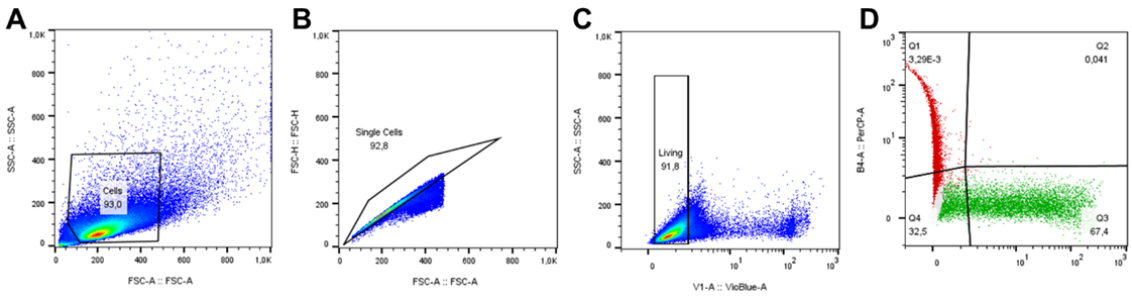

Figure S 12 Gating strategy of flow cytometry experiments. A: *Gating of events determined as cells. Excluding debris and oversize artefacts (FSC-A vs. SSC-A).* ***B:*** *Gating of single cells to exclude cell duplets (FSC-A vs. FSC-H).* ***C:*** *Gating of living cells using DAPI as a viability dye. Excluding events with high blue fluorescence intensity.* ***D:*** *Single stained controls expressing only eGFP (green) or mCherry (red) were used as compensation control and to determine eGFP and mCherry positive events.*

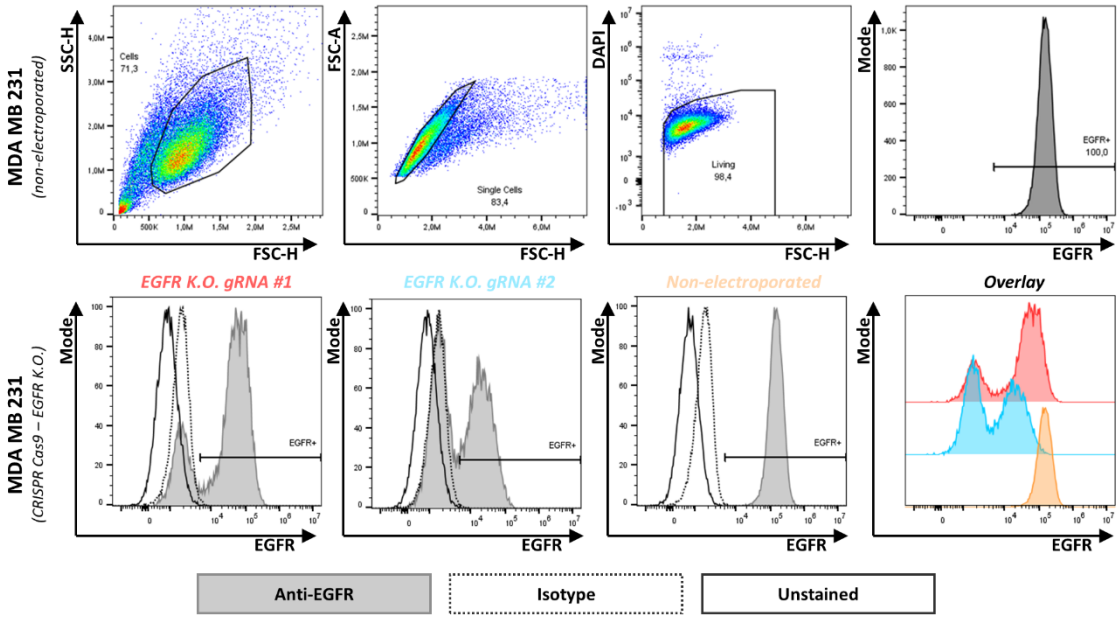

Figure S 13 Flow cytometry analysis of CRISPR Cas9 EGFR knock out in MDA MB 231 cells. Upper Row: *Gating strategy to assess EGFR knock down. Population called "cells" was defined in a FSC-H versus SSC-H scatterplot. Subpopulation of "single cells" was defined in a FSC-H versus FSC-A scatter plot. Living cell population was gated by excluding cells exhibiting enhanced fluorescence in the DAPI channel. WT population (gray) stained with EGFR specific antibody was used to define EGFR+ gate.* ***Lower Row:*** *Isotype control (dotted line) defined unspecific antibody interaction. Unstained population (continuous line) was included to evaluate autofluorescence. Gene editing efficiency was evaluated comparing the edited populations EGFR K.O. gRNA#1 (red) and EGFR K.O. gRNA#2 (blue) with a non-electroporated wildtype sample(orang).*

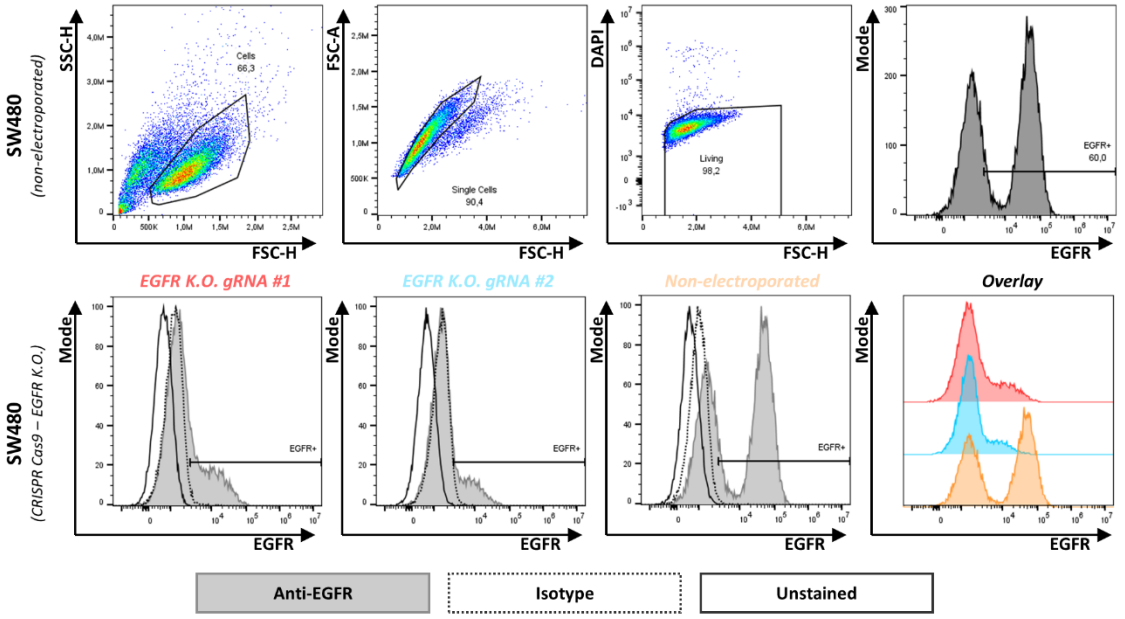

Figure S 14 Flow cytometry analysis of CRISPR Cas9 EGFR knock out in SW480 cells. Upper Row: *Gating strategy to assess EGFR knock down. Population called "cells" was defined in a FSC-H versus SSC-H scatterplot. Subpopulation of "single cells" was defined in a FSC-H versus FSC-A scatter plot. Living cell population was gated by excluding cells exhibiting enhanced fluorescence in the DAPI channel. WT population (gray) stained with EGFR specific antibody was used to define EGFR+ gate.* ***Lower Row:*** *Isotype control (dotted line) defined unspecific antibody interaction. Unstained population (continuous line) was included to evaluate autofluorescence. Gene editing efficiency was evaluated comparing the edited populations EGFR K.O. gRNA#1 (red) and EGFR K.O. gRNA#2 (blue) with a non-electroporated wildtype sample(orang).*

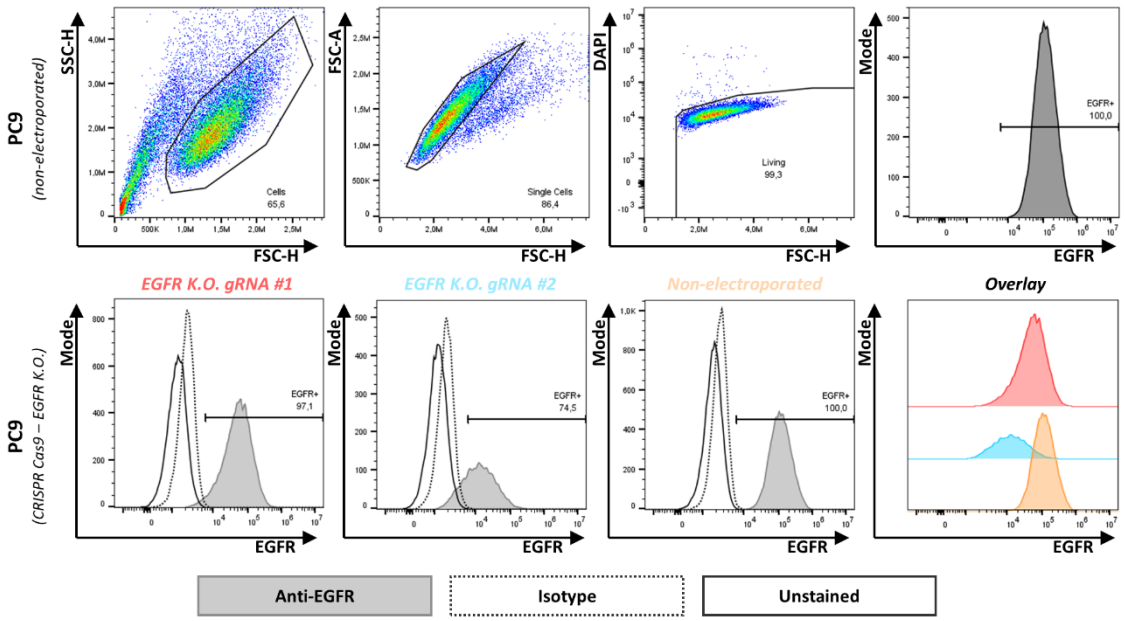

Figure S 15 Flow cytometry analysis of CRISPR Cas9 EGFR knock out in PC9 cells. Upper Row: *Gating strategy to assess EGFR knock down. Population called "cells" was defined in a FSC-H versus SSC-H scatterplot. Subpopulation of "single cells" was defined in a FSC-H versus FSC-A scatter plot. Living cell population was gated by excluding cells exhibiting enhanced fluorescence in the DAPI channel. WT population (gray) stained with EGFR specific antibody was used to define EGFR+ gate.* ***Lower Row:*** *Isotype control (dotted line) defined unspecific antibody interaction. Unstained population (continuous line) was included to evaluate autofluorescence. Gene editing efficiency was evaluated comparing the edited populations EGFR K.O. gRNA#1 (red) and EGFR K.O. gRNA#2 (blue) with a non-electroporated wildtype sample(orang).*

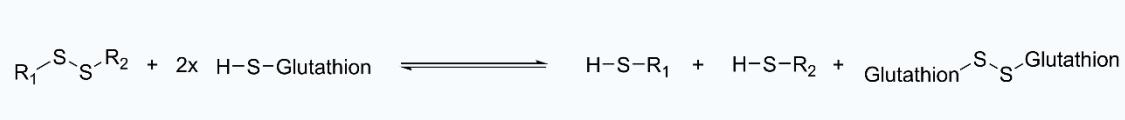

Figure S 16 Reaction equilibrium of disulfide bonds and the thiol group of glutahtion. *In presence of glutahion the disulfide bond is cleaved to two thiols bound to the cleavage products.*

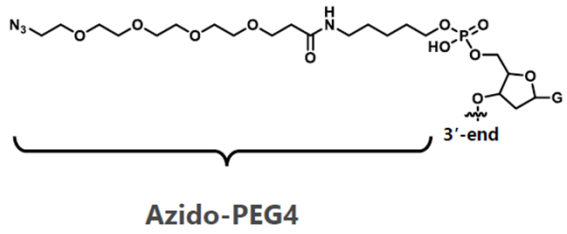

Figure S 17 Chemical structure of the Azido-PEG4 modified Guanin base used for solid phase synthesis of the RNA aptamer CL4.

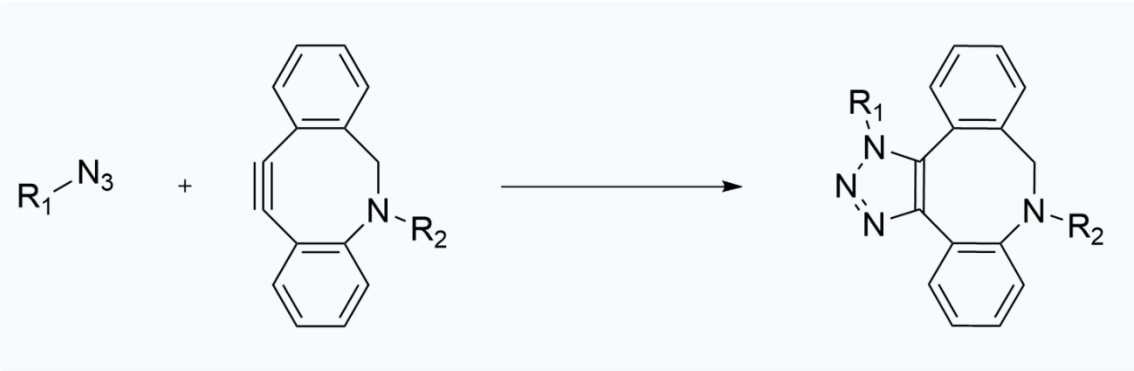

Figure S 18 Strain-Promoted Azide-Alkyne Cycloaddition (SPAAC) reaction of azide (R_1: Aptamer) and dibenzo cyclooctyne (R_2: Linker).

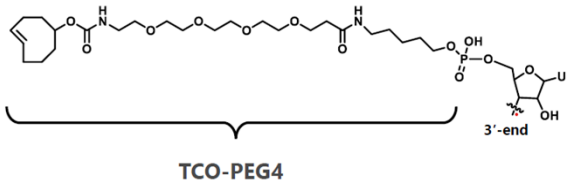

Figure S 19 Chemical structure of the trans-cyclooctene (TCO)-PEG4 modified Uracil base used for solid phase synthesis of the HSat3 targeting ASO.

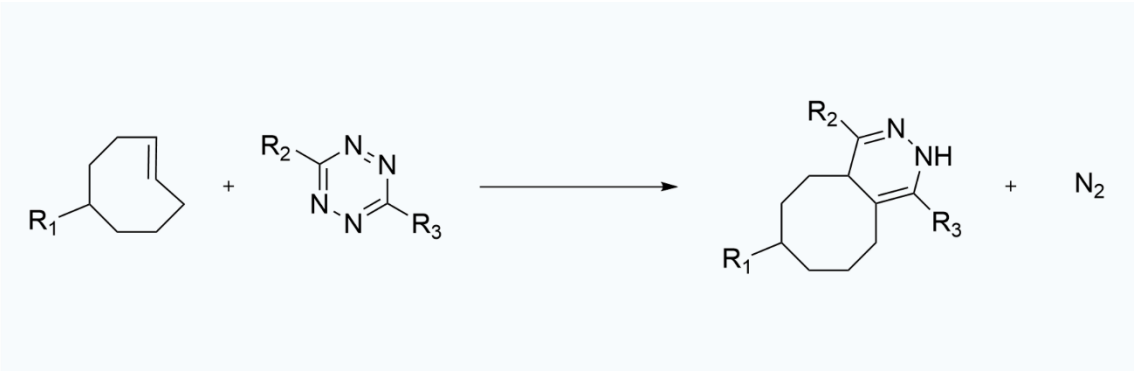

Figure S 20 Inverse Electron Demand Diels–Alder reaction of TCO (R_1: HSat3 ASO) and tetrazine (R_2: Linker, R_3: CH_3).

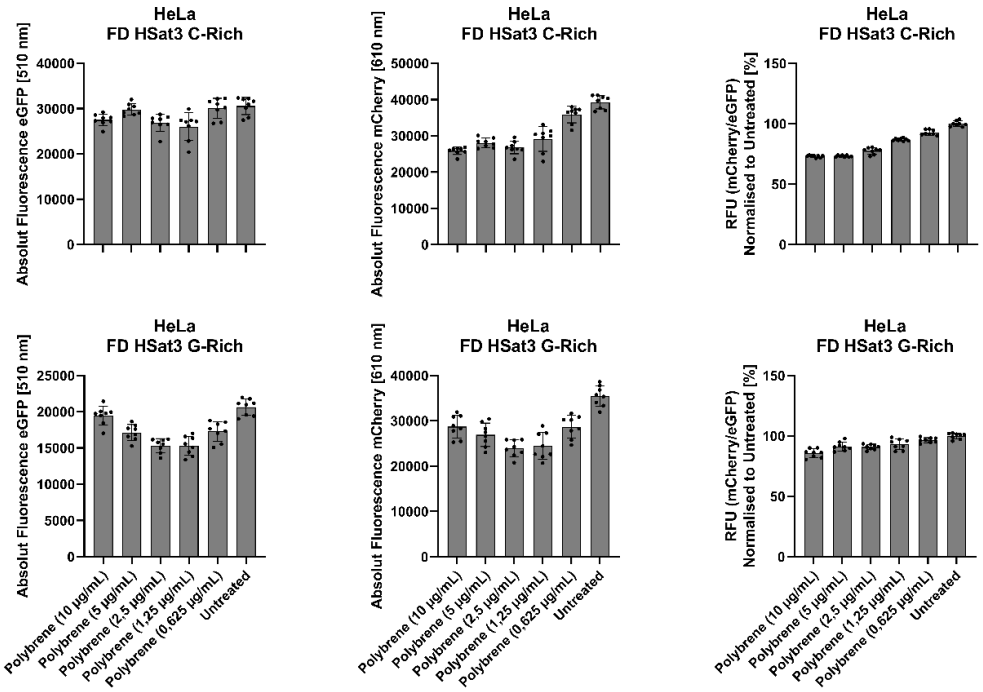

Figure S 21 Raw Data Analysis - Dilution series of polybrene to evaluate the dose dependent artefact intensity. *HeLa cells stably expressing the FluoroDetect HSat3 assay were treated with indicated concentration of polybrene.* ***Column 1 &2:*** *Blanked Fluorescence Values of eGFP and mCherry.* ***Column 3:*** *RFUs of all samples were compared to an untreated control population. Single value displayed are independent technical replicates normalized to an untreated sample (All graphs showing the median ± 95% confidence interval [CI]).*

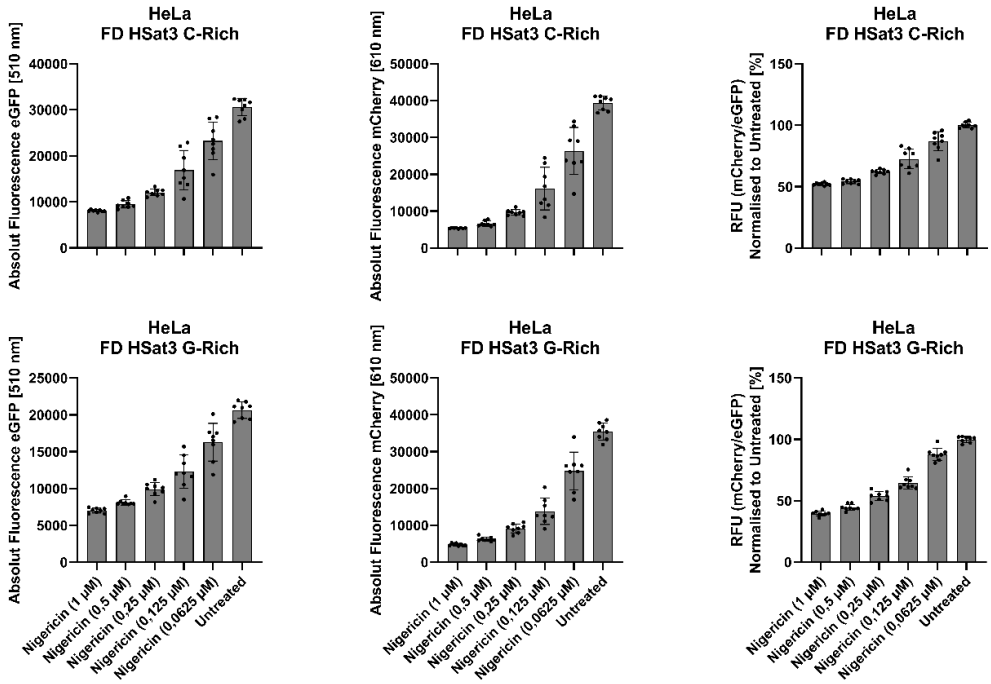

Figure S 22 Raw Data Analysis - Dilution series of nigericin to evaluate the dose dependent artefact intensity. *HeLa cells stably expressing the FluoroDetect HSat3 assay were treated with indicated concentration of nigericin.* ***Column 1 &2:*** *Blanked Fluorescence Values of eGFP and mCherry.* ***Column 3:*** *RFUs of all samples were compared to an untreated control population. Single value displayed are independent technical replicates normalized to an untreated sample (All graphs showing the median ± 95% confidence interval [CI]).*

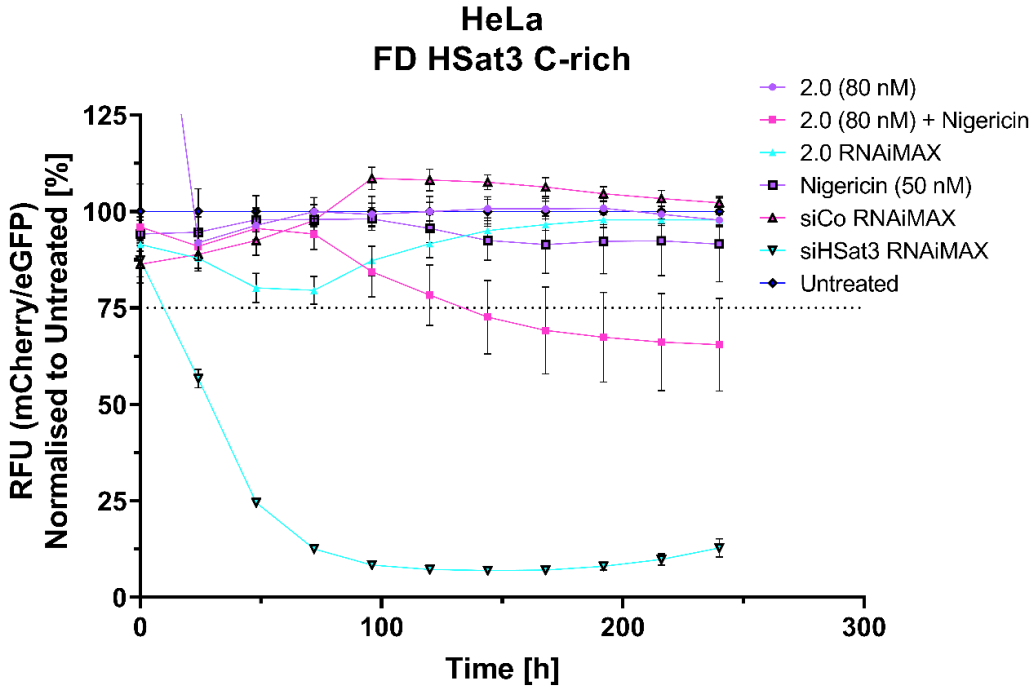

Figure S 23 Evaluation of the knock down activity of the 5th generation vehicle strand loaded with 4th generation payload. *Long term experiment showing the RFUs measured in HeLa cells expressing the FluoroDetect Hsat3 C-rich assay. Time period of 0 h to 240 h. Populations are treated as indicated. Value displayed are represent the median of eight technical replicates normalized to an untreated sample (All graphs showing the median ± 95% confidence interval [CI]).*

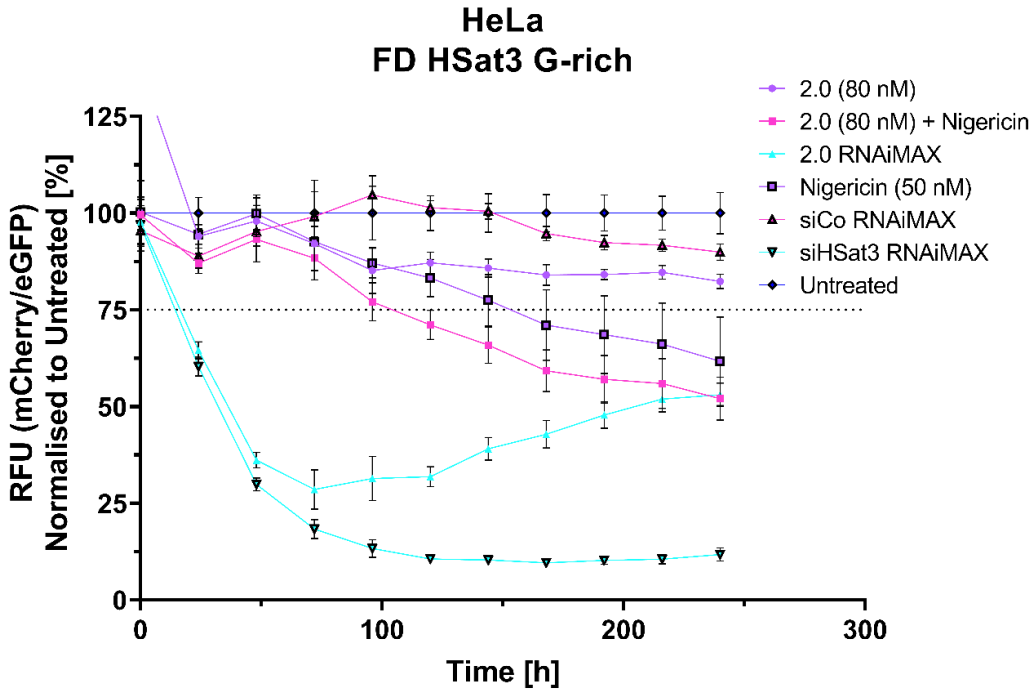

Figure S 24 Evaluation of the knock down activity of the 4th generation payload strand carried by the 5th generation vehicle. *Long term experiment showing the RFUs measured in HeLa cells expressing the FluoroDetect Hsat3 G-rich assay. Time period of 0 h to 240 h. Populations are treated as indicated. Value displayed are represent the median of eight technical replicates normalized to an untreated sample (All graphs showing the median ± 95% confidence interval [CI]).*

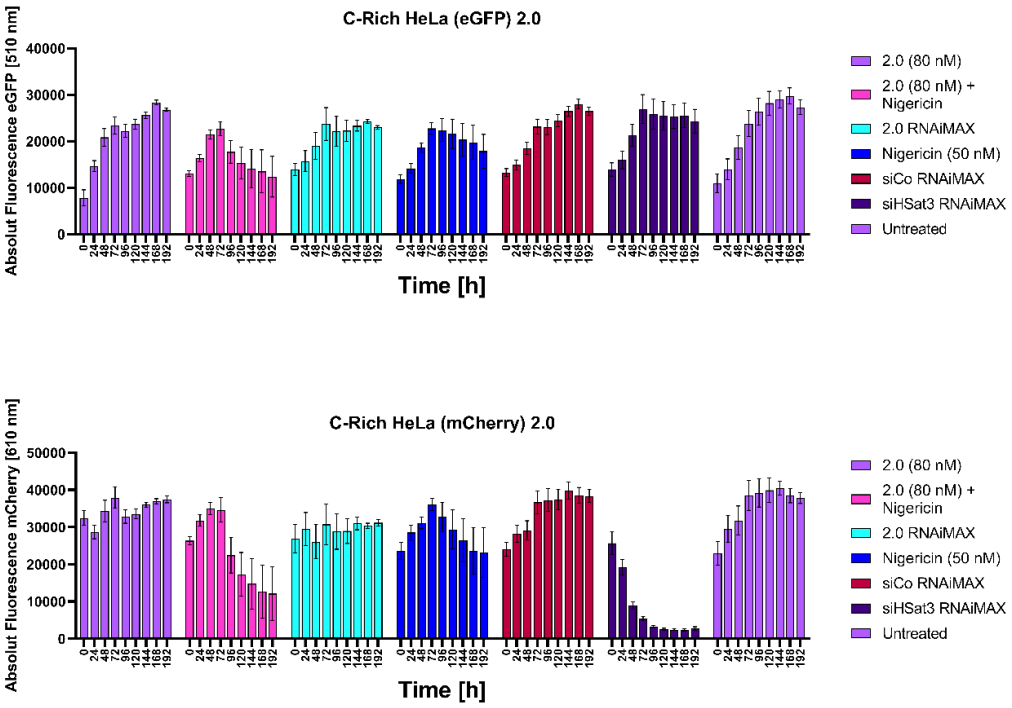

Figure S 25 Raw Data Analysis - Evaluation of the knock down activity of the 5th generation vehicle strand loaded with 4th generation payload. *Long term experiment showing the RFUs measured in HeLa cells expressing the FluoroDetect Hsat3 C-rich assay. Time period of 0 h to 240 h. Populations are treated as indicated. Blanked Fluorescence Values of eGFP and mCherry. Value displayed are represent the median of eight technical replicates (All graphs showing the median ± 95% confidence interval [CI]).*

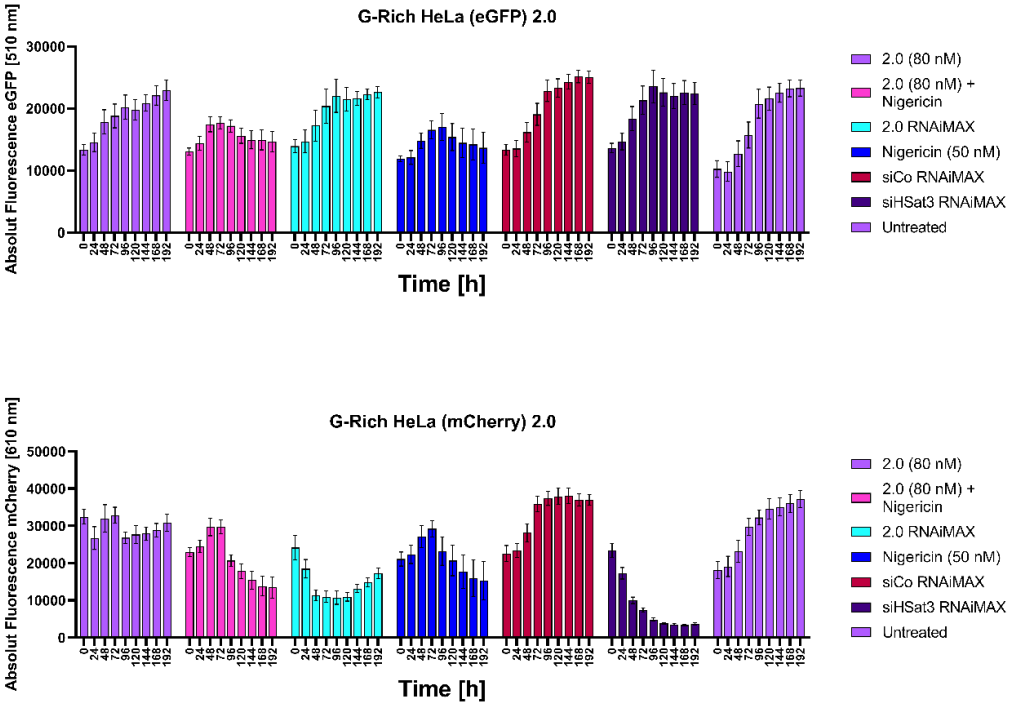

Figure S 26 Raw Data Analysis - Evaluation of the knock down activity of the 4th generation payload strand carried by the 5th generation vehicle. *Long term experiment showing the RFUs measured in HeLa cells expressing the FluoroDetect Hsat3 G-rich assay. Time period of 0 h to 240 h. Populations are treated as indicated. Blanked Fluorescence Values of eGFP and mCherry. Value displayed are represent the median of eight technical replicates (All graphs showing the median ± 95% confidence interval [CI]).*

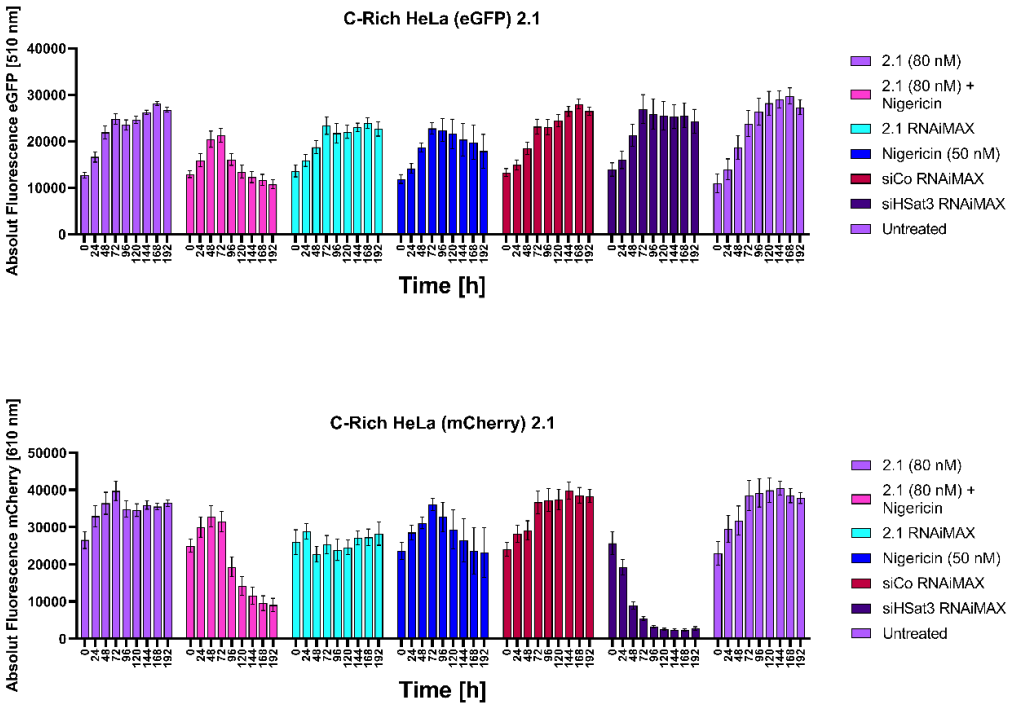

Figure S 27 Raw Data Analysis - Evaluation of the knock down activity of the 5th generation vehicle strand loaded with 5th generation payload. *Long term experiment showing the RFUs measured in HeLa cells expressing the FluoroDetect Hsat3 C-rich assay. Time period of 0 h to 240 h. Populations are treated as indicated. Blanked Fluorescence Values of eGFP and mCherry. Value displayed are represent the median of eight technical replicates (All graphs showing the median ± 95% confidence interval [CI]).*

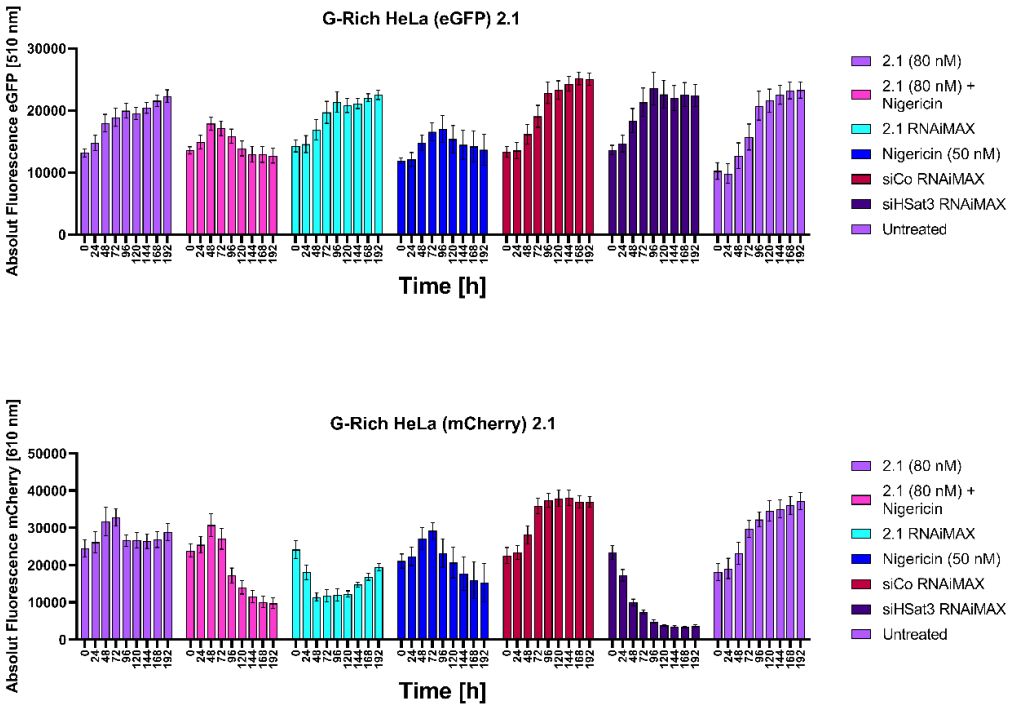

Figure S 28 Raw Data Analysis - Evaluation of the knock down activity of the 5th generation payload strand carried by the 5th generation vehicle. *Long term experiment showing the RFUs measured in HeLa cells expressing the FluoroDetect Hsat3 G-rich assay. Time period of 0 h to 240 h. Populations are treated as indicated. Blanked Fluorescence Values of eGFP and mCherry. Value displayed are represent the median of eight technical replicates (All graphs showing the median ± 95% confidence interval [CI]).*

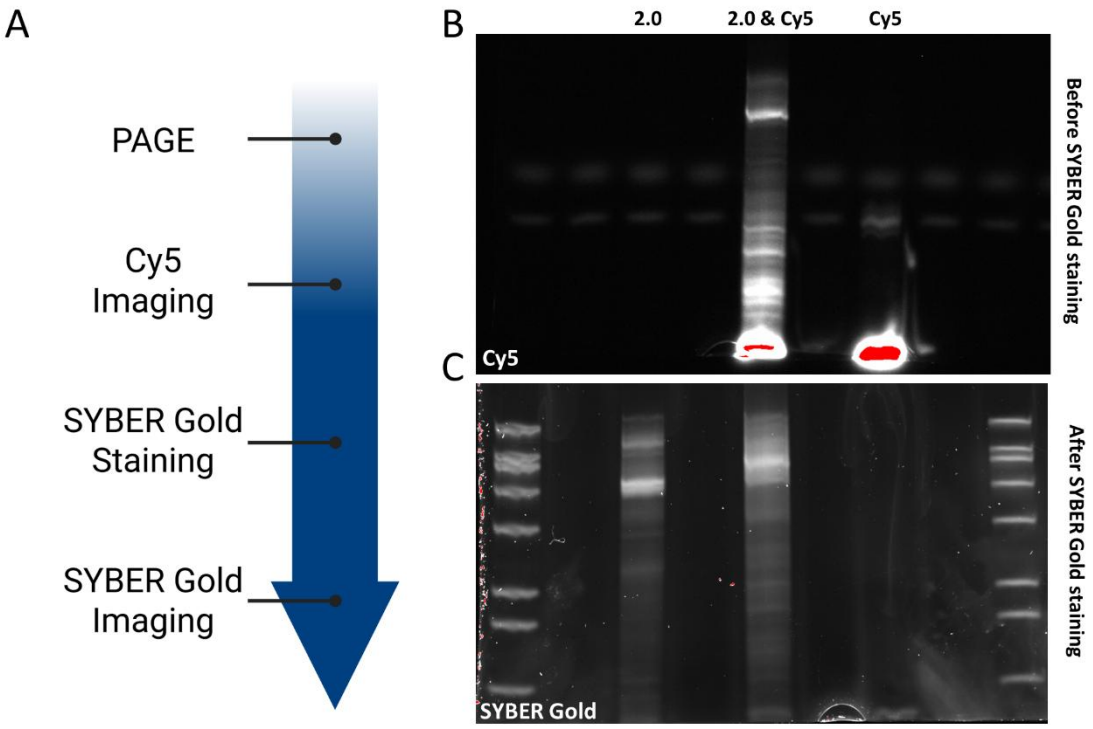

Figure S 29 Hybridization control of vehicle probe conjugates (VPC). A: *Schematic workflow of the VPC hybridization control experiment.* ***B:*** *Polyacrylamide gel electrophoresis (PAGE) the imaged using the CY5 fluorescence of the DNA probe.* ***C:*** *Image of the PAGE gel using the fluorescence of SYBER Gold.*

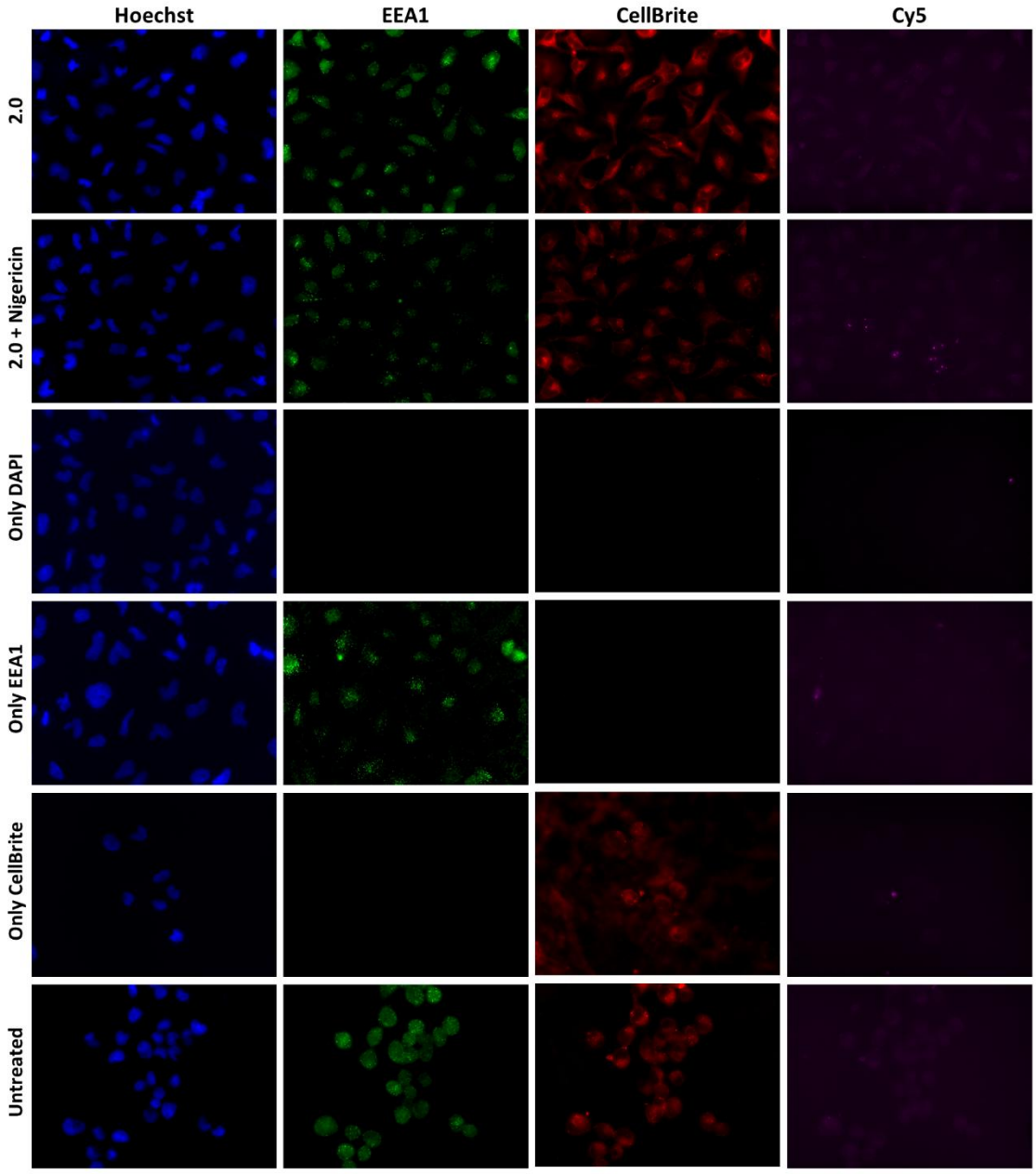

Figure S 30 Immune fluorescence images of VPC treated cells. Images of the nucleus (blue), early endosomes (green), cell membranes (red) and 5th generation VPCs (purple). Full sample set showing hot samples and single staining controls.

Figure S 31 Plasmid map of pCDH EGFP (Neo). *Lentiviral transfer plasmid coding eGFP and G418 resistance gene.*

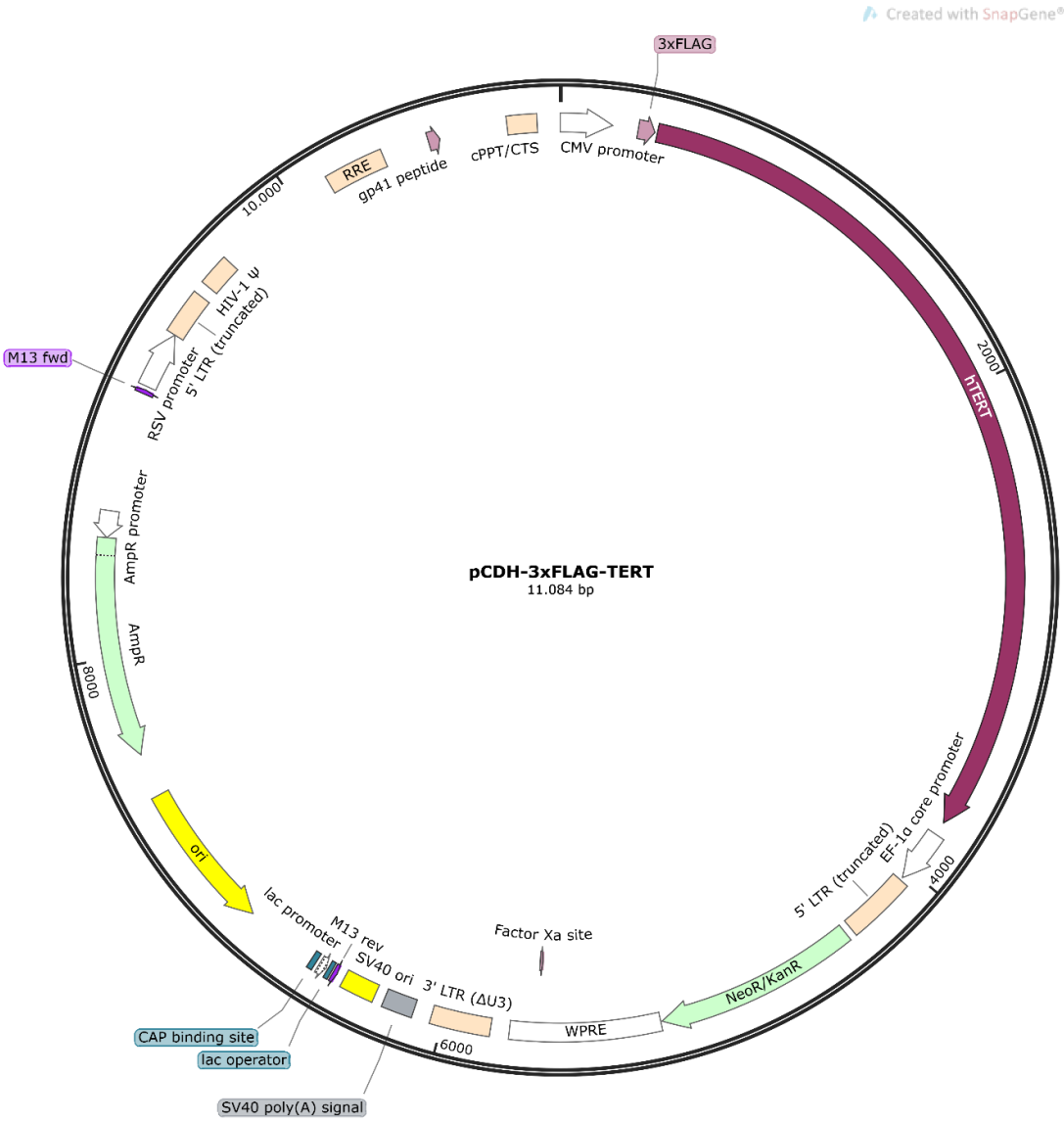

Figure S 32 Plasmid map of pCDH-3xFLAG-TERT. *Lentiviral transfer plasmid coding hTERT and G418 resistance gene.*

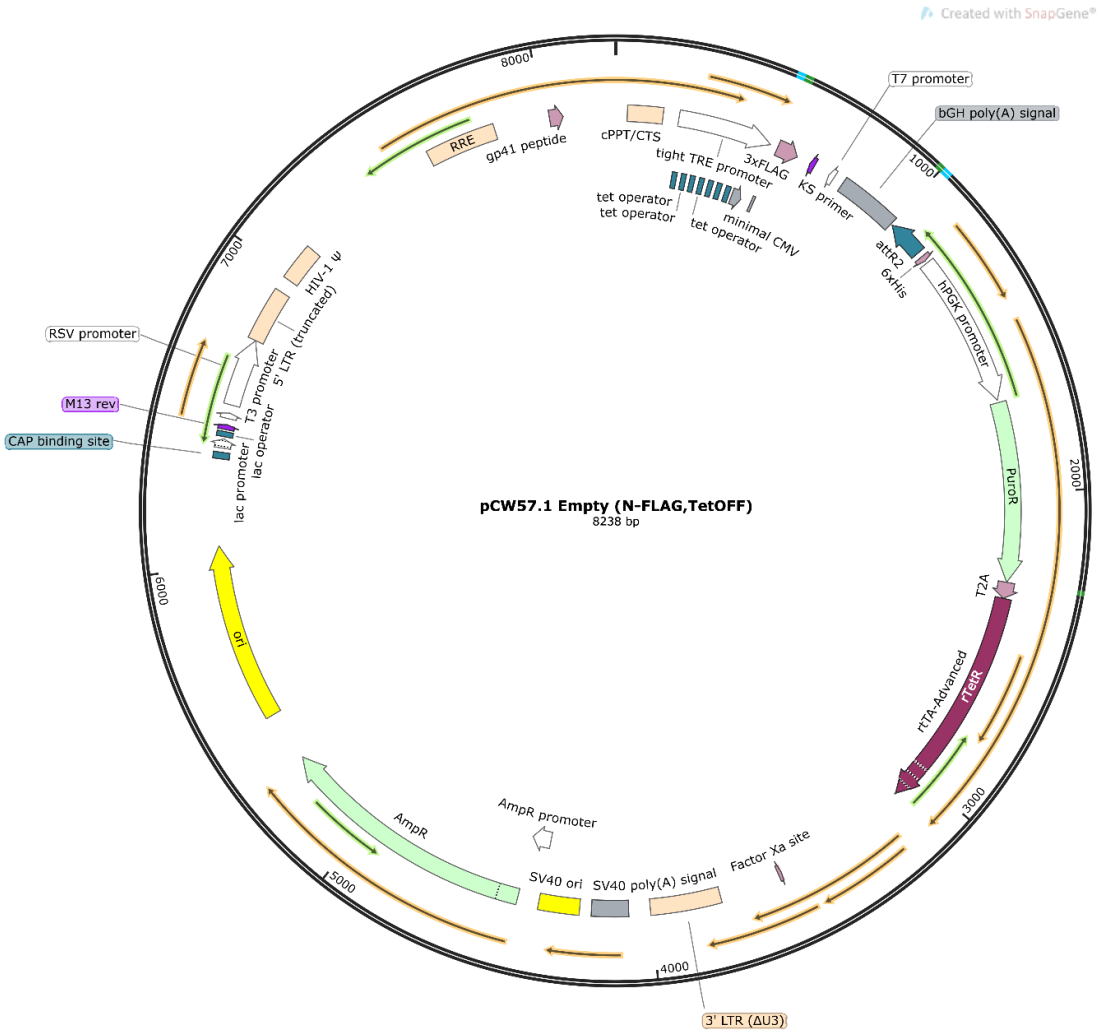

Figure S 33 Plasmid map of pCW57.1. Empty (N-FLAG, TetOFF). *Empti transfer plasmid carrying a TetOff regulated MCS and a T2A bicistronic reding frame coding Puromycin resistance gene and the rTet repressor.*

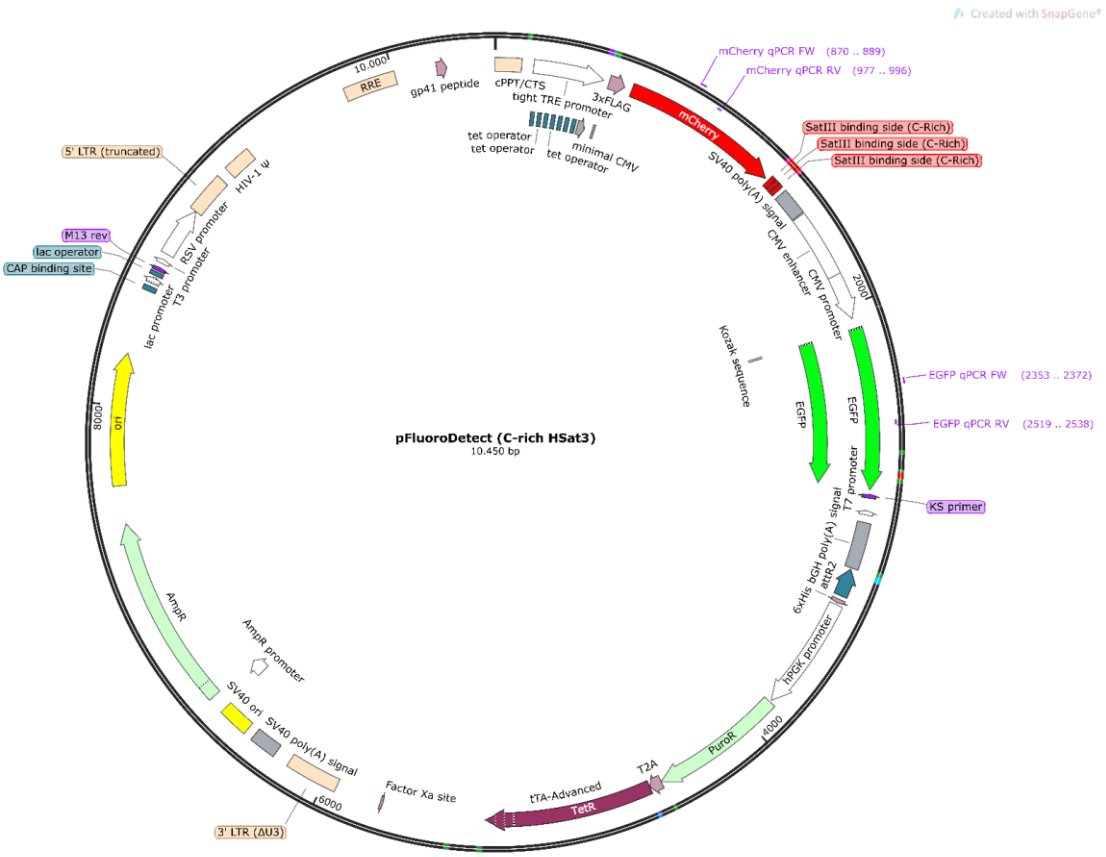

Figure S 34 Plasmid map of pFluoroCheck (C-rich HSat3). *Lentiviral transfer plasmid carrying the FluoroCheck gene modified with the C-rich HSat3 target site in the 3' UTR of the mCherry.*

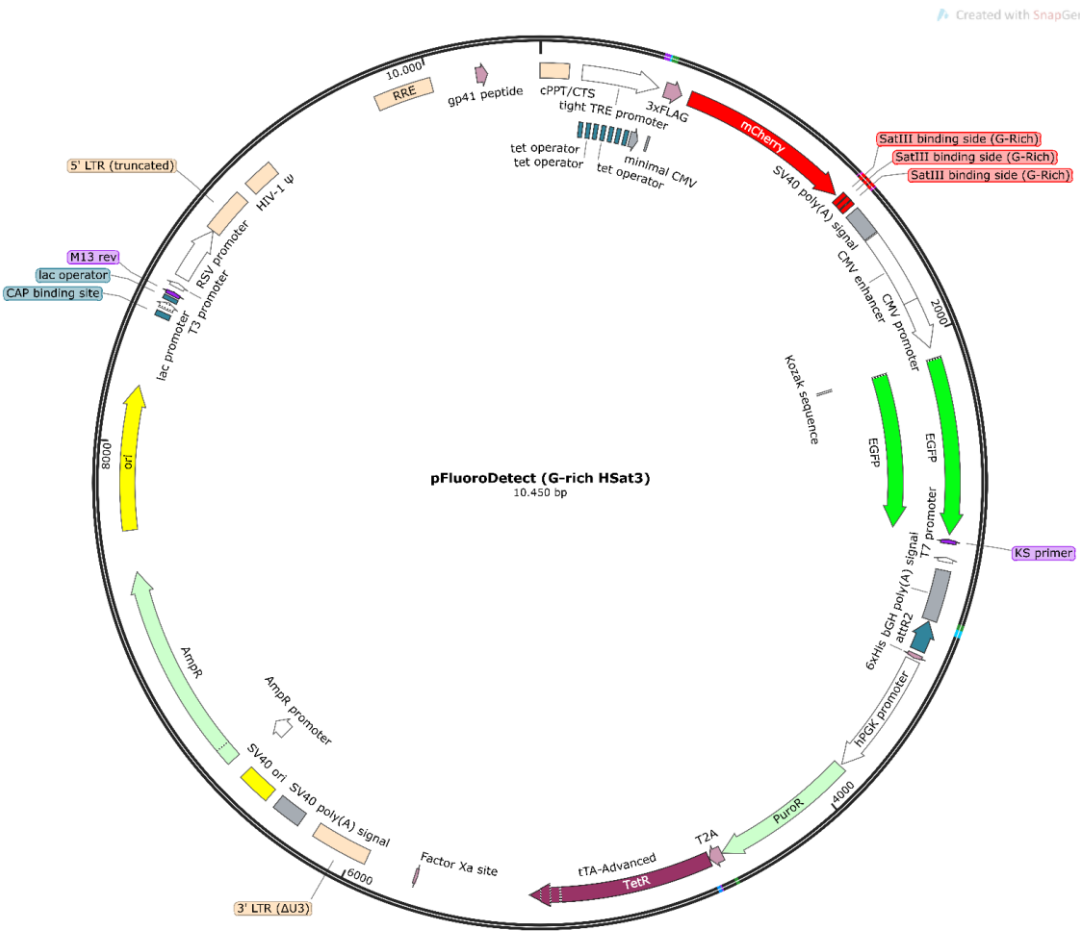

Figure S 35 Plasmid map of pFluoroCheck (G-rich HSat3). *Lentiviral transfer plasmid carrying the FluoroCheck gene modified with the G-rich HSat3 target site in the 3' UTR of the mCherry.*

Figure S 36 Plasmid map of pmCherry G-rich HSat3. *Lentiviral transfer plasmid carrying the C-rich HSat3 target site in the 3' UTR.*

Figure S 37 Plasmid map of pmCherry C-rich HSat3. *Lentiviral transfer plasmid carrying the C-rich HSat3 target site in the 3' UTR.*

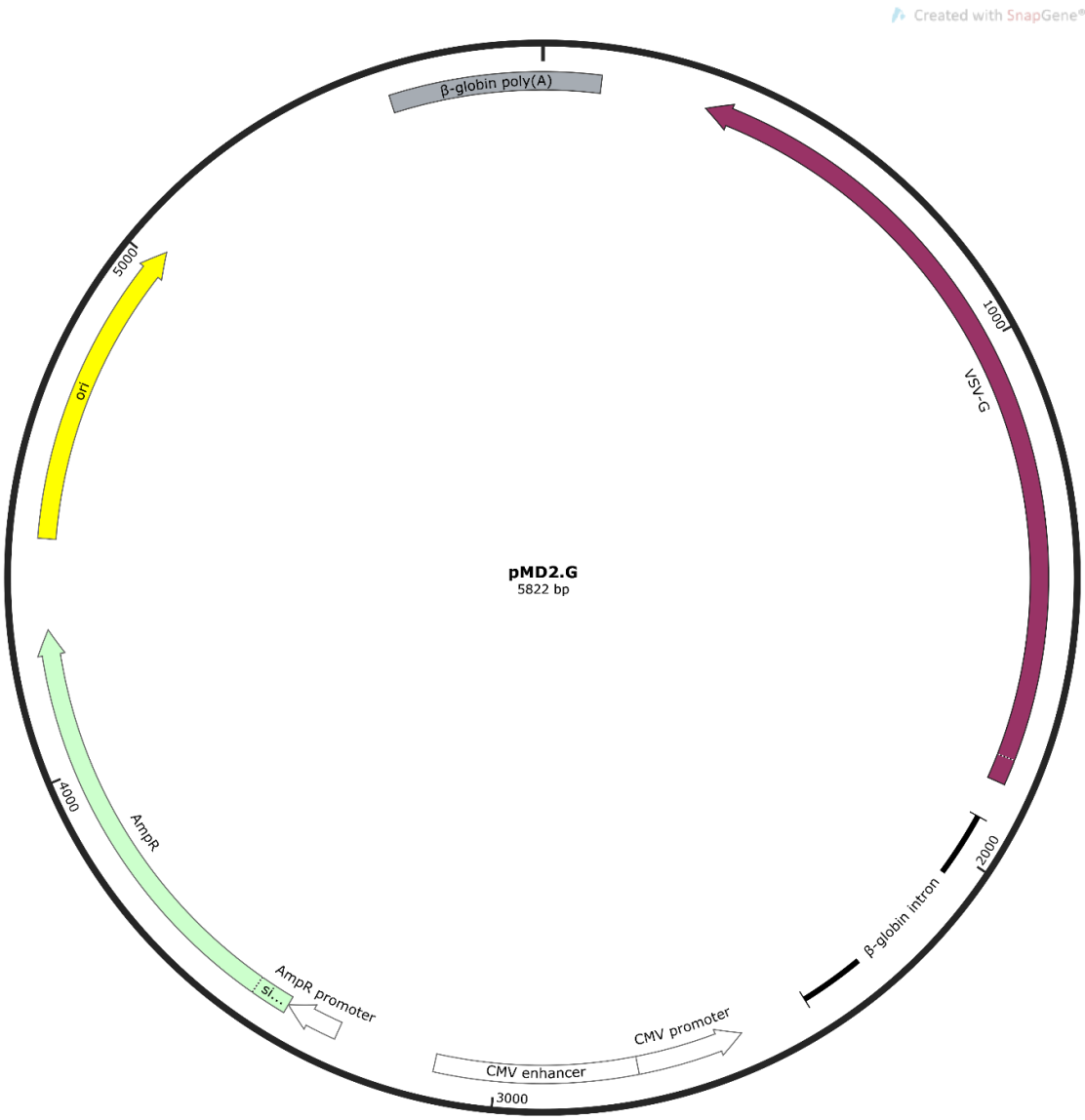

Figure S 38 Plasmid map of pMD2.G. *Lentiviral packaging plasmid coding VSV-G gene.*

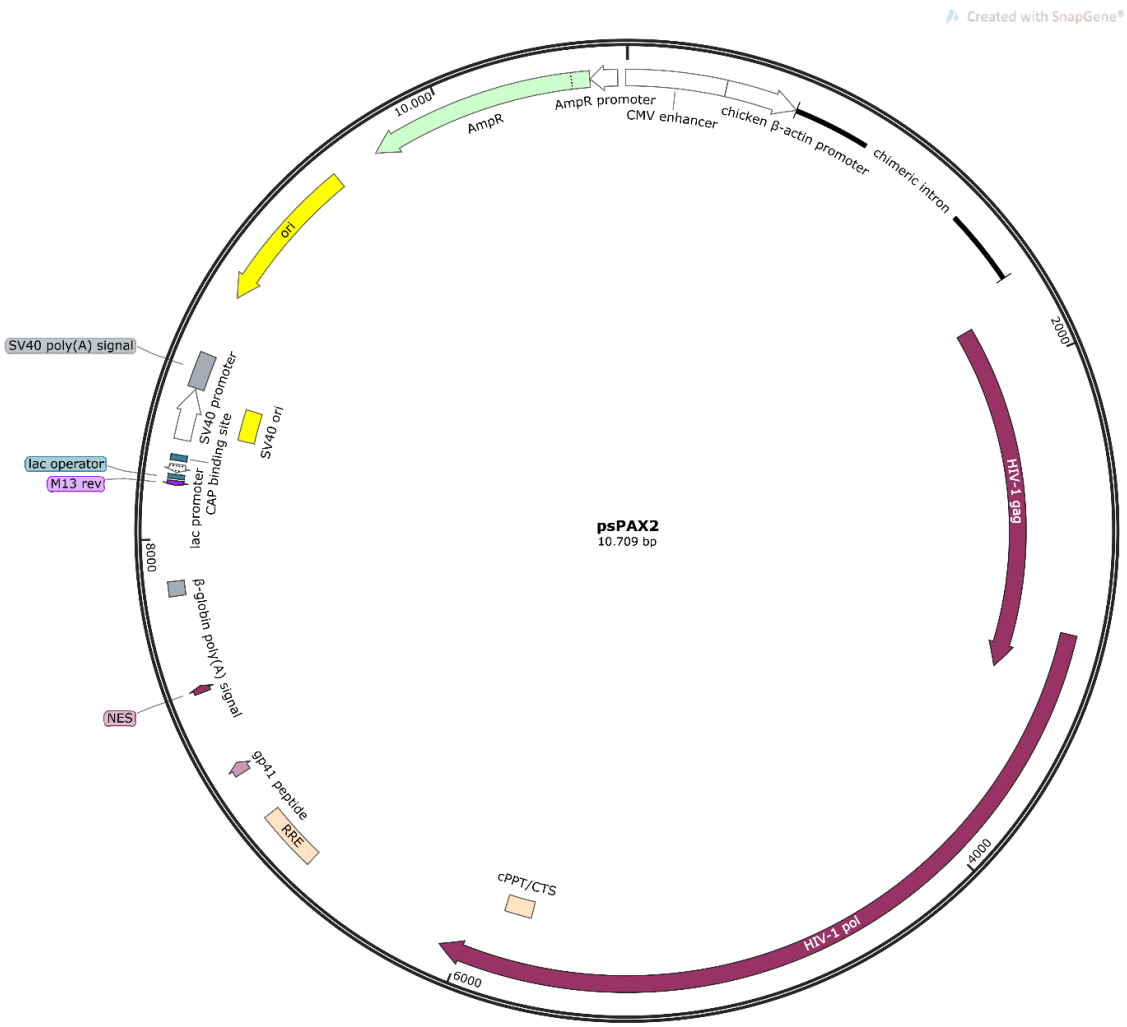

Figure S 39 Plasmid map of psPAX2. *Lentiviral packaging plasmid coding the HIV-1 gag and the HIV-1 pol gene.*

Figure S 40 Plasmid map of pFLAG-PB-Transposase. *Eukaryotic expression plasmid coding the PiggyBac transposase.*

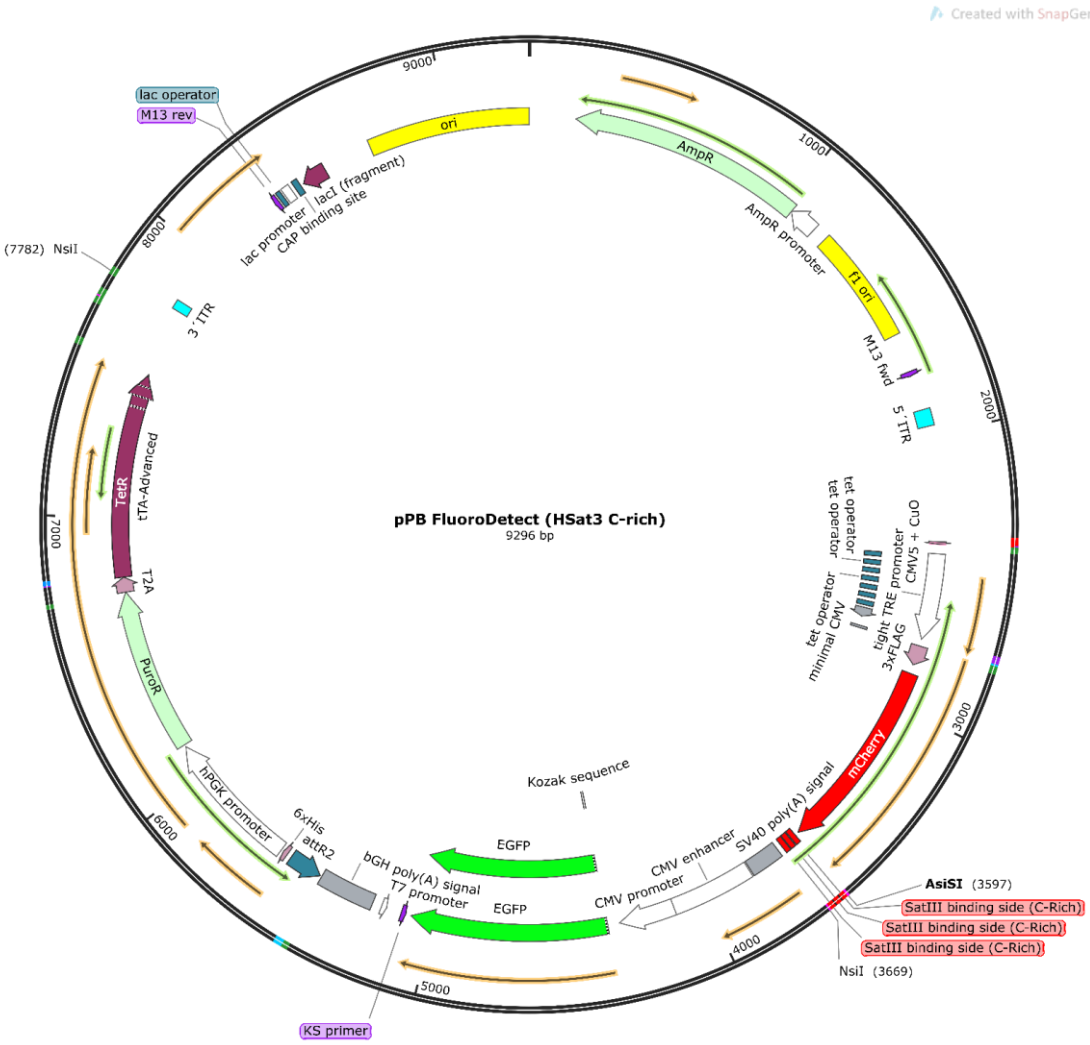

Figure S 41 Plasmid map of pPB FluoroDetect (HSat3 C-rich). *PiggyBac transposon plasmid containing the FluoroDetect (HSat3 C-rich) assay.*

Figure S 42 Plasmid map of pPB FluoroDetect (HSat3 G-rich). *PiggyBac transposon plasmid containing the FluoroDetect (HSat3 G-rich) assay.*

Figure S 43 Plasmid map of pPB FluoroDetect (EGFR). *PiggyBac transposon plasmid containing the FluoroDetect (EGFR) assay.*

Figure S 44 Plasmid map of pPB FluoroDetect (EGFR). *PiggyBac transposon plasmid containing the FluoroDetect (EGFR) assay.*

Table S 1 List of used pegRNA and gRNA sequences.

RNA Name	Sequence (5'-3')
pegRNA EGFR K.O. (Exon L41*)	mA*mG*mU*mA*rArCrArArGrCrUrCrArCrGrCrArGrUrUr GrUrUrUrUrArGrArGrCrUrArGrArArArUrArGrCrArArGr UrUrArArArArUrArArGrGrCrUrArGrUrCrCrGrUrUrArUr CrArArCrUrUrGrArArArArArGrUrGrGrCrArCrCrGrArGr UrCrGrGrUrGrCrArArArArGrUrGrCrCrCrUrArCrUrGrCr GrUrGrArGrCrUrU*mG*mU*mU*mA
EGFR K.O. gRNA #1 (Exon 2, L41*)	mG*mA*mG*rUrArArCrArArGrCrUrCrArCrGrCrArGrUr GrUrUrUrUrArGrArGrCrUrArGrArArArUrArGrCrArArGr UrUrArArArArUrArArGrGrCrUrArGrUrCrCrGrUrUrUr ArUrCrArArCrUrUrGrArArArArArGrUrGrGrCrArCrCr GrArGrUrCrGrGrUrGrCmU*mU*mU*rU
EGFR K.O. gRNA #2 (Exon 9, G343*)	mG*mU*mG*rUrGrUrArArCrGrGrArArUrArGrGrUrArUr GrUrUrUrUrArGrArGrCrUrArGrArArArUrArGrCrArArGr UrUrArArArArUrArArGrGrCrUrArGrUrCrCrGrUrUrUr ArUrCrArArCrUrUrGrArArArArArGrUrGrGrCrArCrCr GrArGrUrCrGrGrUrGrCmU*mU*mU*rU

Table S 2 List of engineered cell lines.

Cell line
HeLa FluoroDetect Hsat3 C-Rich
HeLa FluoroDetect Hsat3 G-Rich
HeLa EGFR K.O.
HeLa EGFR K.O. FluoroDetect Hsat3 C-Rich
HeLa EGFR K.O. FluoroDetect Hsat3 G-Rich
MDA MB 231 FluoroDetect Hsat3 C-Rich
MDA MB 231 FluoroDetect Hsat3 G-Rich
MDA MB 231 EGFR K.O.
MDA MB 231 EGFR K.O. FluoroDetect Hsat3 C-Rich
MDA MB 231 EGFR K.O. FluoroDetect Hsat3 G-Rich
SW480 FluoroDetect Hsat3 C-Rich
SW480 FluoroDetect Hsat3 G-Rich
SW480 EGFR K.O.
PC9 FluoroDetect Hsat3 C-Rich
PC9 FluoroDetect Hsat3 G-Rich
PC9 EGFR K.O.

Table S 3 Sequences of used siRNAs and ASOs.

Name	Sequence (5'-3')
siHSat3	5'- UGGAAUGGAAUGGAAUGGAdTdT-3' 3'- dTdTACCUUACCUUACCUUACCU -5'
siCo	Unknown (IP of IDT)
ASO C-rich (HSat3)	5'-mU*mC*mC*mA*mU*T*C*C*A*T*T*C*C*A*mU*mU*mC*mC*mA-3'
ASO G-rich (HSat3)	5'-mU*mG*mG*mA*mA*T*G*G*A*A*T*G*G*A*mA*mU*mG*mG*mA -3'
ASO HSF1	5'-mU*mU*mU*mC*mC*G*G*A*A*G*C*C*A*T*A*C*mA*mU*mG*mU*mU-3'
ASO EGFR	5'-mA*mC*mA*mC*mU*T*T*G*C*G*G*C*A*A*G*G*mC*mC*mC*mU*mU-3'

Table S 4 Sequences of used reverse transcription and qPCR primers.

Primer Name	Sequence (5'-3')
eGFP qPCR FW	TTCTTCAAGTCCGCCATGCC
eGFP qPCR RV	GTTGTACTCCAGCTTGTGCC
mCherry qPCR FW	CCGACTACTTGAAGCTGTCC
mCherry qPCR RV	ACCTTGTAGATGAACTCGCC
HPRT1 qPCR FW	TGACACTGGCAAAACAATGCA
HPRT1 qPCR RV	GGTCCTTTTCACCAGCAAGCT
M13	CCGTAAAACGACGGCCAG
HuR98	AATCAACCCGAGTGCAATCG
FSM13	CCGTAAAACGACGGCCAGTCAGTGGAAGGCATTAGAATCAAC
RSM13	CCGTAAAACGACGGCCAGTTCCCTTCCATTCCATTATTATCC
Random Hexamers	NNNNNN

Table S 5 Sequences of used IVT templates.

Template Name	Sequence (5'-3')
2.0 FW	TAATACGACTCACTATAGGAATGGAATGGAATGGAACCGGACGGAT-TTAATCGCCGTAGAAAAGCATGTCAAAGCCGGAACCGTCC
2.0 RV	ATTATGCTGAGTGATATCCTTACCTTACCTTACCTTGGCCTGCCTAAATT-AGCGGCATCTTTTCGTACAGTTTCGGCCTTGGCAGG
2.1 FW	TAATACGACTCACTATAGGAAUGGAAUGGAAUGGAAGGACGGAUUU-AAUCGCCGUAGAAAAGCAUGUCAAAGCCGGAACCGUCC
2.1 RV	ATTATGCTGAGTGATATCCTTACCTTACCTTACCTTCCTGCCTAAATTAGCGG-CATCTTTTCGTACAGTTTCGGCCTTGGCAGG

Table S 6 Sequences of used sequencing primers.

Primer Name	Sequence (5'-3')
3' LTR (DeltaU3) FW	GCTAATTCACTCCCAACG
3' LTR (DeltaU3) RV	CGTTGGGAGTGAATTAGC
3'ITR RV	AACCCTAGAAAGATAGTCTGCG
AmpR FW	CTATGTGGCGCGGTATTATCC
AmpR RV	ATAATACCGCGCCACATAGC
bGH poly (A) RV	ATGGCTGGCAACTAGAAGG
CMV FW	CGCAAATGGGCGGTAGGCGTG
CMV Minimal FW	GGTAGGCGTGTACGGTGG
EGFP FW	CGACCACATGAAGCAGCACG
EGFP RV	CGTGCTGCTTCATGTGGTCG
Firefly FW	TGCTCCCTTCTACCCTCTGG
Firefly RV	CCAGAGGGTAGAAGGGAGCA
HIV-1 PSI FW	CTCTCTCGACGCAGGACT
HIV-1 PSI RV	AGTCCTGCGTCGAGAGAG
hPGK-F	GTGTTCCGCATTCTGCAAGC
hPGK-R	GCTTGCAGAATGCGGAACAC
M13 FW	TGTAAAACGACGGCCAG
M13 RV	CAGGAAACAGCTATGAC
mCherry FW	CTCCTCCGAGCGGATGTACC
mCherry RV	GGTACATCCGCTCGGAGGAG
mRFP1 FW	CTTCCACCGAACGTATGTACC
pCW57.1 TET FW	CAGAGCTCGTTTAGTGAACC
pCW57.1 TET RV	GGTTCACTAAACGAGCTCTG
PuroR FW	GCAGCAACAGATGGAAGGC
PuroR RV	GCCTTCCATCTGTTGCTGC
Renilla FW	CGAGAAGCACGCCGAGAACG
Renilla RV	CGTTCTCGGCGTGCTTCTCG
RF #1 pCW57.1 FW	GGGTTTATTACAGGGACAGC
RF #1 pCW57.1 RV	GCTGTCCCTGTAATAAACCC
SV40 Poly (A) RV	GGACAAACCACAACTAGAATGCAGTG
TetR FW	CCTGACGACAAGGAAACTCGC
TetR RV	GCGAGTTTCCTTGTCGTCAGG

Statutory declaration

I hereby declare that I have completed this report independently and without the use of unauthorized third-party aids and without the use of any other aids than those specified. The data and concepts taken directly or indirectly from other sources are marked with the source. This also applies to sources from my own work. I certify that I have not previously submitted this work or uncited parts of it in any other examination procedure. I am aware that my work can be checked for unmarked adoption of third-party intellectual property for the purpose of plagiarism comparison using plagiarism detection software. I certify that the electronic form of my work is identical to the printed version.

Partial publications:

Heß F, Odenthal M, Wasserburger-Zichel E, Grimm C, Schweiger MR, Development of a dual fluorescence-based reporter assay for real time determination of siRNA and antisense oligo nucleotide mediated knock down, Molecular Therapy - Nucleic Acids (2025), doi: https://doi.org/10.1016/j.omtn.2025.102631.

I confirm that all information provided is true to the best of my knowledge and belief, and I undertake to notify the doctoral committee immediately of any changes relating to the above information.

Cologne, 19th May 2026	Felix Heß
Place, date	Signature of the author

Selbstständigkeitserklärung

Ich versichere, dass ich die von mir vorgelegte Dissertation selbstständig angefertigt, die benutzten Quellen und Hilfsmittel vollständig angegeben und die Stellen der Arbeit -einschließlich Tabellen, Karten und Abbildungen -, die anderen Werken im Wortlaut oder dem Sinn nach entnommen sind, in jedem Einzelfall als Entlehnung kenntlich gemacht habe; dass diese Dissertation noch keiner anderen Fakultät oder Universität zur Prüfung vorgelegen hat; dass sie - abgesehen von unten angegebenen Teilpublikationen -noch nicht veröffentlicht worden ist sowie, dass ich eine solche Veröffentlichung vor Abschluss des Promotionsverfahrens nicht vornehmen werde. Die Bestimmungen dieser Promotionsordnung sind mir bekannt. Die von mir vorgelegte Dissertation ist von Prof. Dr. med. Dr. rer. nat. Michal R. Schweiger betreut worden.

Teilpublikationen:

Heß F, Odenthal M, Wasserburger-Zichel E, Grimm C, Schweiger MR, Development of a dual fluorescence-based reporter assay for real time determination of siRNA and antisense oligo nucleotide mediated knock down, Molecular Therapy - Nucleic Acids (2025), doi: https://doi.org/10.1016/j.omtn.2025.102631.

Ich versichere, dass ich alle Angaben wahrheitsgemäß nach bestem Wissen und Gewissen gemacht habe und verpflichte mich, jedmögliche, die obigen Angaben betreffenden Veränderungen, dem Promotionsausschuss unverzüglich mitzuteilen.

Köln, den 19.05.2026	Felix Heß
Ort, Datum	Unterschrift des Autors